Dye Sensitized Solar Cells: From Liquid Electrolytes to Solid State Hole Transport Materials

Inauguraldissertation

zur

Erlangung der Würde eines Doktors der Philosophie

vorgelegt der

Philosophisch-Naturwissenschaftlichen Fakultät

der Universität Basel

von

Ewald Schönhofer

aus Stalden (VS)

Basel, 2015

Genehmigt von der Philosophisch-Naturwissenschaftlichen Fakultät auf Antrag von:

Prof. Dr. Edwin C. Constable

Prof. Dr. Marcel Mayor

Basel, den 11.11.2014

Prof. Dr. Jörg Schibler

Dekan

Namensnennung-Keine kommerzielle Nutzung-Keine Bearbeitung 3.0 Schweiz
(CC BY-NC-ND 3.0 CH)

Sie dürfen: **Teilen** — den Inhalt kopieren, verbreiten und zugänglich machen

Unter den folgenden Bedingungen:

Namensnennung — Sie müssen den Namen des Autors/Rechteinhabers in der von ihm festgelegten Weise nennen.

Keine kommerzielle Nutzung — Sie dürfen diesen Inhalt nicht für kommerzielle Zwecke nutzen.

Keine Bearbeitung erlaubt — Sie dürfen diesen Inhalt nicht bearbeiten, abwandeln oder in anderer Weise verändern.

Wobei gilt:

- **Verzichtserklärung —** Jede der vorgenannten Bedingungen kann **aufgehoben** werden, sofern Sie die ausdrückliche Einwilligung des Rechteinhabers dazu erhalten.
- **Public Domain (gemeinfreie oder nicht-schützbare Inhalte) —** Soweit das Werk, der Inhalt oder irgendein Teil davon zur Public Domain der jeweiligen Rechtsordnung gehört, wird dieser Status von der Lizenz in keiner Weise berührt.
- **Sonstige Rechte —** Die Lizenz hat keinerlei Einfluss auf die folgenden Rechte:
    - Die Rechte, die jedermann wegen der Schranken des Urheberrechts oder aufgrund gesetzlicher Erlaubnisse zustehen (in einigen Ländern als grundsätzliche Doktrin des **fair use** bekannt);
    - Die **Persönlichkeitsrechte** des Urhebers;
    - Rechte anderer Personen, entweder am Lizenzgegenstand selber oder bezüglich seiner Verwendung, zum Beispiel für **Werbung** oder Privatsphärenschutz.
- **Hinweis —** Bei jeder Nutzung oder Verbreitung müssen Sie anderen alle Lizenzbedingungen mitteilen, die für diesen Inhalt gelten. Am einfachsten ist es, an entsprechender Stelle einen Link auf diese Seite einzubinden.

Quelle: http://creativecommons.org/licenses/by-nc-nd/3.0/ch/ Datum: 12.11.2013

Contents

Acknowledgements

I'd like to start by expressing my gratitude to my Ph.D. supervisors, Prof. Dr. Edwin C. Constable and Prof. Dr. Catherine E. Housecroft. For the last four years, I have received a lot of support from them which I am very thankful for. Furthermore, I'd like to thank Prof. Dr. Marcel Mayor for being my co-referee and co-examiner. Dr. Francesca Paganelli and Prof. Dr. Uwe Pieles are gratefully acknowledged for the collaboration in the beginning of my Ph.D. Dr. Thilo Glatzel, Gino Günzburger, Res Jöhr and Ives Pellmont from the physics department are also gratefully acknowledged for all their help. In addition, Liselotte Siegfried is thanked for all her assistance in solar cell fabrication. Thank you to Dr. Colin Martin for conducting SECM measurements. Werner Kirsch and Sylvie Mittelheisser have my gratitude for measuring elemental analyses. I also thank Dr. Jennifer Zampese and Dr. Markus Neuburger for resolving crystal structures. A big thank you goes to PD Dr. Daniel Häussinger, Dr. Heiko Gsellinger and Kaspar Zimmerman for maintaining all the NMR related infrastructure and to Nik Hostettler and Catherine Ertl for conducting NMR measurements. Thank you to Dr. Sven Brauchli and Steffen Müller for ESI and Maldi measurements. Furthermore, I thank Beatrice Erismann for managing all administrative issues and Dr. Bernhard Jung for his assistance in IT questions. Markus Hauri is gratefully mentioned for all material and security matters. The "Werkstatt Team" is acknowledged for fabricating custom made instruments for this work. My gratitude also belongs to the whole team of the "Zentrum für Mikroskopie der Universität Basel" (ZMB) as well as Dr. Collin Morris for their help with FIB/SEM and EDX measurements. Dr. Monika Schönenberger is gratefully acknowledged for AFM measurements. I want to thank Annika Büttner, Martina Garni and Alexandra Wiesler for all their efforts and work during their Wahlpraktika. Dr. Iain A. Wright and Dr. Emma Dunphy are gratefully mentioned for giving me some of their compounds for dye synthesis. Furthermore I thank Prof. Dr. Catherine E. Housecroft and Dr. Biljana Bozic-Weber for proof reading this thesis.

I am deeply grateful for the good atmosphere I had the pleasure to work in which was established by many current and former members of the Constable–Housecroft group as well as some people from other groups. I have really enjoyed your friendship and company in and outside working hours. Thank you for that.

For Financial support, the European Research Council (Advanced grant 267816 LiLo), the Swiss National Science Foundation and the University of Basel are gratefully acknowledged.

Abstract

There is a pressing need to find alternatives for polluting and often non-sustainable fossil fuels. An obvious alternative energy source is the sun, which sends more than enough energy to Earth to satisfy mankind's (current) demands. Modern commercial solar cell technology is still mainly based on silicon, which has to meet very high purity standards and is therefore expensive relative to fossil fuels. A viable alternative could be dye sensitized solar cells (DSCs), which operate with the much cheaper semiconductor titanium dioxide (TiO_2). Since the light is absorbed by a dye rather than the bulk semiconductor material itself, a DSC is much more versatile then a silicon based solar cell.

This thesis discusses the development of dye sensitized solar cells in terms of semiconductor fabrication as well as dye development. Several types of dye sensitized solar cells have been fabricated and tested for various copper(I) and ruthenium(II) dyes. The emphasis was on solid state dye sensitized solar cells (ssDSCs) since liquid electrolyte type DSCs (leDSCs) have a stability disadvantage due to possible leakage and evaporation. SsDSCs rely on a solid hole conductor for charge transport rather than on a liquid electrolyte and charge transport is more dependent on charge hopping through the hole transport material (HTM) than on diffusion of charge carrying ions, like in leDSCs. Among the top performing dyes today are often transition metal complexes based on ruthenium, one of the standards being the ruthenium(II) dye N719. All cell development parts of this thesis (Chapters 3-5) have been almost exclusively conducted with this dye. Since ruthenium is not very abundant in the Earth's crust compared to other metals, the focus in dye development was laid on the cheaper transition metal copper in the last chapter.

Chapter 1 gives a general introduction about energy needs of mankind and why we need to find alternative ways of saturating them.

Chapter 2 gives an overview of the methods and materials used for solar cell fabrication and characterization.

In **Chapter 3**, liquid electrolyte DSCs (leDSCs) based on an I^-/I_3^- redox electrolyte have been fabricated and optimized with home made TiO_2 particles and layers. Not only the bare electrodes, but also scattering layers, whose function it is to retain the light longer in the DSC itself, have been fabricated and tested.

Chapter 4 contains cell development on ssDSCs based on copper(I) iodide (CuI) as the HTM.

In **Chapter 5**, ssDSCs employing polyethylenedioxythiophene (PEDOT) as the HTM have

been assembled and tested for performance.

In **Chapter 6**, several copper(I) metalorganic complex dyes incorporating back to back ligands have been tested for leDSCs and PEDOT ssDSCs. Those dyes have been compared to the standard ruthenium dye (N719) in cell performance.

Chapter 7 Is the conclusion of this thesis.

Experimental and specific cell fabrication details are included in each chapter separately.

Abbreviations

BMII	1-butyl-3-methyl imidazolium iodide
C. electrode	counter electrode
C. layer	compact layer
CO_2	carbon dioxide
CuI	copper(I) iodide
DBEDOT	2,5-Dibromo-3,4-ethylenedioxythiophene
DMSO	dimethyl sulfoxide
DSC	dye sensitized solar cell
e^-	electron
e.g.	exempli gratia (Latin: for example)
FF	fill factor
FTO	fluorine doped tin oxide
h^+	electron hole
HTM	hole transport material
HOMO	highest occupied molecular orbital
I_{SC}	short circuit current
J_{SC}	short circuit current density
LCCT	ligand centered charge transfer
LUMO	lowest unoccupied molecular orbital
leDSC	liquid electrolyte dye sensitized solar cell
Li-TFSI	bis(trifluoromethane)sulfonimide lithium salt
MALDI-TOF	matrix-assisted laser desorption ionization - time of flight
MeCN	acetonitrile
MLCT	metal to ligand charge transfer
MPII	1-Methyl-3-propylimidazolium iodide
nm	nanometer
N719	di-tetrabutylammonium cis-bis(isothiocyanato) bis(2,2'-bipyridyl-4,4'-dicarboxylato)ruthenium(II)
PCE	power conversion efficiency
PEDOT	poly(3,4-ethylendioxythiophene)
Si	silicon
SECM	scanning electrochemical microscopy
spiro-OMeTAD	2,2',7,7'-tetrakis(N,N-di-*p*-methoxyphenylamine) 9,9'-spirobifluorene
ssDSC	solid state dye sensitized solar cell
TiO_2	titanium dioxide

TLC	thin layer chromatography
THT	triethylamine hydrothiocyanate
V_{OC}	open circuit voltage

Chapter 1

Introduction

1.1 Mankind's Energy Needs

From the dawn of human civilisation around 5-7 million years ago to about 1800 A.D., it took the biggest part of human history to reach a population of one billion individuals. After the industrial revolution with all its discoveries (e.g. steam engines [1] and vaccines [2]), the population has grown explosively. Around 1930, it reached the 2 billion mark. What had taken millions of years before was repeated in a mere 130 years. To drive all these new engines a lot of fuel was needed. Since there was a lack of firewood in 18th century Britain (where the industrial revolution started), coal seemed to be the ideal alternative. It was very abundant and usable in its natural form. [3] Coal, along with other fossil fuels like petroleum and natural gas have been formed from dead organic material through geological transformation processes over millions of years. However, burning them is a much faster process. The population has continued to grow and by 2013 it reached 7.2 billion people. By 2100, around 10.9 billion individuals are estimated to live on planet earth. [5] Since the start of the industrial revolution, mankind has relied more and more on fossil fuels. The statistical review of world energy 2014 from BP (former British Petroleum, now Beyond Petroleum) [4] shows the world energy consumption of the year 2013 by fuel

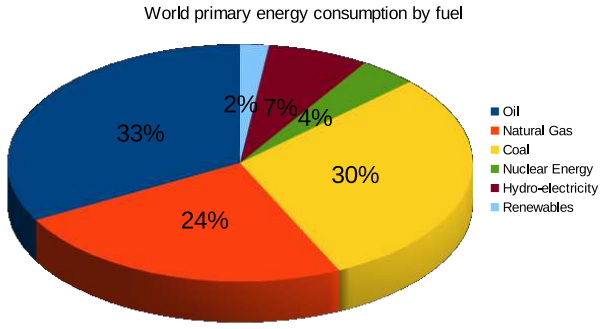

Figure 1.1: World energy consumption by fuel type in percent. Oil was measured in million tons, other fuels in million tons of oil equivalent. [4]

type (See Figure 1.1). Provided current consumption levels stagnate, the remaining natural oil reserves are estimated to last for another 40-50 years, gas reserves for 70 years and coal should be sufficient for more than 200 years to come. [6] It is highly unlikely though that consumption levels will not increase, since rapidly growing economies like China and India will bring a constant increase in global demand. According to the International Energy Agency (IEA), fossil fuels will continue to play a major role in the foreseeable future. One thing however is clear, they will not last forever. [6] Apart from not being infinitely accessible, fossil fuels also have negative effects on the environment by enhancing the natural greenhouse effect and causing global warming. A simplified model of the greenhouse effect is outlaid in Figure 1.2. When sunlight hits the Earth about two thirds of its energy is

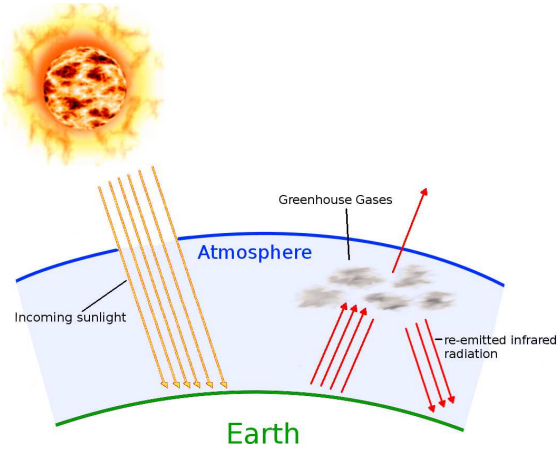

(a) Simplified scheme of the greenhouse effect.

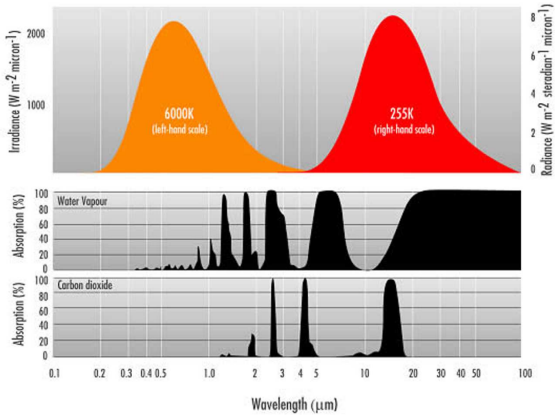

(b) Absorption spectra of water and carbon dioxide compared to the infrared radiation emitted by the Earth. [7]

Figure 1.2: The greenhouse effect

absorbed by the planet's surface, the remaining third is reflected directly back into space by the atmosphere. For the earth to be at a constant temperature, the incoming radiation energy of the sun must equal the outgoing energy. However, the radiation leaving the planet's surface has a much longer wavelength, primarily in the infrared part of the spectrum. This back-scattered irradiation can be absorbed partly by the atmosphere and is therefore warming the planet. The Earth's atmosphere consists largely of nitrogen (78 %) and oxygen (21 %). Both of these gases do not absorb wavelengths in the infrared region very well and hence do not have a big part in the greenhouse effect. More potent greenhouse gases in the atmosphere are water, carbon dioxide (CO_2), methane, chlorofluorocarbons, nitrous oxide and ozone. Although CO_2 (see Figure 1.2b) and other gases as well are basically transparent to the incoming radiation of the sun, the radiation reflected from earth is in the infrared region, exactly where the primary absorbtion band of CO_2 is.

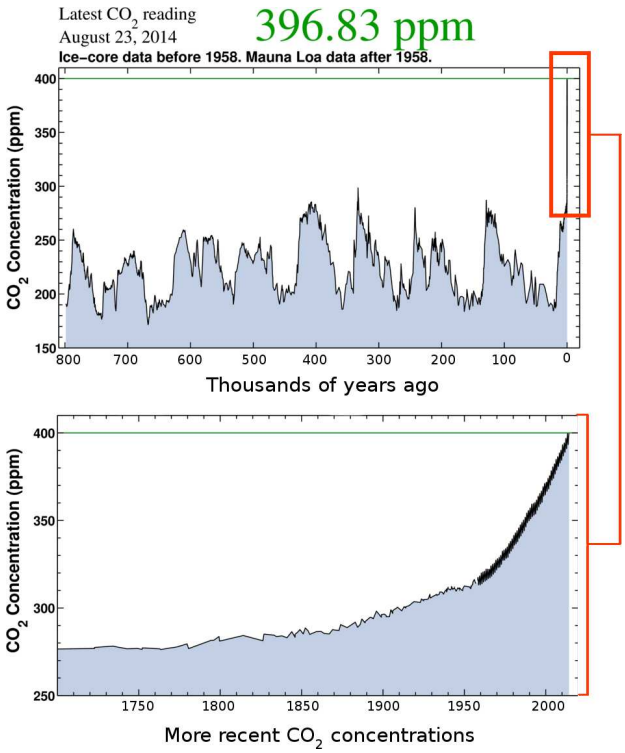

Figure 1.3: CO_2 concentrations from 800000 years ago until the present. [8]

The water in the atmosphere absorbs strongly in the 4-6 µm wavelength region, whereas CO_2 absorbs at 13-19 µm. Most of the outgoing radiation escapes between 7 and 13 µm. The planet has a natural background level of 270 ppm carbon dioxide (CO_2) in the atmosphere, warming the Earth. Without this effect, the average surface temperature of the Earth would be around -18 °C. [9] Nature builds up and regulates the atmospheric concentrations of greenhouse gases by the oceans, plants and animals. For the last 800'000 years, although there were fluctuations in the CO_2 levels, they were relatively stable and periodical. Figure 1.3 shows the CO_2 concentrations of the last 800'000 years obtained from ice cores drilled in Antarctica. From 1958 on, data was obtained from the Mauna Loa Observatory in Hawai. CO_2 concentration maxima have always been around 270 ppm. From the industrial revolution to the present, in a time span of only $\sim$ 200 years, the maximum value has risen to 400 ppm. A value this high has not been reached in the last 800'000 years. The human contribution to the greenhouse effect is primarily due to burning of fossil fuels and thereby generating CO_2 and other greenhouse gases. These additional CO_2 concentrations intensify the greenhouse effect and warm Earth's climate, which results in more water vapour in the atmosphere even reinforcing the warming cycle. [10] The burning of fossil fuels produces around 21.3 billion tonnes (21.3 gigatonnes) of carbon dioxide (CO_2) per year, but it is estimated that natural processes can only absorb about half of that amount, so there is a net increase of 10.65 billion tonnes of atmospheric carbon dioxide per year. [11] According to the intergovernmental panel on climate change, the human influence on the climate is evident from the increasing greenhouse gas concentrations in the atmosphere. The last three decades have been warmer than any decade since 1850. They also state that it is extremely likely that human influence has been the dominant cause of the global temperature rise since the mid-20th century. [12] Although there are doubtful voices about global warming being an anthropogenic cause, 97% of climate scientists agree that the climate-warming trends over the past century are very likely due to human influence. [13]

1.2 Harnessing the Sun's Energy with Dye Sensitized Solar Cells

To uphold today's society and demands a huge amount of energy is needed. With fossil fuels being widely regarded as having negative effects on the environment and given their limited availability in the future, the question of alternatives arises. Nuclear energy, although not producing greenhouse gases, generates radioactive waste which remains hazardous for thousands of years. Ideally, the energy source should be naturally and constantly replenished, it should be renewable. In 2013, only 2% of all consumed energy stemmed from renewable energies (see Figure 1.1). However, the urge to find an alternative for the limited and often polluting non-sustainable fossil fuels on Earth is imminent. One of the most obvious solutions is the largest natural power source available to Earth, the Sun. The amount of solar energy that hits the surface of the Earth in one hour is greater than the total amount of energy that the entire human population requires in a year. [14] There only needed to be a way of energy harnessing. In 1839, the French physicist Edmond Becquerel experimentally demonstrated the photovoltaic effect [1] for the first time. [15, pp. 6] A solar cell is a device

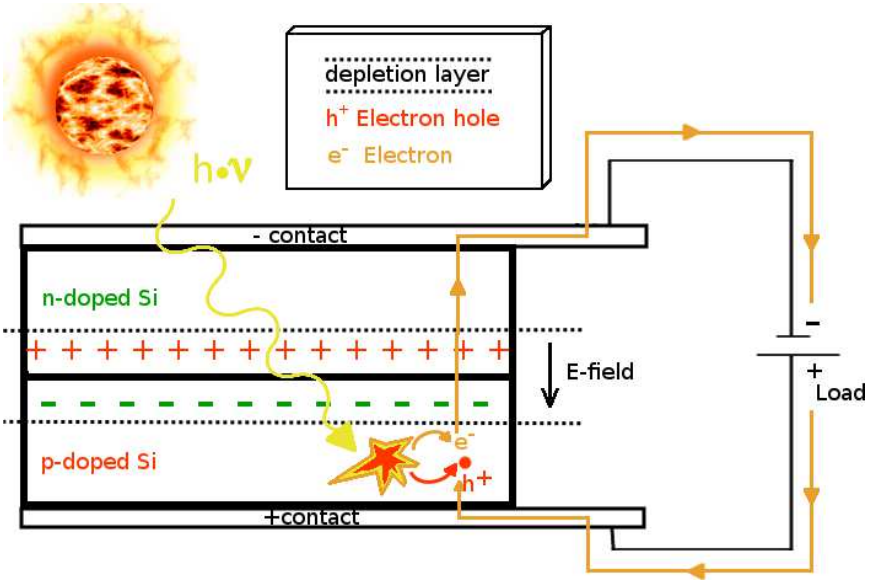

Figure 1.4: Working principle of a silicon heterojunction solar cell.

that uses this effect to generate electricity. 115 years and several inventions later, the first practical solar cell was presented in 1954 by Bell using a silicon waver as the light absorbing material. It had an efficiency of around 4%. Today, this technology has advanced greatly and the average modern commercial wafer-based silicon modules have an efficiency of about

[1] The photovoltaic effect is voltage generation in a material upon exposure to light

16%. In 2013, 90% of all photovoltaic device production relied on this Si-wafer based technology. [16] The laboratory record of mono-crystalline silicon stands at 23%. The principle of such a cell is outlaid in Figure 1.4. As most commercial solar cells today, it featured silicon as the light harvesting and electron conducting material. When light hits the silicon surface, photons are absorbed and electrons extracted from the silicon. By extracting an electron, a positive charge vacancy is generated in the silicon, the electron hole. To give the electron a direction and to prevent it from recombining with the hole, two types of silicon semiconductors are employed in a silicon solar cell, namely p(positive)-type silicon and n(negative)-type silicon. P-type silicon is doped with atoms having one electron less than silicon in their outer energy level like boron or gallium. To form bonds with the surrounding silicon atoms this electron is removed from the bulk generating electron holes and therefore an electron deficiency in the material. N-type silicon is doped with atoms having an extra electron in their outer shell compared to silicon, like phosphorus. The extra electron not involved in the bonding process is free to move in the silicon semiconductor thus generating negative charges. By bringing n and p type silicon together a heterojunction is formed. Electrons from the n-doped silicon diffuse to the p-doped region whereas holes from the p-doped region diffuse to the n-doped silicon. This forms a directional barrier, the depletion zone, in the form of an electric field (see Figure 1.4). By applying a forward bias, electrons are hindered from falling back to the p-doped region by the negative charge in the depletion zone thus minimizing recombination. If the p and the n doped silicon are contacted, electrons will flow against the direction of the electric field around an external circuit and produce a current. [17]. As mentioned above, silicon solar cells are commercially the most successful type of solar cell up to now (90% market share in 2013 [16]). They do have certain disadvantages though. One of the main drawbacks is cost. The fabrication of this type of solar cell requires high purity silicon (99.9999%), which results in high costs and energy payback times. [18] Furthermore, production costs are highly dependent on silicon prices [19], which is also needed in electronics industry. In 1991, Grätzel and O'Regan described a photovoltaic cell based on low to medium cost materials and potentially low cost manufacture. [20] With 7.1-7.9% it featured a realistic commercial energy-conversion efficiency at that time. [21] Since then, the efficiency of DSCs has steadily increased and today lies around 13% for metalorganic dyes. [22] A basic DSC layout is depicted in Figure 1.5. On a lab scale, both contact electrodes usually consist of glass sheets. To make electron transport possible, the glass is covered with a thin conducting layer of fluorine doped tin oxide (FTO). The working electrode features an optically transpartent film of titanium dioxide (TiO_2) nanoparticles on an FTO coated glass sheet. This porous, semiconducting film is then covered with a dye responsible for light harvesting. When light hits the solar cell, the dye is promoted to an excited state, injects an electron into the TiO_2 and is oxidized.

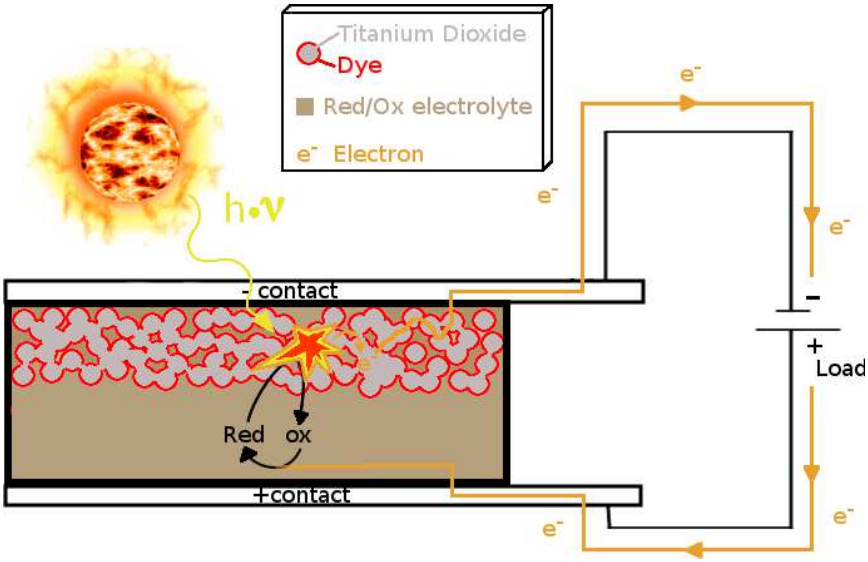

Figure 1.5: Working principle of a DSC.

The dye is reduced again immediately by the redox couple of a liquid electrolyte. Electrons diffuse through the TiO_2 to an external circuit connected to an electrical load. The oxidized electrolyte gets reduced again by the electrons provided by the counter electrode. The detailed working mechanism will be discussed in Chapter 3. Since the light absorption and charge separation processes are separated in this type of cell, it is much more flexible than conventional silicon solar cells. [21] Different chromophores can be used and so the cell is not limited to one material, for example silicon, which has only limited potential for improvement in the light absorbing perspective. Although being a promising alternative to conventional solar cells, DSCs also inherit problems like corrosion, leaking and solvent evaporation due to the liquid and corrosive nature of the electrolyte. This has been addressed by substituting the liquid electrolyte with a solid charge transporter, thus rendering the cell solid state, while keeping the principle of the DSC. Figure 1.6 shows a schematic of such a solid state DSC (ssDSC). The main differences to the liquid electrolyte DSC (leDSC) is the solid state hole transport material (HTM). In ssDSCs, only charges (electrons and holes) are transported rather than ions as in leDSCs. Therefore charge transport is not limited by the diffusion properties of ionic or molecular species. [23] Figure 1.7 shows the solar spectrum that hits the earth's surface. 55% of the radiation lies in the infrared region. The most intense part of the spectrum is visible light, which makes up 40% of the spectrum. [24] Ideally, the dye should be panchromatic, meaning absorbing over all the visible light. [25] Since thin films of TiO_2 appear transparent due to their small particle size (typically $<$50 nm) and absorb mainly in the UV region of the solar spectrum, it is ideally suited as a dye supporting semiconductor. The surface area of this porous network is more than an order of a magnitude greater than the apparent surface area. It is designed as a porous layer to

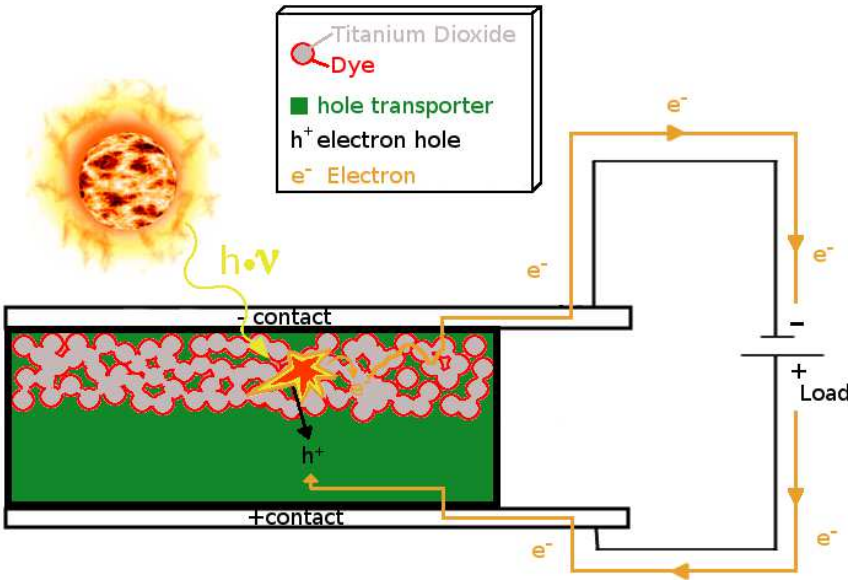

Figure 1.6: Schematic of a ssDSC.

act like a sponge, soaking up dye molecules and trapping light inside. [26] There are three known naturally occuring crystalline forms of titanium dioxide, namely anatase, rutile and brookite. Whereas the anatase and rutile structures have been extensively studied, brookite is naturally much less abundant and hence has been investigated less. Although brookite

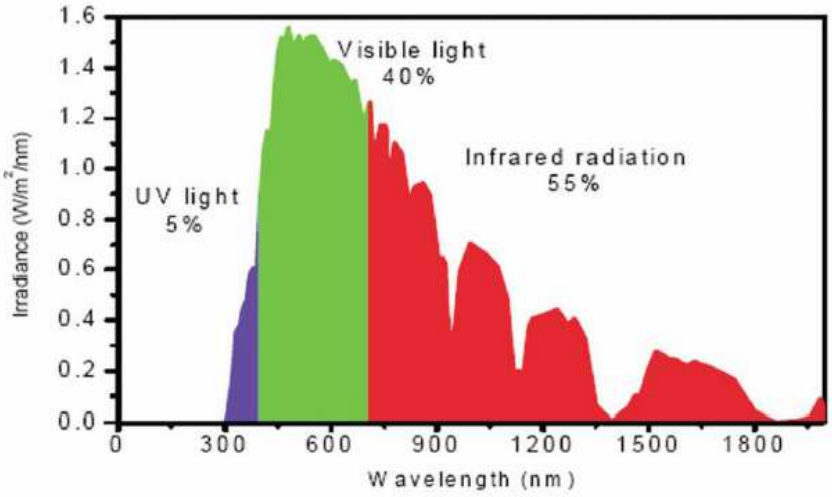

Figure 1.7: Solar spectrum reaching the Earth's surface after having passed the atmosphere. [24]

and rutile inherit a higher thermal stability, their surface area in thin films is believed to be lower than the one of anatase. The conduction band of anatase also lies -0.2 eV above the one of rutile, giving anatase a wider band gap (3.2 eV) compared to rutile (3.0 eV). This leads to potentially higher photovoltages (see Chapter 3) than rutile could provide. [27] [28] [29] In DSCs, the large band gap of the TiO_2 particles <50-70 nm in size (3.2 eV,

wavelength <385nm in the ultraviolet range) leads to an absorption of UV light but not visible light. Unfortunately, only 2-3% of the ultraviolet sunlight can be collected.

1.3 Transition Metal Complexes in Dye Sensitized Solar Cells

In DSCs, as opposed to silicon solar cells, it is the dye that contributes the bulk of the light absorption, not the semiconductor. [30] Transition metal complexes are promising candidates for sensitizers and widely used for DSCs, since additionally to the absorptions of the organic ligand molecules (ligand centered charge transfer (LCCT)), their Metal-to-ligand charge-transfer (MLCT) broadens the absorption of light (See Figure 1.9) [31] [32]. A common example of a Dye used in DSCs is di-tetrabutylammonium cis-bis(isothiocyanato)bis(2,2'-bipyridyl-4,4'-dicarboxylato)ruthenium(II), abbreviated with "N719". Dyesol, a global leader in dye solar cell technology, lists the former as their industry stan-

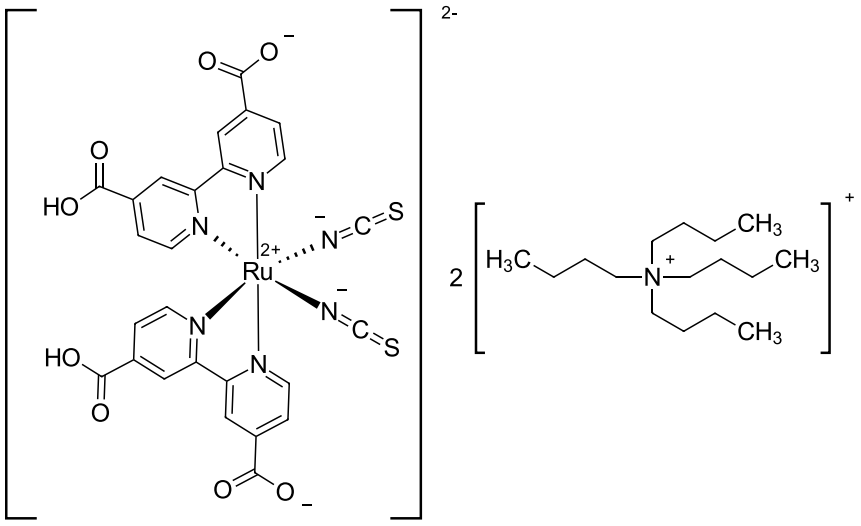

Figure 1.8: Structure of N719

dard. It is the most common high performance dye [33] in general and has therefore been adapted as the standard dye for solar cell configuration testing in this work. Figure 1.8 shows the structure of N719. Figure 1.9 shows an absorption spectrum of N719 with its LCCT and MLCT, resulting in a broad absorption over large regions of the visible spectrum.

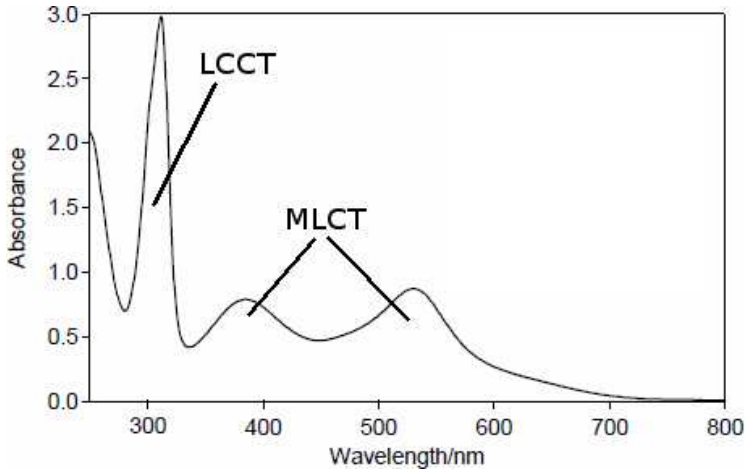

Figure 1.9: Absorption spectrum of N719 in Ethanol [34]

The anchoring to the TiO_2 surface of metalorganic complexes happens through functional groups attached to the ligands of the complex, two of the most common being carboxylic [19, pp. 6632] and phosphonic acids [35].

Chapter 2

Materials and Methods for Dye Sensitized Solar Cells

In the following, general materials and methods used for solar cell development, characterization and performance testing are presented. The structure of a DSC can be described in terms of three main parts, the working electrode, the counter electrode and a hole transport material or liquid electrolyte connecting the two. The working electrode is the one including the TiO_2 layer. Electrode dimensions were almost exclusively 1.5 cm x 2.0 cm, in rare cases 1.6 cm x 2.0 cm. Electrolytes and hole transport materials will not be discussed in detail in this section, since they vary from chapter to chapter.

2.1 General Materials

Fluorine doped tin oxide (FTO) glass plates for working and counter electrodes were purchased from Solaronix: TCO22-7, 2.2 mm thickness, sheet resistance 7 Ω/sq. Ultraviolet Ozone (UVO) cleaning treatments have been carried out with a UVO-Cleaner from Jelight Company, Inc. Model 42A SERIES. The platinum catalyst employed for self made counter electrodes (Platisol T) also was acquired from Solaronix. Commercial TiO_2- pastes used were either 18NR-T transparent titania paste or 90-T transparent titania paste (thin use), both from Dyesol. Commercial P25 TiO_2 nanoparticles used for TiO_2 paste preparation were purchased from Degussa (Evonik). Ethyl cellulose and terpineol for titania pastes were purchased from Aldrich. The standard dye N719 was purchased from Solaronix. Commercial test cell kits including working electrodes, counter electrodes and sealing materials for liquid DSCs were bought from Solaronix (ref 74991). Thicknesses of TiO_2 layers have been measured with a KLA Tencor Alpha-Step D-100 profilometer. Specific reagents and solvents

for electrolytes, paste fabrication and synthetic procedures will be listed in the respective chapters and were either purchased from Sigma-Aldrich, Brunshwig, Acros Organics or abcr.

2.2 Working electrodes

Working electrodes were either acquired commercially from Solaronix test kits or self-fabricated. For self-fabrication of working electrodes, TiO_2 particles were formulated in pastes containing organic binders (e.g. ethyl cellulose), which were deposited in one or multiple layers on an FTO glass substrate. These pastes were either bought from Dyesol (Dyesol 90-T transparent titania paste or Dyesol 18NR-T transparent titania paste) or self-fabricated. The fabrication of TiO_2 particles and pastes is discussed in each chapter separately. For paste deposition onto the FTO-glass sheets, two main procedures were applied, namely doctor blading (Section 2.2.1) and screen printing (Section 2.2.2). After paste deposition, the TiO_2 particles are adhered to each other ant fixated to the FTO glass substrate by a sintering[1] process, which is explained in Section 2.2.3.

2.2.1 Doctor Blading

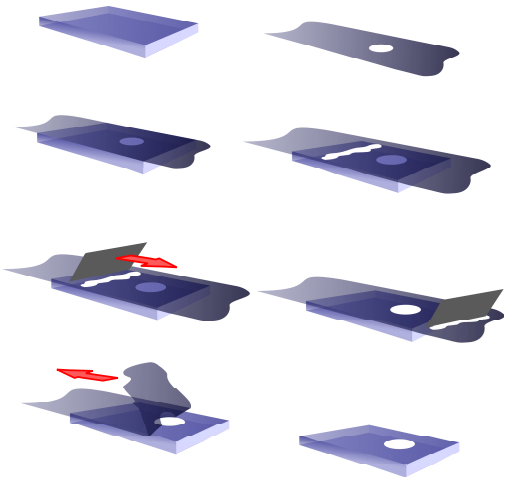

Figure 2.1: Schematic presentation of the doctor blade technique.

The word "doctor blade" was derived from the "ductor blade", which is used in rotogravure printing to remove excess ink from non-engraved areas of an image carrier. [37, pp. 62] It has been extensively used in DSC fabrication on a laboratory scale. Figure 2.1 depicts the actual procedure. A hole of a certain diameter (6.0 mm in this work) and area (0.33 cm^2) is punched into an adhesive tape (in this work Scotch™Magic™3M) strip which is pasted onto the glass sheet serving as the working electrode. After flattening the tape carefully with a glass rod, TiO_2 paste has been applied in front of the tape opening. A slider (usually a glass rod) is then used to fill the opening of the tape with TiO_2 paste. The tape is removed carefully and the electrode is estab-

[1]Sintering is the process of heating a loose powder material below its melting point until its particles adhere to each other. [36]

lished, ready for sintering. The thickness of the TiO_2 layer depends on the thickness of the scotch tape. However, the pressure applied while blading also has an influence on the layer thickness of the final electrode. This is an error source which depends exclusively on the consistency of the operator. For doctor bladed electrodes, an area of ~0.33 cm^2 has been set, which was assessed by optical microscopy measurements.

2.2.2 Screen Printing

Screen printing can eliminate the aforementioned pressure error. For self made electrodes, a custom made fixed aluminium frame and squegee slider have been employed (see Figure 2.2). With this technique, by applying an appropriate printing template frame, multiple TiO_2 electrodes (in this case 40) can be screen printed at once. The TiO_2 paste is pressed through a mesh (90-48Y PET mesh from Serilith AG) coated with a resin except at the 40 spots intended for the print. TiO_2 electrodes have been built up layer wise and depending on the amount of layers the thickness of the electrode can be tuned. First, the mesh is filled with a filling stroke without any glass in the metal (aluminium) base. For the mesh filling step a slider with an angle α of 45° has been found to be suitable. The angle is crucial in this setup. If it is too big the mesh will not be filled to a sufficient amount and electrodes will only be printed partially. If it is too small the TiO_2 is already partially pressed through

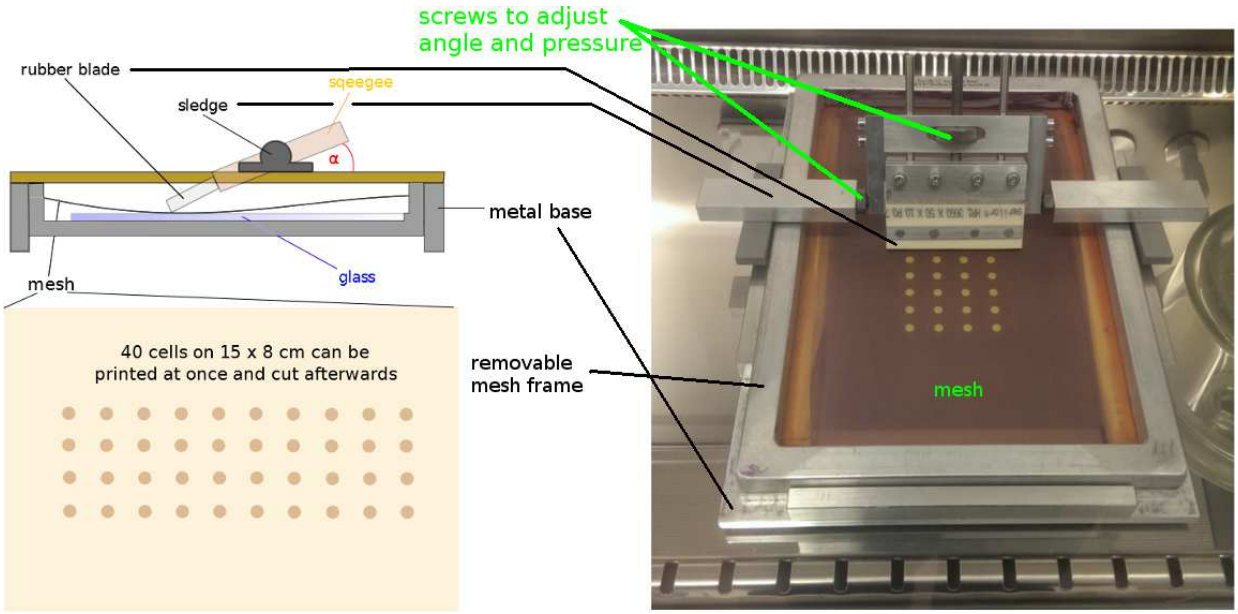

Figure 2.2: Screen printing setup.

the mesh, which results in the paste touching the outer edges of the mesh opening during the print and therefore in broader and less defined spots. After the filling step, a cleaned glass plate of 15 cm x 8 cm is placed into the base of the device. The mesh was then placed

on top, the distance between mesh and glass substrate being 1 mm. Another slider with a steeper angle of 70-80°was slid over the filled mesh and the TiO_2 paste in the pores is pressed onto the glass to print a layer. The pressure of the sliders can be regulated by a hand screw if necessary. It had to be strong enough to ensure a stable print on all the cells but not as strong as to bend the rubber blade too much, leading to an unwanted forceful execution of the print. The freshly printed layer is placed into a desiccator containing a saturated ethanol atmosphere for leveling the layer and thus correcting irregularities. The substrate is left in this ethanol atmosphere for 1.5 minutes for the first layer and for 3 minutes for every successive layer there after. Following each leveling step, the glass plate is placed on a heating plate preheated to 125 °C for 6 minutes to evaporate residues of the ethanol solvent and other liquid components, establishing a firm ground structure for further printing cycles. After the last layer has been printed, the whole electrode glass plate was gradually heated (sintered) according to a temperature ramping program (see Section 2.2.3). If sintered to 450 °C on a hot plate directly[2], the layer structure of the electrode can be observed. Figure 2.3 shows such a quickly heated screen printed electrode featuring 9 layers. By close examination one can see the singular layers. The small stripe which measures around 500 nm in thickness that separates the screen printed TiO_2 layers from the glass is the conducting fluorine doped tin oxide layer. For screen printed electrodes, an area of $\sim$0.288 cm^2 has been set, which was assessed by 3D laser microscopy (Keyence VK–X200).

2.2.3 Sintering of Titanium Dioxide Pastes

Once printed, the electrodes were sintered with a temperature ramp program labeled P1, shown in Figure 2.4, which is an altered version from the literature. [38, pp. 46] P1 sintered electrodes reach 450 °C after around 80 min. Electrodes sintered directly up to 450 °C on a hot plate reach that temperature much faster. Figure 2.5 depicts a hot plate sintered electrode compared to one sintered with P1 in a programmable oven (Nabertherm N 15/65HA). As can be observed, the slower sintered electrode featured much less cracks. This could be partially attributed to the step at 75°C at 30 min. With this temperature just below the boiling point of ethanol and the extended time, most of the residual ethanol will be slowly removed, whereas direct heat up will cause it to evaporate quickly, presumably destroying the layer. In Figure 2.5b, one can still see the mesh imprints from the screen print. This indicates that the electrode has not been left in the ethanol athmosphere for long enough and therefore not all irregularities have been smoothened out.

[2]The electrode with the freshly printed TiO_2 layers was placed on a heating plate and heated up directly to 450 °C as fast as possible.

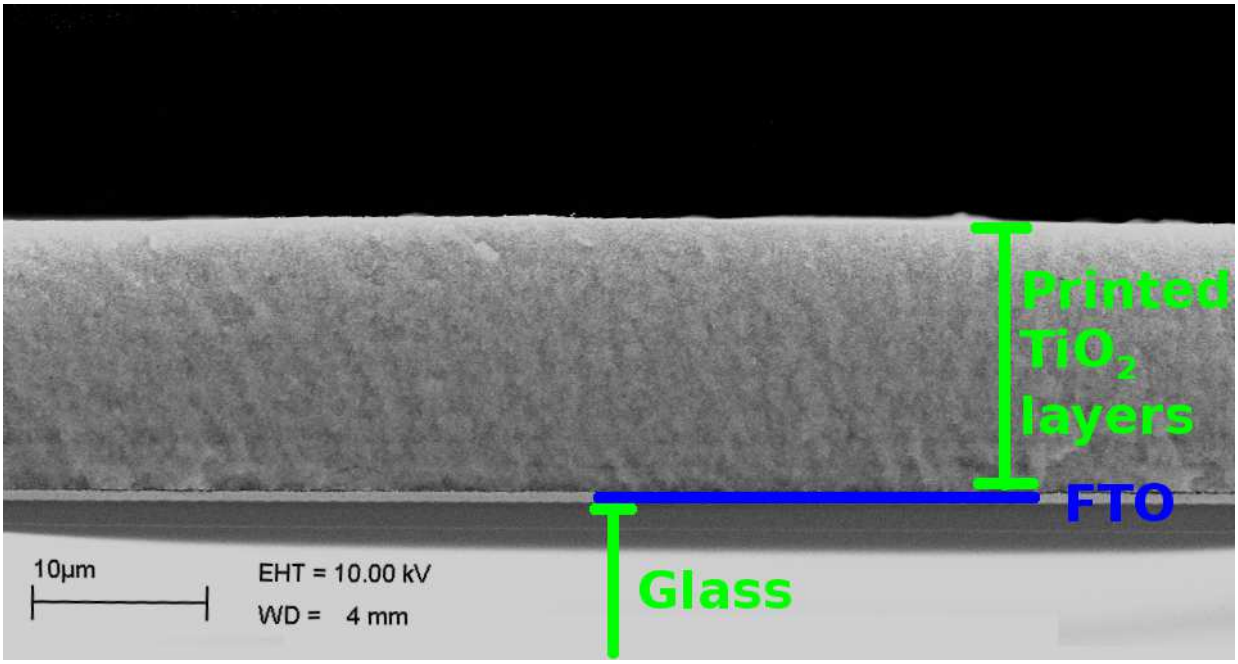

Figure 2.3: Scanning electron microscope (see Section 2.5.5) picture showing the cross section of a quickly sintered screen printed electrode.

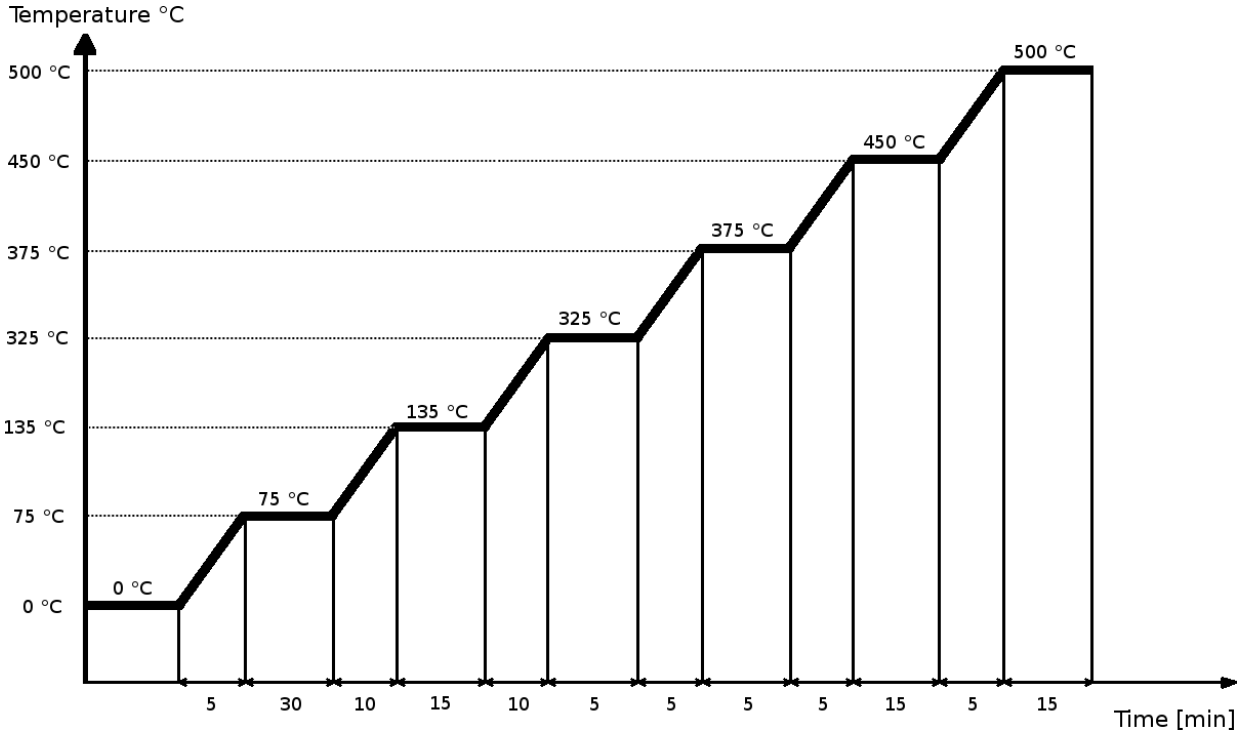

Figure 2.4: Sintering program P1

2.3 Counter electrodes

Counter electrodes have either been used directly from Solaronix test cell kits or self-fabricated. Non-commercial electrodes have been made by applying a platinum precursor

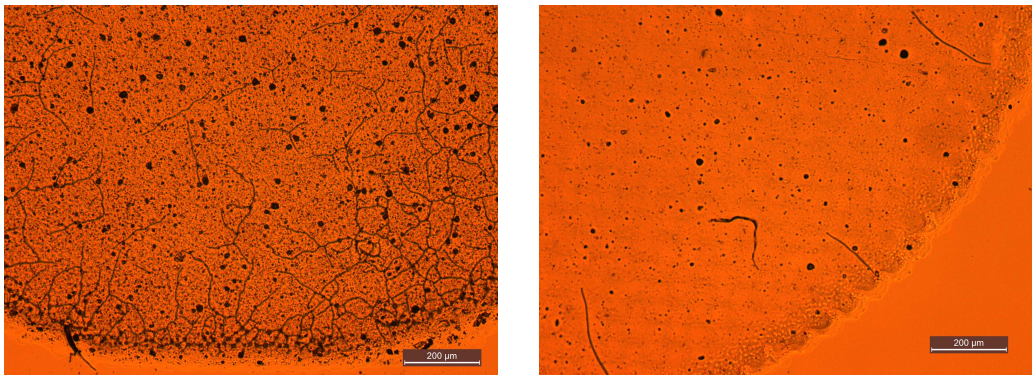

(a) Heating plate sintered electrode (b) Oven sintered electrode

Figure 2.5: Optical microscope pictures of electrodes sintered on directly on a hot plate or in an oven with a temperature ramping program.

solution (Platisol T from Solaronix) on an FTO glass sheet followed by a heat treatment at 450 °for 30 minutes, resulting in an activated platinum layer [39]. For the solid state dye sensitized solar cells in Chapter 5, counter electrodes have been fabricated by solid state polymeristation. A precursor solution of 2,5-dibromo-3,4-ethylenedioxythiophene (DBEDOT) was deposited onto an FTO glass sheet and polymerized by a mild heat treatment, resulting in a conducting polymer film. In some experiments of Chapter 4, the counter electrode (gold or silver) was evaporated on top of the working electrode. Detailed counter electrode fabrication is discussed in each chapter separately.

2.4 Cell assembly

Whereas working electrode and counter electrode of solid state DSCs have merely been glued or clipped together, liquid electrolyte type DSCs have been sealed together with a hot melt sealing foil (Solaronix, Meltonix 1170-25 Series, 25 microns thick) with a soldering iron. To prevent overheating and therefore degradation or desorption of dyes from the TiO_2 surface, a custom made tip was applied, featuring a hole in the middle to spare the active area the bulk of the heat (around 200-250 °C on the soldering iron display). After sealing the electrodes together, electrolyte was filled into the cell through the pre-drilled hole in the platinized counter electrode (around 1 mm in diameter). An Eppendorf pipette tip was pushed into the hole and the construct was placed under a bell-shaped top connected to a Schlenk line. The tools are depicted in Figure 2.6. The cell was evacuated (to at least 10^{-2} mBar) and refilled with nitrogen three times before placing a small amount of electrolyte into the Eppendorf tip. Then vacuum was applied gently until the electrolyte dropped to the bottom of the plastic tip and by switching to nitrogen the electrolyte was pushed into

the cell. Another piece of sealing foil and a small glass cap were used to seal the cell off. Finally, at the contacts of the cell, conducting silver paint was applied.

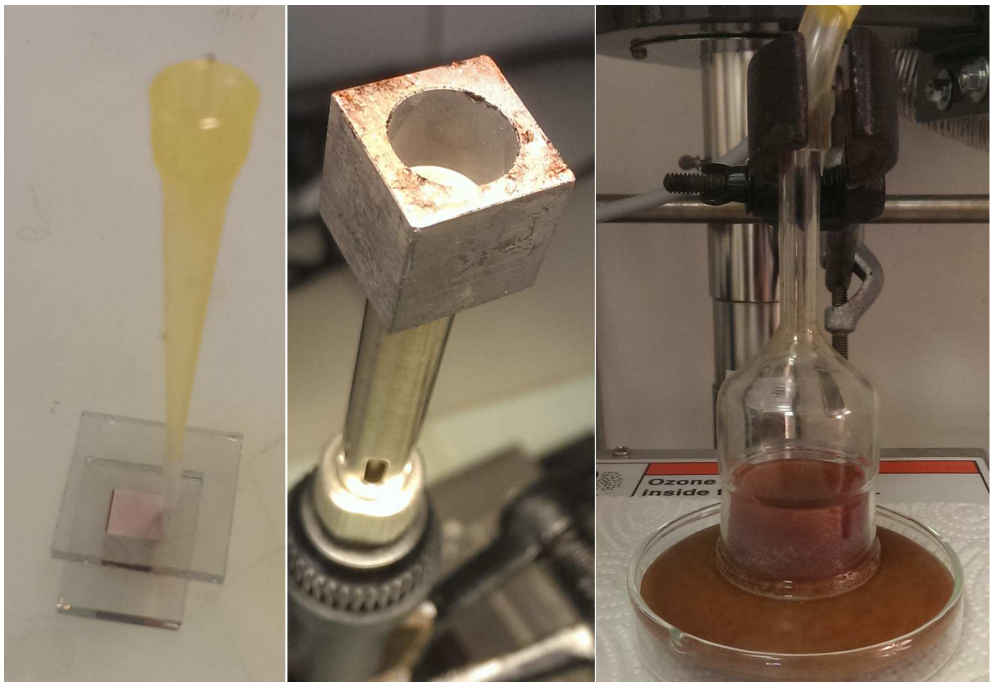

Figure 2.6: Back filling and sealing tools for liquid electrolyte DSCs. On the far left, a DSC right before back filling is depicted.

2.5 Photocurrent Density-Voltage (J-V) Measurements and Performance Parameters

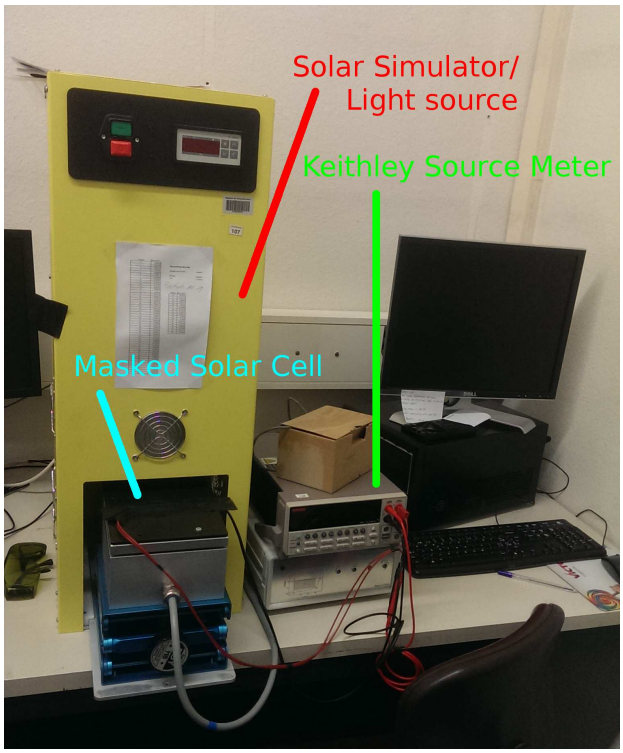

Figure 2.7: IV measurement setup featuring a solaronix solar simulator and a Keithley 2400 source meter

Photocurrent density-voltage measurements were made by irradiating solar cells using a SolarSim 150 solar simulator from Solaronix as the light source. The light irradiance was calibrated to be 100 mW cm^2 = 1 Sun via a silicon photodiode. Figure 2.7 shows the measurement setup. The cells were masked (see Section 2.5.1) and prior to measurement irradiated for 10 minutes [3]. The current produced by the cell was measured against applied voltage by a Keithley 2400 source meter. A typical photocurrent density-voltage-curve is depicted in Figure 2.8. The main parameters used for DSC characterisation were the short circuit current (I_{SC}), the short circuit photocurrent density (J_{SC}), the open circuit voltage (V_{OC}), the fill factor (FF) and the photon to electrical power conversion efficiency (PCE, η). I_{SC} corresponds to the current at 0 V and it is the maximum current the cell can produce. During the measurement the voltage is increased until the cell does not produce any current anymore representing an open circuit. The voltage at this value is the open circuit voltage V_{OC}. It is the maximum voltage the cell can provide to an external circuit. [40] Electrical power is defined as the product of voltage and current. The point of the IV-curve with the most power output is the maximum power point (P_{max}). The voltage and current at P_{max} are labelled I_{max} and V_{max}. The fill factor (FF), which is defined in equation 2.2 is a measure of quality for the solar cell. The maximum theoretical generated electrical power is the product of I_{SC} and V_{OC}. The actual maximum electrical power is given at the maximum power point through the product of V_{max} and I_{max}. The FF is the quotient of these two values and accounts for internal losses in the cell. If no losses were present in the solar cell the fill facor would be 1.

[3] Except for the copper(I) iodide solid state dye sensitized solar cells in Chapter 4, which due to stability problems have been measured directly, without prior irradiation.

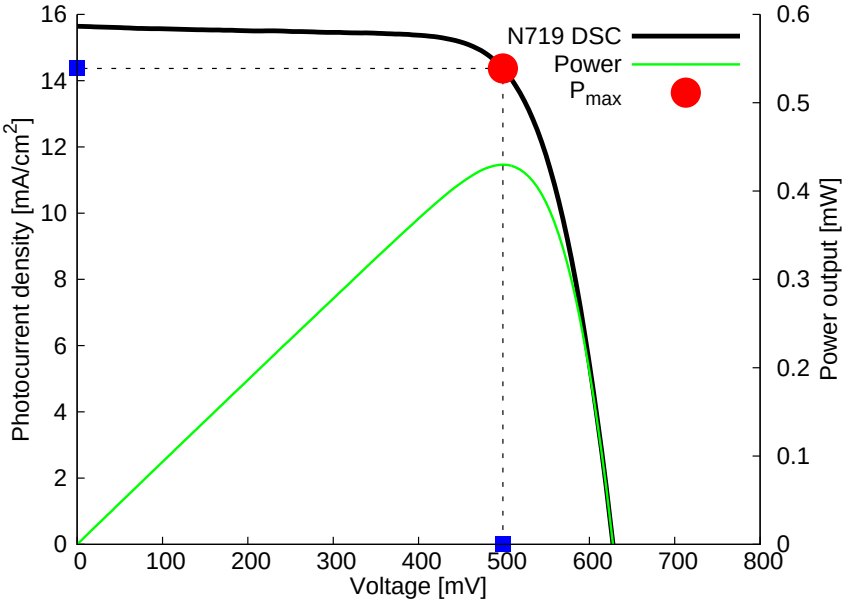

Figure 2.8: J-V measurement of an N719 DSC

Device Name	J_{SC} [mA/cm^2]	I_{SC} [mA]	V_{OC} [mV]	FF [%]	η [%]
N719 DSC	15.7	0.940	628	72.9	7.2

Table 2.1: Parameters of an N719 DSC

The most important parameter of a solar cell is its photon to power conversion efficiency (η), which is also commonly abbreviated with PCE. It can be obtained like described in equation (2.1)

$$\eta = \frac{P_{max}}{P_{in}} = \frac{I_{sc} \cdot V_{oc} \cdot FF}{P_{in}} \tag{2.1}$$

$$FF = \frac{I_{max} \cdot V_{max}}{I_{sc} \cdot V_{oc}} \tag{2.2}$$

$$P_{max} = I_{sc} \cdot V_{oc} \cdot FF = I_{sc} \cdot V_{oc} \cdot \frac{I_{max} \cdot V_{max}}{I_{sc} \cdot V_{oc}} = I_{max} \cdot V_{max} \tag{2.3}$$

P_{in} is the power of the incident (sun)light, which is set as $I_S = 1000$ W/m^2 or 100 mW/cm^2 or 1 Sun for all measurements in this thesis. To calculate the efficiency of a DSC with any given active area, this area is taken into account by defining the integral photocurrent density J_{SC}=I_{SC}/(active solar cell area in cm^2). [25, pp. 20] [41]

$$\eta = \frac{P_{max}}{P_{in}} = \frac{I_{sc} \cdot V_{oc} \cdot FF}{P_{in}} = \frac{J_{sc} \cdot V_{oc} \cdot FF}{I_s} \tag{2.4}$$

Since each mask had a slightly different defined area, photocurrent density J was plotted against voltage for each measurement. The PCE, particularly of the liquid electrolyte

DSCs, can increase over several days (see Figure 2.9), usually stabilizing a few days after cell assemblage, before eventually decreasing again.

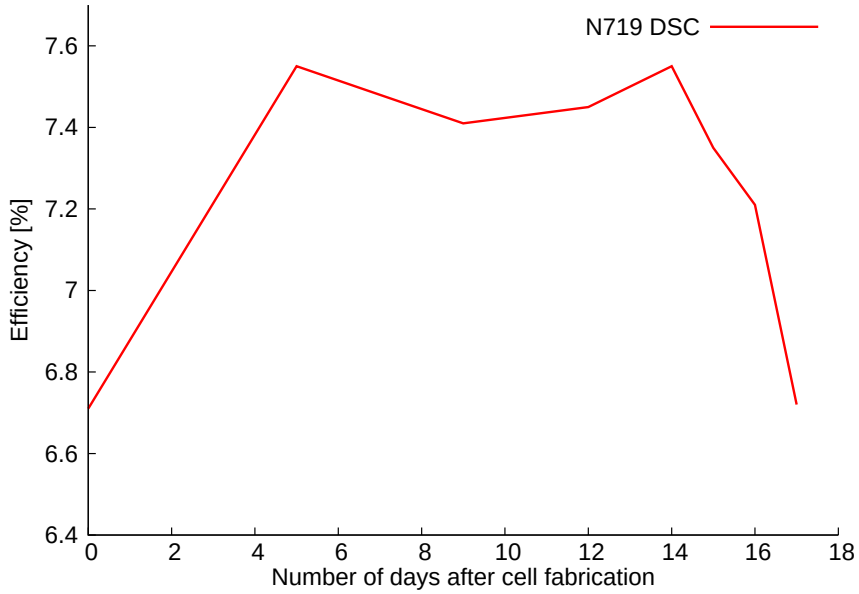

Figure 2.9: Efficiency values of an N719 DSC over several days

Days after sealing →	**0**	**5**	**7**	**9**	**12**	**14**	**15**	**16**	**17**
η [%] →	6.71	7.55	7.48	7.41	7.45	7.55	7.35	7.21	6.72
FF [%] →	71.1	69.7	70.2	69.7	69.9	69.3	69.4	69.6	70.7
$\mathbf{V}_{OC}$ **[mV]** →	667	684	694	695	696	694	699	698	675
$\mathbf{J}_{SC}$ **[mA/cm^2]** →	14.1	15.8	15.3	15.3	15.3	15.7	15.2	14.8	14.1

Table 2.2: Performance parameters of an N719 DSC.

If measured over several days, the efficiency value of DSCs usually improved over the first few days after sealing and eventually dropped again. V_{OC} and J_{SC} followed that trend as well. The FF was the only constant parameter.

2.5.1 Solar cell masking

Photon to electrical conversion efficiencies (PCEs) are the most common variable on which advances in solar cell technologies are judged. [42] However, not all solar simulators are constructed in the same way. Some feature a more open architecture, others have closed sides (see Figure 2.10). Particularly the ones with a more closed design generate reflections of the incident light off the sides of the chassis. Even if they are both perfectly calibrated, the lighting conditions are not exactly the same. This makes it difficult to compare measurements of different instruments. [43] Scattered light entering the sides of an unmasked

(a) Solaronix 150 solar simulator.

(b) LOT Quantum Design LS0811 solar simulator.

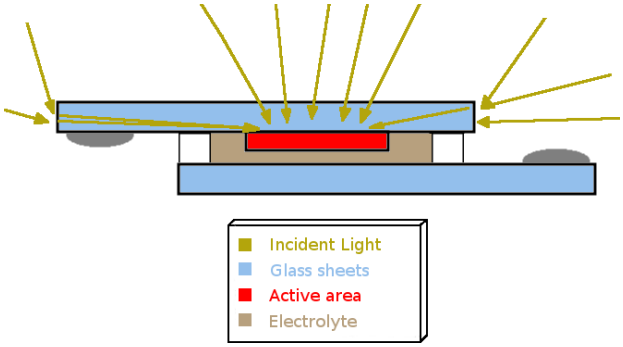

(c) Light piping in an unmasked cell.

Figure 2.10: Solar simulators and light piping in an unmasked DSC.

DSC enhances the current of the cell and therefore the PCE by light piping through the top electrode. [42] [20] If not indicated otherwise, DSCs in this thesis were masked to prevent this. Masking was achieved with copper foil masks coated with a black finish. A 0.1 mm thick copper sheet has been cut to 1 cm x 1 cm squares. They featured a circular opening of 0.06 cm^2 which had been punched beforehand into the copper sheet with a corresponding hole punch. The masks were coated with a beamless black finish to prevent reflections from the shiny copper surface. Mask application was realized by taping them over the middle of the active area and a bigger black scotch tape with an opening for the mask was pasted on top to hinder lateral light entrance (see Figure 2.11). In total, 120 masks have been

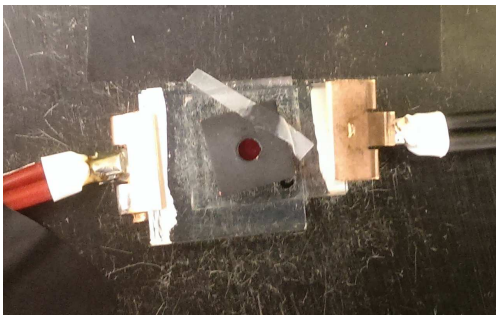

(a) DSC with mask over the active area.

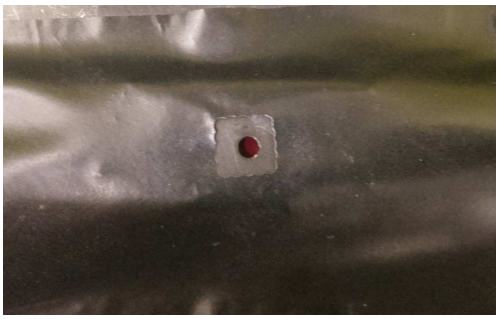

(b) DSC with mask taped off by a bigger piece of scotch tape.

Figure 2.11: Pictures of a cell with the copper mask applied 2.11a and a fully masked cell 2.11b

produced in two batches and their area was measured out by scanning them in and using the program ImageJ [44] on the scan to get the area values on each mask individually. To verify that method, 4 masks of each batch were measured by 3D laser microscopy (Keyence

VK–X200) and compared to the values obtained from the scan. Measurements for one batch are depicted in Table 2.3. The error in those samples was one percent at maximum. The standard deviation of all the scanned values was 1.86%.

Mask #	Area Laser Microscope [cm^2]	Area Scan [cm^2]	Error [cm^2]	Error [%]
41	0.06083	0.06018	0.00065	1.07
50	0.05992	0.06035	-0.00043	0.718
20	0.06165	0.06188	-0.00023	0.373
50	0.06086	0.06062	0.00024	0.394

Table 2.3: Measuring the opening of the copper foil masks.

Figure 2.12 shows the influence of the masking on an N719 DSC. The current and efficiency values are much higher when measuring unmasked cells. [42] The fill factor on the other hand has improved by 20% when measuring the DSC with a mask.

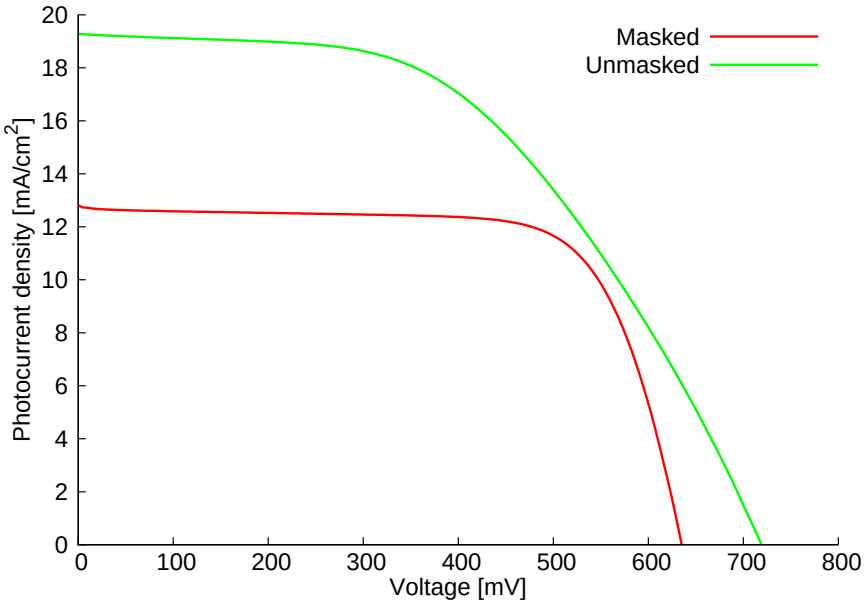

Figure 2.12: IV–measurement of the same N719 DSC masked and unmasked.

Device Name	J_{sc} [mA/cm^2]	I_{sc} [mA]	V_{oc} [mV]	FF [%]	η [%]
Unmasked N719 DSC	19.4	6.98	719	50.0	6.96
Masked N719 DSC	11.6	0.688	655	70.6	5.34

Table 2.4: Parameters of an N719 DSC masked and unmasked.

2.5.2 Incident Photon to Current Efficiency (IPCE) measurements

Incident photon to current efficiency describes the overall charge injection measured at monochromatic light irradiation. It is synonymous to the external quantum efficiency (EQE). The EQE is the ratio of the number of photons converted to electrons by the solar cell to the number of incident photons, meaning the photons of a given energy/wavelength that actually hit the cell (See Equation 2.5). If an EQE value at a given wavelength is high or low depends on how much light is absorbed by the solar cell and how much of the absorbed light is actually converted to electrons. If all absorbed photons of a given energy were converted to electrons, the EQE value would be 100 % at that wavelengt.[45] The short circuit current I_{sc} can also be expressed as the integral of all EQE values measured over the whole solar spectrum multiplied by the incident light intensity at the given wavelength. [25, pp. 20]

$$EQE(\lambda) = \frac{electrons\,out(\lambda)}{IncidentPhotons(\lambda)} = \frac{J_{sc}(\lambda)}{q\Phi(\lambda)} = \frac{hc}{q} \cdot \frac{J_{sc}(\lambda)}{\lambda \cdot P_{in}(\lambda)}$$

$$= 1240 \cdot \frac{[W \cdot s \cdot nm]}{[A \cdot s]} \cdot \frac{J_{sc}(\lambda)[A \cdot cm^{-2}]}{\lambda[nm] \cdot P_{in}(\lambda)[W \cdot cm^{-2}]} \tag{2.5}$$

$$I_{sc} = \int_0^\infty EQE(\lambda) \cdot I_s(\lambda) d\lambda \tag{2.6}$$

The EQE also depends on the optical properties of the solar cell itself. It does not take into account light that does not enter the cell because of reflection or light that is transmitted through the cell and not being absorbed. The internal quantum efficiency does incorporate transmission and reflection of photons. Only the photons that actually contribute to charge generation are taken into account. The IQE is defined in Equation 2.7, where T is the hemispherical transmission and R the hemispherical reflectance of the solar cell at a given wavelength. [46]

$$IQE(\lambda) = \frac{EQE(\lambda)}{1 - R(\lambda) - T(\lambda)} \tag{2.7}$$

In this work, only the EQE was used as an analytical method and measurements were carried out over a range of wavelengths, usually 350 to 740 nm. The external quantum

efficiency is used to determine the light absorption and electron injection properties of chromophores over a part of the Sun's irradiation spectrum, mainly the visible and near infrared region, since that is where the intensity of the sunlight is the highest (See Figure 1.7). The cells have not been masked for the EQE measurements. Figure 2.13 depicts an EQE measurement of an N719 cell using commercial Solaronix test cell kits as an example. EQE

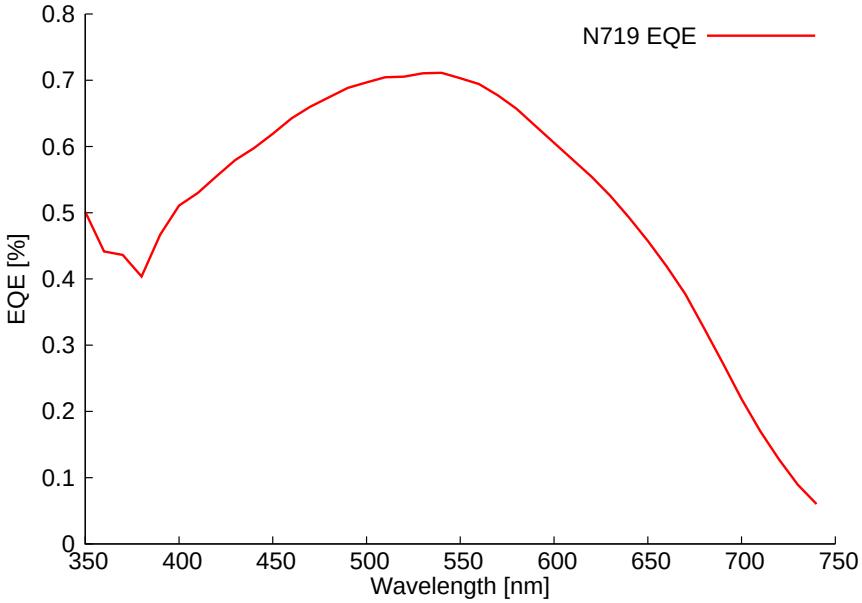

Figure 2.13: EQE measurement of an N719 cell.

measurements have been performed on an Spe-Quest quantum efficiency setup from Rera Systems (Netherlands) equipped with a 100 W halogen lamp (QTH) and a lambda 300 grating monochromator from Lot Oriel. The monochromatic light was modulated to 3 Hz using a chopper wheel from ThorLabs. The cell response was amplified with a large dynamic range IV converter from CVI Melles Griot and then measured with an SR830 DSP Lock-In amplifier from Stanford Research. [47]

2.5.3 Solid state UV-Vis and reflectance spectra

Solid state UV-Vis spectra have been recorded either on an Agilent Carry5000 UV-Vis-NIR instrtrument or an Agilent 8453 UV-spectrophotometer. Diffuse reflectance spectra have been recorded with a Carry5000 UV-Vis-NIR instrtrument from Agilent employing the diffuse reflection accessory Varian internal DRA 2500.

2.5.4 Brunauer-Emmet-Teller (BET)

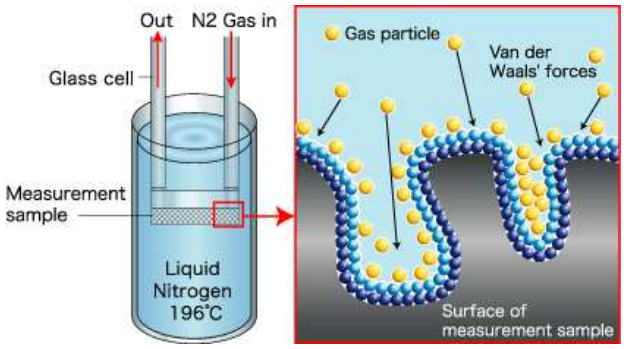

Figure 2.14: Principle of a BET surface area measurement. [48]

The BET Theory was named after Brunauer, Emmet and Teller, who proposed a mathematical model for the process of gas adsorption and desorption. The theory describes the adsorption of gas to solid surfaces, the physisorption. If a clean solid surface is exposed to gas, the gas molecules will adsorb into the pores and other surface features of the material structure. The specific surface area can be estimated from the amount of gas molecules adsorbed in relationship with its pressure. When a sample is measured, it is first chilled, and the gas is adsorbed at the sample surface. When the sample is warmed up again, the gas molecules desorb. The amount of gas adsorbed respectively desorbed can be measured by the change in pressure of the gas leaving the sample. [48][49][50][51]

2.5.5 Scanning Electron Microscopy (SEM)

SEM images were recorded with a field emission scanning electron microscope (FESEM) from ZEISS (LEO Supra 35 with a GEMINI electron optical coloum), a Philips XL30 ESEM, or a FEI Nova Nano SEM230.

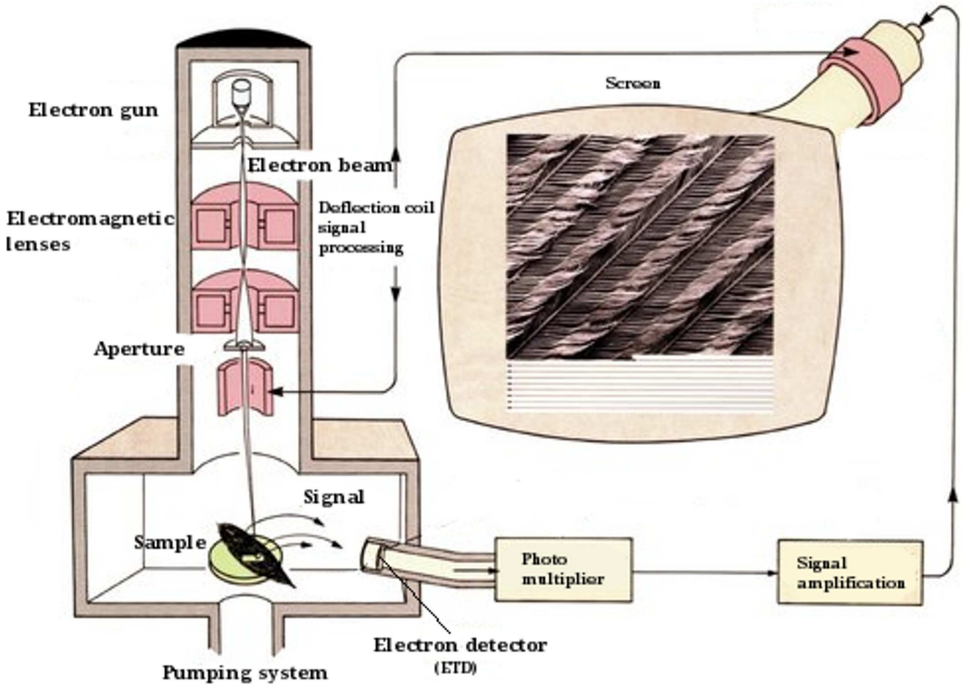

Figure 2.15: Simplified structure of an SEM[52].

Figure 2.15 shows a simplified set up of a scanning electron microscope. It consists of an electron gun at the top, which generates an electron beam. The beam position is controlled by a deflection coil and scans the image in lines, hence the name "scanning" electron microscope. After having passed several electromagnetic lenses, the electrons hit the sample placed on a mechanical stage. Multiple signals are emitted which are detected by one of several possible detectors. The most important emissions for the measurements conducted hereafter are secondary electrons, back scattered electrons and X-rays. Secondary electrons give information about topography, whereas back scattered electrons give more information about material contrast. X-rays enable the possibility to perform elemental analysis via electron diffraction X-ray spectroscopy (EDX) using a special semiconducting detector. EDX will be applied in Chapters 4 and 5, which feature solid state DSCs. On an FEI Nova Nano SEM230 instrument, cross sections can be milled into the sample with a focused ion beam (FIB) to generate a clean and defined surface for the SEM image. [52] [53]

2.5.6 Atomic Force Microscopy (AFM)

Atomic force microscopy measurements were performed on a Bruker Dimension 3100 AFM. It was used to determine the morphology and thickness of a spin coated compact layer presented in Chapter 4/Section 4.2.2. In an AFM measurement, a sharp probing tip is attached to a cantilever-type spring which is moved over a surface. A laser is pointed at the back of the tip. The force between tip and sample causes cantilever deflections which are monitored by a photodiode deflection sensor. [54] [55] A simplified scheme is depicted in Figure 2.16.

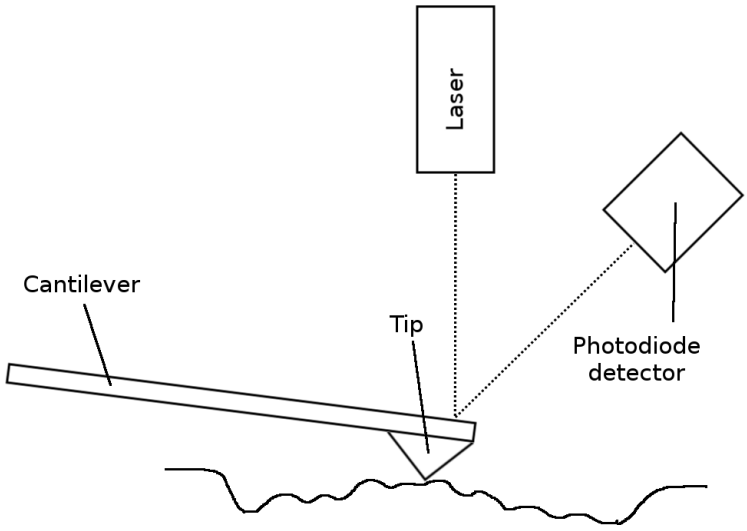

Figure 2.16: Simplified structure of an AFM.

2.5.7 Scanning Electrochemical Microscopy (SECM)

The setup for SECM scans was a standard three electrode electrochemical cell featuring an active redox electrolyte. The potential between these electrodes is kept constant by a potentiostat and an ultramicroelectrode (UME) is used as the working electrode. When the UME approaches a substrate, the diffusion behavior of the electrolyte to the UME is changed and leads to a variation of the tip current, which is monitored. A conducting substrate leads to an increase in tip current, an insulator to a decrease (see Figure 2.17). All measurements have been conducted in feedback mode at a negative potential. In this mode, by scanning over a surface at a distance of 3-5 µm, the change in tip current can be depicted as a 3D surface plot (see Figure 2.18), indicating areas of tip current increase as a well and areas of tip current decrease as a hill. An FTO/TiO_2/dye working electrode was used as an unearthed substrate and the charge generation on the dyed TiO_2 surface upon

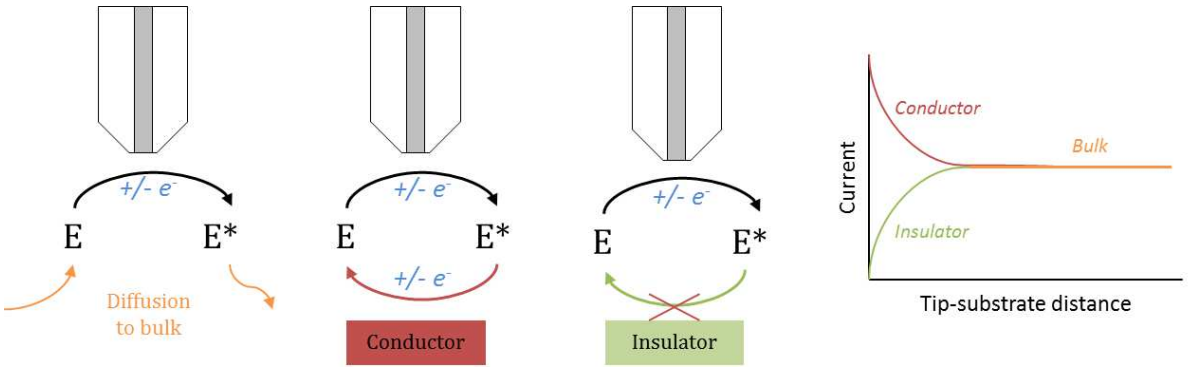

Figure 2.17: Interaction of the UME with conductors, insulators and the bulk electrolyte [56]

external illumination[4] was indirectly measured over the electrolyte and the UME. With this setup, the interfacial region between the dye and the electrolyte could be investigated. By changing the dye and hence the electron injection and reduction properties of the system, the observed tip current is varied at the working UME, giving the possibility to compare charge injection and reduction properties of dyes relative to each other. [56] Upon illumination

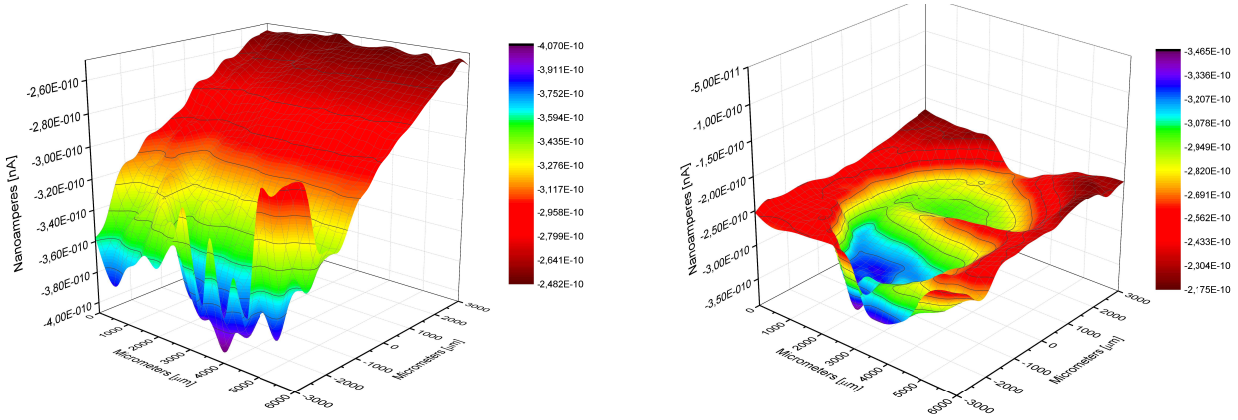

(a) Dyed Electrode measured in the Dark

(b) Dyed Electrode measured under illumination

Figure 2.18: SECM area scans of a dyed TiO_2 electrode in the dark and under illumination

the dye is elevated into an excited state, injects electrons into the TiO_2 layer and is thereby oxidized. A positive charge layer is generated at the electrolyte/dye interface. As a result of this the relative concentration of oxidized electrolyte (E) close to the surface increases. This leads to an increase in current flow at the UME as the rate of reduction back to the reduced form (E*) increases. If measured in the dark, the dye molecules are mostly present in their ground state reduced form and can hence contribute less to electrolyte oxidation. As a consequence the tip current response is lower. This can be observed in Figure 2.18. Upon

[4] A Thorlabs OSL1-EC halogen lamp source coupled to a Thorlabs BFH48-1000 optical wire (Ø1000 µm core) using an SMA connector was employed. The conical lighted area had a diameter of 4 mm.

illumination the plot on the right shows a circular shape, representing the light cone. Where the light hit the electrode, an increased current was observed. Assuming that the TiO_2 is fully covered by dye, this also means that dyes that are less likely to reach their excited state and inject electrons under illumination (for example due to poor light absorption, poor electron injection, recombination or due to a mismatch in potential energy respective to the TiO_2) induce a lower current response at the UME tip. This opens up the possibility for a qualitative comparison of dyes and the TiO_2 surface.

Apart from area scans, retraction curves of several dye loaded TiO_2 surfaces have been recorded in the dark and at several light intensities. For these the tip was placed at a distance of 2-3 µm to the TiO_2 surface and slowly retracted to a distance of 1 mm. SECM scans have been employed in Chapter 6. The redox electrolyte (for both, the area and retraction measurements) consisted of 7,7'-8,8'-tetracyanoquinodimethane (TCNQ) and tetrabutylammonium hexafluorophosphate ($TBAPF_6$) in 3-methoxypropionitrile. For retraction curve measurements the concentrations of TCNQ and $TBAPF_6$ were 1 mM and 0.02 M respectively. For area scans the more diluted concentrations of 0.33 mM and 6.67 mM respectively have been used.

Chapter 3

Liquid Electrolyte Dye Sensitized Solar Cells (leDSCs)

In Sections 3.1 and 3.2, a theoretical background on leDSCs is given. Section 3.3 describes experimental procedures for TiO_2 particle and paste preparation as well as detailed cell fabrication. Although several things had to be altered due to different equipment, experimental procedures have been retrieved from literature and are referenced to it. The original work on leDSCs starts in Section 3.4 ("Cell development"), where several literature procedures have been altered or combined by changing the electrolyte or introducing a scattering layer. Section 3.5 gives a small summary of the Chapter. All TiO_2 particles and pastes have been self fabricated in this Chapter except for one comparative measurement with a commercial Solaronix test cell kit at the end. These are our first attempts to prepare TiO_2 particles and pastes for DSCs. Also screen printing as a manufacturing process for electrodes has been introduced to our research group with this work.

3.1 Working principle of a leDSC

The basic working principle of a DSC is shown in Figure 3.1. When light hits the back of the working electrode of the DSC, dye molecules are promoted to an excited state. An electron is promoted from the highest occupied molecular orbital (HOMO) to the lowest unoccupied molecular orbital (LUMO), which ideally lies above the Fermi level [1] of the conduction band of the TiO_2 semiconductor. The dye is oxidized after injection of an elec-

[1]The Fermi level is the top of the collective of electron energy levels at 0 K. [57] If there is a non-equilibrium between the conduction and valence band, and this is the case for most semiconductor devices under conditions of current flow, the fermi level can be split into two quasi fermi levels, one regulating the electron density of the conduction band, the other one regulating the electron density in the valence band.

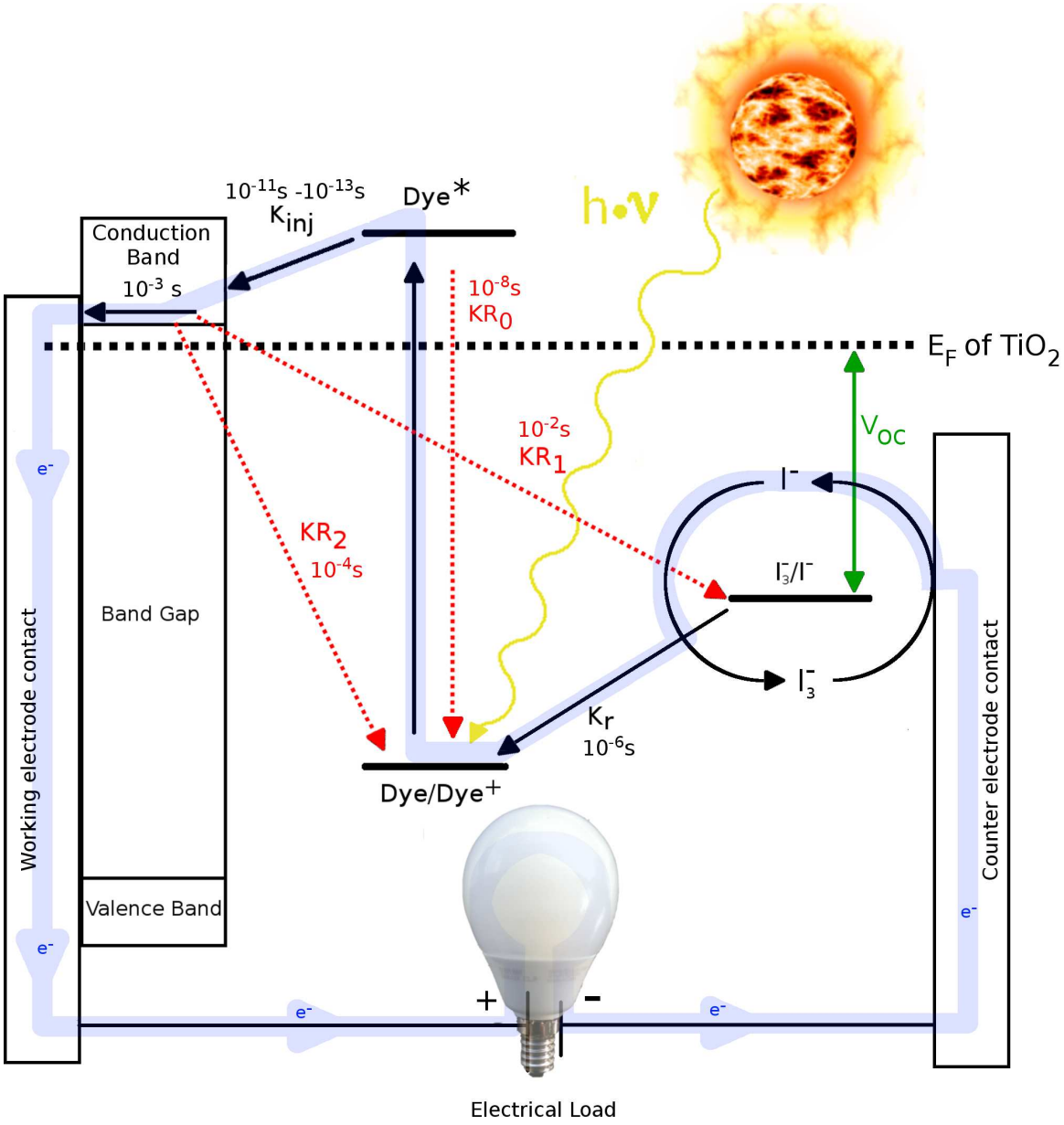

Figure 3.1: Schematic presentation of a dye sensitized solar cell employing an I^-/I_3^- electrolyte. Rate constants [19, pp. 6603] refer to processes with irradiation of 1 Sun.

tron into the conduction band of the nanocrystalline semiconductor. The injected electrons diffuse through the TiO_2, reach the anode and travel through an external circuit passing an electrical load. The oxidized dye molecules are reduced by the I^- anions of the redox mediating ion couple I^-/I_3^-. Consequently, the I^- anions are oxidized to I_3^- ions, which travel to a platinum coated counter electrode and get reduced again to I^- by the electrons from the cathode. The charge separation process is believed to be mainly dependent on electron kinetics at the TiO_2/dye/electrolyte interface rather than on an electric field as is

When the quasi fermi level of TiO_2 is mentioned hereafter, it will be referred to as the quasi fermi level of the conduction band of the TiO_2 semicunductor. [58]

the case with silicon solar cells (See Figure 1.4). [25, pp. 119] Ideally, the electrons follow the blue path in Figure 3.1. However, there are a few unwanted shortcuts which electrons can take and these are commonly referred to as recombination reactions. If charges recombine before they reach the electrodes, the photocurrent is diminished. [59] These processes are indicated as red arrows, labelled KR_0, KR_1 and KR_2. For a DSC to operate efficiently, the rate of electron injection into the semiconductor (K_{inj} in Figure 3.1) must be faster than the decay rate of the excited state of the dye (KR_0). Moreover, the rate of reduction of the dye from the electrolyte (K_r in Figure 3.1) must be faster than the rate of the recombination reaction of electrons from the conduction band of the TiO_2 with the oxidized dye (KR_2 in Figure 3.1). For most sensitizers, the electron injection into the TiO_2 takes place in the femtosecond to picosecond region, which is much faster than the decay rate of the excited state of the dye. The I^- ions are typically very highly concentrated (around 0.5 M) in standard electrolytes to ensure a quick dye reduction, therefore the influence of KR_2 is limited and can be neglected. [25, pp. 119] Since nanoparticulate TiO_2 has quite a low diffusion coefficient (D_n $<10^{-4}$ cm^2 s^{-1}), the back donation of electrons to I_3^- occurs more frequently and has a greater influence on the cell performance. The ion I_3^- can also be reduced at the bare FTO on the anode directly where no TiO_2 is present. To minimize these back-donations, a TiO_2 blocking layer is commonly introduced via $TiCl_4$ treatment (Section 3.3.4) before TiO_2 layer application and after. Further reasons for this treatment are to generate a better contact between the FTO and the nanoporous TiO_2 layer and to roughen up the TiO_2 surface for better dye adsorption. [60] Since I^- is reduced at the surface of the dyed TiO_2 film, more I^- is present at the anode, whereas the I_3^- ions travel to the cathode to be reduced again. I^- has a higher diffusion coefficient than I_3^-, so the limiting factor in charge transport is the I_3^- ion. [25, pp. 119, 120] The maximum voltage the cell can produce is the difference of the Fermi level and the redox potential of the electrolyte (highlighted green in Figure 3.1). [19, pp. 6602] In the case of I^-/I_3^- the maximum obtainable voltage is $\sim$1 V [61].

3.2 Main components of leDSCs

3.2.1 The semiconductor

One of the main factors for the discovery of a working DSC by Grätzel in 1991 [21] was the surface area of the semiconductor. It is desirable to collect as much light as possible and hence to load it with as much dye as possible. By using a nanocrystalline mesoporous transparent electrode instead of the bulk material the surface area increases by a factor of

~1000. [19, pp. 6613] TiO_2 is nontoxic and is naturally occurring. In macroscopic crystals, rutile is the thermodynamically most stable form. For crystals on the nanoscale smaller than ~10-20 nm in size, anatase is considered to be more stable. [25, pp. 45] Because of its larger bandgap (3.2 eV in comparison to rutile 3.0 eV) however, anatase is generally the preferred form of TiO_2 since this leads to a higher V_{OC}. The most common way of preparing TiO_2 nanoparticles is the hydrolysis of a titanium precursor like titanium(IV) isopropoxide with water and acid with a subsequent dispersion step and finally hydrothermal crystal growth in an autoclave. [19, pp. 6614] [62] By adding polymers like ethyl cellulose the resulting particles are transformed into a nanoparticulate paste which is then spread on an FTO-glass sheet by either doctor blading or screen printing. To remove organic components and establish electrical contact to the substrate, the film is sintered. Porosity of the film can be controlled by the amount of organic binders present in the TiO_2 paste. The main driving

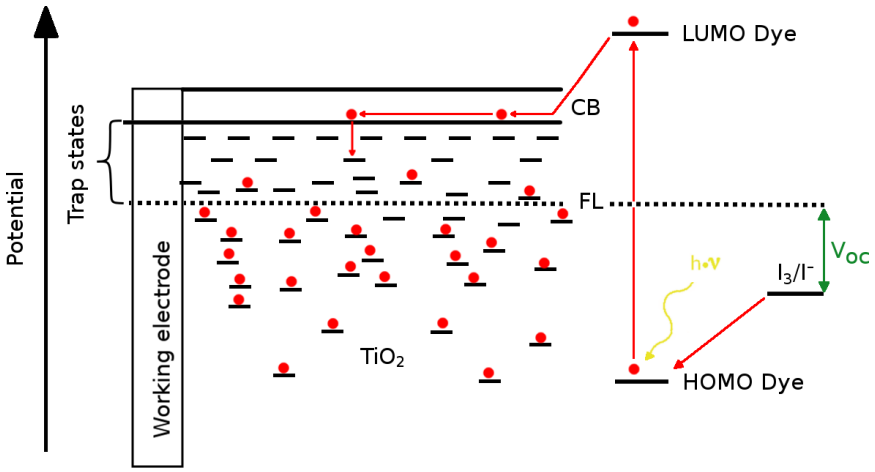

Figure 3.2: Illustration of trapping sites in a TiO_2 electrode. FL: Fermi level of the TiO_2, CB: Conduction band of the TiO_2. Electrons are depicted as red dots.

force for electron transport in TiO_2 seems to be the gradient in electron concentration, the electron transport occurs via diffusion. [63] The diffusion coefficient in single crystalline TiO_2 anatase (~0.4 $cm^2\ s^{-1}$) is a few orders higher than the one of nanocrystalline TiO_2 film (D_n <10^{-4} $cm^2\ s^{-1}$). This phenomenon is commonly explained by a multiple trapping model [64], which postulates that electrons are mostly trapped in states below the conduction band and upon thermal activation they can be promoted to it (see Figure 3.2). [19, pp. 6610] V_{OC} is the difference in potential of the Fermi level of the TiO_2 and the electrolyte. The closer the electrons in the semiconductor get towards the conduction band, the higher the Fermi level is raised and consequently V_{OC} will be higher as well. If separated charges recombine before reaching the electrodes, the photocurrent will be diminished. This also has an indirect influence on the open circuit voltage, because less losses will result in better filling of the trap states, raising the Fermi level and hence increasing V_{OC}. [59] Structure

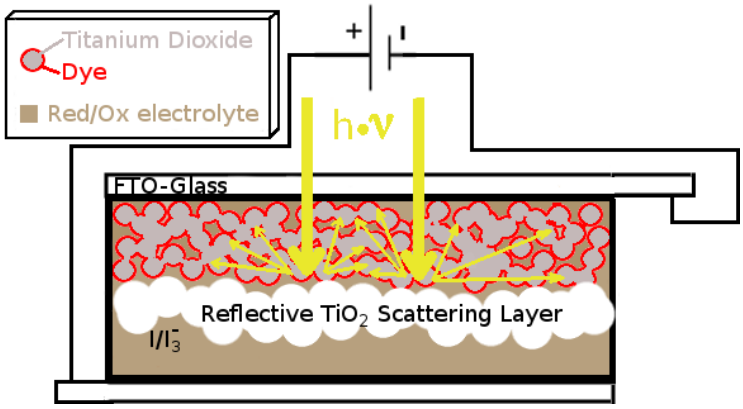

Figure 3.3: Illustration of a light scattering layer and its effect on incoming light.

and morphology of the semiconductor layer play an important role on the performance of a DSC. For the work described in this chapter, the TiO_2 particles and pastes as well as the working and counter electrodes were self fabricated following the procedure described by Grätzel et. al. [60] Next to a transparent working electrode, TiO_2 can also serve as a light scattering layer by using larger microcrystalline TiO_2 particles around 100–400 nm in diameter. [65] Due to their reduced surface, these particles only take up a limited amount of dye and hence even after dipping into dye solutions often stay white or at least less colored than the nanocrystalline underlayer. Although scattering layers participate actively in electron injection as well [60], their striking feature is their light scattering properties. The purpose of a scattering layer is to keep as much light as possible in the electrode for as long as possible. [66] A scattering layer is usually applied on top of the working electrode layer consisting of nanocrystalline TiO_2 particles. [60] When light shines on the back of the cell, it passes through the transparent nanoporous working electrode. The microcrystalline scattering layer scatters non absorbed photons in all directions, forcing it to pass the dyed TiO_2 multiple times. In this way, the chances for photon uptake are enhanced (see Figure 3.3). Several approaches have been taken to realize such a scattering layer. Results of the influence of the respective scattering layers can be looked up in Sections 3.4.3.

3.2.2 Electrolytes and their additives

The most important part of an electrolyte is the redox couple, which reduces the dye and mediates charges between the electrodes. Since the invention of the DSC, I^-/I_3^- has been the redox couple of choice for a very long time. Even today, it still yields among the most stable and efficient DSCs. [67] The mechanism for the reduction of the dye by the redox

couple has remained controversial. There is, however, a general consensus that for the I^-/I_3^- redox couple, dye regeneration is a multi charge transfer process. There are four iodide molecules and two holes required to form one triiodide and one iodide species. [59]

$$\begin{aligned} D^+ + I^- &\rightarrow (D \cdots I) \\ (D \cdots I) + I^- &\rightarrow (D \cdots I_2^{-\bullet}) \\ (D \cdots I_2^{-\bullet}) &\rightarrow D + I_2^{-\bullet} \\ 2I_2^{-\bullet} &\rightarrow I_3^- + I^- \end{aligned} \tag{3.1}$$

First, the oxidized dye (D^+) and the iodide (I^-) form a complex. The iodide would most probably not form a radical due to energetic reasons. With a second iodide, the complex $D \cdots I_2^{-\bullet}$ is formed, which subsequentially dissociates to D and $I_2^{-\bullet}$. In a last step, 2 $I_2^{-\bullet}$ disproportionate to I_3^- and I^-. [19, pp. 6609], [68], [59] During these charge transfer processes, I^- is oxidized at the surface of the TiO_2 film covered with dye. Once oxidized, the I_3^- ions have to migrate all the way to the counter electrode, where they are reduced to I^- again. The same migration applies in the other direction for I^-. The concentration of I^- is in excess and around ten times greater than the concentration of I_3^- in typical electrolytes. Furthermore the diffusion coefficient of I^- is higher than the one of the I_3^- ion. This leads to the conclusion that charge transfer processes between the electrodes and hence the current are mainly restricted to the diffusion of the I_3^- ion. [25, pp. 120] It has been found that the performance of a DSC can be increased by adding certain additives to the electrolyte. With 4-*tert*-butylpyridine (4-^{t}BP) or N-methylbenzimidazole (N-MBI) as additives for example, V_{OC} can be increased without affecting J_{SC}, which is due to the suppression of recombination (KR_2 in Figure 3.1) at the dye/TiO_2/electrolyte interface. This occurs because the basic pyridine molecules, adsorb on parts of the TiO_2 that were not covered with dye. [69] They deprotonate the TiO_2 and shift its conduction band edge to more negative potentials. [70] Furthermore, without the presence of 4-^{t}BP, triiodide ions would have been adsorbed promoting the back donation of electrons from the TiO_2 to the electrolyte. This has been observed with other nitrogen containing heterocyclic compounds as well. [25, pp- 124] Guanidinium thiocyanate (GuNCS) shares the effect of shielding the TiO_2 surface from triiodide ions. But instead of inducing a negative shift in the potential of the conduction band, it accumulates positive charges (its cations) on the surface and induces a shift to a positive potential. This results in a higher electron injection efficiency due to a bigger potential drop and hence increases the current. [70] Other additives providing cations, such as lithium idodide, have a similar effect. [25, pp. 122]

3.2.3 Dye

For development of TiO_2 electrodes, N719 has been used as the dye. As mentioned in Chapter 1.1, N719 is a high performance dye and is used as the industry standard by Dyesol. [33]

3.2.4 Counter electrodes

At the counter electrode, the following reaction takes place:

$$I_3^- + 2e^- \rightarrow 3I^- \tag{3.2}$$

To guarantee a fast reduction to iodide, the counter electrode must be catalytically active. [19, pp. 6613] Platinum is generally used because it shows good electrocatalytic properties and is chemically stable. [71, pp. 256] [25, pp. 30] The electrodes in this section were prepared by applying a droplet of Platisol T (Solaronix) to a cleaned FTO coated glass sheet and subsequent sintering at 450 °C for 30 min. Other than that commercial Solaronix test cell kit platinum counter electrodes have been used where indicated.

3.3 Experimental procedures

The experimental procedures consist mainly of the preparation of TiO_2 particles and pastes. Particles have been fabricated by precipitation from a titanium oxide precursor and subsequent hydrothermal growth at high temperature and pressure in an acid digestion vessel. They have been transferred to a TiO_2 paste by adding an organic binder (ethyl cellulose here) and a solvent for the binder, in this case terpineol.

3.3.1 TiO_2 paste preparation for transparent mesoporous layers

TiO_2 particle preparation

To prevent metal contamination, the use of syringes or any other metal instrument was avoided throughout the entire TiO_2 paste preparation procedure. Plastic spatulas, beakers

and pipettes were used instead. All glassware was cleaned with 0.1M hydrochloric acid (HCl) in ethanol (EtOH) prior to use.

In advance of this experiment, two 10 wt% solutions of ethyl celluloses (Aldrich, #46070 & #46080) were prepared as stock solutions for later use in the experiment, since dissolution to a turbid viscous liquid takes up to 12 h. At least 20 g of each solution was prepared.

Acetic acid (2.60 g, 2.49 ml, 43.3 mmol) was slowly added to titanium tetraisopropoxide (12.8 g, 13.4 ml, 45.1 mmol) while stirring. The mixture was stirred for a further 15 min and H_2O (63.5 ml) was added very quickly all at once while stirring vigorously. Stirring continued for 1 h at least. Afterwards concentrated nitric acid (65 %, 0.9 ml) was added and the mixture was heated up gradually from room temperature to 80 °C in a timespan of 40 min. The mixture was kept stirring at 80 °C for further 75 min. The final volume was adjusted to 80 ml with H_2O and transferred to a Teflon lined stainless steel acid digestion bomb (Parr instruments Model 4748, 125 ml) for 12 h at 250 °C. **Important note: This should be divided to multiple vessels or carried out on a smaller scale. After performing this reaction around 6 times, the Teflon liner of the acid digestion bomb did not stand the pressure generated with this amount of reagents anymore! It is strongly advised to check the manual of the respective autoclave as well!** The acid digestion bomb was left to cool down to room temperature **inside** the oven. The mixture was poured into a beaker, treated with concentrated nitric acid (65%, 0.530 ml) and sonicated (30 x 2 s and 2 s rest in between). It's volume was reduced to 13 $\%_{wt}$ TiO_2 on a rotary evaporator and centrifuged 4-5 times with water (9000 rpm for 30-40 minutes each time using plastic centrifuge tubes from Greiner Bio One) to remove nitric acid. The water was decanted and checked for pH neutrality with pH paper. Afterwards it was centrifuged 3 times with ethanol with the same speed and time to remove the water. The particles were redispersed in ethanol by sonication 30 x 2 s and stirring for 15 minutes. This procedure was carried out three times or until a fine dispersion was reached. The total volume of the colloid was reduced to 40 $\%_{wt}$. Under no circumstances should the colloid be reduced to dryness.

TiO_2 paste preparation

Ethyl cellulose (10 %, 10.1 g) in ethanol (Aldrich, #46070), ethyl cellulose (10 %, 7.88 g) in ethanol (Aldrich, #46080) and terpineol (14.6 g, 94.7 mmol) were added to the obtained dispersion (Section 3.3.1) while stirring. After dilution with ethanol ($\sim$ 18.0 ml) to reach a final volume of 63 ml, the mixture was alternately sonicated and stirred until most of it was dispersed and everything was removed from the walls of the vessel. Then a mixer

(IKA ultraturrax, speed 2 with plastic disperser) was applied to the solution for 5 min followed by consecutive sonication for 10 min. The mixing/sonicating cycle was repeated three times or until a fine colloid/dispersion was reached. All solvent was removed on the rotary evaporator. It should be evaporated until a pressure of 10 mbar at 40 °C could be reached. The paste was milled with a three roll mill (EXAKT 50 EC) for 15 min to finalize it. The two gaps of the rolls were set to 1 and 4-6 respectively. [60]

3.3.2 TiO_2 paste preparation for scattering layers

TiO_2 scattering particle preparation

Methylamine (0.0130 g, 0.052 ml, 0.416 mmol) and a stoichiometric amount of water were added to a mixture of ethanol (10.4 ml) and acetonitrile (8.32 ml) while stirring. After stirring for 5 min., titanium tetraisopropoxide (TTIP, 0.179 ml, 2.490 mmol) stabilized in ethanol (2.08 ml) followed by water (0.179 ml, 9.98 mmol) was added to the solution. Upon addition the mixture turned turbid in a matter of a few seconds. The diameter size of the TiO_2 scattering particles was controlled by the ratio of TTIP and water. A ratio of 1/4 is expected to result in a particle diameter of 450 nm according to literature. To obtain the amorphous particles, the reaction mixture was stirred for 1h. Then the TiO_2 spheres were collected by centrifuging and transferred into a teflon lined stainless steel acid digestion bomb (Parr instruments Model 4748, 125 ml) containing a mixed solution of water (21.9 ml) and ethanol (21.9 ml). The mixture was hydrothermally treated by heating to 230 °C for 5 h. The particles were collected by centrifuging and washed three times with ethanol. They were dried at 100°C to yield 0.137 g of nanoporous TiO_2 spheres. [72]

TiO_2 scattering paste preparation

Ethyl cellulose (10% in ethanol, 0.400 g, Aldrich #46080), lauric acid (5.00 mg, 0.0250 mmol) and terpineol (0.500 g, 0.535 ml, 0.00300 mol) were dissolved in ethanol (10.0 ml). Then the TiO_2 scattering particles prepard as above (0.100 g) were added and the reaction mixture was stirred for 1 h. Ethanol (30.0 ml) was added and the resulting dispersion was mixed for 5-10 min. (IKA ultraturrax, speed 1 with plastic disperser). In a last step, the solvent was removed under reduced pressure. [72]

3.3.3 SiO_2/TiO_2 paste preparation for scattering layers

SiO_2/TiO_2 core/shell scattering particle preparation

For the preparation of submicron SiO_2 particles, a modified Stöber method was used. [73] To obtain a diameter size of 350 nm, ammonia (28%, 6.50 ml), water (18.5 ml) and ethanol (25.0 ml) were mixed in a beaker. This solution labelled "A" was stirred at a speed of 1100 rpm for 5 min. For the preparation of solution "B", tetraethyl orthosilicate (4.20 g, 4.50 ml, 0.0202 mol) (TEOS) was mixed with water (45.5 ml). Afterwards solution B was quickly poured into solution A and everything was stirred together for one further minute at a speed of 1100 rpm. The beaker was sealed with parafilm and the stirring speed reduced to 400 rpm. The reaction was stirred for 2 more hours, after which submicron SiO_2 particles have precipitated. They were collected by centrifuging at a speed of 8000 rpm for 5 min. After decanting off the solvent, they were redispersed and washed with ethanol four times in the centrifuge. The product was dried at 80 °C to receive a final yield of 1.22 g submicron SiO_2 particles. For the preparation of the submicron SiO_2/TiO_2 core/shell particles, a solution labelled "A" containing a mixture of tetrabutyl titanate (5.00 g, 5.00 ml, 0.0147 mol) (TBOT) dissolved in ethanol (10.0 ml) was prepared. The previously prepared submicron SiO_2 particles (0.500 g) were dispersed in solution A using an ultrasonic bath for 10-20 min. Afterwards, an ethanol/water mixture (volume ratio 5:1, 20.0 ml) was added dropwise over 20-30 min to solution A. The reaction mixture was kept stirring for 1 h followed by centrifuging for 10 min at a speed of 7000 rpm. After having centrifuged the produced particles and washed them three times with ethanol, the suspension was dried at 80 °C over night in a ventilated drying furnace. To obtain the final product the dried particles were calcined at 500 °C for 3 h to give of 1.66 g of the submicron SiO_2/TiO_2 core/shell particles. [73]

SiO_2/TiO_2 scattering paste preparation

For the preparation of the scattering paste an ethyl cellulose (Aldrich, #46080) solution in ethanol (10%, 2.00 g), lauric acid (25.0 mg, 0.125 mmol) and terpineol (2.5 g, 2.651 ml, 0.0162 mol) were mixed. Then the previously prepared SiO_2/TiO_2 core/shell particles (0.500 g) and ethanol (15.0 ml) were added. The resulting reaction mixture was stirred for 1 h, diluted with ethanol (35.0 ml) and mixed (Mixer IKA, speed 1, with a plastic disperser) for 5-10 min. To obtain the final screen-printing paste for the scattering layer all solvents were removed under reduced pressure. [72]

3.3.4 Working electrode preparation

For the preparation of the DSC working electrode an FTO glass plate (15x8 cm) was first cleaned in a 2% soap solution (Sanoswiss cleaner in water Milli-Q) by sonicating for 15 min. Then the plate was washed with water and ethanol before treatment in an UV-O_3 system (Model 256-220, Jelight Company Inc) for 18 min. Afterwards the glass plate was immersed into a 40 mM aqueous $TiCl_4$ solution at 70 °C for 30 min. The plate was again washed with water and ethanol and left to dry. The previously prepared (see Section 3.3.1) nanocrystalline TiO_2 paste was screen printed as described in Section 2.2.2. Not every batch of TiO_2 paste had exactly the same viscosity. Depending on the paste batch, 7-8 layers were usually printed, until a final layer thickness of 14 ± µm of the TiO_2 layer was reached. The thickness of the TiO_2 layer was determined with either the SEM or a profilometer. If a scattering layer was used, this is the moment it was applied. Four more layers of the respective scattering paste were printed on top of Paste 1. For the acid treated scattering layer, the 8th printed layer was simply not dried and the electrodes were immersed into 2 M nitric acid for 20 minutes, washed with water and left to dry at room temperature (RT). Afterwards the respective electrodes were sintered with program P1 (see Section 2.2.3). The $TiCl_4$ treatment was repeated and the electrodes were sintered at 450 °C for 30 minutes.

3.3.5 Dying the working electrodes

After cooling down to about 80 °C, the electrodes were immersed into a solution of N719 (0.5 mM) in EtOH for at least 12 h. The dyed working electrodes were rinsed with ethanol and left to dry in air.

3.3.6 Counter electrode preparation

A hole of 1 mm diameter size was drilled into an FTO glass plate (1.50 x 2.00 cm). The plate was washed with water, 0.1 M HCl solution in ethanol and finally cleaned in acetone for 10 minutes using a sonicator. The plate was then heated to 400 °C for 15 min to remove organic residuals. The platinum catalyst (PlatisolT, Solaronix) was deposited on the FTO glass by spreading one drop on each electrode carefully with a glass rod. After drying, the counter electrodes were heated to 400 °C for 15 min.

3.3.7 Electrolyte

The electrolytes employed in this chapter are labelled as follows:

Electrolyte 1: Solution of 0.6 M 1-methyl-3-butylimidazolium iodide (MBII), 0.03 M I_2, 0.10 M guanidinium thiocyanate and 0.5 M 4-*tert*-butylpyridine in a mixture of acetonitrile and valeronitrile (volume ratio, 85:15).
Electrolyte 2: Solution of 0.1 M LiI, 0.05 M I_2, 0.5 M methylbenzimidazole and 0.6 M MBII in 3-methoxypropionitrile.

Electrolyte 1 was prepared by the method of Grätzel et al. [60] Electrolyte 2 is the common standard at our laboratory. [47] Electrolyte 2 additionally contains the ionic liquid methylbutylimidazolium iodide, which acts as an iodide source as well as a solvent. [25, pp. 133]

3.3.8 Cell assembly

Working and counter electrode have been sealed together using a thermoplast hot melt sealing foil (Solaronix, Meltonix 1170-25 Series, 25 microns thick). This was achieved by sandwiching the sealing foil between the electrodes and applying pressure onto the outside of the counter electrode glass with a hot soldering iron. The electrolyte was introduced into the cells by vacuum back filling through the hole of the Pt–counter electrode (see Chapter 2/Section 2.4). Then the hole in the Pt–counter electrode was sealed using the same sealing foil and a cover glass. To improve the conductivity and increase the electrical contact the edge of the FTO glass of each electrode was coated with high purity silver paint. The cells were masked and measured afterwards like described in Sections 2.5 and 2.5.1.

3.4 Cell development

TiO_2 electrodes manually prepared with the doctor blade method are prone to layer irregularities (see Section 2.1) and could only be prepared one at a time. Screen printing on the other hand enables the simultaneous fabrication of electrodes, their number being dependent on the design of the screen printing frame (See Chapter 2/Section 2.2.2). For these reasons, screen printed electrodes have been used for all experiments in this chapter. Detailed TiO_2 particle fabrication, the resulting TiO_2 paste as well as electrode fabrication are described in the experimental procedures (Section 3.3). The transparent working electrodes were screen printed to a thickness of 14 $\pm$ 2 µm, which usually took about 7-8

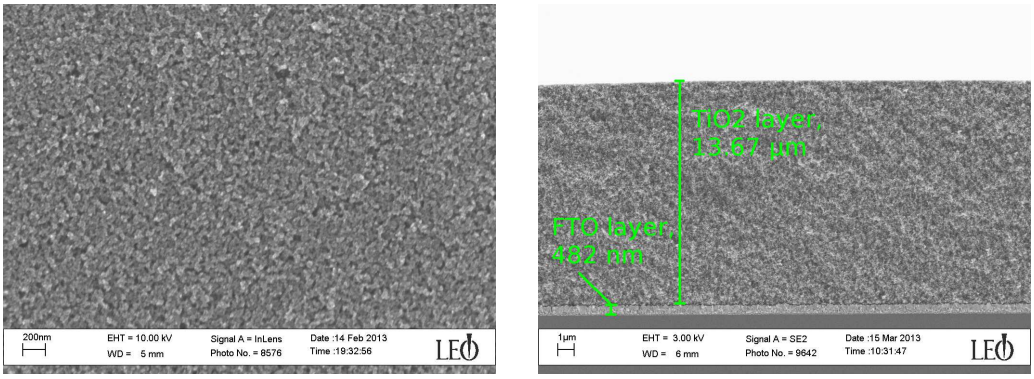

(a) Surface of a screen printed electrode.

(b) Cross section of a screen printed electrode.

Figure 3.4: Sintered TiO_2 electrode investigated with SEM.

layers to achieve, depending on the consistency of the TiO_2 paste batch. Figure 3.4 shows SEM images of the surface and cross section of such a screen printed electrode. Individual particle sites have been measured with scanning electron microscopy. They were all in the range of 20-40 nm. In the cross section, the FTO layer (486 nm) and the TiO_2 layer (13.67 µm) were observed. The home made electrodes have been put to the test by following the procedure of Grätzel et al. [60]

3.4.1 Fabricating a standard (Std.) N719 cell with home made TiO_2 electrodes

Five identically built cells have been fabricated after Grätzel et al. [60] The only exception was the scattering layer mentioned in literature, which is not yet included in these experiments. Electrolyte 1 (abbreviated El 1 in tables and figures) has been employed and the DSCs reached efficiencies over 10 % (Figure 3.5 and Table 3.1), which would be in agreement with literature. [60] The active area was 0.288 cm^2 which was measured out by laser microscopy (Keyence VK–X200). In literature, cells have been masked. However, the measurements and values depicted here stem from unmasked cells. Hence the obtained numbers are not accurate (See Chapter 2/Section 2.5.1 for details on masking). What these results do show though is that reproducible cells were fabricated with home made TiO_2 particles, a home made TiO_2 paste and successful paste application to build up working electrodes.

3.4.2 Changing the electrolyte

Since acetonitrile is present in Electrolyte 1 those cells were hard to make due to evaporation of the solvent during cell fabrication, for example while sealing or back filling. A less

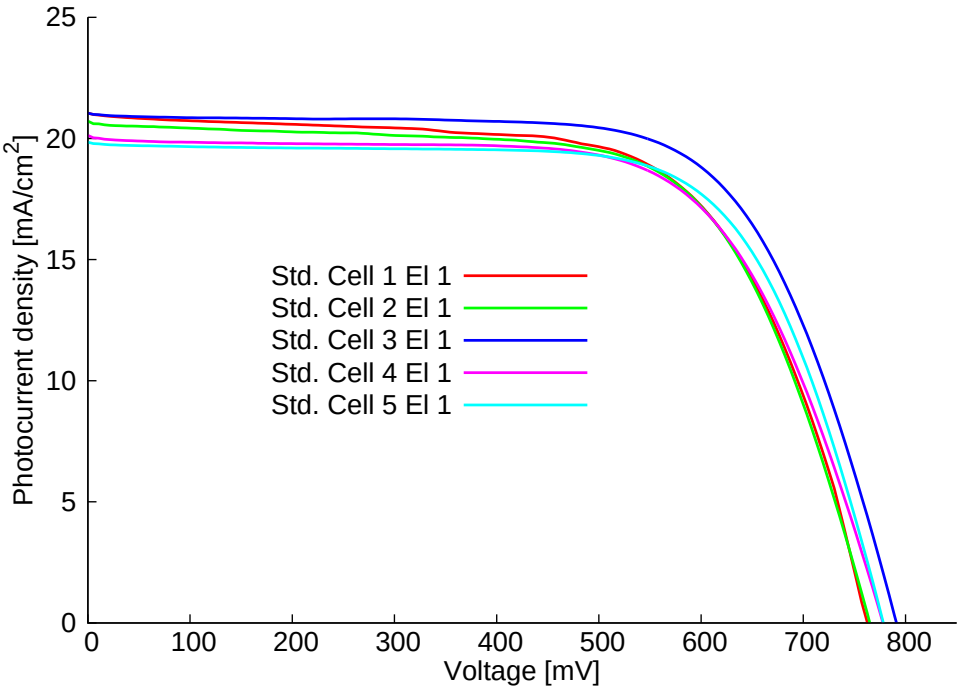

Figure 3.5: J-V curves of five identically fabricated unmasked standard (Std.) screen printed N719 DSCs with self made TiO_2 paste.

Device name	J_{sc} [mA/cm^2]	V_{OC} [mV]	FF [%]	η [%]
Std. Cell 1 El 1	21.0	762	65.2	10.5
Std. Cell 2 El 1	20.7	762	66.1	10.4
Std. Cell 3 El 1	21.0	789	68.0	11.3
Std. Cell 4 El 1	20.1	773	66.6	10.4
Std. Cell 5 El 1	19.9	773	69.3	10.6

Table 3.1: J-V parameters of five identically fabricated unmasked Std. screen printed N719 DSCs with self made TiO_2 paste.

volatile electrolyte solvent is desirable also because of long term cell stability reasons. As a consequence, Electrolyte 2 (see Section 3.3.7), which features 3-methoxypropionitrile as a less volatile solvent has been compared to Electroyte 1 in cell performance (See Figure 3.6 and Table 3.2). Two identical cells have been prepared for each electrolyte. All cells have been masked, reducing their active area to around 0.06 cm^2 with only minor deviations, depending on which mask was applied. Initially, Electrolyte 2 performed fairly similar to Electrolyte 1. This trend continued over time[2] (see Table 3.7 and Figure 3.16). After reaching efficiencies of 6.78% and 7.48% for the two individual cells, by day ten after sealing the Electrolyte 1 cells performed at values of 7.07% and 6.99%. The Electrolyte 2 cells on the other hand, although initially lower in efficiency (6.60% and 6.49%) have increased

[2]For a clearer view, time dependent measurements of certain solar cell types are detailed and referred to as Appendices at the end of the chapter.

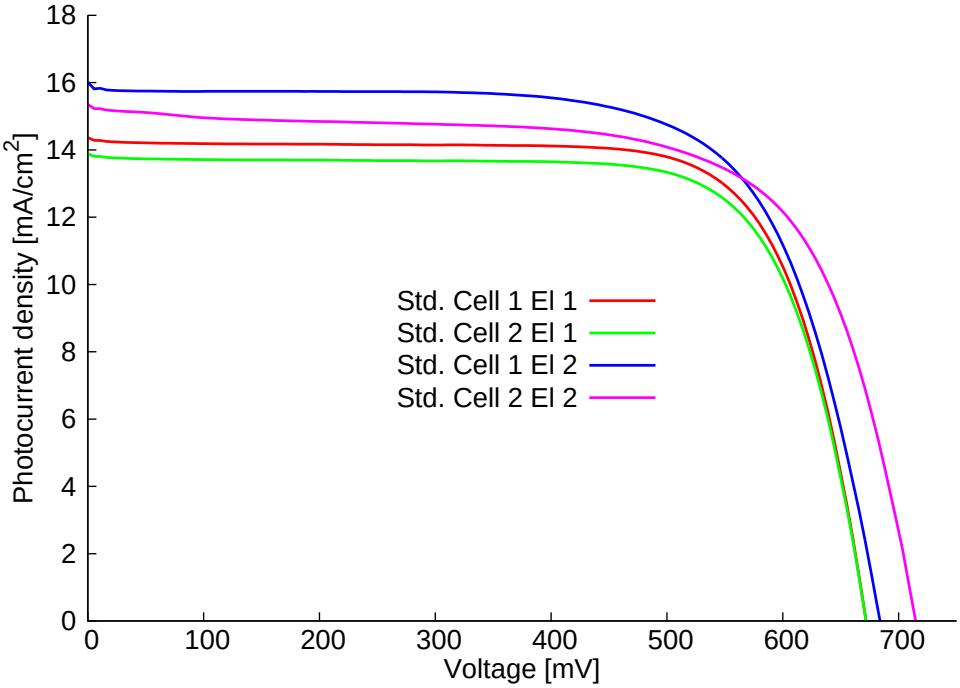

Figure 3.6: J-V curves of masked Std. screen printed N719 standard DSCs comparing Electrolytes 1 and 2 (labeled El1 and El2) at their peak performance (day 3 after sealing).

Device name	J_{SC} [mA/cm^2]	V_{OC} [mV]	FF [%]	η [%]
Std. Cell 1 El 1	14.3	672	74.3	7.13
Std. Cell 2 El 1	14.2	717	72.7	7.40
Std. Cell 1 El 2	15.8	683	69.7	7.55
Std. Cell 2 El 2	15.3	714	68.2	7.44

Table 3.2: J-V parameters of masked screen printed N719 standard DSCs comparing Electrolytes 1 and 2 at their peak performance (day 3 after sealing).

over time. By day ten they generated values of 7.54% and 7.36% which means they performed better than their Electrolyte 1 counterparts. Electrolyte 2 has the advantage of being less volatile which facilitates cell fabrication at steps such as filling or sealing the cell (see Chapter 2/Section 2.4). In terms of long time stability, Electrolyte 2 performed better (See Appendix 3.A), which could be due to the lower volatility of 3-methoxypropionitrile compared to acetonitrile. For these reasons Electrolyte 2 was employed exclusively henceforth. In addition, if not indicated otherwise, all cells have been masked from now on like outlaid in Section 2.5.1.

3.4.3 Introducing a scattering layer

TiO_2 scattering layer

One of the most effective ways of improving the photovoltaic performance of a DSC is the introduction of a scattering layer.[73] Since the 400 nm TiO_2 scattering particles mentioned by Grätzel and coworkers [60] were not readily available commercially, the approach of Lee et al. [72] was taken. Highly porous submicron-sized TiO_2 spheres were fabricated by a controlled hydrolysis of titanium tetraisopropoxide followed by hydrothermal treatment at 230 °C. After having prepared a paste with these particles (see Section 3.3.2), it has been screen printed on top of a standard nanocrystalline TiO_2 layer. Following this literature procedure [72], the particles should have a diameter of around 450 nm. Measurements of two

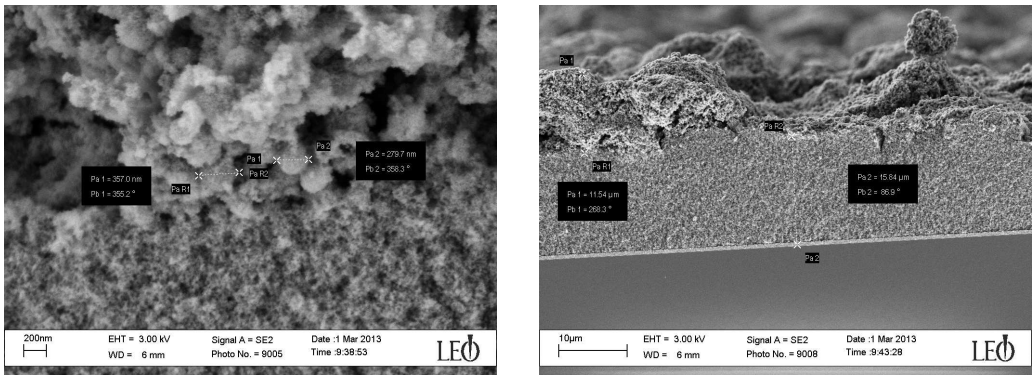

(a) SEM close up of the interface between nanocrystalline and scattering layer

(b) SEM cross section of a screen printed electrode

Figure 3.7: Sintered TiO_2 electrode including a scattering layer

selected particles in Figure 3.7a showed values of 280 nm and 357 nm. Even though they did not reach the desired size, single particles can be distinguished from the layer. However, there is a visible amount of smaller sized particles. The scattering layer surface of the composite layer in Figure 3.7b does look rather irregular compared to the nanocrystalline layer beneath it. Figure 3.8 and Table 3.3 show the results of two standard cells and two cells incorporating the fabricated scattering layer. The cells were measured directly after sealing and the ones with the scattering layer have reproducibly enhanced cell efficiency by about 0.8% compared to cells without a scattering layer. (See Table 3.3).

Measurements over time were conducted and are given in Appendix 3.B. These values show a consistently higher performance for cells with a scattering layer compared to cells without it.

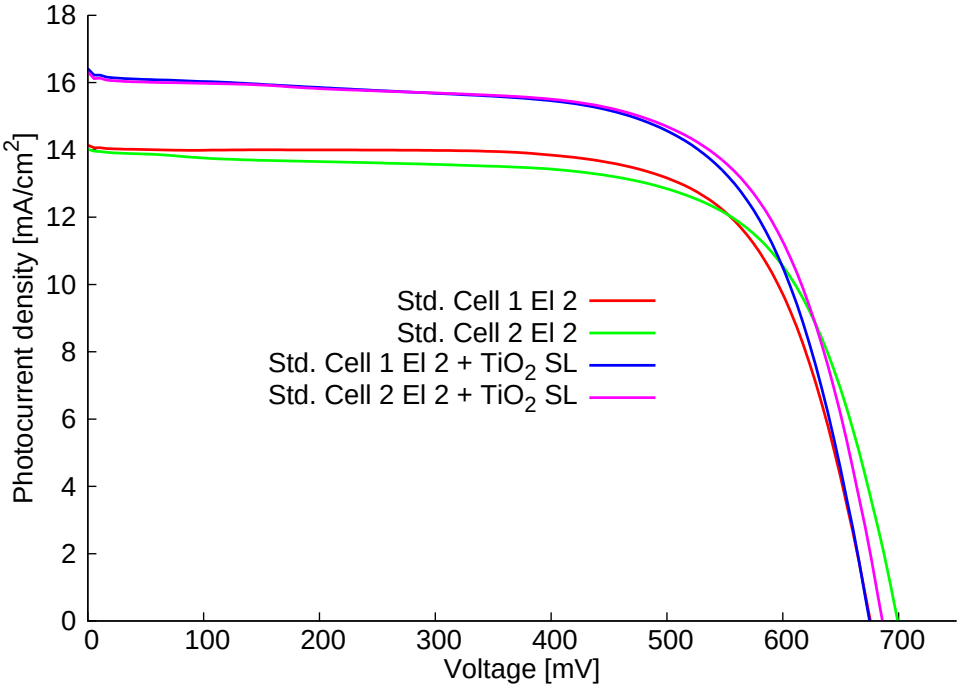

Figure 3.8: J-V curves of Std. N719 DSCs compared with Std. N719 DSCs with a TiO_2 scattering layer. Measurements were peformed on the day of sealing. All cells were masked.

Device name	J_{SC} [mA/cm^2]	V_{OC} [mV]	FF [%]	η [%]
Std. Cell 1 El 2	14.07	675	70.7	6.72
Std. Cell 2 El 2	13.97	699	68.3	6.67
Std. Cell 1 El 2 + TiO_2 SL	16.24	675	67.4	7.39
Std. Cell 2 El 2 + TiO_2 SL	16.14	686	67.9	7.51

Table 3.3: J-V parameters of Std. N719 DSCs compared with Std. N719 DSCs with a TiO_2 scattering layer. Measurements were peformed on the day of sealing. All cells were masked.

SiO_2/TiO_2 core/shell particle scattering layer

Since the TiO_2 particles were not found to be very uniform the approach of Guoping et al. was taken. [73] They described fabricating silica submicron spheres first and coating them with a TiO_2 shell afterwards. Furthermore, SiO_2 and TiO_2 have a large difference in their respective refractive indexes and therefore submicron SiO_2/TiO_2 core/shell particles should show a strong light scattering effect. [73] Figure 3.9(a) depicts an open scattering particle where the SiO_2 core is actually visible inside the TiO_2 wrapping. The SiO_2 particles have been very uniform before the TiO_2 shell was applied (see Figure 3.9(c)). The diameter of selected silica particles was determined to be around 400 $\pm$ 20 nm. By surrounding them with the TiO_2 shell, they grew further to diameters of 470-660 nm. The shell of the particle in Figure 3.9(a) was determined to be 175 nm in thickness. The diameter of the whole

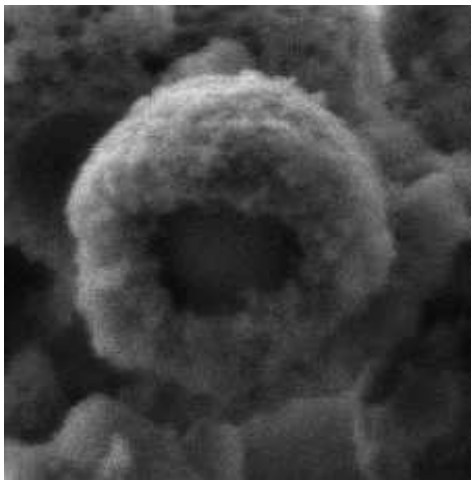

(a) Close-up of an SiO_2/TiO_2 scattering particle.

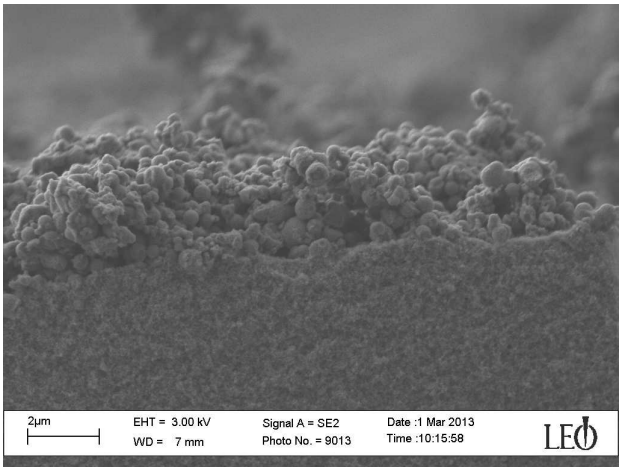

(b) Interface of the mesoporous TiO_2 layer and the SiO_2/TiO_2 scattering layer.

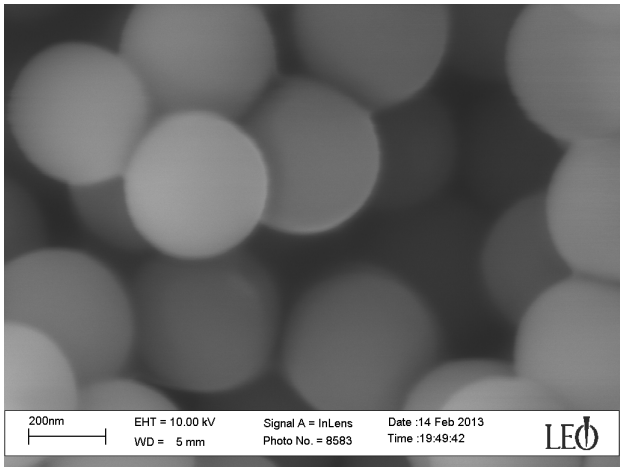

(c) SEM image of uniform SiO_2 particles

Figure 3.9: Image (a) shows an SiO_2/TiO_2 core-shell light scattering particle. Image (b) depicts a cross section of a sintered TiO_2 electrode including an SiO_2 core-shell scattering layer. The bottom image (c) shows a zoom-in on pure SiO_2 nanoparticles.

particle measured 645 nm. The scattering layer was about 2-4 µm thick (see Figure 3.9(b)).

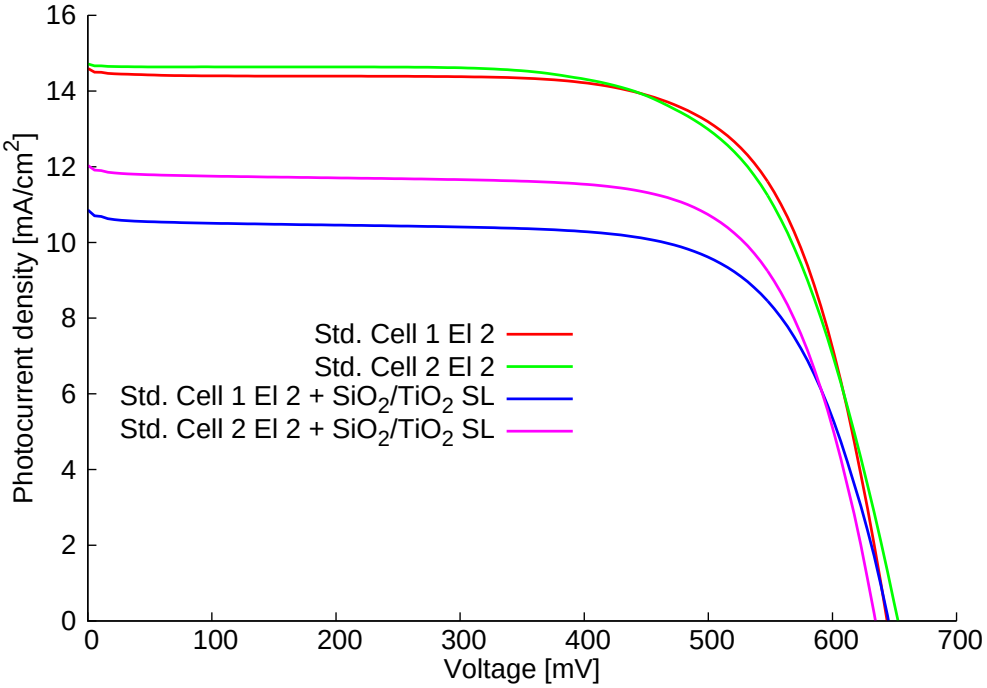

Figure 3.10: J-V curves of Std. N719 DSCs compared with Std. N719 DSCs with a TiO_2/SiO_2 scattering layer. Measurements were peformed on the day of sealing. All cells were masked.

Device name	J_{SC} [mA/cm^2]	V_{OC} [mV]	FF [%]	η [%]
Std. Cell 1 El 2	14.51	644	70.8	6.61
Std. Cell 2 El 2	14.67	653	67.9	6.50
Std. Cell 1 El 2 + TiO_2/SiO_2 SL	10.70	645	69.8	4.82
Std. Cell 2 El 2 + TiO_2/SiO_2 SL	11.91	635	71.0	5.37

Table 3.4: J-V parameters of Std. N719 DSCs compared with Std. N719 DSCs with a TiO_2/SiO_2 scattering layer. Measurements were peformed on the day of sealing. All cells were masked.

Unlike the TiO_2 scattering layer (see Figure 3.8, Table 3.3), the SiO_2/TiO_2 core/shell particle scattering layer did not enhance cell performance. It even seems to have lowered it as Figure 3.10 and Table 3.4 indicate. With the fill factor being comparable in all measured cells, the main difference after applying the scattering layer is in current generation. Although the scattering layer is supposed to enhance the photocurrent of the cell, it actually decreased in these experiments for no obvious reasons.

Acid treatment induced scattering layer

Another aproach to generate a scattering layer is the one of Watson and co-workers. [66] They have found a way to introduce a scattering layer via acid treatment of the deposited TiO_2 paste before sintering. They doctor bladed a TiO_2 layer onto the FTO substrate and

dipped it directly into 2 M nitric acid. Here, the screen printing approach was kept and the last printed TiO_2 layer was not dried on a hot plate (see Section 2.2.2), but immersed into 2 M nitric acid for 20 minutes. Upon dipping the electrode into the acid solution it turned from transparent to opaque almost instantly. The effect of this treatment can be seen on the sintered electrodes in Figure 3.11. By close examination of Figure 3.11a,

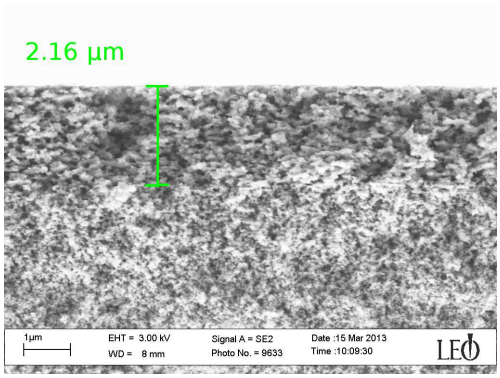

(a) Cross section of a sintered TiO_2 electrode with a previously acid treated top layer.

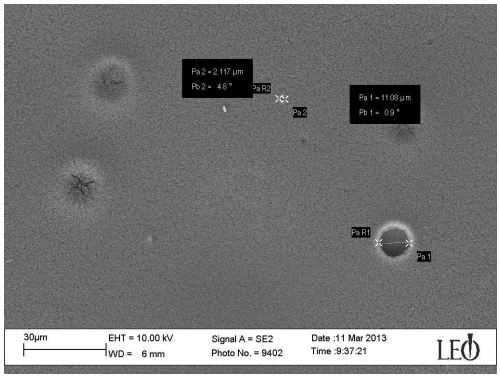

(b) Surface of the acid treated top layer of a TiO_2 electrode.

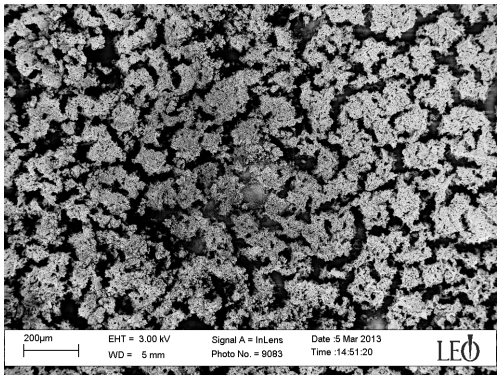

(c) Surface of a doctor bladed TiO_2 layer which has been acid treated directly after blading and subsequentially sintered.

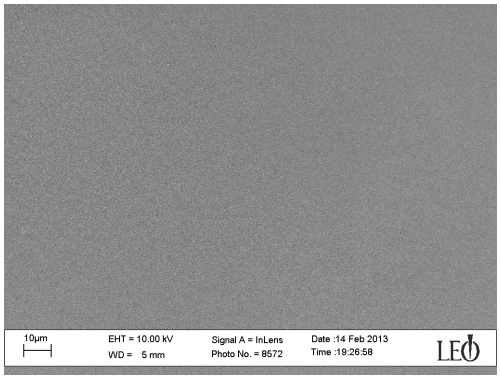

(d) Surface of a sintered TiO_2 layer that has been dried at 125 °C before acid treatment and subsequent sintering. No change in surface morphology has been observed

Figure 3.11: Sintered acid treated TiO_2 electrodes.

one can see a clear change in morphology of the last printed layer having a thickness of around 2.6 µm. Watson et al. [66] suggest a hydrolytic degradation of the organic binder in the TiO_2 paste, the ethyl cellulose, caused by nitric acid. They propose that by the degradation of the cellulose polymer chains, small amounts of water are released into the paste. Since not all the cellulose will degrade at the exact same time, the water is repelled by the organic medium it originated of. These water pockets force the the TiO_2 particles to rearrange. [66] The acid treatment only worked when the solvent (terpineol) was still present directly after printing. When the electrode was heated to evaporate the terpineol, no change in surface morphology was observed (See Figure 3.11d). When a TiO_2 layer

is doctor bladed and dipped directly into the acid however, the whole layer deforms to a pillar like macrostructure up to a point where the FTO on the bottom of the layer is visible (see Figure 3.11c). Dipping the electrode in water alone did not alter the surface of the TiO_2 layer, which means the acid is a necessary means of inducing the morphology change. Figure 3.12 and Table 3.5 show the results of the acid treated electrodes on the day of sealing. The acid treatment did neither affect V_{OC} nor the fill factor, the current of the acid treated cells however has been increased due to the light scattering acid treated layer. Figure 3.11b shows the surface of an acid treated TiO_2 layer. The crater that has formed as a consequence of the treatment measured 11 µm in diameter. These features were found all over the acid electrode surface.

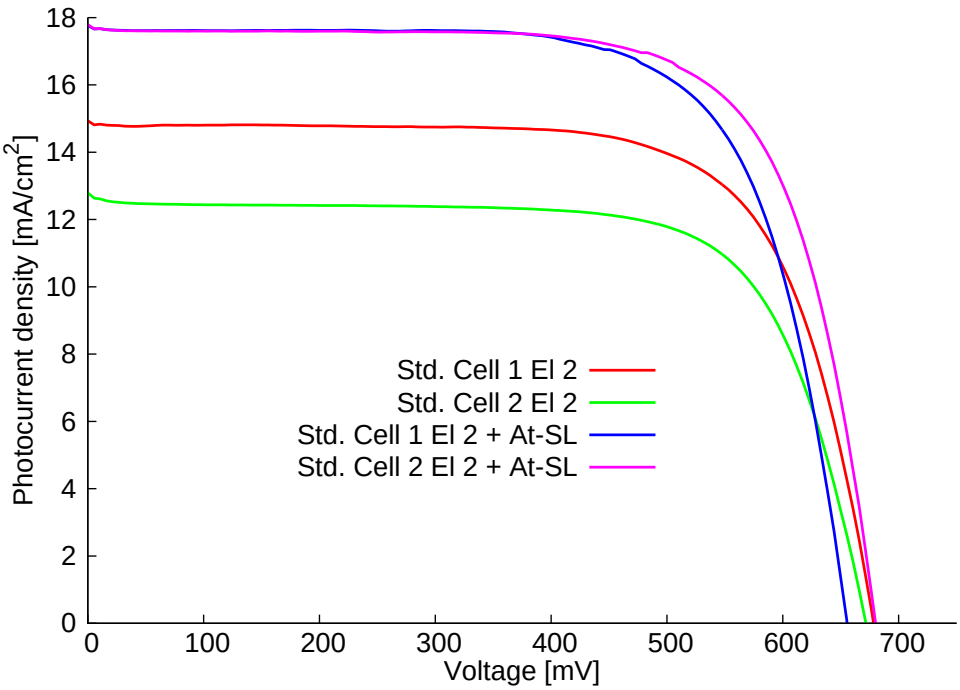

Figure 3.12: J-V curves of Std. N719 DSCs with and without an acid treated (At) top TiO_2 layer (Figure 3.11a). Cells have been measured directly after sealing. All cells were masked.

Device name	J_{SC} [mA/cm^2]	V_{OC} [mV]	FF [%]	η [%]
Std. Cell 1 El 2	14.9	678	71.1	7.18
Std. Cell 2 El 2	12.2	671	71.1	5.82
Std. Cell 1 El 2 + At SL	16.7	655	70.7	7.75
Std. Cell 2 El 2 + At SL	17.0	680	71.5	8.29

Table 3.5: J-V parameters of Std. N719 DSCs with and without an acid treated (At) top TiO_2 layer (Figure 3.11a). Cells have been measured directly after sealing. All cells were masked.

The EQE of DSCs featuring a scattering layer introduced by acid treatment was enhanced over the whole spectrum compared to DSCs without a scattering layer (see Figure 3.13).

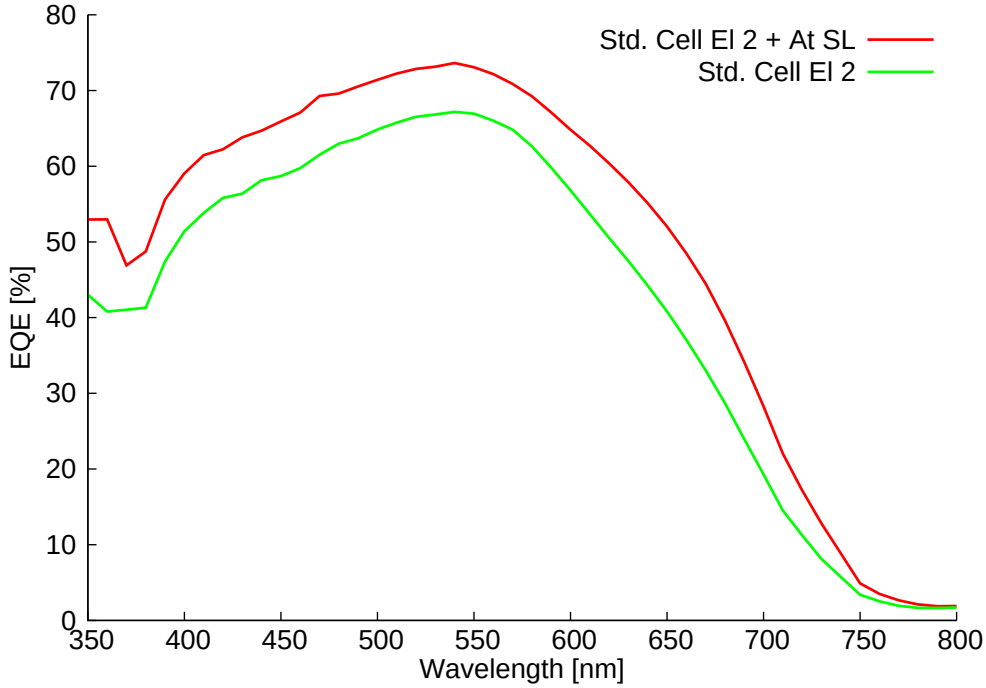

Figure 3.13: EQE spectrum of a Std. Cell and a Cell with an acid treated (At) top TiO_2 layer

3.5 Summary

TiO_2 particles and pastes have been fabricated in house and applied successfully in reproducible dye sensitized solar cells. This opens up the option of altering the semiconducting material and therefore a range of possibilities for cell optimization, e.g. porosity and structure of the semiconductor film. Furthermore, self made scattering layers have been applied to DSCs and proved to enhance the performance of the cells to a level competing with commercial solar cell test kits from Solaronix when using Electrolyte 2 (see Figure 3.14 and Table 3.6). 14 days after assembly, the DSC consisting of self made electrodes without a scattering layer was still more efficient than the commercial Solaronix test kit cell. The current density J_{SC} is comparable, but V_{OC}, the fill factor and hence the efficiency are all higher in the DSC built of self made electrodes. This is remarkable, because in the Solaronix electrodes, a 3 µm thick scattering layer is already included (see Figure 3.15). By applying a TiO_2 scattering layer to the standard home made electrode, its DSC efficiency is even higher with 8.30% 15 days after sealing. However, the transparent noncrystalline TiO_2 layer of a Solaronix electrode is only 10 µm thick (without the opaque scattering

layer), whereas the transparent noncrystalline layer of self made working electrodes already measures around 13.7 µm in thickness. By including a TiO_2 scattering layer the electrode

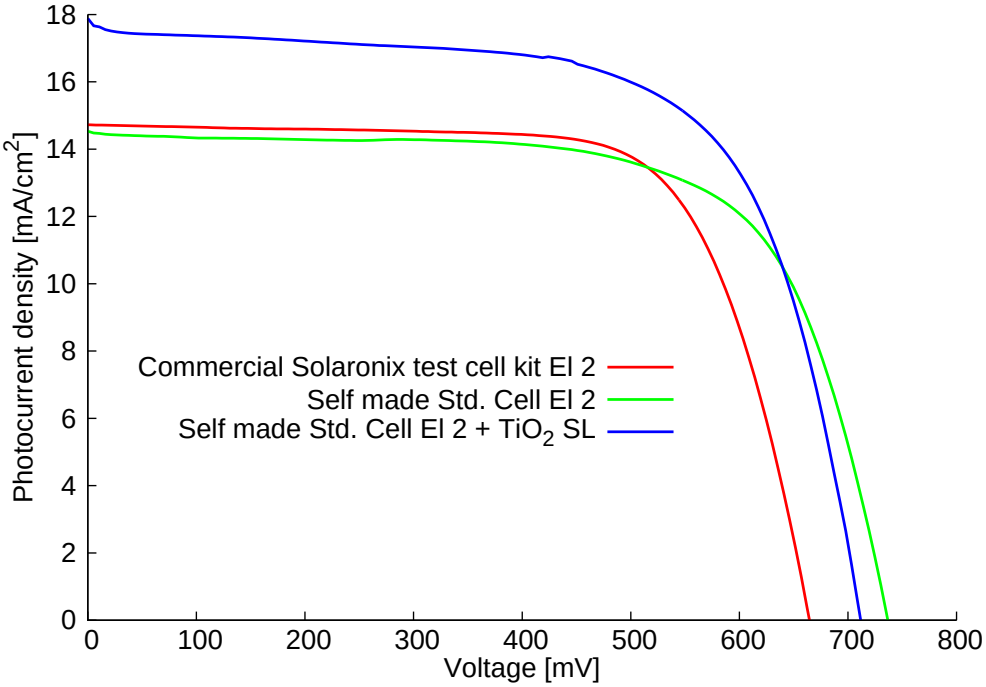

Figure 3.14: J-V curves of a self made standard working electrode compared to a Solaronix commercial DSC test cell kit. Both have been measured 14 days after fabrication. A self made standard working electrode incorporating a TiO_2 scattering layer measured on day 15 after sealing is depicted as well. All cells were masked.

Device name	J_{SC} [mA/cm^2]	V_{OC} [mV]	FF [%]	η [%]
Self made Std. Cell El 2 + TiO_2 SL	17.6	711	66.2	8.30
Self made Std. Cell El 2	14.5	736	68.3	7.29
Solaronix test cell kit El 2	14.8	670	70.7	6.94

Table 3.6: J-V parameters of cells with self made electrodes compared to a Solaronix test cell kit, measured 14 days after sealing. All cells have been measured with Electrolyte 2 and were masked.

even gets thicker. DSCs with the scattering layer induced by acid treatment showed an efficieny of 8.29% at fabrication day (the Solaronix DSC performed at 7.14% at that point) and 8.49% the day after, which was the highest reached efficiency. By acid treatment of the top screen printed layer the electrode thickness was not altered and hence comparable to a commercial electrode (Self made: 13.65 µm vs commercial: 10.0 µm + 3.34 µm scattering layer, depicted in Figure 3.15). Unfortunately the available equipment (autoclave) has been proven not to be strenuous or big enough for hydrothermal TiO_2 particle preparation on a sensible scale. Hence for further cell development commercial TiO_2 particles or a commercial TiO_2 paste from Dyesol were used. For liquid electrolyte DSCs commercial Solaronix

test cell kits were utilized exclusively from this point on. This has reduced the necessary time and effort for screening dyes in leDSCs greatly.

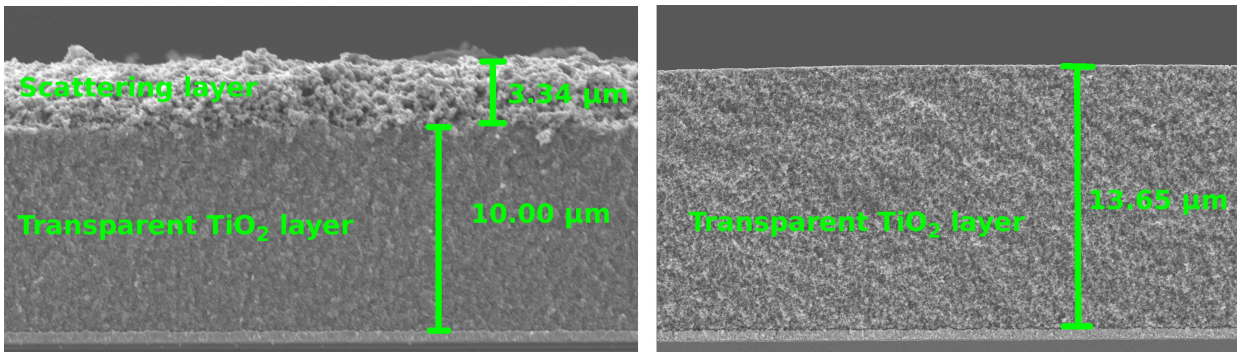

Figure 3.15: A commercial electrode from Solaronix (on the left) is compared to a self printed TiO_2 electrode with 8 printed layers.

Appendix 3.A Std. DSCs with Electrolytes 1 and 2 measured over time.

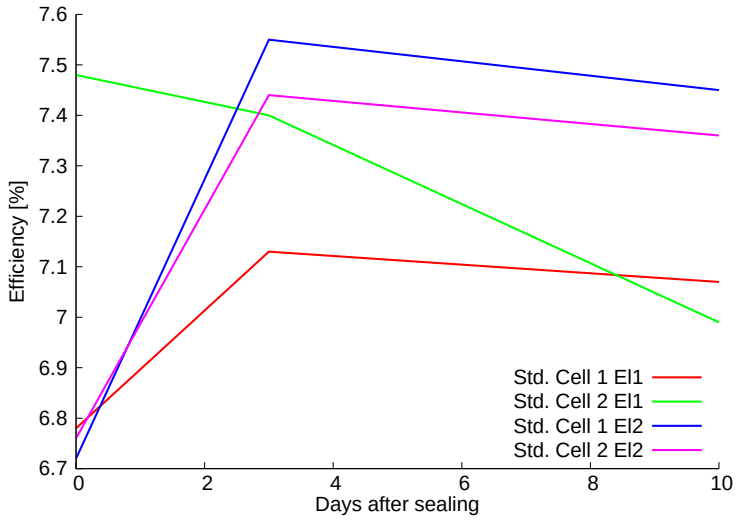

Figure 3.16: Efficiency comparison of Electrolytes 1 and 2 over time.

Days after sealing [#] →		**0**	**3**	**10**
η [%] →	Std. Cell 1 El 1	6.79	7.13	7.01
	Std. Cell 2 El 1	7.48	7.40	7.00
	Std. Cell 1 El 2	6.72	7.54	7.45
	Std. Cell 2 El 2	6.67	7.44	7.36
ff [%] →	Std. Cell 1 El 1	73.4	74.3	73.4
	Std. Cell 2 El 1	71.7	72.7	72.7
	Std. Cell 1 El 2	70.7	69.7	69.9
	Std. Cell 2 El 2	68.3	68.2	67.3
$\mathbf{V}_{OC}$ **[mV]** →	Std. Cell 1 El 1	651	672	690
	Std. Cell 2 El 1	712	717	709
	Std. Cell 1 El 2	675	684	696
	Std. Cell 2 El 2	699	714	723
$\mathbf{J}_{SC}$ **[mA/cm²]** →	Std. Cell1 El1	14.2	14.3	14.0
	Std. Cell2 El1	14.7	14.2	13.57
	Std. Cell1 El2	14.1	15.8	15.3
	Std. Cell2 El2	14.0	15.2	15.1

Table 3.7: J-V parameters of Std. DSCs measured over time for Electrolytes 1 and 2.

Appendix 3.B Std. DSCs with and without TiO_2 scattering layer measured over time.

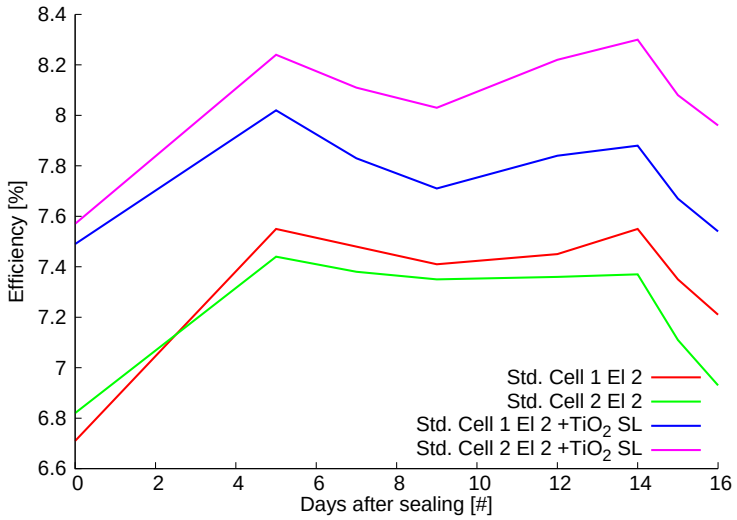

Figure 3.17: Efficiency of DSCs with and without TiO_2 scattering layer measured over time.

Days after sealing [#] →		**0**	**3**	**6**	**8**	**10**	**13**	**15**	**16**	**17**
η [%] →	Std. Cell 1 El 2	6.71	6.72	7.55	7.48	7.41	7.45	7.55	7.35	7.21
	Std Cell 2 El 2	6.82	6.67	7.44	7.38	7.35	7.36	7.37	7.11	6.93
	Std. Cell 1 El 2 + TiO_2 SL	7.49	7.38	8.02	7.83	7.71	7.84	7.88	7.67	7.54
	Std. Cell 2 El 2 + TiO_2 SL	7.57	7.51	8.24	8.10	8.03	8.22	8.30	8.08	7.97
ff [%] →	Std. Cell 1 El 2	71.1	70.7	69.7	70.2	69.7	69.9	69.4	69.4	69.6
	Std. Cell 2 El 2	70.0	68.3	68.2	67.8	67.4	67.3	67.2	66.7	65.8
	Std. Cell 1 El 2 + TiO_2 SL	69.9	67.4	65.6	65.2	63.9	64.8	64.5	64.4	64.4
	Std. Cell 2 El 2 + TiO_2 SL	69.6	67.9	66.0	66.2	64.8	66.1	66.2	65.8	65.9
$\mathbf{V}_{OC}$ **[mV]** →	Std. Cell 1 El 2	667	675	684	694	695	696	694	699	698
	Std. Cell 2 El 2	688	699	714	723	717	723	721	721	722
	Std. Cell 1 El 2 + TiO_2 SL	658	675	690	702	703	706	704	703	703
	Std. Cell 2 El 2 + TiO_2 SL	666	686	700	709	705	709	711	713	707
$\mathbf{J}_{SC}$ $\mathbf{[mA/cm^2]}$ →	Std. Cell 1 El 2	14.1	14.1	15.8	15.3	15.3	15.3	15.7	15.2	14.8
	Std. Cell 2 El 2	14.2	14.0	15.3	15.1	15.2	15.1	15.2	14.8	14.6
	Std. Cell 1 El 2 + TiO_2 SL	16.3	16.2	17.7	17.1	17.2	17.1	17.3	17.0	16.7
	Std. Cell 2 El 2 + TiO_2 SL	16.3	16.1	17.8	17.3	17.6	17.5	17.6	17.2	17.1

Table 3.8: J-V parameters over time for Std. DSCs with and without TiO_2 scattering layer.

Appendix 3.C Std. DSCs with and without SiO_2/TiO_2 scattering layer measured over time.

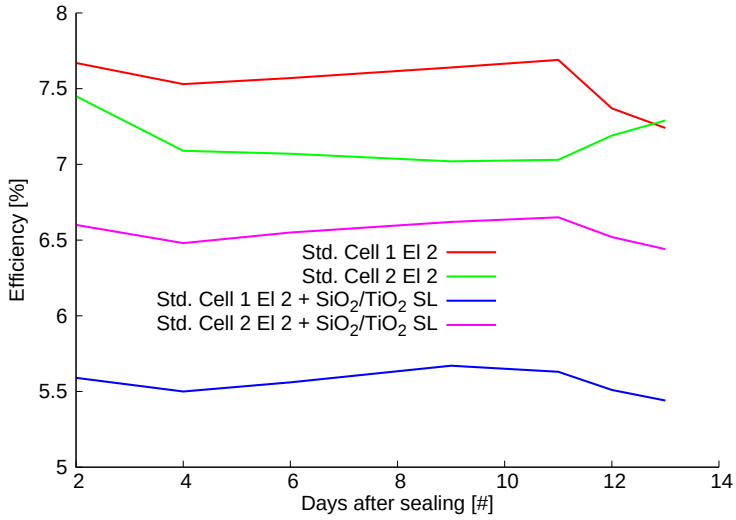

Figure 3.18: Efficiency of DSCs with and without SiO_2/TiO_2 scattering layer measured over time.

Days after sealing [#] →		**0**	**3**	**5**	**7**	**10**	**12**	**13**	**14**
η [%] →	Std. Cell 1 El 2	6.61	7.67	7.53	7.57	7.64	7.69	7.37	7.24
	Std. Cell 2 El 2	6.50	7.45	7.09	7.07	7.02	7.03	7.19	7.29
	Std. Cell 1 El 2 + SiO_2/TiO_2 SL	4.82	5.59	5.50	5.56	5.67	5.63	5.51	5.44
	Std. Cell 2 El 2 + SiO_2/TiO_2 SL	5.40	6.60	6.48	6.55	6.62	6.65	6.52	6.44
ff [%] →	Std. Cell 1 El 2	70.1	66.7	66.9	67.1	66.9	65.9	66.1	65.7
	Std. Cell 2 El 2	67.9	65.8	64.9	63.9	62.8	62.5	66.5	68.3
	Std. Cell 1 El 2 + SiO_2/TiO_2 SL	69.8	68.6	68.6	69.3	69.1	68.2	68.2	67.2
	Std. Cell 2 El 2 + SiO_2/TiO_2 SL	71.0	70.4	71.2	71.0	70.7	70.1	70.2	70.1
$\mathbf{V}_{OC}$ **[mV]** →	Std. Cell 1 El 2	644	713	730	731	735	734	733	733
	Std. Cell 2 El 2	653	714	731	736	738	734	734	736
	Std. Cell 1 El 2 + SiO_2/TiO_2 SL	645	701	713	721	729	723	720	720
	Std. Cell 2 El 2 + SiO_2/TiO_2 SL	635	698	709	714	719	719	722	720
$\mathbf{J}_{SC}$ **[mA/cm^2]** →	Std. Cell 1 El 2	14.5	16.1	15.4	15.4	15.5	15.9	15.2	15.0
	Std. Cell 2 El 2	14.7	15.9	15.0	15.0	15.2	15.3	14.7	14.5
	Std. Cell 1 El 2 + SiO_2/TiO_2 SL	10.7	11.6	11.2	11.1	11.2	11.4	11.2	11.2
	Std. Cell 2 El 2 + SiO_2/TiO_2 SL	11.9	13.4	12.8	12.9	13.0	13.2	12.9	12.8

Table 3.9: J-V parameters measured over time for Std. DSCs with and without SiO_2/TiO_2 scattering layer.

Appendix 3.D Std. DSCs with and without acid treatment (At) measured over time.

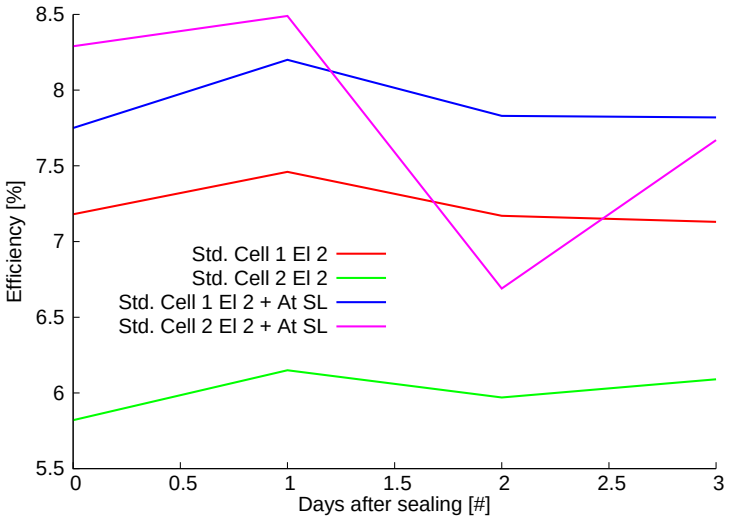

Figure 3.19: Efficiency of DSCs with and without At scattering layer measured over time.

Days after sealing [#] →		**0**	**1**	**2**	**3**
η [%] →	Std. Cell 1 El 2	7.18	7.46	7.17	7.13
	Std. Cell 2 El 2	5.82	6.15	5.97	6.09
	Std. Cell 1 El 2 + At SL	7.75	8.20	7.83	7.82
	Std. Cell 2 El 2+ At SL	8.29	8.49	6.69	7.67
ff [%] →	Std. Cell 1 El 2	71.1	70.8	70.4	70.2
	Std. Cell 2 El 2	71.1	71.0	70.3	70.5
	Std. Cell 1 El 2 + At SL	70.7	70.7	70.1	69.1
	Std. Cell 2 El 2 + At SL	71.5	71.2	59.9	67.0
$\mathbf{V}_{OC}$ **[mV]** →	Std. Cell 1 El 2	678	698	698	702
	Std. Cell 2 El 2	671	688	692	694
	Std. Cell 1 El 2 + At SL	655	675	679	687
	Std. Cell 2 El 2 + At SL	680	697	683	700
$\mathbf{J}_{SC}$ $[\mathbf{mA/cm^2}]$ →	Std. Cell 1 El 2	14.9	15.1	14.6	14.5
	Std. Cell 2 El 2	12.2	12.6	12.3	12.4
	Std. Cell 1 El 2 + At SL	16.7	17.2	16.5	16.5
	Std. Cell 2 El 2 + At SL	17.1	17.1	16.4	16.4

Table 3.10: J-V parameters of Std. DSCs with and without an At scattering layer measured over time.

Chapter 4

Copper(I) Iodide Solid State Dye Sensitized Solar Cells (ssDSCs)

In Sections 4.1 and 4.2, a theoretical background on copper(I) iodide (CuI) ssDSCs is given as well as some general experimental procedures for this chapter. Although several things had to be altered due to different equipment and experience, experimental procedures have been retrieved from literature and are referenced to it. The original work on CuI ssDSCs starts in Section 4.3 ("Cell development"), where several literature procedures have been changed or combined by altering the morphology of the TiO_2 layer or introducing a new dye. Section 4.5 gives a small summary of the chapter. Commercial TiO_2 particles have been used throughout in this chapter. All TiO_2 pastes have been self fabricated. These are our first attempts to assemble ssDSCs.

4.1 Working principle of a solid state DSC

SsDSCs eliminate several disadvantages of liquid electrolyte DSCs, such as leakage of the electrolyte and evaporation of volatile solvents by employing a solid state hole transport material (HTM). Moreover, ssDSCs can be very flexible in design and lightweight. Consequently, much research has been conducted on ssDSCs since the prototypes have been fabricated in 1995 by Tennakone et al. [74] and in 1998 by Grätzel et al. [25, pp. 165] [75] [76] [77] [25, pp. 163]. An example of the working principle of a ssDSC is depicted in Figure 4.1. When sunlight hits the cell, the dye is elevated to an excited state above the conduction band of the semiconductor. This permits electron injection into the conduction band of the TiO_2, oxidizing the dye. By generating a positive charge vacancy in the hole transporter, labeled as an electron hole (h^+), the dye is reduced again. Electrons

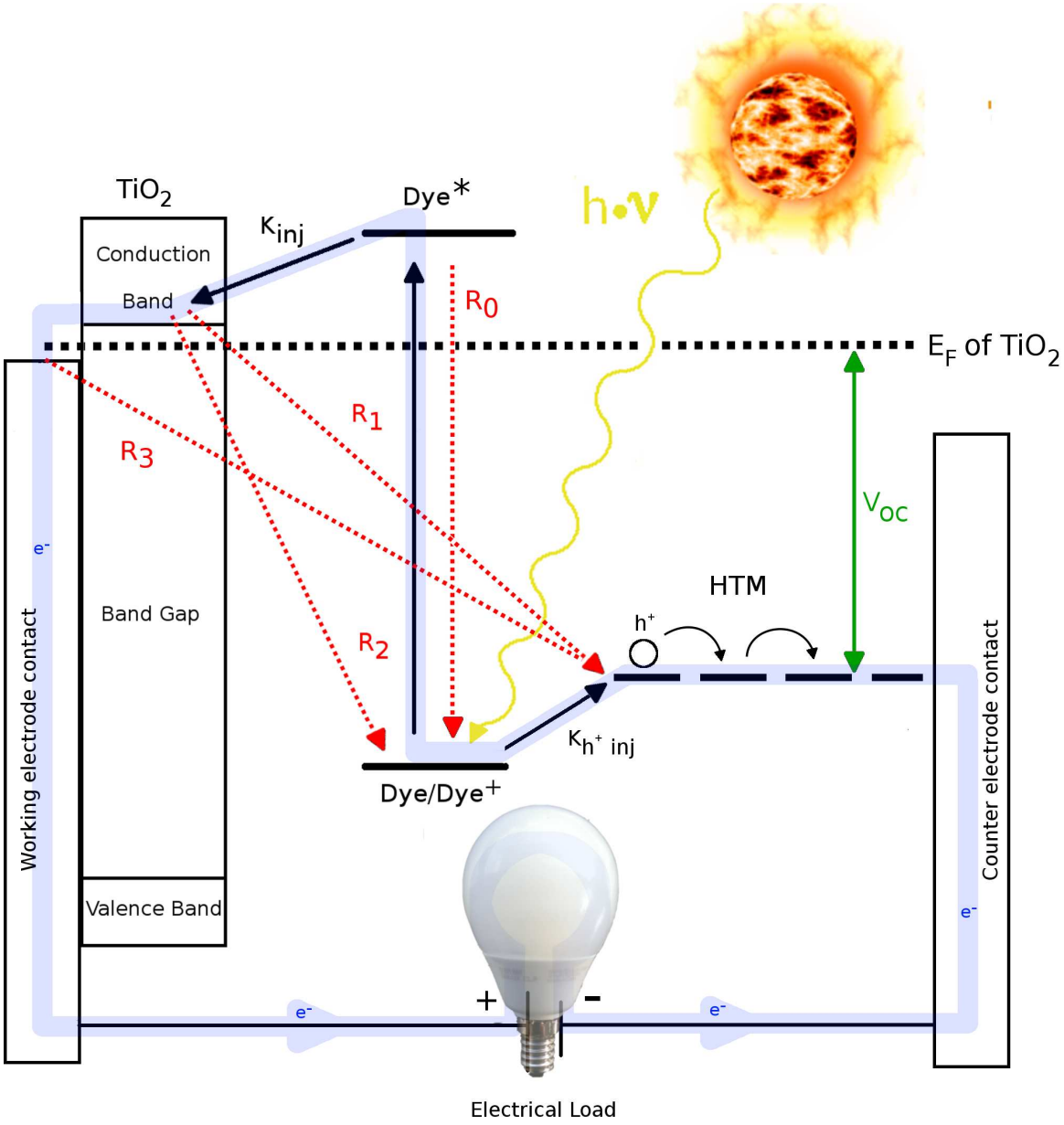

Figure 4.1: Scheme of a ssDSC, representing the TiO_2/HTM junction. Processes in favour of cell performance are highlighted in black, the ones detrimental to cell performance in red (recombination reactions). The blue path depicts the hole electric circuit

are conducted through an external circuit, pass an electrical load (e.g. a light bulb) and recombine with the holes in the HTM. However, there are also processes detrimental to the cell performance, indicated by the red arrows in Figure 4.1. When electrons in the conducting band of the TiO_2 recombine with the oxidized dye (R_2) or the holes in the hole conductor (R_1), cell performance is decreased. An especially important recombination in this type of cell is R_3. This recombination occurs in liquid DSCs as well, but is not very severe. In the literature it is indicated that this is due to a large overpotential between the I^-/I_3^- redox couple and the FTO, meaning the redox electrolyte is lying at a much more

negative potential (actual potential values for FTO have not been found in literature). [78] [79, pp. 7] However, in solid state DSCs this interface forms an ohmic contact [79] leading to short circuits. Grätzel and co-workers have approached this problem by putting an additional compact layer of TiO_2 between the FTO and the nanocrystalline TiO_2 layer to avoid contact of the HTM with the FTO. [78] A TiO_2 compact layer has been reported to increase the current output of ssDSCs by three to four orders of magnitude and hence is indispensable to avoid short circuits. (See Figure 4.2a). [78] Figure 4.2b shows energy level values compared to vacuum of a ssDSC. Since the energy level of the FTO is above the one of CuI conduction band, recombination of electrons and holes takes place. According to Manmeeta et al. [80] the I^-/I_3^- redox couple has a redox potential of -4.83 eV vs vacuum, which would be less than half the potential difference (0.37 eV) from FTO to copper iodide (CuI). This would explain the larger driving force of R_3 in ssDSCs featuring CuI as the hole conductor compared to liquid I^-/I_3^- electrolyte DSCs and therefore the necessity of a compact TiO_2 underlayer to prevent the latter. One of the very first reports of the concept of a ssDSC was released in 1995 by Tennakone et al., and this cell featured CuI as an inorganic hole transporter. Three years later, Grätzel et al. demonstrated their first ssDSC incorporating the organic dye 2,2',7,7'-tetrakis(N,N-di-*p*-methoxyphenylamine) 9,9'-spirobifluorene (spiro-OMeTAD) as the hole transport material. Both cells had a similar power conversion efficiency (PCE) of 0.7-0.8 %. [74] [75] As opposed to the most common liquid electrolyte DSC system (I^-/I_3^-), where four iodide ions and two holes are involved in each dye reduction (see Equations 3.1), here only a one-electron process takes place. Therefore, a lower driving force should be needed for the dye regeneration and thus for hole transporter based systems compared to their liquid counterparts. [25, pp. 173] Figure 4.3 shows an exemplary cross sectional schematic of a CuI ssDSC as prepared in this Chapter. Working and counter electrodes have been either clipped together by strong metal clamps or sealed with Araldite. At the contacts, conducting silver paste was applied.

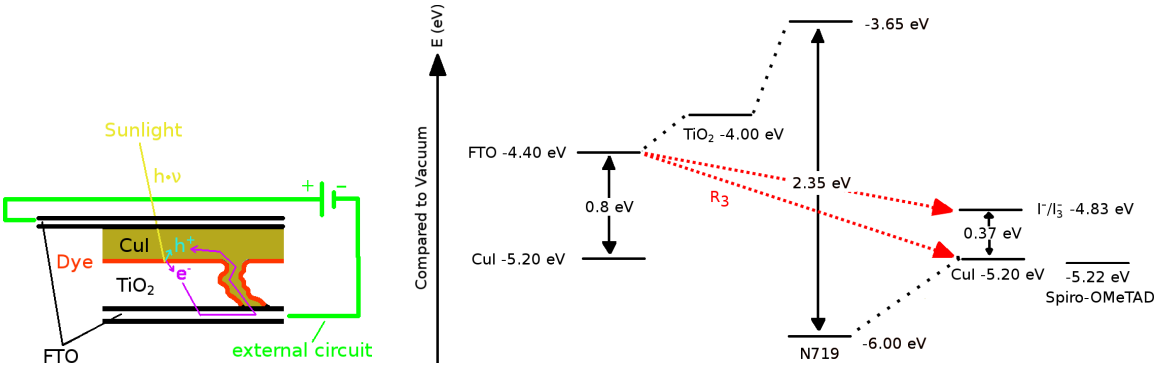

(a) Short circuit by CuI touching the back contact

(b) Energy levels compared to vacuum

Figure 4.2: Short circuit in ssDSCs and energy level diagrams compared to vacuum. The approximate values have been gathered from several sources [61][81][82][83][84][85][86]

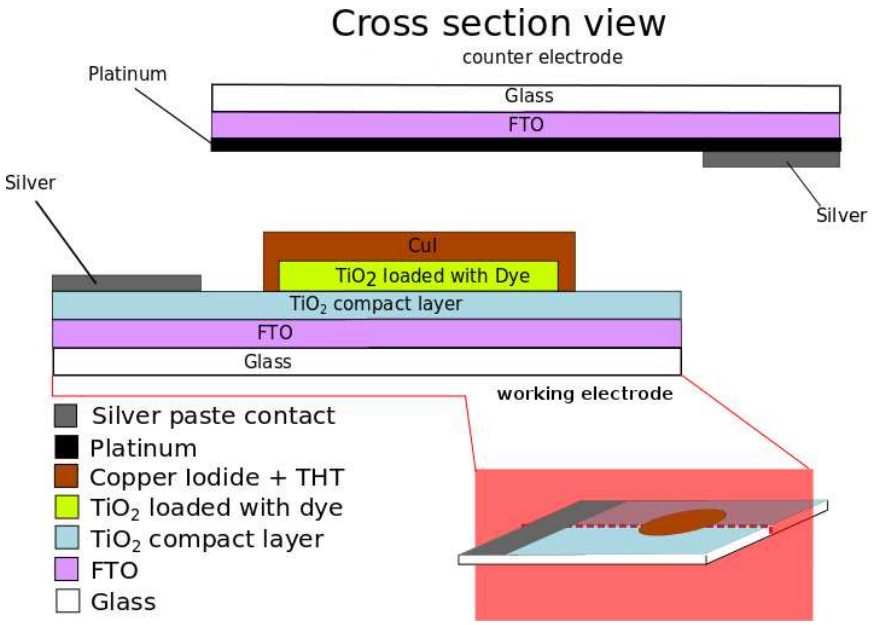

Figure 4.3: Architecture of a CuI ssDSC

4.2 Main components of ssDSCs

4.2.1 The compact layer

As explained in Section 4.1, a compact layer is indispensable in solid state DSCs. Electrons will always take the shortest route to a positive counter charge. When the hole conductor goes all the way down to the FTO, an ohmic contact is formed and electrons are not forced to travel through the external circuit or the electrodes of any device, the cell will not produce

any current and a short circuit is established, highlighted pink in Figure 4.2a. Although this has been generally accepted, the first CuI ssDSC reported did not feature a compact TiO_2 layer underneath the TiO_2 semiconductor layer. This could presumably be omitted because of the way the TiO_2 was applied and the resulting morphology. According to Tennakone et al. the TiO_2 layers applied in this way are largely free of interconnected pores that reach the FTO of the anode. By dropping the TiO_2 paste 1 slowly on a hot plate, sintering it and repeating that procedure multiple times a film dense enough to prevent the copper iodide from contacting the FTO seems to be established. [87] However, by using numerous other commercial and self-made pastes, which are preferred due to their easier and faster way of application by doctor blading or screen printing, a compact layer is necessary to prevent short circuits. Compact layers in this Chapter have either been sprayed as described by Kavan et al [88] [89, pp. 20] or spin coated after a modified procedure from Hörhold et al. [90]. In the following discussion, these will be referred to "sprayed compact layer" and "spin coated compact layer". The detailed experimental method for the sprayed and spin coated compact layers is given in section 4.2.2. Whereas the sprayed compact layer could not be observed by microscopic methods except when applying 30 spraying cycles which resulted in a thickness of 1.4 µm (See Figure 4.5a). The spin coated compact layer could be confirmed to be around 40-170 nm thick by AFM and SEM/FIB microscopy. (See Figures 4.4a and 4.4b

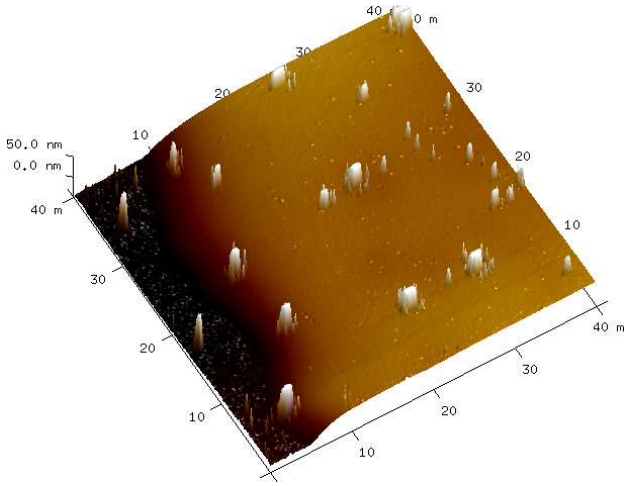

(a) AFM image of the compact layer

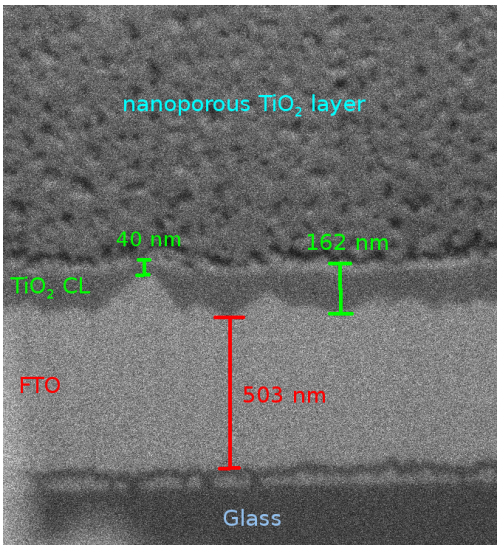

(b) SEM/FIB image of the compact layer

Figure 4.4: Spin coated compact layer thickness

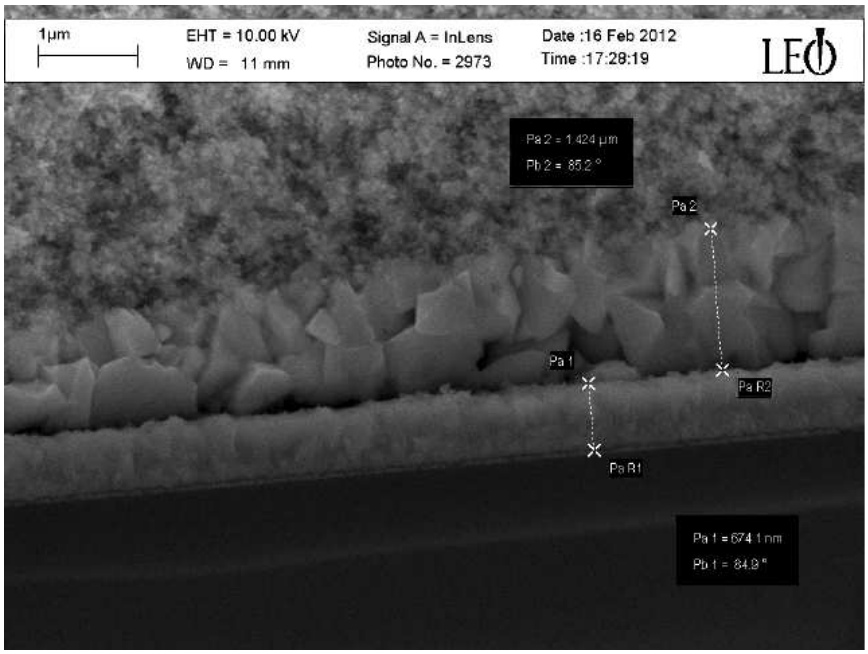

(a) SEM/FIB image of a sprayed compact layer with 30 cycles

Figure 4.5: Compact layer thicknesses

4.2.2 Compact layer fabrication

Two types of compact layers have been fabricated, they will be referred to as "sprayed" and "spin coated" compact layer. As mentioned above, the sprayed compact layer has not been confirmed by microscopic methods whereas the spin coated one has.

Sprayed compact layer

Sprayed compact layers have been fabricated with nitrogen as the carrier gas with 0.5 bar closed pressure. To achieve this, the substrate was heated to 450 °C and a 0.2 M solution of titanium acetylacetonate (TAA) in isopropanol was sprayed at intervals of 5 x 3 s intervals. After every 3 s, the cells were annealed for 1 min. After the hole spray procedure, the electrodes were annealed for 30 minutes at 500 °C. The layout of the glass sheet and the spraying setup can be seen in Figure 4.6. After having cooled down, the glass was broken into 20 working electrodes. [89, pp. 20–21]

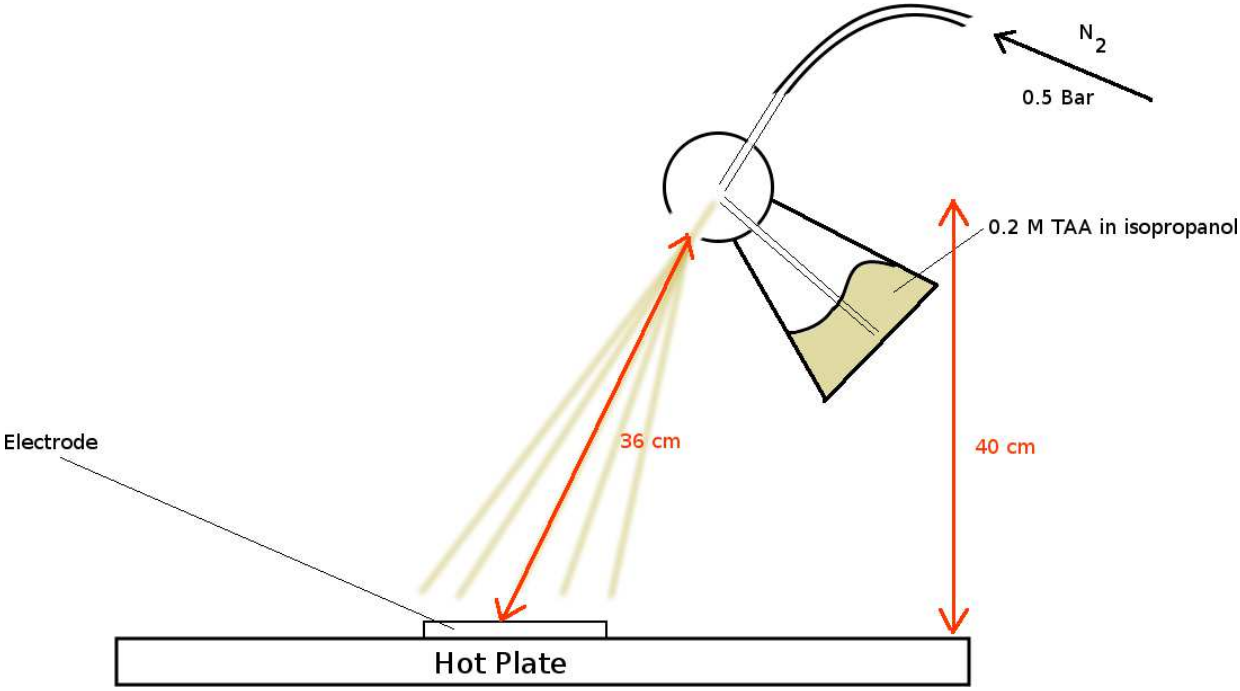

Figure 4.6: Spraying setup

Spin coated compact layer A glass sheet of 8x8 cm has been sonicated for 15 min. in a 2% solution of sonoswiss cleaner. It has been rinsed with tap water to remove soap traces, then with H_2O miliq and finally with ethanol. After having dried in air it was put into a UV/ozone cleaner for 20 minutes. The glass plate was placed on a spin coater and vacuum was applied (the last impurities on the glass plate were blown off with nitrogen before.) The whole surface area of the glass sheet was covered with a spin coat solution consisting of hydrochloric acid (4.40 ml 38 %), H_2O (1.00 ml), Ethanol (40.0 ml) and titanium ethoxide (4.00 ml). Around 1.5 ml were was needed to cover the whole substrate. The glass sheet was spun at 3000 rpm for 60 s (acceleration and deceleration were set to 1 s.). Afterwards, plate was cleaned thoroughly on the bottom side with a dust free tissue and ethanol. It was put in an oven at 78 °C for 45 min and was annealed subsequently for 30 min at 540 °C. [90] After cooling down, each glass plate was cut carefully into 20 cells per plate, each measuring 1.5 cm x 2 cm.

4.2.3 The semiconductor

As with the liquid-state DSCs in Chapter 3, the most common semiconductor applied with ssDSCs is nanoparticulate titanium dioxide. As mentioned in Section 4.1, crystalline HTMs like CuI suffer inherit a reduced pore filling ability compared to liquid electrolytes. Several measures have been taken to make the TiO_2 films more porous, usually by adding a filling material like polyethylene glycol (PEG) which is burned in the film sintering process and leaves the semiconductor layer with cavities/large pores to be filled by the HTM. [91] Four pastes have been prepared for ssDSC fabrication, all with commercial P25 particles from Degussa/Evonik. Paste 1 was fabricated after Tennakone et al. [87], paste 2 after Grätzel et al. [92] and paste 3 & 4 after Konno et al. [91]. Paste1 did not contain any organic binder. It had a very liquid consistency compared to the others. Very dense, sheet like structures could be built up with this paste. Paste 2 was used for liquid state DSCs by Grätzel and coworkers [92]. Pastes 3 & 4 were fabricated identically to paste 2, but polyethylene glycol (PEG600 for paste 3 and PEG20000 for paste 4) has been added to enhance porosity and make the paste more susceptible to penetration from the HTM. Due to its fluidity, paste 1 cannot be doctor bladed or screen printed and application after Tennakone et al. [87] involves a time consuming drop coating/sintering process outlaid in section 4.3.1. It was desirable to fabricate pastes suitable for doctor blading with a similar structure. Figure 4.7 shows the surface SEM images of all four fabricated pastes with approximately the same magnification. The experimental procedure for all the TiO_2 pastes is given in Section 4.2.4. As can be observed, PEG20000 in paste 4 had the biggest effect on the surface morphology compared to paste 2 without any PEG additive and paste 3 with PEG600 added. These pastes were not suitable for screen printing. The PEG addition rendered them too viscous and the pastes would have clogged the screen printing mesh. They were therefore applied by doctor blading exclusively.

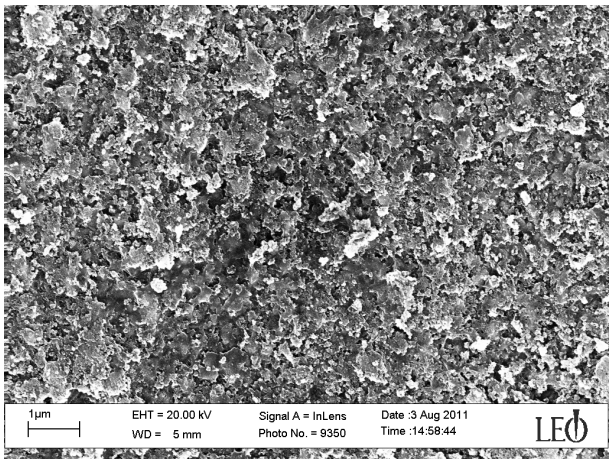

(a) Paste1: Brittle, sheet-like surface

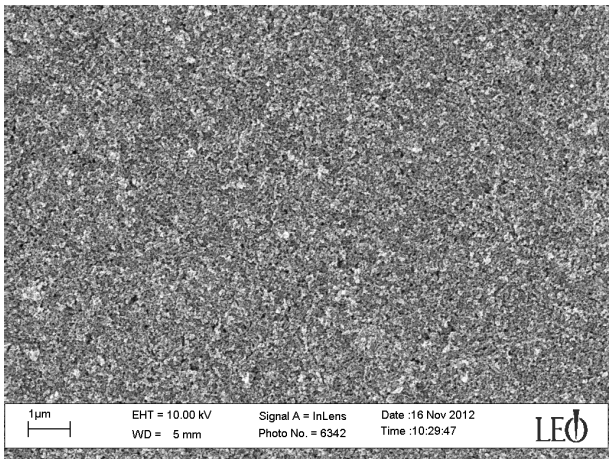

(b) Paste2: smooth surface, no PEG addition

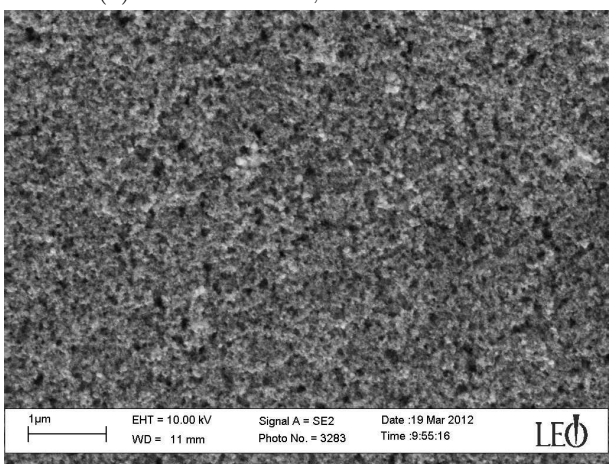

(c) Paste3: PEG600 addition

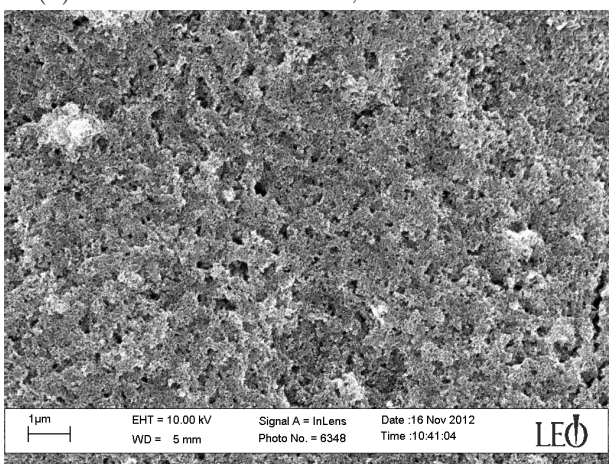

(d) Paste4: PEG20000 addition

Figure 4.7: Surfaces of sintered films of pastes 1-4

4.2.4 TiO_2 Paste fabrication

Chemicals (all from Sigma Aldrich):

Ethyl Cellulose CAS: 9004-57-3 Prod. # 46070-250G-F Ethyl Cellulose CAS: 9004-57-3 Prod. # 46080-250G-F Terpineol: CAS: 8000-41-7 Prod. # 86480-250ML Ethanol: 99.999 % Water: Deionized from laboratory tap. TiO_2 particles: P25 Degussa/Evonik

Paste 1 (Drop coating paste)

A mixture of titanium tetra-isopropoxide (5.00 ml), propan-2-ol (15.0 ml) and acetic acid (5.50 ml) was hydrolyzed by slow and drop wise addition of water (4.50 ml added in total). 0.65 g of TiO_2 nanoparticle powder was added and the mixture was agitated ultrasonically for 1 h. [87]

Pastes 2-4 (no PEG, PEG20000 and PEG600 containing pastes)

For pastes 2-4, the scheme in Figure 4.8 can be applied. For paste 4, double the scale was used. Apart from that, the only difference is in the variables X and Y in the red encircled step. They are indicated for each paste separately. All additions have been made slowly and dropwise. The ethyl cellulose solutions (two types, each 0.75 g (total 1.5 g) dissolved in Ethanol to a 10%wt solution, 15 g in total) have been prepared beforehand. A porcellain mortar was used as well as plastic spatulas and beakers to avoid metal contamination.

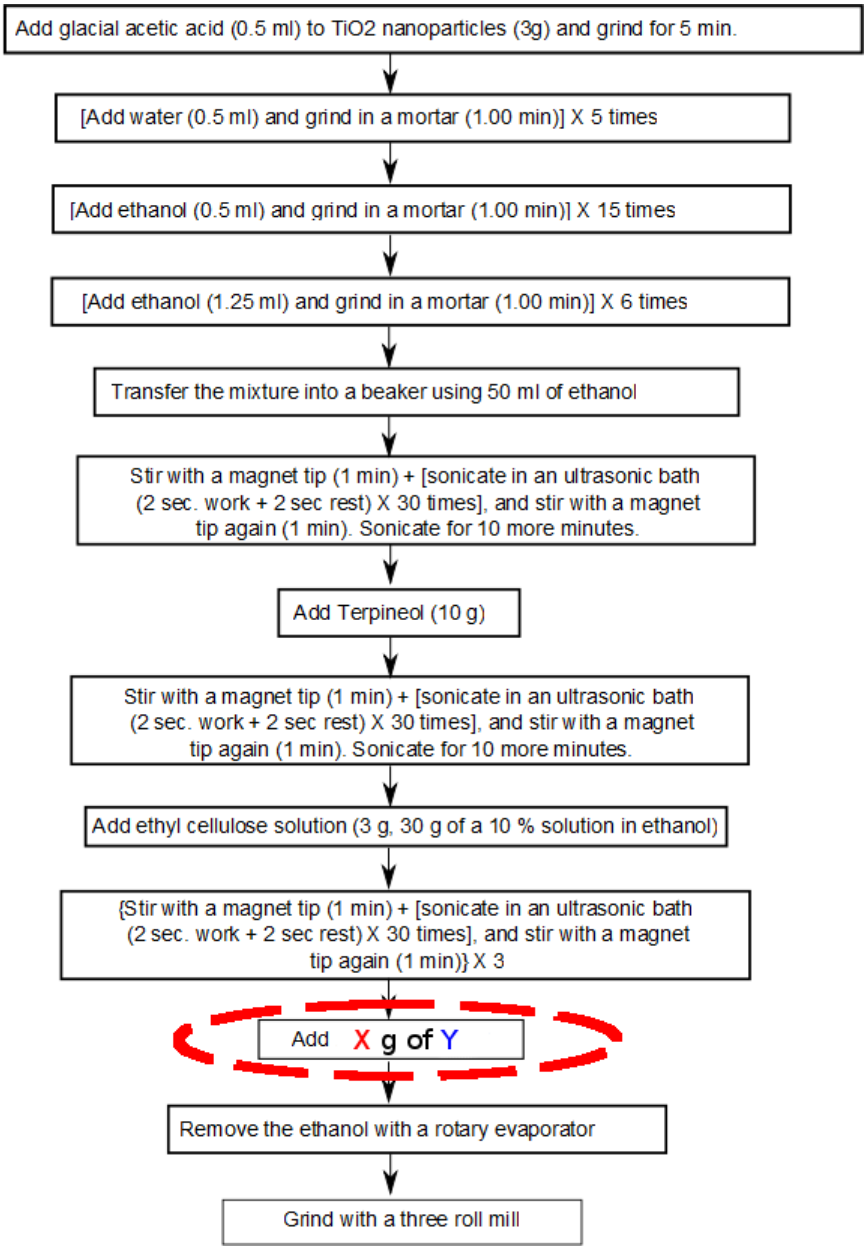

Figure 4.8: Paste fabrication scheme for pastes 2-4

Paste 2: X=0, Y=none **Paste 3**: X=2.5 g Y= PEG600 **Paste 4**: X=2.5 g Y= PEG20000

Three roll mill grinding was done until a homogenous paste was obtained, which took around 10 min for the most dense paste (paste 4), so this was set as the standard.

4.2.5 Dyes

Two dyes have been investigated for CuI ssDSCs, one of them being N719. The other one is a combination of the anchoring ligand labeled "ALP1" and the HTM CuI (ALP1-CuI), depicted in Figure 4.9. The N719 dye was obtained commercially and the anchoring ligand

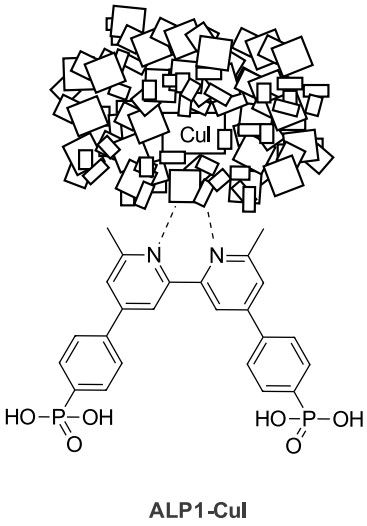

Figure 4.9: CuI coordinating to anchoring ligand ALP1 in CuI ssDSCs

ALP1 was provided by Dr. Iain A. Wright [47]. With ALP1-CuI, an enhanced electron and especially hole injection was hoped to be achieved, since the HTM itself forms the dye and is directly connected to it.

4.2.6 The hole transport material (HTM)

In the last twenty years, many hole conductors have been investigated, inorganic as well as organic ones [19, pp. 6637–6639] Grätzels cell from 1998 was the first to incorporate an organic HTM, namely 2,2',7,7'-tetrakis(N,N-di-*p*-methoxyphenylamine) 9,9'-spirobifluorene (spiro-OMeTAD), see Figure 4.10) and reached a power conversion efficiency of 0.7%. Almost a decade after this discovery, spiro-OMeTAD still continued to be the hole conductor with the highest efficiency, amounting to over 5% in 2010. [25, pp. 163-203]. Although this is a relatively efficient HTM, there are some disadvantagesto it, above all it has a relatively high price. In 2013, the commercial price of spiro-OMeTAD was over ten times higher than the one of gold and platinum. Even though the price might drop

on a large scale for commercialization, the synthetic methods and the high purity needed for this particular application in a solar cell suggest otherwise. There are other potential HTMs that could be used for a much lower cost, and on example is copper iodide (CuI). [93] CuI has three crystalline forms, α-, β- and γ-CuI. Below 350 °C, CuI is present in the γ-Form. From 350 to 392 °C β-CuI is the stable form and above 392 °C it transforms to α-CuI. [94] Here, only the low temperature γ-form is used. Copper(I) iodide is highly conductive, exceeding 10^{-2} S cm^{-1}, and can be applied directly from solution. Pure spiro-OMeTAD on the other hand only has a conductivity of $2.5 \cdot 10^{-7}$ S cm^{-1}. It can be raised up to $3.0 \cdot 10^{-5}$ S cm^{-1} or even higher by doping with bis(trifluoromethane)sulfonimide (Li-TFSI) or other additives, but the conductivity of the pure material is lower than the one of CuI. [25, pp. 181] [95] [96] Moreover, the valence band energy level of CuI is very similar to the one of spiro-OMeTAD, which can be observed in Figure 4.11a. Another advantage of a solid hole conductor like copper iodide or spiro-OMeTAD are the theoretically higher open circuit voltages (V_{OC}). In Figure 4.11b, the approximate potentials have been compared against the normal hydrogen electrode. The TiO_2 conducting band lies at -0.5 V. The iodide/triiodide (I^-/I_3^-) redox potential lies at 0.5 V, which means a maximum theoretical V_{OC} of ∼1 V can be achieved. The CuI potential on the other hand lies at around 0.92 V, which means theoretically (without recombination reactions) the solar cell could reach a V_{OC} of around 1.42 V. The same applies to Spiro-OMeTAD, since it has a very similar valence band potential. The first ssDSC featuring copper iodide as the hole conducting material was demonstrated by Tennakone et al. [74]. They applied CuI by solution casting after prior dissolution in acetonitrile. However, one disadvantage of using crystalline inorganic hole conductors is their tendency to rapidly crystallize out of solution. This interferes with pore filling, which is a crucial parameter in a ssDSC. [87]. Because of the limited penetration of HTMs into the TiO_2, the active layers are usually thinner than with leDSCs, whose layers are reported to be up to 14 µm [60]. Among the best PCEs for ssDSCs have been reported for cells with a 2 µm thick TiO_2 layer. To alleviate this problem, a crystal growth inhibitor is used. [97] [98]. In this work, triethylamine hydrothiocyanate (THT) has been employed. It was synthesized from ammonium thiocyanate and triethylamine according to the equation below [98].

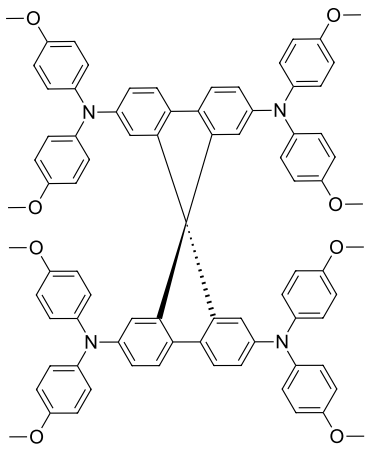

Figure 4.10: Chemical structure of spiro-OMeTAD

$$(C_2H_5)_3N + NH_4^+SCN^- \implies (C_2H_5)_3NH^+SCN^- + NH_3$$

For a detailed experimental procedure, see Section 4.2.8. THT is a molten salt and liquidizes

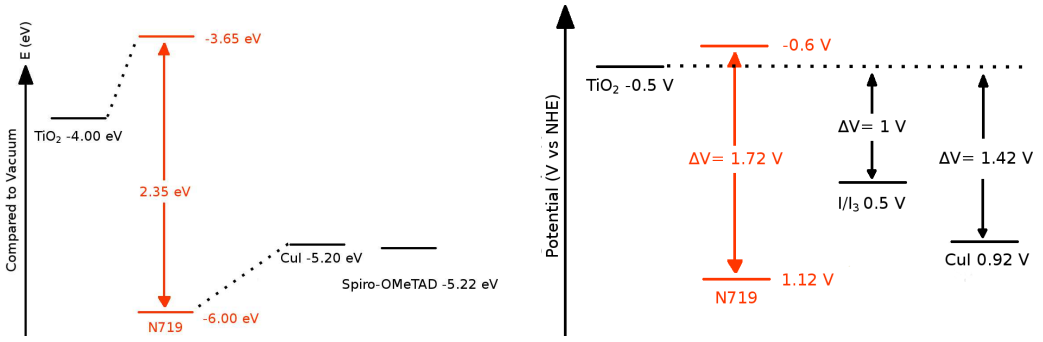

(a) Energy levels compared to vacuum.

(b) Potentials compared to the normal hydrogen electrode.

Figure 4.11: Energy levels of an ssDSC compared to vacuum and the normal hydrogen electrode. The approximate values have been gathered from several sources [61][81][82][83][84][85]

at room temperature (25 °C). Thiocyanate salts prevent crystal growth of CuI because the SCN^- ions adsorb very strongly to the CuI surface crystallites. This adsorption is followed by further adsorbing of cations and a monolayer forms around the CuI crystallite preventing growth of the particle. Figure 4.12 shows the effect of the crystal growth inhibitor. With no THT present in the coating solution, the copper iodide crystallizes to big crystals over one micron in size (Figure 4.12a). By adding trace amounts of THT into the coating solution, only sub micron crystals are formed upon drying (Figure 4.12b). Another very similar hole

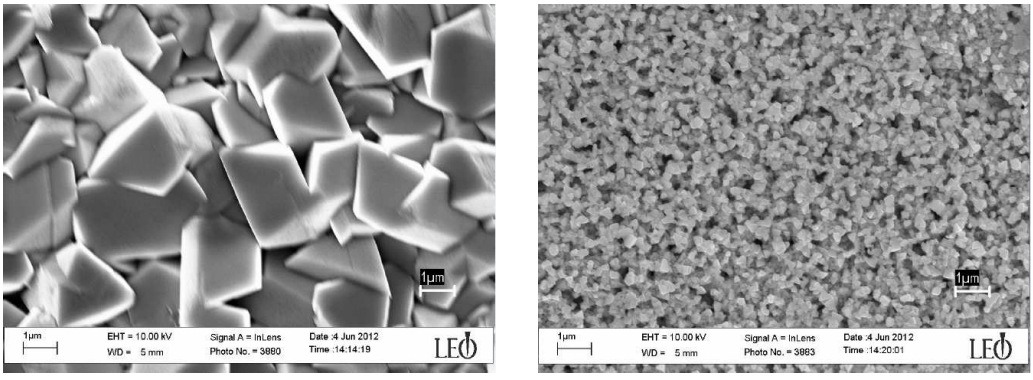

(a) CuI without THT

(b) CuI with THT

Figure 4.12: Dried films of copper iodide with and without the addition of THT.

transporting material is copper(I) thiocyanate (CuSCN). It has a larger band gap than CuI (CuSCN: 3.6 eV, CuI: 3.1 eV) and also meets all energy level requirements for a ssDSC. However, it is poorly soluble in organic solvents and thus is more limited in it's application than CuI. [99] Due to its promising properties and low cost, copper iodide was the HTM of choice in the following work. As mentioned above, a crystal growth inhibitor is vital to the performance of this type of ssDSC. Besides crystal growth, another problem affects the stability of CuI ssDSCs. [100] [101] [102] Light of wavelength equal to or bigger in energy

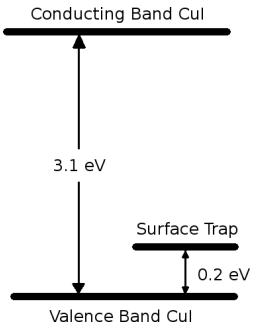

Figure 4.13: Iodine induced surface trap

than the CuI band gap photodecomposes CuI liberating iodine (for example CuI=Cu+I). An excess of iodine in the bulk CuI material acts as an electron acceptor for electrons from the valence band of CuI, generating I^- ions. Thus p-type conductivity is induced, using iodine as the dopant.[103] However, this excess iodine diffuses to the surface and has the detrimental effect of generating hole trapping sites (Figure 4.13) located at arount 0.2 eV above the valence band edge of the copper iodide, trapping electron holes and mediating recombination. If holes are trapped in a slightly elevated position the electrones from the conduction band of the TiO_2 can recombine with it. Therefore cell performance is decreased. According to Tennakone et al. [100] this is most likely the major cause of recombination in CuI ssDSCs and is also mentioned in more recent literature. [101] [102]

4.2.7 HTM application

The Copper Iodide has beed deposited on to of the TiO_2 layer (see Figure 4.3) either by spraying or drop coating a solution of CuI (0.300 g)in acetonitrile (10.0 ml) containing THT (4.00 mg).

4.2.8 Triethylamine hydrothiocyanate (THT) synthesis

$$(C_2H_5)_3N + NH_4^+SCN^- \implies (C_2H_5)_3NH^+SCN^- + NH_3$$

Ammonium thiocyanate (4.00 g) was dried for 30 minutes under a high vacuum. Prior distilled triethylamine (12.0 ml) was added and the mixture was stirred under nitrogen at 70 °C for 1.5 h. The temperature was increased to 125 °C for further 30 minutes and the reaction was left to cool down to 293 K. Gas production was checked with a bubbler. The end of gas production indicates completion of the reaction. The reaction mixture was transferred to a separation funnel and washed with hexane (3x 30.0 ml) to remove excess of triethylamine. After that it was washed with dichloromethane (50.0 ml) to precipitate

unreacted ammonium thiocyanate, which was filtered off. The remaining THT solution was was treated with charcoal, filtered, and the solvent was removed under reduced pressure. THT was obtained as a colorless viscous liquid (5.08 g). [98]

4.2.9 Magnesium oxide layers blocking recombination

On the semiconductor surface, there are likely to be areas of bare TiO_2 uncovered by the dye. CuI and TiO_2 are in direct contact, readily admitting trapmediated recombination. As a countermeasure, Taguchi et al. [104] and Kumara et al. [87] fabricated solid-state DSSCs with a MgO-coated TiO_2 nanoporous film. These solar cells showed improved conversion efficiency and stability which is due to inhibition of electron back transfer from TiO_2 to the hole conductor. [105][106][98][107][100]

Magnesium oxide layers were introduced by boiling the sintered TiO_2 electrode in a $2 \cdot 10^{-3}$ M solution of magnesium acetate ($Mg(OAc)_2$) in a solution of 85% ethanol in water for 1 min. The electrodes have been washed with ethanol to remove magnesium acetate inside the pores and sintered again at 450 °C for 30 minutes. Hydrolysis of $Mg(OAc)_2$ covers the TiO_2 particle surface with a layer of MgO.

4.2.10 Counter electrode

The counter electrode material in a ssDSC should be highly conductive and have a good mechanical, electrochemical and chemical stability. Noble metals such as platinum, gold or silver are frequently used as counter electrodes in this type of cell.

4.2.11 Counter electrode fabrication

The counter electrodes were prepared similar to Grätzel and coworkers [60]. The FTO coated glass was first washed with a 2%wt sonoswiss detergent solution for 15 min. It was rinsed with deionized water, miliQ water and ethanol subsequentially. The glass sheets were left to dry in air and ozone treated with a UV-Ozone cleaner to remove organic residues. The plates were cut into 1.5x2.0 cm pieces, coated with 2 drops Platisol T (Solaronix) solution on the FTO side and left to dry in air. The Platisol coated electrodes were heated to 450 °C for 30 minutes and left to cool down.

4.3 Cell development

For cell development, the approach of Tennakone et al was taken. [87] [74] If not indicated otherwise, cells have not been masked in this section. In contrast to all other DSCs in this thesis, the CuI ssDSCs were not irradiated for 10 minutes before measuring. They were directly measured without irradiating them first. In each of the following experiments, a small table[1] with details about the cell construction is given above the J-V graph.

4.3.1 Producing a working copper iodide ssDSC

Figure 4.14 shows the layout of a fabricated CuI ssDSC. Paste 1 was used as well as a

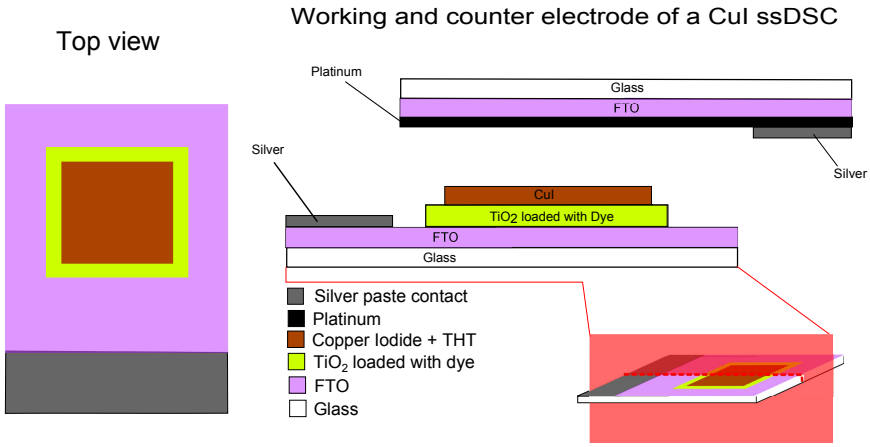

Figure 4.14: Layout of a CuI ssDSC incorporating paste 1

blocking oxide layer (MgO). N719 was adapted as the dye. No compact layer was applied to this experiment and platinum was used as the counter electrode. The CuI was sprayed from solution on a layer of paste 1 with a Hansa paintbrush (See detailed cell construction). To avoid contact with the FTO, the CuI was applied slightly inwards-shifted leaving some space at the TiO_2 edges (See Figure 4.14). One measurement was done masked, the other one unmasked. Even though the experiment produced a working ssDSC (see Table 4.1), the efficiency was low compared to the reported values for this type of cell (4.7%, [87]). Figure 4.16 shows a SEM image of a cross section of the fabricated electrode [2]. Since the electrode in Figure 4.16 was slightly tilted to the side, some surface information can be obtained as well. The surface in general seemed to be very irregular, featuring big

[1] Compact layer was abbreviated with "Comp. layer", counter electrode with "C. electrode"

[2] To record this image, the working electrode was scored on the back (non-FTO) side and broken apart in a way that a cross sectional view on the TiO_2 layer was enabled. The cut was made ideally like the red plane depicts in Figure 4.3.

aggregates of CuI up to 12 µm and higher. The height of the TiO_2 layer was measured to be around 2.6 µm at the indicated position. In the literature, layers up to 10 µm are reported though. [87]

TiO_2	HTM	Dye	C. electrode	Comp. layer
Paste1	CuI + THT	N719, 0.5 mM	Platinum	None

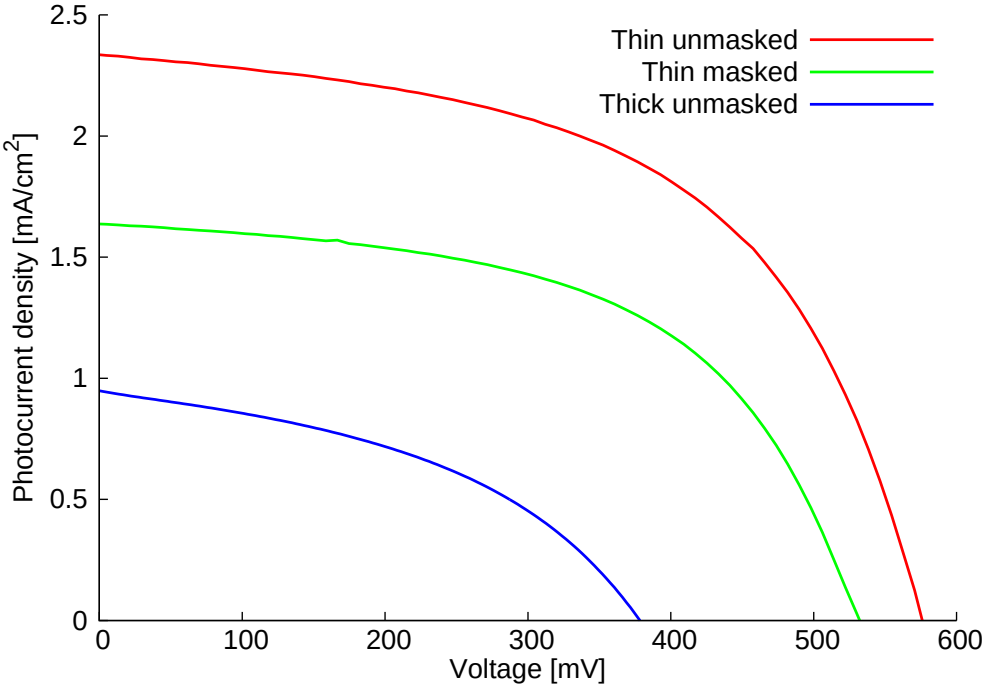

Figure 4.15: J-V curves of our first CuI ssDSCs. Two cells have been measured, one with a 2.6 µm thick TiO_2 electrode (labelled "Thin") and one with a 10 µm thick TiO_2 electrode (labelled "Thick").

Device Name	J_{SC} [mA/cm^2]	V_{OC} [mV]	FF [%]	η [%]
Thin unmasked	2.34	571	54.5	0.727
Thin masked	1.64	530	54.7	0.474
Thick unmasked	0.955	378	42.4	0.153

Table 4.1: J-V parameters of our first CuI ssDSCs. Two cells have been measured, one with a 2.6 µm thick TiO_2 electrode (labelled "Thin") and one with a 10 µm thick TiO_2 electrode (labelled "Thick").

By repeating the experiment with a 10 µm thick TiO_2 layer (labelled "Thick unmasked" in Figure 4.15 and Table 4.1), the efficiency of the cells dropped to around 0.5%. Also the electrodes were visibly less colored than their thinner counterparts, especially close to the FTO of the working electrode. It is suspected that the built up structure was too dense and therefore took up less dye. The parameters of the thinner ssDSC were monitored over time. The result can be observed in Figure 4.17. Ten days after the first measurement, J_{SC}

Figure 4.16: Cross section of a drop coated solid state DSC

had dropped from 2.34 mA to 2.02 mA. 35 days after cell assembly, J_{SC} had fallen to 1.72 mA. The efficiency was 0.55% at that point. The open circuit voltage of the cell remained remarkably stable over this time. In between measurements, the cells were stored in the dark in an ambient atmosphere.

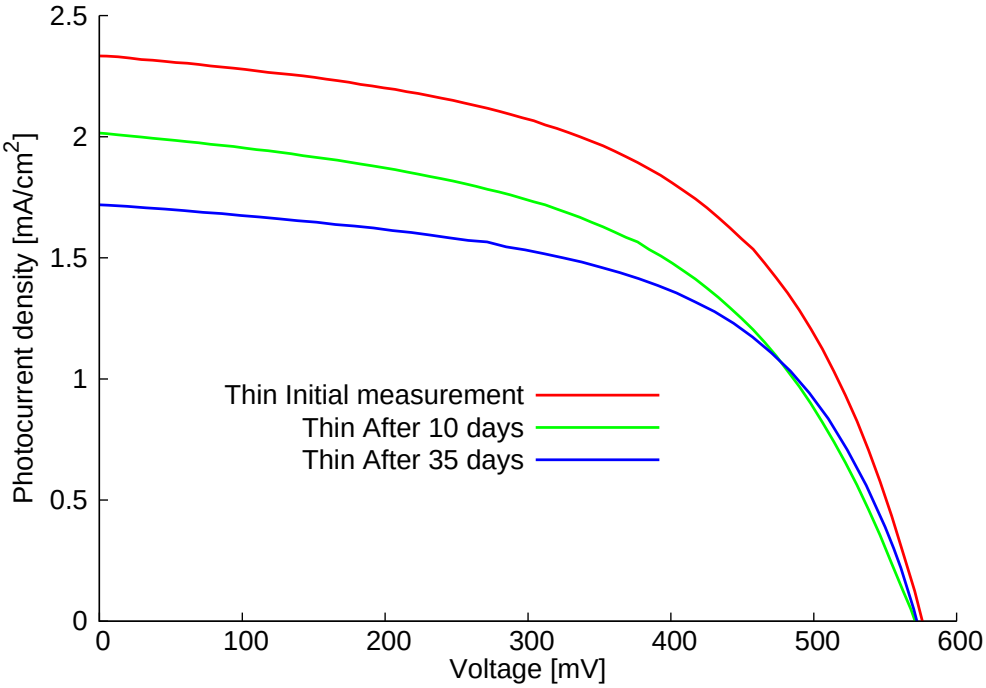

Figure 4.17: J-V curves of the Cell with the thinner TiO_2 electrode measured over time. All measurements were conducted with an unmasked cell.

Device Name	J_{SC} [mA/cm^2]	V_{OC} [mV]	FF [%]	η [%]
Initial measurement	2.34	571	54.6	0.727
After 10 days	2.02	571	52.3	0.593
After 35 days	1.72	572	56.8	0.550

Table 4.2: J-V parameters of the Cell with the thinner TiO_2 layer measured over time. All measurements were conducted with an unmasked cell.

Spraying copper iodide was the first reported way of applying CuI as a hole transporter. [74] However, this method of application is not very reliable, because the nozzle of the Hansa 481 airbrush pistol clogged very frequently and a lot of stains stayed on the cell that could not be washed off again. Also, the pulling force of the hood was deflecting the spraying beam considerably. Due to these reasons, the spraying approach was abandoned and CuI was applied by solution casting, as reported in more recent publications. [87] [108]. Also, since thicker layers of paste 1 resulted in poorer cell performance, it was abandoned and focus was laid on pastes suitable for more time efficient ways of deposition like doctor blading.

Detailed Cell construction

An FTO glass sheet, measuring 1.6 x 2 cm, was cleaned by subsequently sonicating it in an aqueous soap solution, acetone and ethanol, each for 10 min. Then the glass plate was blown dry with nitrogen. The glass sheets were masked with a double layer of scotch (3M Magic) tape, leaving a square area of 1 cm^2 open. The masked glass substrate was heated to (95-110 °C) and the unmasked area was covered with TiO_2-paste 1. The paste was left to dry and the emerging lose crust was wiped off with cotton wool. This procedure was repeated 4 times. Then the cell was sintered at 450°C for 20 minutes and left to cool down to 95-110 °C. The whole dropping/sintering cycle (4 times paste deposition followed by sintering at 450°C) was repeated seven times.[3] The electrode was boiled a $2 \cdot 10^{-3}$M solution of magnesium acetate ($Mg(OAc)_2$) in a solution of 85% ethanol in water for 1 min. Then the electrode has been washed with ethanol to remove magnesium acetate inside the pores and sintered again at 450 °C for 30 minutes. Dying was accomplished by dipping the electrode in a 0.5 mM solution of N719 for 24 h. 1 mm on each side of the TiO_2 was then masked off with scotch (M3 Magic) tape before applying copper(I) iodide, leaving 0.64 cm^2 of the TiO_2 uncovered. The THT containing CuI solution (0.600 g CuI, 20.0 ml MeCN, 8.00 mg THT) was sprayed at the 110°C warm substrate from a distance of 20.0 cm with a Hansa 481 airbrush pistol. 10 spraying cycles have been applied, between the cycles there was a 10 s break. The pressure was 1 bar with the pressure gauge closed. A platinum counter electrode (prepared as in Section 4.2.11 was clipped on top of the copper

[3]To reach 10 µm, this procedure has been repeated 20x7 times insteat of 4x7 times

iodide surface with crocodile clips. The cell was measured twice, once with a tape mask covering also the dyed parts not coated with CuI (highlighted light green in the top view of Figure 4.14. As the active area for cell parameter calculation, the sprayed copper iodide surface was chosen (0.64 cm^2, highlighted brown in the top view of Figure 4.14). [87]

4.3.2 Changing the TiO_2 semiconductor morphology

As stated in literature [77] [109] [91], ssDSCs can also be made by incorporating TiO_2 pastes suitable for doctor blading and/or screen printing instead of Tennakone's paste (paste 1) drop coating approach. Paste 1 resulted in a rough, sheet like, and dense structure largely free of interconnected pores going up to the back contact [87], therefore no compact layer was needed for ssDSCs to work. Pastes suitable for doctor blading and/or screen printing on the other hand are often on the basis of organic fillers like ethyl cellulose and terpineol as the solvent (pastes 2-4). Their sintered structure results in very porous films where the pores go all the way through to the back contact. To prevent short circuits a dense TiO_2 compact layer is required underneath the TiO_2 nanoporous layer. Figure 4.18 shows the layout of cells produced with pastes on the basis of ethyl cellulose. Since a compact layer was present, less care had to be taken not to form a short circuit at the edges and the whole TiO_2 could be covered with CuI. Whereas none of the cells produced with paste 2 and N719

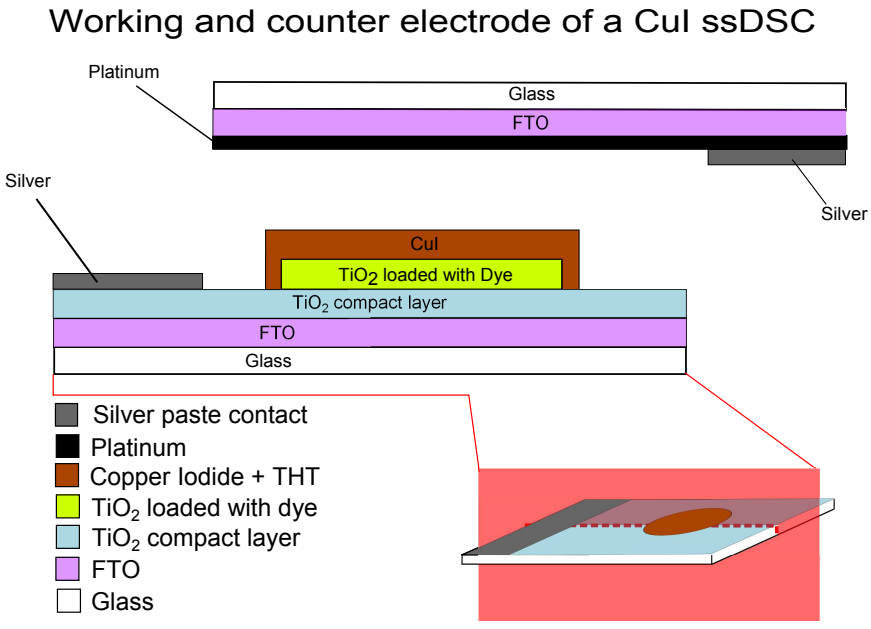

Figure 4.18: Layout of a CuI ssDSC incorporating pastes 2-4

as the dye had yielded any working ssDSCs, the first trials with paste 4 and a spin coated compact layer resulted in working cells, even if they were very inefficient. To determine

whether the contact of the CuI to the top platinum counter electrode was the problem, a droplet of the acetonitrile/CuI/THT solution used for applying[4] (see Section 4.2.7) the copper iodide was placed in between the electrodes. Afterwards, the cell was left in the sun simulator and measured again in certain time intervals indicated in Table 4.3. When the acetonitrile solution was added, the cell was labelled with "Cell A" in Figure 4.19. As can be seen in Figure 4.19, upon addition of the acetonitrile/CuI/THT solution, J_{SC} increased dramatically over its initial level. After 4 minutes, it was even higher than after the addition of the acetonitrile/CuI/THT solution. After 8 minutes however, cell performance started to decrease again and after 12 minutes in the sun simulator it had reached it's initial value, which means the acetonitrile had dried out by that point. This curves could be reproduced by applying another droplet of the solution. The same has been tried with the ionic liquid

TiO_2	HTM	Dye	C. electrode	Comp. layer
Paste 4	CuI + THT	N719, 0.5 mM	Platinum	spin coated

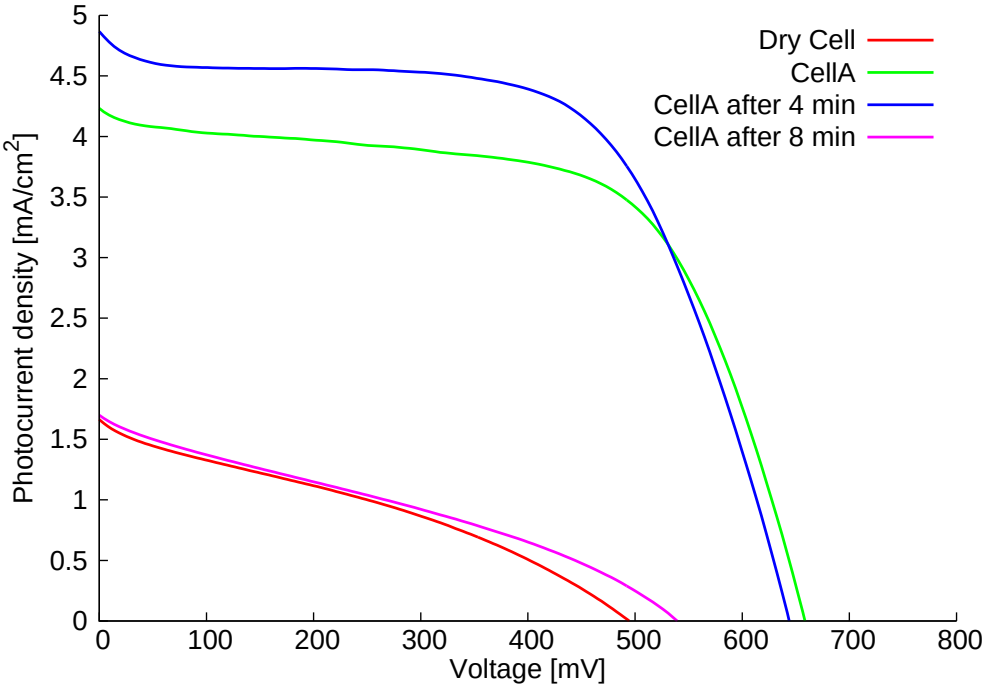

Figure 4.19: J-V curves of a CuI ssDSC incorporating paste 4 with and without addition of the acetonitrile/CuI/THT solution. The cell was measured unmasked.

1-methyl-3-butyl imidazolium iodide (MBII), which raised the efficiency as well, but with a maximum value of 0.401 % not nearly as high as the MeCN/CuI solution (see Figure 4.20). After 3 minutes of illumination, the efficiency stagnated already at a much lower value than it did with the addition of CuI/MeCN but did not fall back to its initial value.

[4]CuI (0.300 g) in acetonitrile (10.0 ml) containing THT (4.00 mg)

Device Name	J_{SC} [mA/cm^2]	V_{OC} [mV]	FF [%]	η [%]
Dry Cell	1.71	495	30.6	0.260
CellA	4.27	658	60.9	1.71
CellA after 4 min	4.87	643	60.1	1.88
CellA after 8 min	1.72	538	30.2	0.280

Table 4.3: J-V parameters of a CuI ssDSC incorporating paste 4 with and without the addition of the acetonitrile/CuI/THT solution. The cell was measured unmasked.

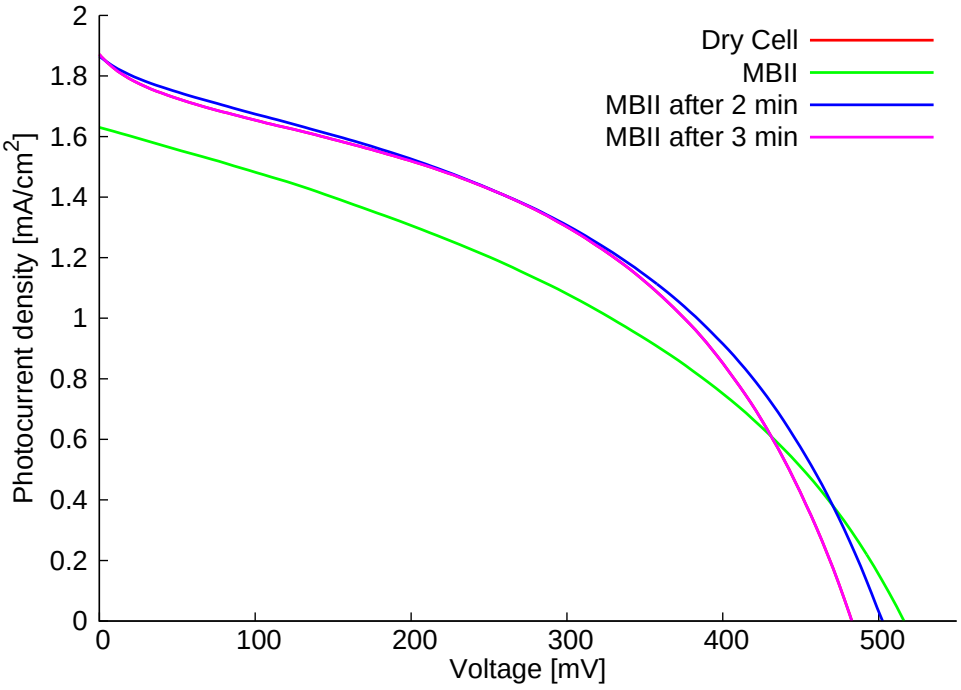

Figure 4.20: J-V curves of a CuI ssDSC incorporating paste 4 with and without addition of MBII. The cell was measured unmasked.

Device Name	J_{SC} [mA/cm^2]	V_{OC} [mV]	FF [%]	η [%]
Dry Cell	1.72	538	30.2	0.280
MBII	1.63	515	39.1	0.328
MBII after 2 min	1.89	502	42.3	0.401
MBII after 3 min	1.90	482	43.2	0.396

Table 4.4: J-V parameters of a CuI ssDSC incorporating paste 4 with and without addition of MBII. The cell was measured unmasked.

Detailed Cell construction

All heat treatments have been conducted on a Ceran plate (which was placed on a hot plate) to prevent contamination of the electrodes. A compact layer has been spin coated as described in Section 4.2.2. TiO_2 paste 4 has been applied by doctor blading (single scotch tape, M3 scotch magic), and sintered at 450 °C for 30 min. The cells were masked in a way that only the active TiO_2 area was uncovered. This was achieved by punching a hole into an adhesive tape (nopi® Malerkrepp) and applying it to the glass sheet. The electrodes were put on a hot plate at 115 °C and left there for a few minutes to reach that temperature. A CuI (0.300 g) solution in acetonitrile (10.0 ml) containing THT (4.00 mg) was applied. Each electrode was coated with 0.06 ml of the solution (applied with an Eppendorf pipette). After each carefully applied drop (it was taken care that most of the solution stayed in the punched hole and did not spill over the borders), the acetonitrile evaporated quickly and the cell was left for a few seconds to dry before application of the next drop until all 0.06 ml had been deposited. The cells were left to cool down and the masking tapes were removed. Working and platinum counter electrodes (Section 4.2.11) have been clamped together and silver paste was applied at the contacts.

4.3.3 Incorporating the HTM into the dye

So far, the short circuit current density, fill factor and hence efficiency were rather low. Photon absorption, charge separation and recombinations all take place nearly exclusively at the TiO_2/Dye/HTM interface in ssDSCs. [110] N719 anchors to the TiO_2 surface with the carboxylic groups of it's bipyridine ligands. By anchoring a free bypridine domain onto the TiO_2 surface, a coordination site is generated and the CuI HTM could potentially directly form a copper complex with the anchoring ligand. This might make the electron and hole injection processes more efficient since the HTM would be part of the dye itself. For this purpose, anchoring ligand ALP1, which is known to be incorporated in DSCs on the basis of metalorganic copper dyes [47] [111], was anchored with its phosphonic acid groups to the TiO_2 surface and CuI was applied directly on top of it (see Figure 4.21). Figure 4.23 depicts solid state UV-Vis spectra of several TiO_2 films. A bare TiO_2 electrode served as the blank. As can be observed, the titanium dioxide film with adsorbed anchoring ligand ALP1 did not have any significant absorption. TiO_2 combined with copper iodide showed a maximum absorption of about 0.5 (independent of the presence of THT). However, if the anchoring ligand and copper iodide are both present on the TiO_2 film, an intense absorption in the region of 360 nm is observed. Even by eye, the difference is noticeable (see Figure 4.22). This strengthens the assumption that the copper has coordinated to the anchoring ligand generating a light absorbing complex.

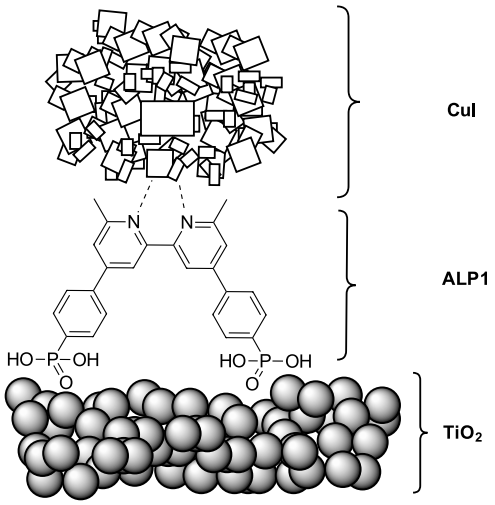

Figure 4.21: CuI coordinating to anchoring ligand ALP1 in CuI ssDSCs.

Figure 4.22: Sintered TiO_2 electrodes treated either with only CuI (on the left, TiO_2+CuI) or with ALP1 and CuI (on the right, TiO_2+ALP1+CuI). The colors of the cells are clearly differing.

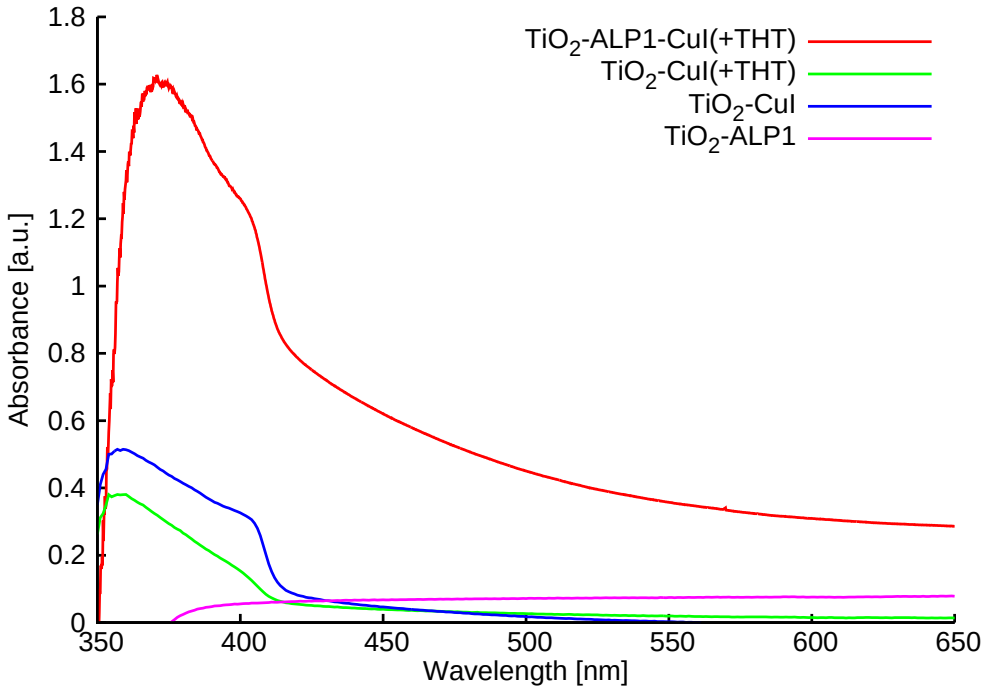

Figure 4.23: Solid state UV-Vis of several TiO_2 films

TiO_2	HTM	Dye	C. electrode	Comp. layer
Paste 4	CuI + THT	ALP1-CuI	Platinum	spin coated

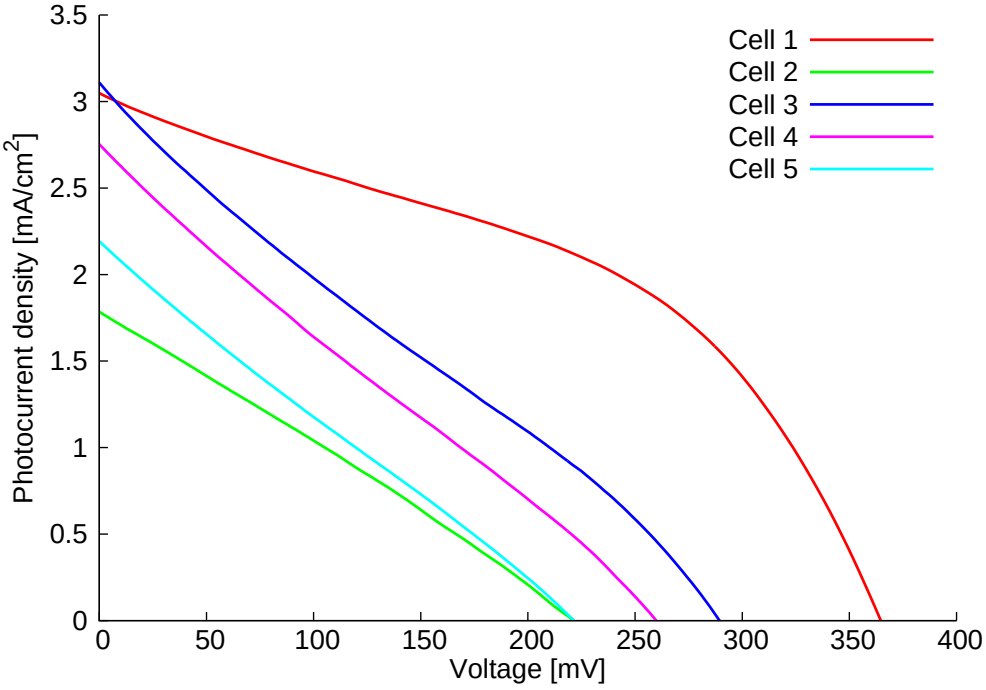

Figure 4.24: J-V curves of five identically fabricated unmasked ssDSCs with the ALP1-CuI dye.

Device Name	J_{SC} [mA/cm^2]	V_{OC} [mV]	FF [%]	η [%]
Cell 1	3.06	364	43.6	0.486
Cell 2	1.80	221	26.8	0.106
Cell 3	3.12	289	25.5	0.230
Cell 4	2.77	259	24.7	0.177
Cell 5	2.20	221	24.7	0.120

Table 4.5: J-V parameters of five identically fabricated unmasked ssDSCs with the ALP1-CuI dye.

Five identical cells were built with ALP1-CuI as the dye. The results are depicted in Figure 4.24 and Table 4.5. Although all five cells produced a photocurrent and the efficiency was raised compared to the N719 ssDSC (See Table 4.4), the cells were not reproducible with scattered η values from 0.120-0.486%.

Detailed Cell construction

The cells were built in the same way as the cells in Section 4.3.2, except for the dying process. The electrodes were dipped into a 1 mM solution of ALP1 in DMSO for 12 h. After washing them with DMSO, CH_2Cl_2 and MeCN they were left to dry. CuI application

and everything else was according to Section 4.3.2.

4.3.4 Adding a non-volatile liquid component

In Section 4.3.2 it was observed that by the addition of an acetonitrile/CuI/THT solution, the efficiency of the cell could be shortly enhanced by a considerable amount, much more so than with MBII. The boiling point of acetonitrile is quite low though (82 °C), which under illumination would lead to quick evaporation and negate the positive effects on the solar cell. 3-Methoxypropionitrile, which is used frequently in leDSCs is a less volatile liquid. A droplet was added between the electrodes of the same cells [5] as in Section 4.3.3 and the cells were measured again.

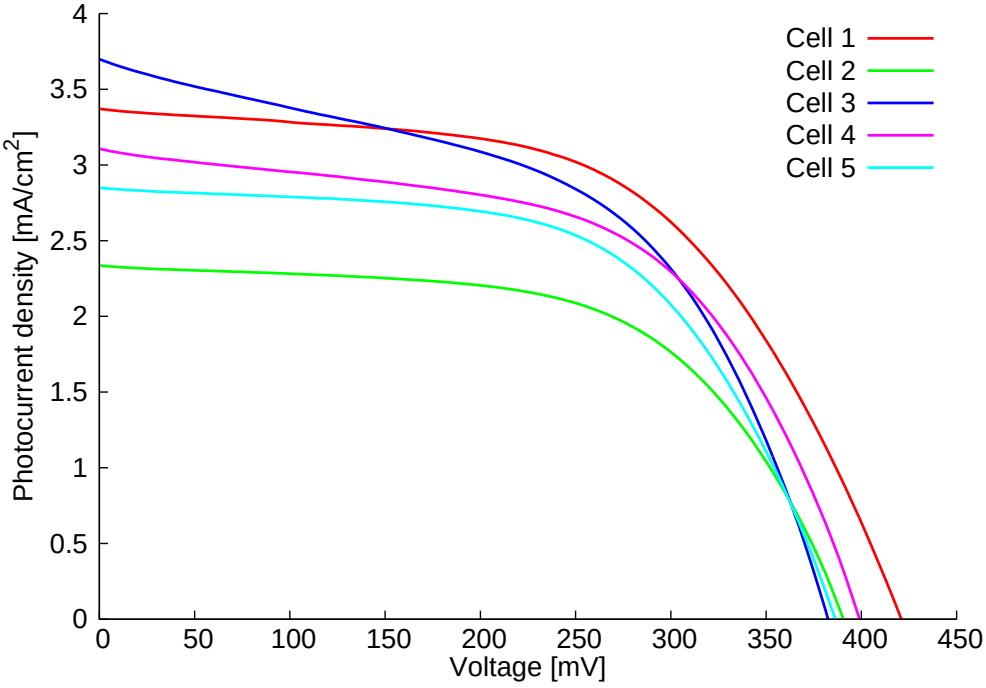

Figure 4.25: J-V curves of five identically fabricated unmasked 3- methoxypropionitrile treated ssDSCs with the ALP1-CuI dye.

As a result of the methoxypropionitrile treatment, all cell parameters were enhanced and the cells were more reproducible as well as the less scattered values in Table 4.6 compared to the untreated ssDSCs in Section 4.3.3 show. These results indeed indicate substantial current losses generated due to an insufficient contact at the interface of the ssDSC.

[5] This could be done since the electrodes were just clipped together.

Device Name	J_{SC} [mA/cm^2]	V_{OC} [mV]	FF [%]	η [%]
Cell 1	3.39	421	55.6	0.792
Cell 2	2.35	390	59.0	0.541
Cell 3	3.71	382	51.0	0.724
Cell 4	3.12	399	55.9	0.696
Cell 5	2.86	386	58.8	0.649

Table 4.6: J-V parameters of five identically fabricated unmasked 3-methoxypropionitrile treated ssDSCs with the ALP1-CuI dye.

4.3.5 Masking the cells

The cells of Section 4.3.4 have been masked and remeasured. By doing so, Cell 1 still featured an efficiency of 0.57%. Cells 2 and 5 dropped to an efficiency of 0.36% and 0.42%. Cells 3 and 4 stopped working after the masking. This is probably due to a shift of the electrodes (since they are only held together by a metal clamp) happening while applying the mask.

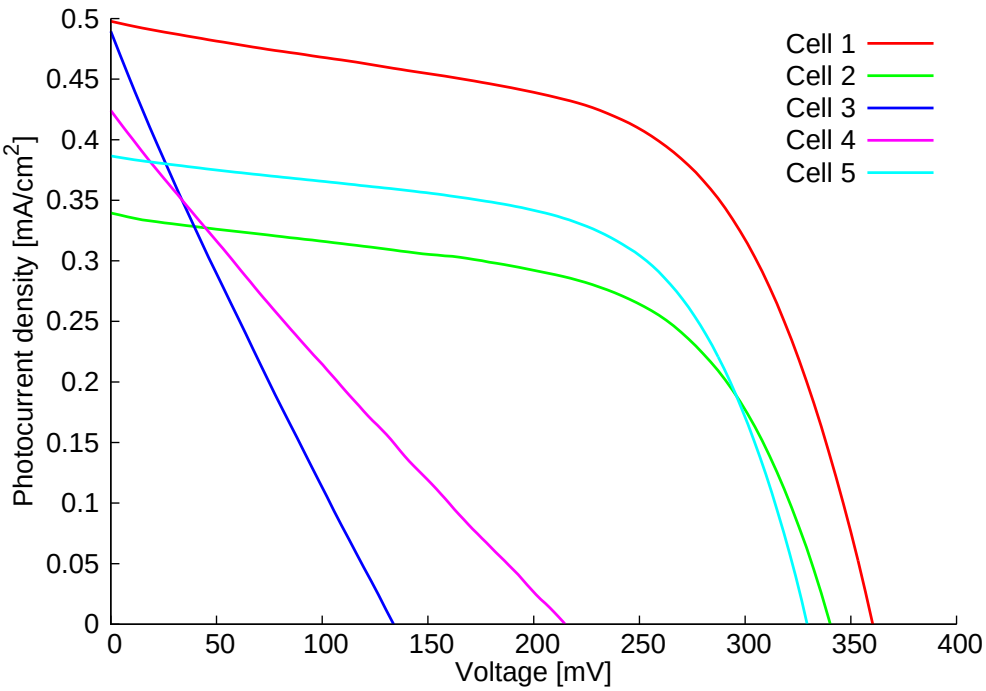

Figure 4.26: J-V curves of five identically fabricated masked 3- methoxypropionitrile treated ssDSCs with the ALP1-CuI dye.

Detailed Cell construction

These cells were the same ones as Sections 4.3.4 and 4.3.3 and have been prepared accordingly.

Device Name	J_{sc} [mA/cm^2]	V_{OC} [mV]	FF [%]	η [%]
Cell 1	2.75	360	58	0.57
Cell 2	1.87	340	57	0.36
Cell 3	2.60	209	24	0.13
Cell 4	2.34	213	24	0.12
Cell 5	2.13	329	60	0.42

Table 4.7: J-V parameters of five identically fabricated masked 3- methoxypropionitrile treated ssDSCs with the ALP1-CuI dye.

4.3.6 IPCE measurements and reproducibility

To record EQE values of ALP1-CuI dye, a new set of five identical cells was prepared identically to the 3-methoxypropionitrile treated ones in Section 4.3.4. EQE measurements as well as JV-curves of masked and unmasked cells have been recorded. The results of the EQE measurements can be seen in Figure 4.27. The performance parameters of masked and unmasked J-V measurements are listed in Tables 4.8 and 4.9. These cells have a

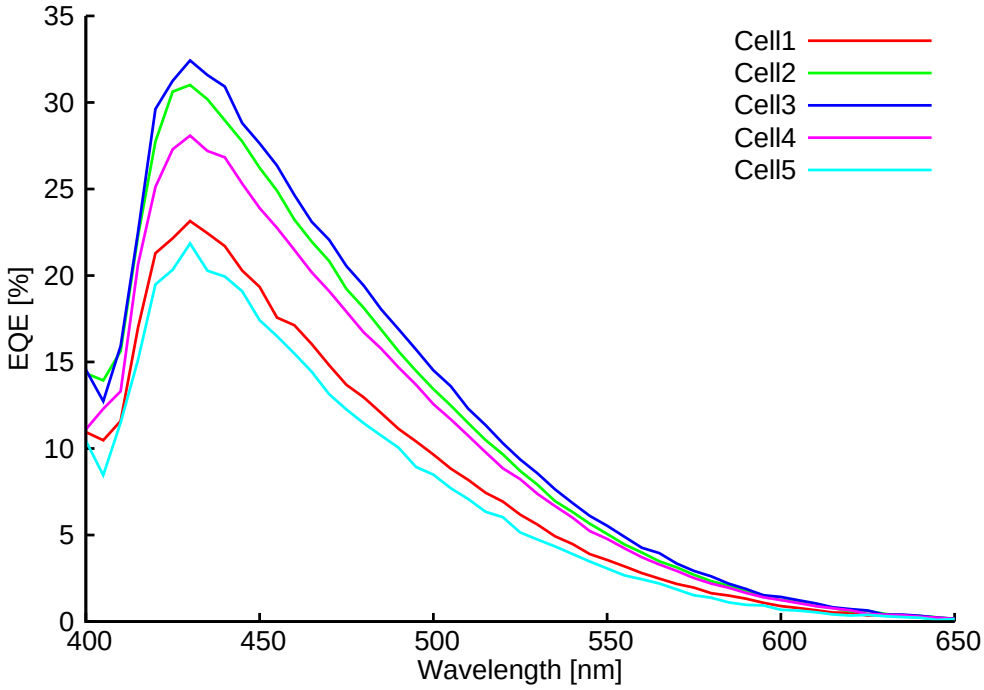

Figure 4.27: Quantum efficiency curves of five identically fabricated masked 3- methoxypropionitrile treated ssDSCs with the ALP1-CuI dye.

maximum quantum efficiency at λ_{max} = 430 nm, which is another indication that the copper in the copper iodide effectively coordinated to the anchoring ligand. Also, the EQE maximum is fairly similar to already reported copper complexes in leDSCs [47] with a blue shift of ~40 nm. Since these cells feature a liquid (3-methoxypropionitrile) the problem of

Device Name	J_{SC} [mA/cm^2]	V_{OC} [mV]	FF [%]	η [%]
Cell 1	3.08	399	42.5	0.523
Cell 2	4.17	418	60.4	1.05
Cell 3	3.71	469	46.5	0.809
Cell 4	3.42	426	60.9	0.889
Cell 5	2.36	388	55.7	0.511

Table 4.8: J-V parameters of five identically fabricated unmasked 3- methoxypropionitrile treated ssDSCs with the ALP1-CuI dye.

Device Name	J_{SC} [mA/cm^2]	V_{OC} [mV]	FF [%]	η [%]
Cell 1	1.70	155	24.8	0.0657
Cell 2	2.63	362	63.3	0.604
Cell 3	3.42	2.11	16.8	0.000550
Cell 4	2.22	351	41.3	0.322
Cell 5	0.95	52.6	23.9	0.0120

Table 4.9: J-V parameters of five identically fabricated masked 3- methoxypropionitrile treated ssDSCs with the ALP1-CuI dye.

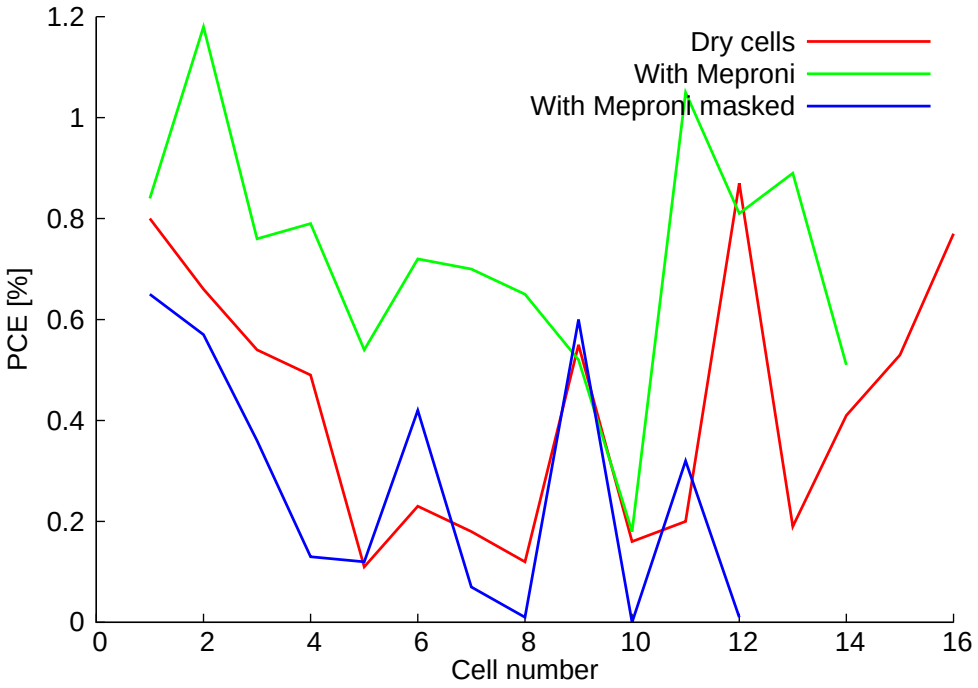

Figure 4.28: Efficiency values of all measured cells dyed with ALP1-CuI.

solvent evaporation is still present. Even though the boiling point of 3-methoxypropionitrile is relatively high (165 °C), applied as a thin film sandwiched between the electrodes it evaporates rather quickly. Figure 4.28 is a plot of all efficiencies measured of cells dyed with ALP1-CuI to visualize reproducibility. The values have been distinguished in dry cells and 3-methoxypropionitrile (Meproni in the plot) treated cells. Only some of the 3-

methoxypropionitrile treated cells were masked as well since the efficiency of dry cells was generally not high enough for masking. Unfortunately, the cells were not very consistent in terms of performance. However, by adding 3-methoxypropionitrile, a general rise in efficiency could be observed. As expected, most cells decreased in efficiency when masked. The efficiency of one cell (cell number 9 in Figure 4.28) however was raised. Since the cells are just clipped together with a metal clamp this is believed to be due to a change in the cell conformation upon applying the mask to the clipped electrodes.

4.3.7 Evaporating the counter electrode for better contact

In the above experiments, applying a liquid between the electrodes raised the efficiency of the cell significantly. This indicates that either the back contact of the CuI to the counter electrode or the contact of the CuI to the TiO_2 is not established enough. Grätzel et al. [75] have published a different cell architecture when presenting their first ssDSC in 1998. The counter electrode was evaporated directly onto the hole conductor. This guarantees a secure contact to the back electrode compared to just clipping the electrodes together. In contrast to Grätzel et al. however, copper iodide was continued to be used as the hole conductor instead of the much more expesive spiro-OMeTAD. Figure 4.29 shows the architecture used for this cell. In this architecture, part of the FTO had to be etched away

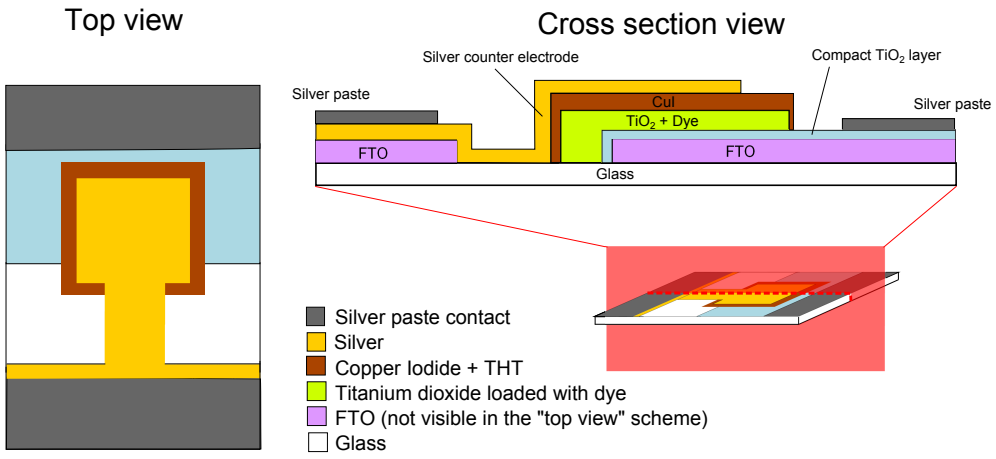

Figure 4.29: Layout of a ssDSC with an evaporated counter electrode

to prevent short circuits with the evaporated gold electrode. The spin coated compact layer would not work properly here because of the step where the FTO was etched away. The compact layer was sprayed instead according to Section 4.2.2. Paste 2 was compared with paste 3 (PEG600 addition). As can be seen in Figure 4.30 and Table 4.10, the more PEG600 was added, the better the cell performance was. This shows the importance of porosity. An SEM comparison of these three pastes can be seen in Figure 4.31. From these

images it is also obvious that PEG600 did not alter the surface as much as PEG20000 did (see also Figure 4.7). However, unfortunately no working cell has yet been achieved in this architecture with paste 4 (PEG20000).

TiO_2	HTM	Dye	C. electrode	Comp. layer
paste 3	CuI + THT	N719	Silver (evaporated)	sprayed

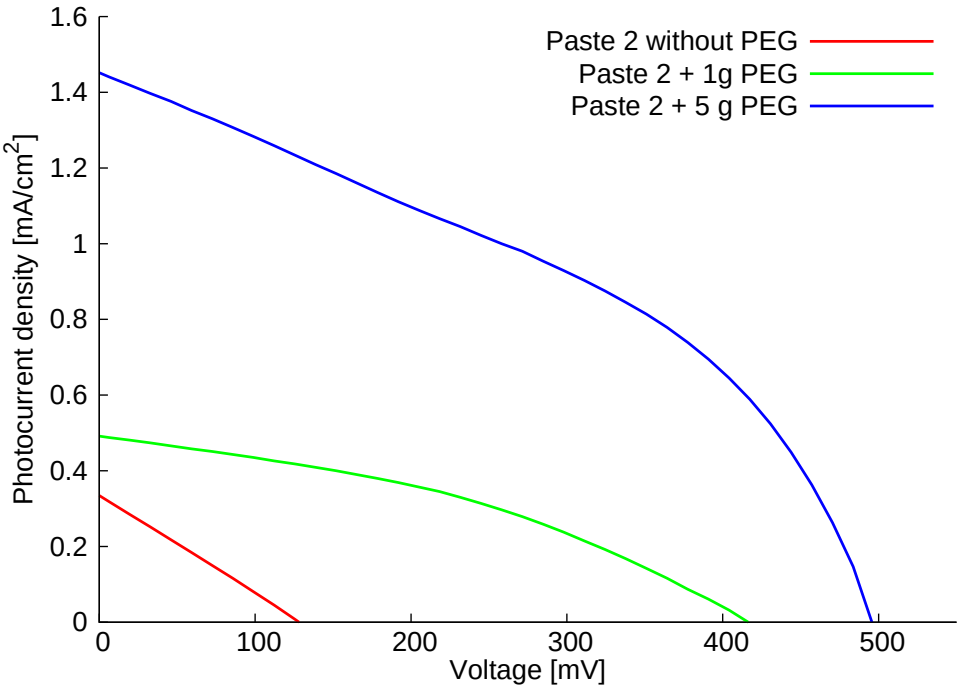

Figure 4.30: J-V curves of ssDSCs with different amounts of PEG600 in their respective TiO_2 pastes. All measurements were conducted with unmasked cells.

Device Name	J_{SC} [mA/cm^2]	V_{OC} [mV]	FF [%]	η [%]
0 % PEG	0.319	139	24.6	0.0109
5 % PEG	0.488	417	37.8	0.0769
25 % PEG	1.44	497	39.9	0.286

Table 4.10: J-V parameters of ssDSCs with different amounts of PEG600 in their respective TiO_2 pastes. All measurements were conducted with unmasked cells.

The received efficiency values were comparable or worse to the cells with separate electrodes clipped together. With the back contact being established, it is suspected that, if there is a contact problem, it is located at the TiO_2/Dye/CuI interface.

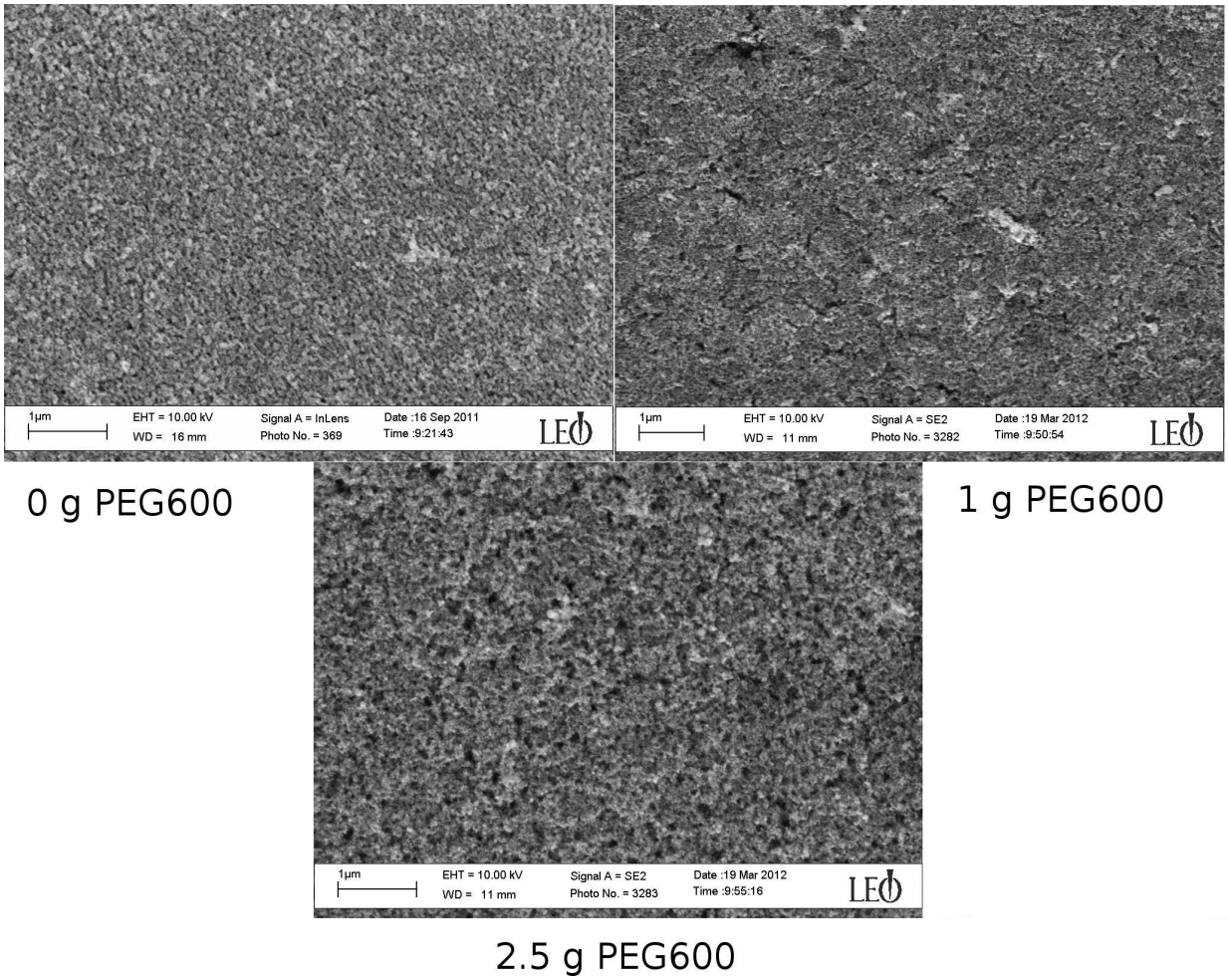

Figure 4.31: Comparison of sintered films of PEG600 containing pastes

Detailed experimental:

FTO-glass has been cut to electrode strips of 4 x 15 cm. 20 electrodes have been scored into the glass but not broken apart yet (2x10 electrodes). The glass sheet was covered with scotch (M3 magic) tape in a way that only a strip of 1.6 cm was uncovered in the middle (See Figure 4.32). Zinc dust was spread on the uncovered part and the FTO was etched away by dropping 4 M HCl onto the zinc and leaving it for a few seconds. The zinc and the acid were wiped away with cotton wool and the glass was rinsed with water. The scotch tape was removed and the glass sheets have been washed by sonicating for 10 minutes in each solvent of the following sequence: 1 x acetone, 2 x ethanol, 1 x sonoswiss cleaner in miliQ water (2%), 3 x water, 2 x Ethanol. They have been cleaned in an UV/Ozone cleaner for 20 minutes. A compact layer was sprayed as shown in Figure 4.2.2. The cells were broken apart (See Figure 4.32) and paste 4 was applied by doctor blading (1 cm^2 square) with one scotch M3 magic tape as the spacer in a way that the semiconductor reached over the edge of the FTO. (See Figure 4.29). The cells were sintered in a programmable oven with the

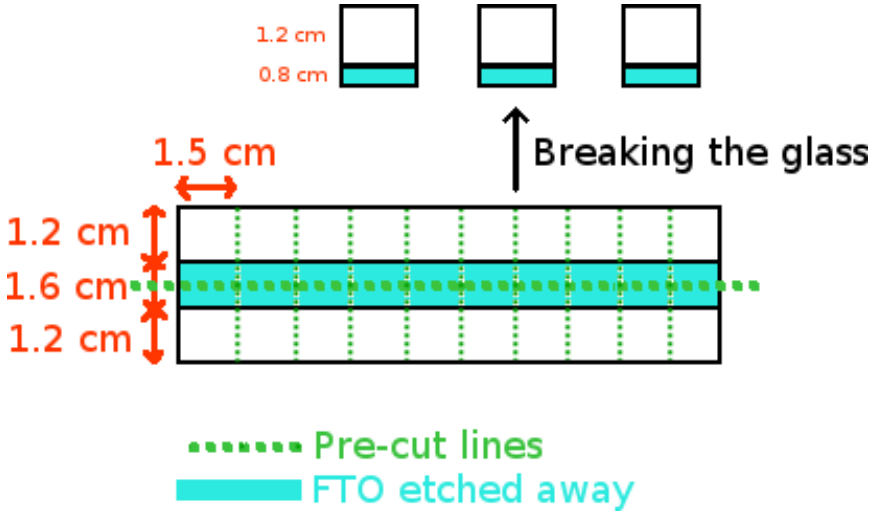

Figure 4.32: Schematic of etched electrodes. The compact layer was sprayed before breaking them apart.

program P1 (See Section 2.2.3) The cooled down electrodes were treated with magnesium oxide by boiling the them in a $2 \cdot 10^{-3}$ M solution of magnesium acetate in 85% ethanol in water for 1 min. They have been washed with ethanol and sintered again at 450 °C for 30 minutes. The electrodes have been immersed into a 0.5 mM solution of N719 over night. They were rinsed with ethanol and masked with tape (nopi® Malerkrepp) so that only the TiO_2 surface and a little part of the FTO-free glass were uncovered (see Figure 4.29). The masked electrodes have been heated to 110 °C and a 0.7 ml of a solution of CuI (0.600 g) and THT (8.00 mg) in acetonitrile (20.0 ml) have been applied to each electrode. They were left on the heating plate for 30 minutes at 110 °C. After that, the electrodes were masked with regular printing paper and 200 nm silver was evaporated on top of the counter electrode. Conducting silver paste was applied to both contacts. [89][87]

4.4 Possible reasons for inconsistent cell performances

Overall the CuI HTM cells produced were not very reproducible. As stated above, the degree of pore filling is a crucial factor of cell performance. To assess the pore filling, an EDX measurement was conducted on a cross section of an electrode built with paste 4 (see Figure 4.33[6]). In the SEM image, the CuI layer can be clearly distinguished as the lighter area on top of the TiO_2 layer. The lighter spots inside the TiO_2 layer indicate

[6]This is a FIB cross section. It is not the actual electrode that the measurements were performed on. FIB cross sections are not ideal for EDX measurements because of the cavity that is cut into the surface which makes detection harder. This cell was depicted because it shows other features well like the HTM deposition layers. The positions of the measurements were the same as indicated in the Figure.

penetration of the semiconductor layer with CuI. EDX measurements confirmed that the CuI concentration decreased the lower in the TiO_2 layer was measured. There was still CuI present at the bottom though, which means the HTM could penetrate the whole layer at least to some extent. Other possible reasons could be mechanical ones, deduced by

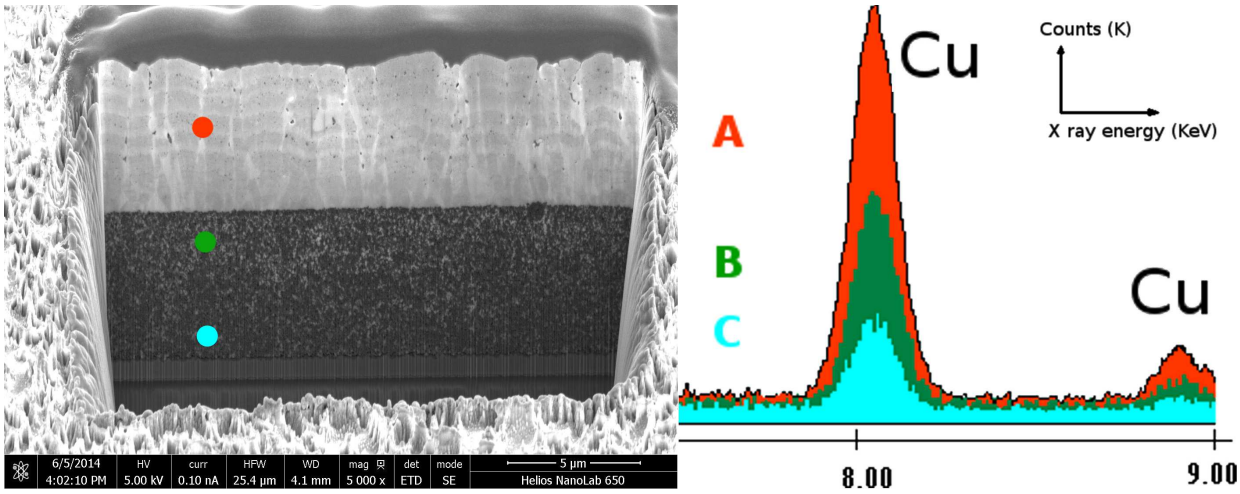

Figure 4.33: FIB/SEM image and EDX measurement of a cross section of a paste 4 CuI ssDSC

an irregular surface of the copper iodide for example. Figure 4.33 shows an SEM image of a cross section of an ssDSC with TiO_2 and copper iodide. Different layers of copper iodide applied by the drop coating method are clearly distinguishable. The top surface of the HTM seemed to be quite rough, possibly impeding a good contact to the counter electrode. Another factor is the way the electrodes were attached to each other. Since they were just held together with metal clamps they could easily shift and thereby hinder cell performance reproduction, maybe even destroying CuI layers by friction. Considering the vast improvement upon adding liquid solvent between the electrodes, it is nearby to assume that either the top contact or the contact at the TiO_2/dye/HTM interface has a lot of room for improvement. Evaporating the back electrode on top should provide an excellent contact for the back electrode. Unfortunetly, the cell performance remained low as demonstrated in Section 4.3.7. This evaporated counter electrode approach has also been tried for the ALP1-CuI dyed cells. One set with an evaporated gold as well as one set with an evaporated platinum as the counter electrode has been fabricated, even a conducting silver glue was tried. None of those cells worked. It is known from the literature that CuI p-type ssDSC's suffer from serious stability problems. They have been reported to degrade about two hundred times faster than liquid I^-/I_3^- DSCs. [106] These problems have been reported to be associated with the deterioration of the contact at the dye-CuI interface or the deterioration of the CuI itself [112][77] through oxidation by air or light for example. Sirimanne and Coworkers [106] also state that excessive iodine in the CuI film

strongly decreases the photocurrent of the cell by competing with oxidized dye molecules in accepting electrons from CuI, which decreases the cell performance. Furthermore it is unknown to which extent the semiconductor surface was covered in the dyeing process. Any gaps in dye coverage result in direct contact of TiO_2 with CuI, which is detrimental to cell performance as shown in Section 4.2.

4.5 Summary

Inorganic p-type semiconductors like CuI appear to be an ideal choice for a hole transport material because of high stability, ease of synthesis and hence low cost. [113] Although CuI ssDSCs have not been reproducibly built, working ssDSCs have been fabricated for the first time in our research group. Furthermore, a new type of ssDSC has been assembled by incorporating the hole conductor directly into the light absorbing dye. This opens up potentially new ways of designing ssDSCs and their dyes with CuI as a relatively cheap and versatile hole conducting material.

Chapter 5

Poly(3,4-Ethylenedioxythiophene) (PEDOT) Solid State Dye Sensitized Solar Cells

In Sections 5.1 and 5.2, a brief theoretical background on PEDOT ssDSCs is outlined as well as some basic characterisation of the PEDOT ssDSC electrodes. PEDOT ssDSCs have been fabricated by combining two literature procedures. [90] [114] Cell fabrication is described in Section 5.3 and cell performance in Section 5.4. Section 5.5 gives a small summary of the chapter. Commercial Dyesol 90-T transparent TiO_2 paste has been used throughout in this chapter. These are our first attempts to assemble PEDOT ssDSCs.

5.1 Working principle of PEDOT ssDSCs

The contact problems arising from crystalinity [115] in hole transport materials (HTMs) like copper iodide can potentially be overcome by employing an organic polymer hole conductor. Other than that, the basic working principle is the same as in the copper iodide ssDSCs. Here, PEDOT has been employed as a hole conductor and the approach of Kim and coworkers has been adapted. [114]

5.2 Main components of PEDOT DSCs

5.2.1 The semiconductor

As the semiconductor, the commercial paste Dyesol90-T has been used exclusively for this DSC type.

5.2.2 The hole transport material

PEDOT is known to have a high hole mobility, stability, and transparency in the visible-light region. [116] To establish a good contact between polymer and dyed semiconductor, an organic monomer, 2,5-dibromo-3,4-ethylenedioxythiophene (DBEDOT), was dissolved in ethanol and applied to a dyed TiO_2 electrode. DBEDOT is a white crystalline solid and soluble in all common organic solvents. [117] By heating the electrode, DBEDOT was polymerized to PEDOT via solid state polymerisation over 24 h. Figure 5.1 shows a comparison

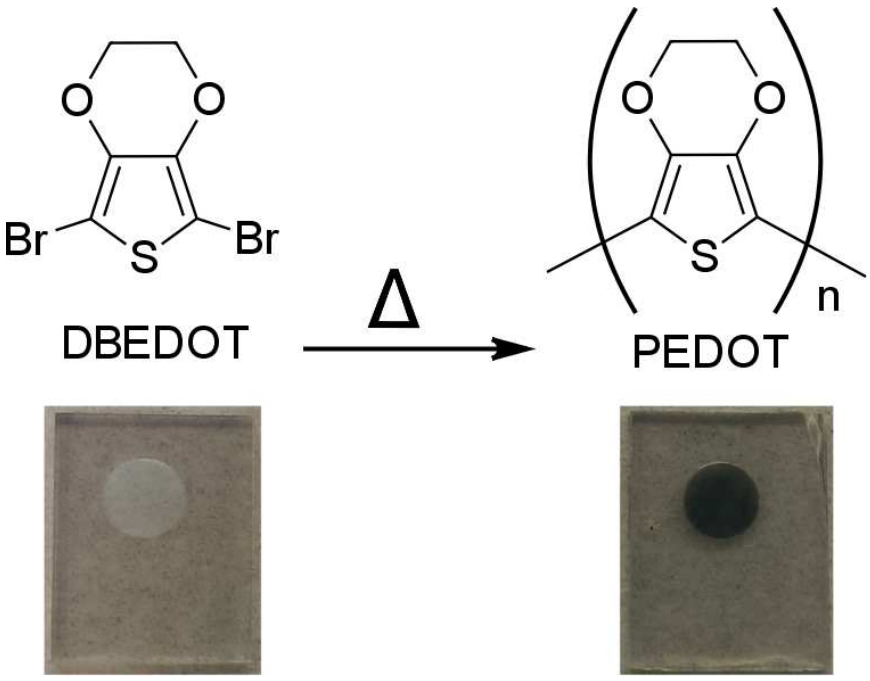

Figure 5.1: Illustration of a bare TiO_2 electrode and a TiO_2 electrode covered with PEDOT after solid state polymerisation

of a blank TiO_2 electrode compared with one with the polymerized material. During polymerisation the colorless monomer is transformed to a black polymer and elemental bromine is released. [117] It is important to heat below the melting point of DBEDOT (96 °C),

since it would melt and prevent solid state polymerisation. This would results in dramatically reduced conductivities (20-80 S cm^{-1} vs 0.1 S cm^{-1} when above the melting point), which implies that retaining the crystal structure of DBEDOT is important for a conductive polymerisation. Wudl and coworkers [117] found that in the polymerized solid bromine is present as two Br_3^- units every five EDOT units, therefore doping the formed polythiophene and enhancing electron conductivity. By removing the tribromide from the polymer with hydrazine in acetonitrile they observed a decrease in conductivity, which could be partially restored by exposing the polymer to iodine vapour. [117] Solid state UV-Vis spectroscopy revealed that the undyed PEDOT treated electrode continuously absorbed from 400 to 800 nm. A blank TiO_2 electrode served as the reference. Because of this absorbtion of the PE-

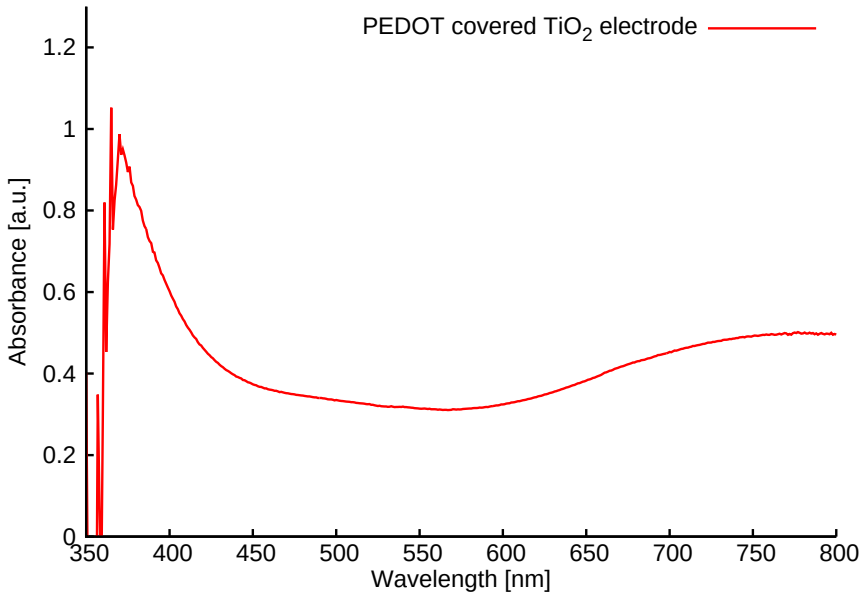

Figure 5.2: UV-Vis spectrum of a PEDOT covered undyed electrode after solid state polymerisation. No dye was applied.

DOT alone, a DSC has been fabricated to check performance as an active light absorbing species. However, the DSC, masked and unmasked, only produced very little current as Table 5.1 and Figure 5.3 show. Although those cells produced current and voltage, it has not been determined to which extend this can be attributed to the PEDOT or to the TiO_2, which absorbs in the UV region.

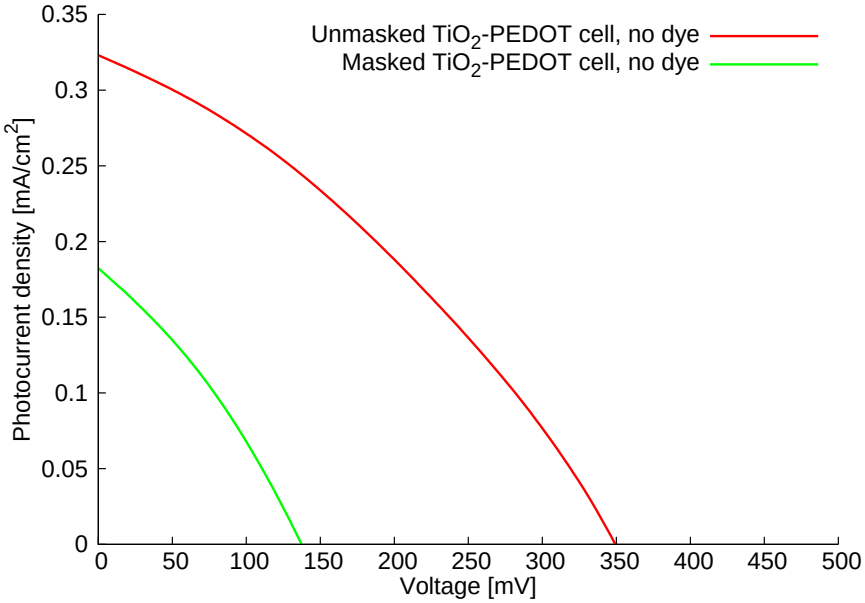

Figure 5.3: J-V curves for a masked and unmasked PEDOT ssDSC using an undyed TiO_2-PEDOT electrode.

Device Name	J_{sc} [mA/cm^2]	V_{OC} [mV]	FF [%]	η [%]
Unmasked	0.323	348	33.5	0.04
Masked	0.18	137	31.4	0.01

Table 5.1: J-V parameters for a masked and unmasked PEDOT ssDSC using an undyed TiO_2-PEDOT electrode.

EDX measurements of a cross section of an electrode after polymerisation have been carried out to determine the penetration into the TiO_2 layer. Sulphur could be found all over the TiO_2 layer, bromine on the other hand was not detected. (Figure 5.4).

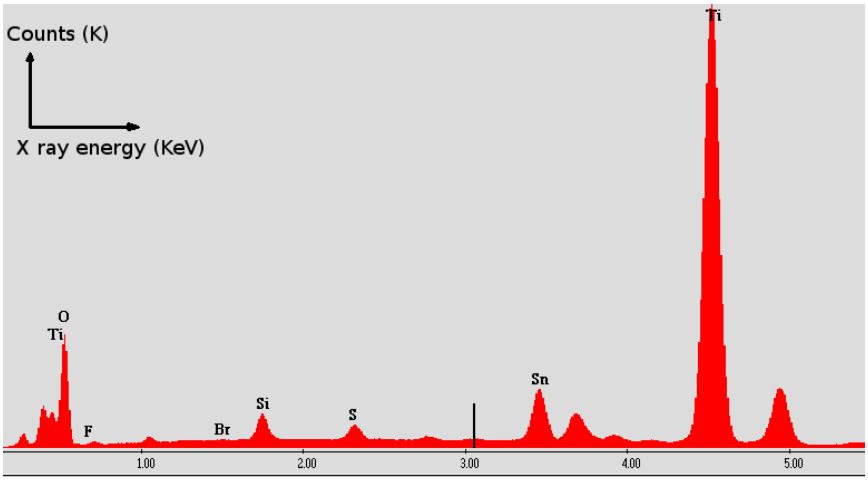

Figure 5.4: EDX measurement of a cross section of the PEDOT infiltrated into the TiO_2 layer.

5.2.3 Additives

As outlined in Chapter 4, the contact between working and counter electrode is vital for DSC performance. To enhance contact between those electrodes, the ionic liquid 1-methyl-3-propylimidazolium iodide (MPII) was added together with some additives by solution casting after the solid state polymerisation. The solution contained methyl propyl imidazolium iodide (MPII) (1.0 M), lithium bis(trifuoromethanesulfonyl)imide (LiTFSI, 0.2 M), and *t*-butylpyridine (0.2 M) in acetonitrile. The solvent (acetonitrile) was evaporated afterwards. The role of *t*-butylpyridine as an additive was described in Chapter 3 and it serves the same purpose here in ssDSCs. LiTFSI, which is depicted in Figure 5.5, has been observed to increase the efficiency of ssDSCs [118] with organic HTMs by enhancing the conductivity of the HTM. [119] Electron injection into the semiconductor is enhanced as well because the positive lithium ions adhere to the semiconductor surface and therefore lower the conduction band of the TiO_2 to a more positive potential, increasing the driving force for electrons to be injected. [120]

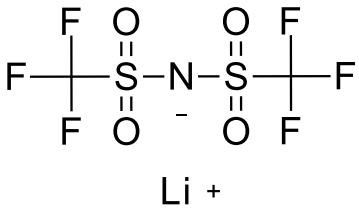

Figure 5.5: Structure of LiTFSI.

5.2.4 Dye

N719 was used as the standard dye, although several other dyes have been tested for this cell type and will be discussed in Chapter 6.

5.2.5 Working and counter electrodes

For the working electrodes, the commercial paste Dyesol 90T has been used throughout. Five layers have been screen printed onto an FTO glass sheet previously covered with a spin coated compact layer (see Section 4.2.2). The resulting TiO_2 layer thickness was 13-14 µm. Tests with a scattering layer have not been conducted yet. The TiO_2 layers peeled off from the FTO surface upon acid treatment (see Section 3.4.3), which might be due to another paste ingredient composition compared to the paste used in Chapter 3. In the end,

the scattering layer was omitted and the electrodes have been used with the transparent TiO_2 layer exclusively. The counter electrodes consisted of commercial solaronix test cell kit electrodes covered with a PEDOT film based on the method of Kim et al. [114]

5.3 Experimental procedures

The DBEDOT was synthesized as described in the literature. [114]

5.3.1 Cell Assembly

A glass plate of 8 x 8 cm was sonicated in detergent (2 wt% in H_2O miliQ) for 15 minutes. Afterwards it was rinsed with water and ethanol and left to dry in air. The glass sheet was treated with ozone in an UV/O_3 cleaner for 20 min. A compact layer was spin coated as described in Section 4.2.2 onto the FTO glass plate. 5 layers of Dyesol 90T TiO_2 paste were screen printed onto the compact layer and the electrodes were sintered with heating program P1 (see section 2.2.3) in the oven. After cooling down, the electrodes were post treated by immersing the glass sheet in a 40 mM aqueous solution of $TiCl_4$ for 30 minutes at 70 °C. They were washed with water and ethanol and subsequently heated to 450 °C on a hot plate. The electrodes were cut to 2 cm x 1.5 cm in size and were dyed by immersing them into a 0.5 mM solution of N719 in ethanol overnight (14-16 h), washed with ethanol and left to dry in air for a few minutes. A tape (nopi® Malerkrepp) with a circular opening of a 1 cm diameter was used to mask the active area. A droplet of a 1 $\%_{wt}$ solution of DBEDOT in ethanol was deposited by an Eppendorf pipet (17 µl per droplet) onto the dyed surface and left to evaporate. This was repeated 5 times. After that, 5 droplets of a 3 $\%_{wt}$ DBEDOT solution have been deposited in the same way.

The base of the counter electrodes consisted of the already pre-platinized counter electrodes from the Solaronix test cell kits. They were cut to 1.5 x 2.0 cm and heated to 450 °C for 30 minutes to remove water and possible organic residues. After having cooled down, DBEDOT was deposited in the same way as for the working electrodes, except two droplets were applied each time instead of one (5 x (2 x 17 µl 1 $\%_{wt}$ solution) + 5 x (2 x 17 µl 3 $\%_{wt}$ solution) because the entire glass sheet had to be covered and more solution was necessary.

The working as well as counter electrodes were placed in an oven at 60 °C for 24 h to enable solid state polymerisation to PEDOT. Then, a droplet (17 µl) of a solution of LiTFSI (0.2 M), *t*-butylpyridine (0.2 M) and MPII (1.0 M) in acetonitrile was placed on the active area. The electrodes were put in an oven at 60 °C for 1 h to evaporate the bulk of the

acetonitrile. Then working and counter electrode were clipped together by a metal clamp. Araldite® 90 sec. glue was applied on the two longer sides of the sandwiched structure and the cell was placed into the oven again, this time at 100 °C for 1 h to evaporate residues of the acetonitrile and to harden the glue. After that, the cell was left to cool down and conducting silver paste was applied on the electrode contact ends. [121] [114]

5.4 Photocurrent density-voltage (J-V) measurements

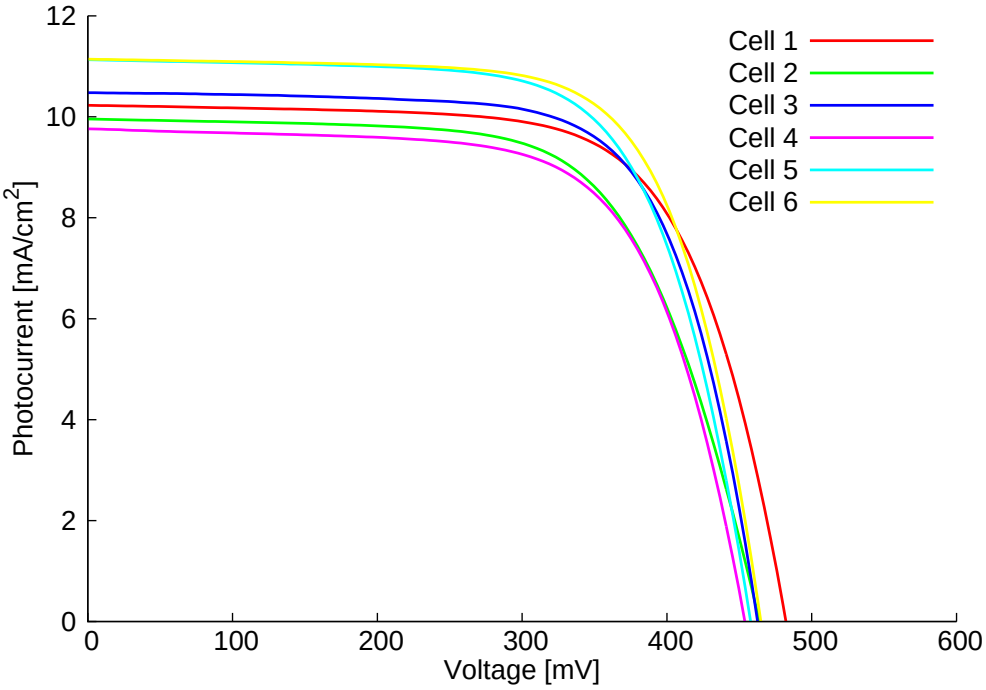

Figure 5.6: J-V curves of 6 identically fabricated masked PEDOT ssDSCs and plotted on day 22. The cells have been dyed with N719.

Device Name	J_{sc} [mA/cm^2]	V_{OC} [mV]	FF [%]	η [%]
Cell 1	10.2	482	68.2	3.36
Cell 2	10.0	464	65.4	3.02
Cell 3	10.5	462	69.7	3.38
Cell 4	9.75	454	67.1	2.97
Cell 5	11.1	458	68.3	3.48
Cell 6	11.1	465	69.6	3.61

Table 5.2: J-V parameters of 6 identically fabricated masked PEDOT ssDSCs plotted on day 22. The cells have been dyed with N719.

Six identical ssDSCs featuring PEDOT as the HTM have been fabricated. As Figure 5.6 and Table 5.2 show, they perform similarly in a range of 2.97-3.61%. As well as the liquid

electrolyte type DSCs, their efficiency increased over time. Even 22 days after sealing, there was no drop in performance as observed in Appendix 5.A.

5.5 Summary

In summary, successful assembly and reproduction of ssDSCs featuring a solid state PEDOT HTM has been achieved with the standard dye N719. They have been stable over 22 days with exposure to air since they have not been sealed off completely. After this time period they still did not show any signs of performance decrease. This encouraged further trials with other dyes, which have been conducted in Chapter 6.

Appendix 5.A J-V measurements over time of masked N719 PEDOT ssDSCs

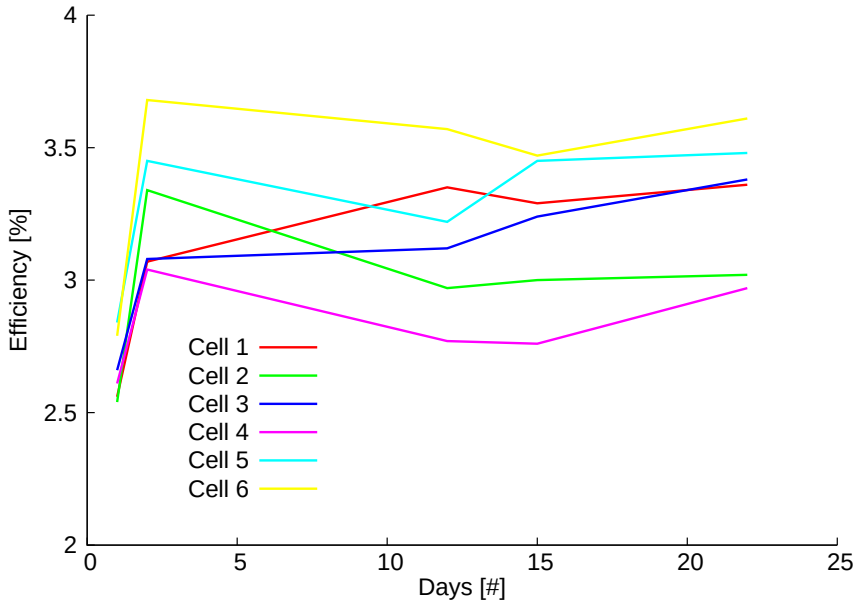

Figure 5.7: Efficiency of six identical N719 PEDOT ssDSDs plotted over time.

Days after sealing [#] →		**1**	**2**	**12**	**15**	**22**
η →	Cell 1	2.56	3.07	3.35	3.29	3.36
	Cell 2	2.33	3.34	2.97	3.00	3.02
	Cell 3	2.66	3.08	3.12	3.24	3.38
	Cell 4	2.61	3.04	2.77	2.76	2.97
	Cell 5	2.85	3.45	3.22	3.45	3.48
	Cell 6	2.70	3.68	3.57	3.47	3.61
ff →	Cell 1	66.5	70.4	70.1	70.5	68.2
	Cell 2	60.4	72.2	69.1	67.8	65.4
	Cell 3	66.8	71.5	70.2	69.9	69.7
	Cell 4	66.5	69.8	68.2	66.5	67.1
	Cell 5	66.7	71.2	70.6	69.1	68.3
	Cell 6	59.5	71.6	71.8	70.5	69.6
V_{OC} →	Cell 1	415	507	511	519	482
	Cell 2	397	492	485	494	464
	Cell 3	399	486	482	496	462
	Cell 4	393	483	465	464	454
	Cell 5	390	484	477	485	458
	Cell 6	405	490	484	494	465
J_{SC} →	Cell 1	9.28	8.58	9.37	9.00	10.2
	Cell 2	9.72	9.40	8.88	8.96	9.96
	Cell 3	9.99	8.87	9.43	9.33	10.5
	Cell 4	10.3	9.01	8.73	8.94	9.75
	Cell 5	11.0	10.0	9.56	10.3	11.1
	Cell 6	11.2	10.5	10.2	9.96	11.1

Table 5.3: J-V parameters of six identical N719 PEDOT ssDSDs plotted over time.

Chapter 6

Synthetic dye development

In Section 6.1 a theoretical background on dyes in DSCs is briefly outlined. Cell fabrication is discussed in Section 6.3.1. The original work on dyes starts in Section 6.2. Section 6.5 gives a small summary of the chapter. Commercial Dyesol 90-T transparent TiO_2 paste has been used throughout in this chapter for PEDOT ssDSCs. For leDSCs solaronix test cell kits have been used exclusively with Electrolyte 2 (see Section 3.3.7).

6.1 Introduction and motivation

There are many factors that determine an efficient sensitizer for DSCs. As seen in Chapter 3, additives like 4-tert-butylpyridine can adhere to the TiO_2 surface and raise the Fermi level of the semiconductor. V_{OC} increases therefore, but the driving force for electron injection is decreased, and with it the photocurrent density J_{SC} . Additives containing cations like Li^+ lower the quasi Fermi level of TiO_2 and therefore enhance the driving force of the electron injection, making it faster, and enhancing the current. V_{OC} on the flip-side is decreased in that way. The challenge is to find a good balance between parameters. [122] In the same way, the acidity of the dye (complexes carrying anionic functional groups or protic ones for example) can also induce these changes. [25, pp. 91] Another very important quality of a dye is of course its ability to absorb photons in the most intense region region of the solar spectrum. The HOMO/LUMO gap of a metalorganic complex can be tuned by either introducing a ligand with a low lying π^* orbital, lowering the LUMO, or by introducing a strong σ-donor ligand (for example NCS^-), and therefore destabilizing the t_2g orbital of the metalorgainc complex, raising the HOMO. Both would result in an extension of the MLCT absorption band to the red region [25, pp.99]. In addition to that, a dye should also have good electron injection properties. It has been

shown that an additional phenyl ring between the anchoring group and the rest of the electron donating part of the ligand enhances cell performance in metalorganic complexes [47]. Kim et al. state that the extra π-bridge diminishes the back electron transfer of the charge separated state and hence lessens recombination between TiO_2 and the oxidized dye. [123] Therefore ALP1 has been frequently used as the anchoring ligand in our group. In organometallic dyes, the metal center is of crucial importance. Ruthenium for example is one of the most common metals for metal-organic complex sensitizers, its availability however is limited which results in expensive prices. Purely organic dyes potentially would be a cheaper alternative, but their application in DSCs is held back by the disadvantage of typically having limited absorption ranges of around 200 nm. [123] There have been numerous reports incorporating other more abundant and hence cheaper transition metals than ruthenium, one of the most promising being copper. [124] [47] [43] Dye discovery for DSCs is still largely based either on serendipity or on empirical data by systematically introducing new substituents for a specific class of compound known to be suitable as a chromophore in DSCs. One such example is the work of Lee et al. [125] on screening differently substituted porphyrins for DSC performance. This is a valuable approach and can result in improvements in a known class of DSC suitable compounds. [126] [127] [21]

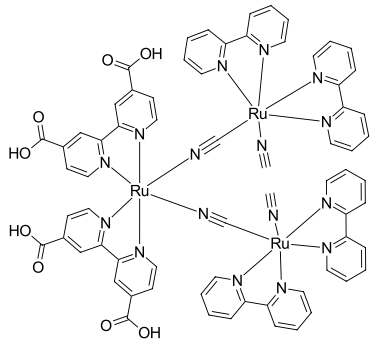

Figure 6.1: Trinuclear ruthenium dye [21]

Another strategy of increasing light harvesting is to mimic nature's antenna effect. Ideally, multiple light absorbing moieties, or pigments would be aligned to absorb light and transfer it vectorally to a final pigment anchored on the TiO_2 which would then inject the gathered electrons. When the additional dyes do not take up more space on the semiconductor surface, this potentially enhances the possible dye absorption of the system. Even one of the first complex efficiently used in a DSC was a multinuclear ruthenium complex (See Figure 6.1). However, the cis-geometry of the complex resulted in a relatively large footprint on the surface. [128] Additionally, the complex was not built up on the surface directly but synthesized beforehand through covalent bond formation. [127] The complex is therefore limited in its chain building ability. The principle of building up metalorganic dyes on a semiconductor by dipping in consecutively in solutions of the anchoring ligand followed by a metal introducing complex and a capping ligand has been used extensively for copper dyes in the past [47] [43].

In this work, back to back 2,2'-bipyridine ligands have been synthesized and their ability to form multinuclear chains on the semiconductor surface as well as their performance in DSCs has been investigated. By this very versatile approach, chain build up on the surface can be easily accomplished by dipping into solutions of ligands and metals sequentially. It also opens up the possibility of introducing multiple metals in one chain, possibly enhancing light absorption through charge transition from the antenna molecules all the way to the anchoring ligand (see Figure 6.2).

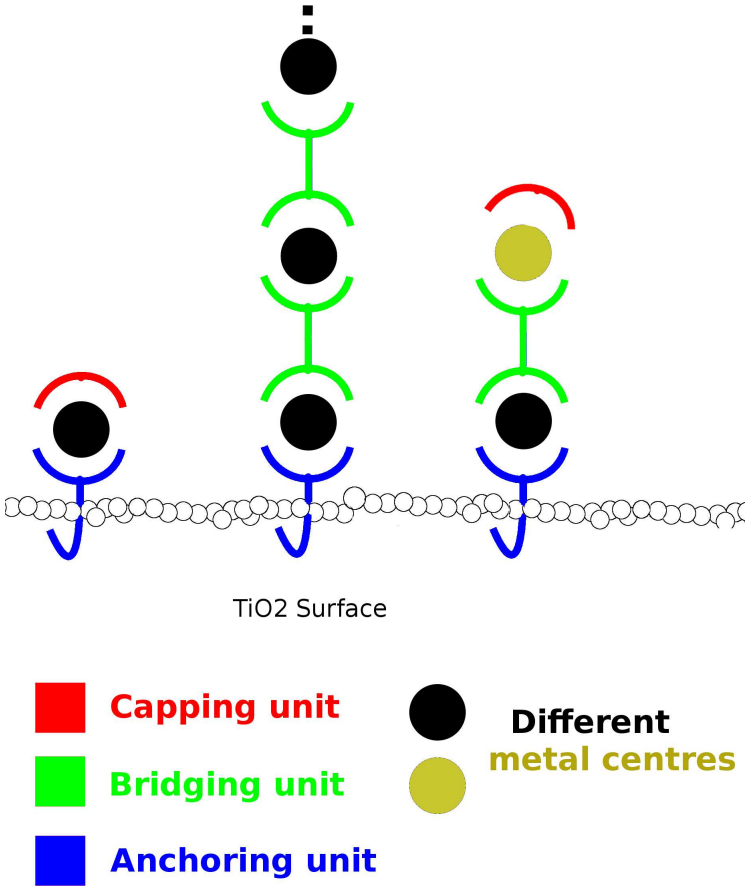

Figure 6.2: Building block approach on TiO_2

6.2 Back to back Ligands

Figure 6.3 shows three synthesized back to back ligands (labelled NoMe, MonoMe and DiMe) and their respective building blocks (labelled NoMe/2, MonoMe/2 and DiMe/2). The ligand NoME will only play a minor role in performance testing related to methyl substitution. Section 6.3.2, since it is not directly comparable to the other two due to its shorter chainlength. The back to back ligands have been synthesized by coupling the

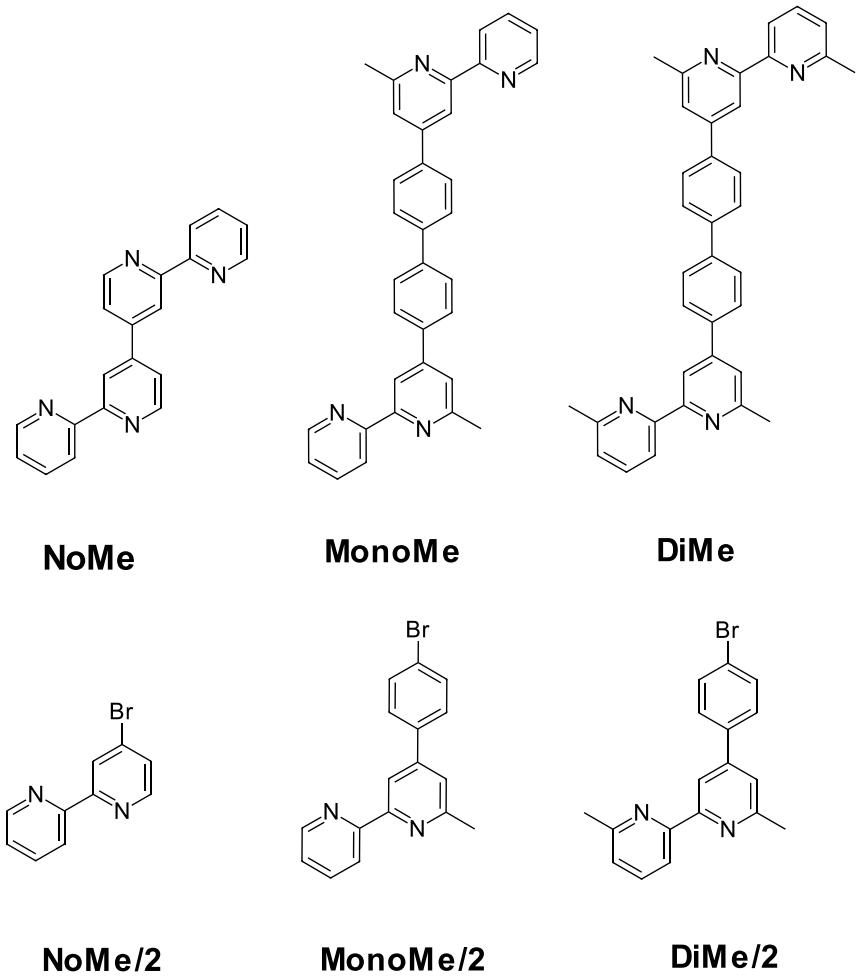

Figure 6.3: Synthesized ligands back to back ligands and their building blocks.

monomers NoMe/2, MonoMe/2 and DiMe/2 by a nickel-phosphine complex mediated homo coupling reaction. [129]. A reaction scheme is depicted (using MonoMe as an example) in Figure 6.4.

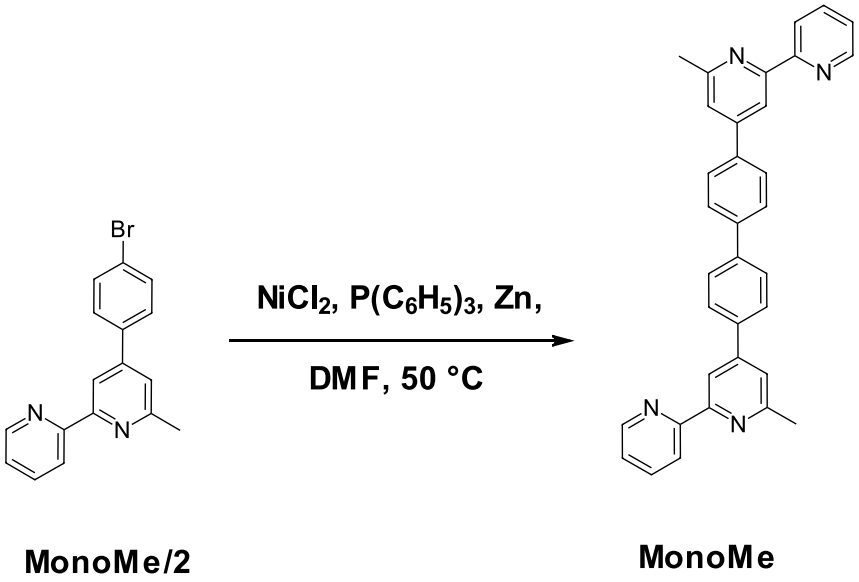

Figure 6.4: Ligand synthesis on the example of MonoMe

Figure 6.5 shows the crystal structure packing of MonoMe. It is a triclinic crystal system and there is a torsion in the molecule between the two bipyridine units. The torsion angle of the two planes incorporating the methylated pyridine rings amounts to 76.7 °. As a consequence, a helical structure is built up. The spacegroup is PI and the distance between the centroids of the methylated bipyridine rings is 4.55 Å. The interplanar distance of the methylated bipyridine rings is 3.53 Å, which indicates π-stacking [130]. Important crystallographic data is listed in Table 6.1. Unfortunately, no crystals could be obtained for DiMe yet. The structure of NoMe is described in literature [131].

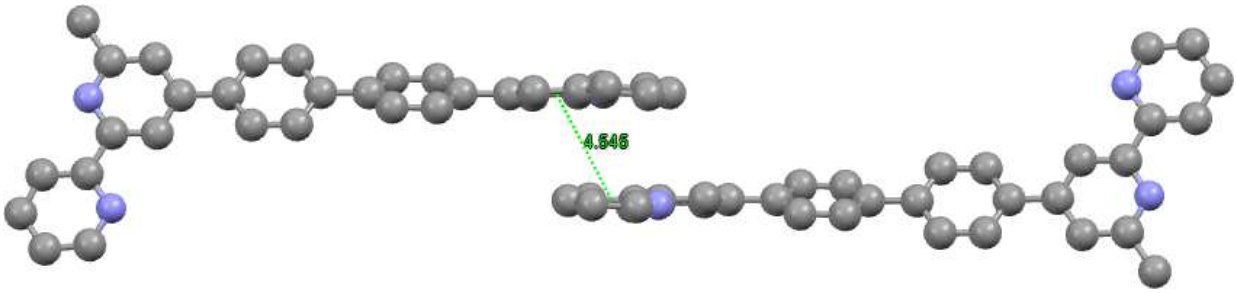

Figure 6.5: Crystal structure packing of MonoMe. The dotted line represents the distance between the centroids of the methylated biyridine rings

Crystal system	Unit cell: a,b,c [Å] / $[\alpha, \beta, \gamma]$ °	Space group	R1	wR2	gof
Triclinic	a 8.9001(9), b 10.1205(11), c 14.4840(18)/ α 78.320(6), β 82.262(6), γ 9.959(6)	P -1	0.0498	0.1114	0.997

Table 6.1: important crystal structure parameters

UV-Vis Measurements in solution

Figure 6.6 depicts the UV-Vis absorption spectra in solution of the ligands mentioned in Figure 6.3. Both back to back ligands had an absorption maximum at 304 nm, although the disubstituted ligand absorbed stronger than the monomethylated counterpart. NoMe absorbed most at 240 nm and 283 nm. The building blocks MonoMe/2 and DiMe/2 did not have any strong absorptive properties compared to their coupled dimers.

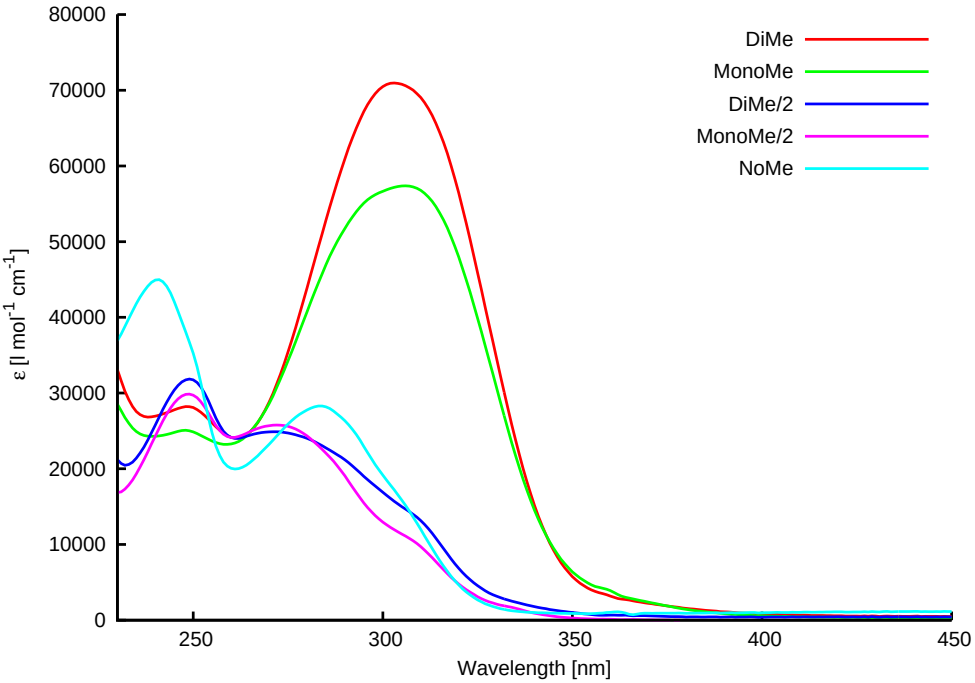

Figure 6.6: UV-Vis spectra of the synthesized back to back ligands and building blocks.

6.3 Performance testing in DSCs

6.3.1 Cell assembly

To anchor dyes on the TiO_2 surface, ALP1 has been used exclusively. Dyes have been built up on the surface by consecutive dipping of the working electrode in solutions of ALP1, then $Cu(MeCN)_4PF_6$ to introduce a copper center, and finally into a capping ligand solution. The concentrations and solvents were as follows: 1mM in DMSO for ALP1, 2mM in acetonitrile for $Cu(MeCN)_4PF_6$ and 1mM for the capping ligand unit in dichloromethane. After having dipped the electrode in each solution for 24 h, the electrode was rinsed with the solvent it has just been in order to remove excess of the material deposited on the

surface. It was rinsed with the solvent it was about to be immersed in next as well. The adsorption of a mixed metal dye on TiO_2 via a stepwise manner is illustrated in Figure 6.7. For leDSCs in this Chapter, commercial Solaronix test cell kits and Electrolyte 2 (see Section 3.3.7) have been used exclusively. PEDOT ssDSCs were assembled like described in Chapter 5. All CuI ssDSCs built with the described ligands have failed and they have not been investigated further due to their low performance and insufficient reproducibility. All cells in this chapter were masked before measuring.

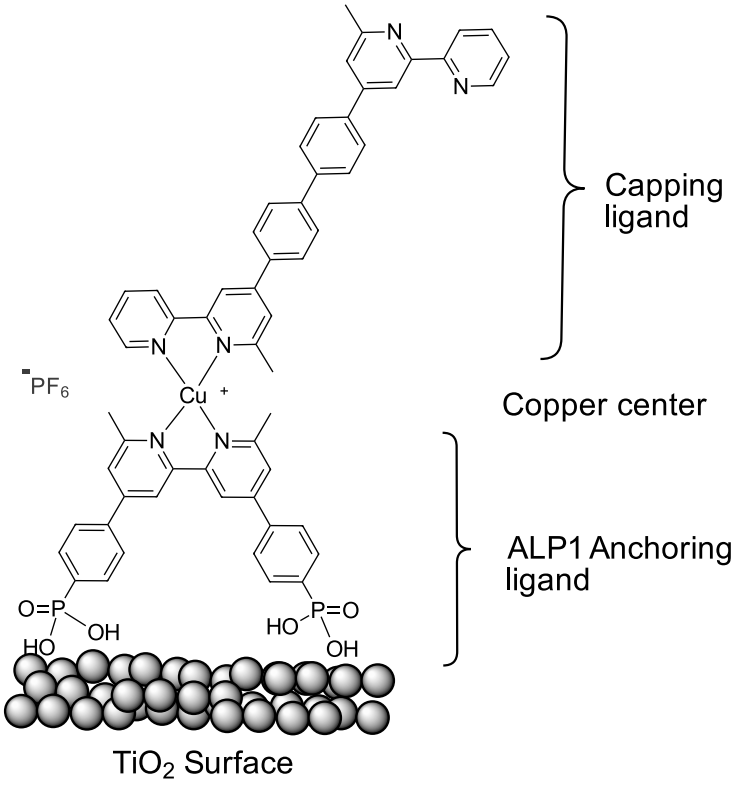

Figure 6.7: Assembly of a mixed metal dye via stepwise surface functionalization.

6.3.2 Copper(I) dye performance in liquid electrolyte type DSCs

The J-V curves and parameters of all tested cells on the day of fabrication are depicted in Figure 6.8 and Table 6.2. DiMe performed better in every aspect than MonoMe. The monomethylated Ligand performed better than the unsubstituted one. The current as well as the open circuit voltage (See Table 6.6) are higher, the more substituted the ligand is. This is most probably a consequence of the better shielding of the copper center by the two methyl groups instead of one, leading to less recombination of the dye with the I^-/I_3^- ions of the electrolyte. Although it has been previously reported that methyl groups in the 6,6'-position are a requirement on bipyridine ligands to stabilize the copper center,

[47] DSCs built with the MonoMe and even NoMe ligand showed a remarkably stable performance over 21-22 days in both, solid state PEDOT DSCs and liquid electrolyte DSCs (See Appendices 6.D and 6.C). The quantum efficiencies correlate well to the J-V

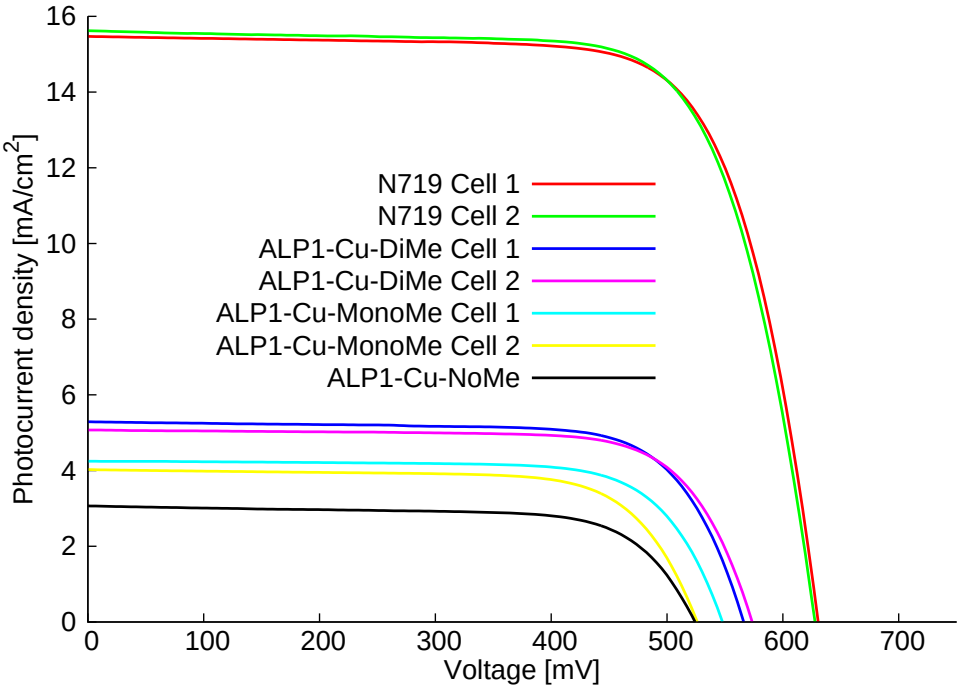

Figure 6.8: J-V curves of N719, ALP1-Cu-NoMe, ALP1-Cu-MonoMe and ALP1-Cu-DiME in leDSCs on the day of fabrication. Electrolyte 2 was used, all cells were masked.

Device Name	J_{sc} [mA/cm^2]	V_{OC} [mV]	FF [%]	η [%]
N719 Cell 1	15.5	630	73.3	7,14
N719 Cell 2	15.7	628	72.9	7.17
ALP1-Cu-DiMe Cell 1	5.20	566	73.3	2.16
ALP1-Cu-DiMe Cell 2	5.13	573	74.0	2.18
ALP1-Cu-MonoMe Cell 1	4.18	548	73.7	1.69
ALP1-Cu-MonoMe Cell 2	4.11	526	72.0	1.56
ALP1-Cu-NoMe	3.13	524	70.9	1.16

Table 6.2: J-V parameters of N719, ALP1-Cu-NoMe, ALP1-Cu-MonoMe and ALP1-Cu-DiME in leDSCs on the day of fabrication. Electrolyte 2 was used, all cells were masked.

measurements as can be observed in Figure 6.9. All copper complexes showed the same maximum at 472 nm independent of the ligand. More ligand substitution resulted in more efficient photon conversion over the whole spectrum. The maximum values were 34 % for the DiMe complex, 31% for the MonoMe and 24% for the NoMe complex on the TiO_2 surface. The maximum EQE for the reference N719 cell was 72%.

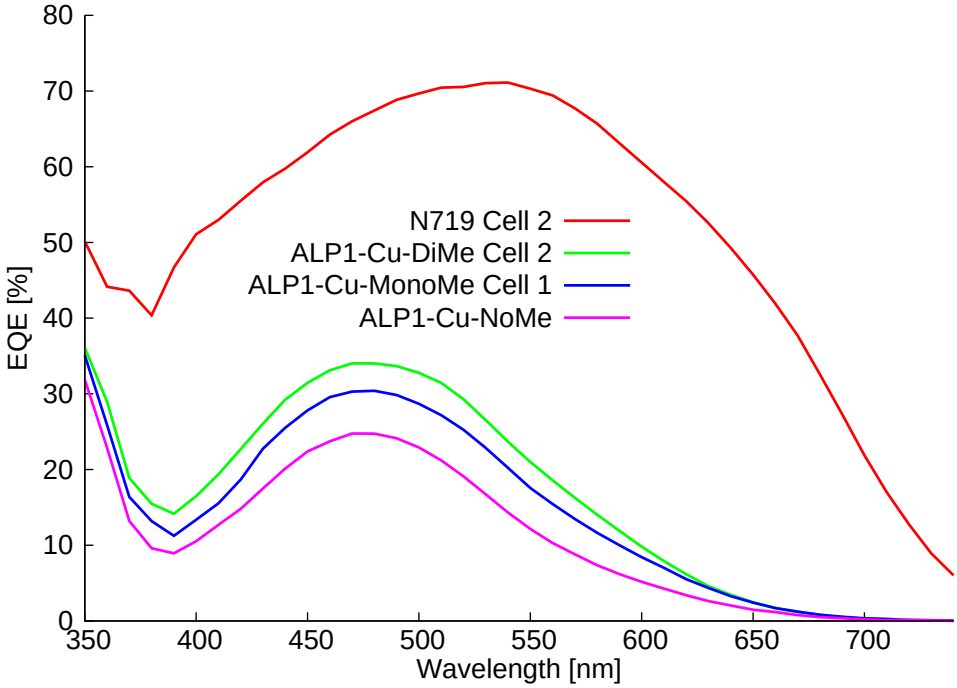

Figure 6.9: EQE measurements of N719, ALP1-Cu-NoMe, ALP1-Cu-MonoMe and ALP1-Cu-DiME in leDSCs on the day of fabrication. Electrolyte 2 was used.

6.4 Metalorganic chain-building experiments

Since the back to back ligands have two coordination sites they have the ability to build up metalorganic chains on the surface of the TiO_2. Blank TiO_2 electrodes were dipped subsequentially into a 1 mM solution of ALP1 in DMSO, a 2 mM $[Cu(MeCN)_4][PF_6]$ solution and finally into a 1mM solution of the DiMe back-to-back ligand in CH_2Cl_2. This marked one dipping cycle. The DiMe ligand was chosen because it had produced the most efficient DSCs out of the mentioned ligands. After each dipping, the electrode was washed to remove excess material adsorbed to the surface. First the electrode was dipped into the anchoring ligand, then into $[Cu(MeCN)_4][PF_6]$ and finally in DiMe. This marked the first dipping cycle. Every subsequent dipping cycle was another dipping in the $[Cu(MeCN)_4][PF_6]$ and the back to back ligand solution as illustrated in Figure 6.10. Solid state UV-Vis experiments were carried out with an undyed electrode as the blank (see Figure 6.11). The respective chain lengths did not show any large differences in absorption or absorption intensity. Although the absorption was slightly higher in the three dipping cycle electrode, the absorptions of electrodes with one, two or three dipping cycles were very similar. Additional experiments were made to determine whether the chains were built up at all or whether the anchoring ligand had just not been saturated completely after the first dipping and more copper had coordinated to the anchoring ligand after subsequent dipping cycles, making

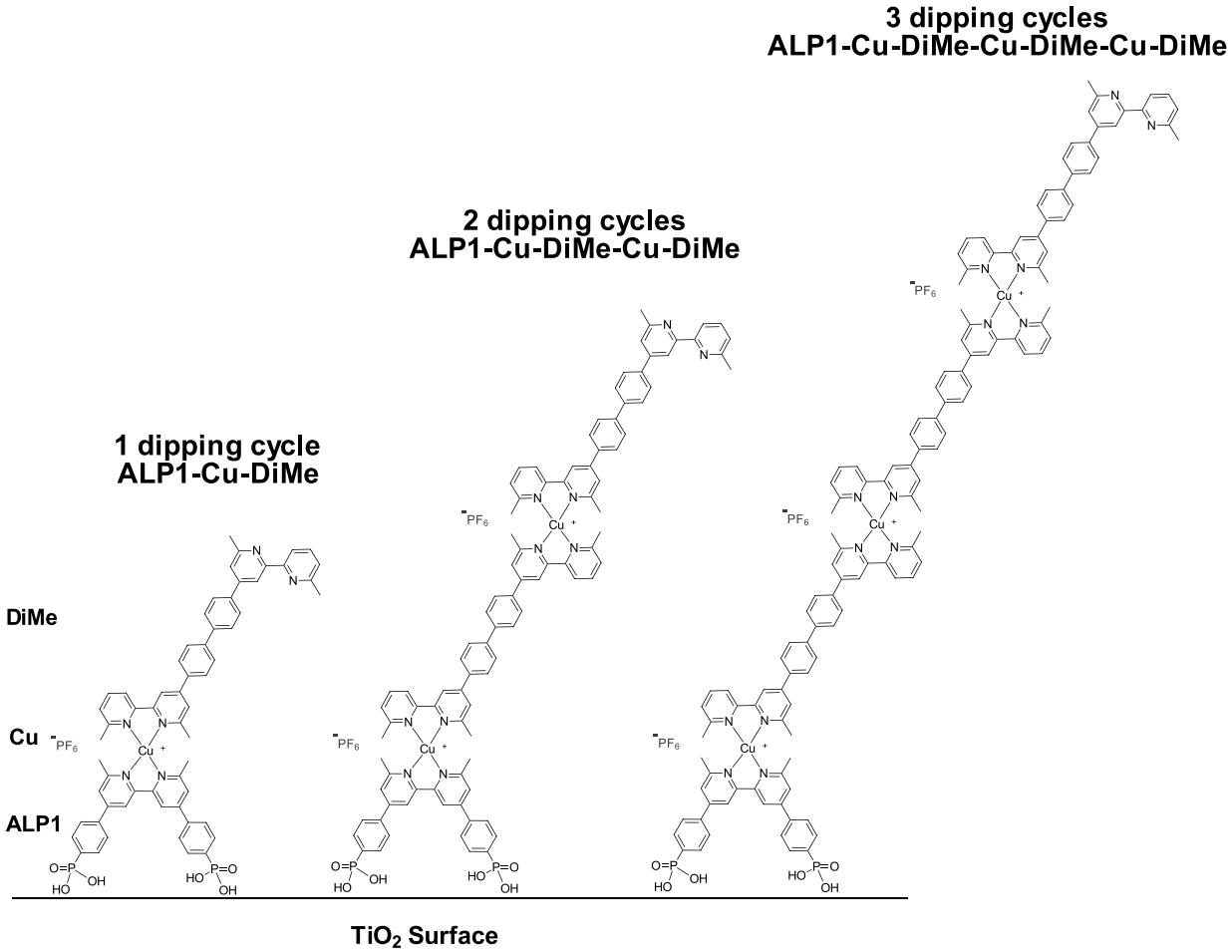

Figure 6.10: Schematic presentation of the dipping cycles on the TiO_2 surface.

the electrode appear darker. To characterize these layers and gain more information about the dye/electrolyte interface, SECM area scans were run in the dark and under illumination (see Appendix 6.A). No matter if one, two or three dipping cycles had been carried out, there has been a definite response upon illuminating the sample compared to the sample measured in the dark. That means the dye has been excited and is therefore most likely injecting electrons into the TiO_2 semiconductor upon illumination. However, this does not clarify if chains have been built up or if complex building has stopped after the first dipping cycle. Additionally to the area scans, retraction scans (Figure 6.12) were conducted by placing the UME tip at a distance of about 3-5 µm to the dyed TiO_2 surface and retracting it slowly to 1 mm. This was also measured in the dark and under illumination. What can be observed is that the more dipping cycles have been conducted, the more response from the UME tip was recorded. This could either mean electron injection is enhanced by building up a metalorganic oligomer which is absorbing more photons and injecting them, or just that more copper(I) atoms are available for reduction, which would lead to a current increase as well. This would still not clarify if the copper centers are in a metalorganic chain

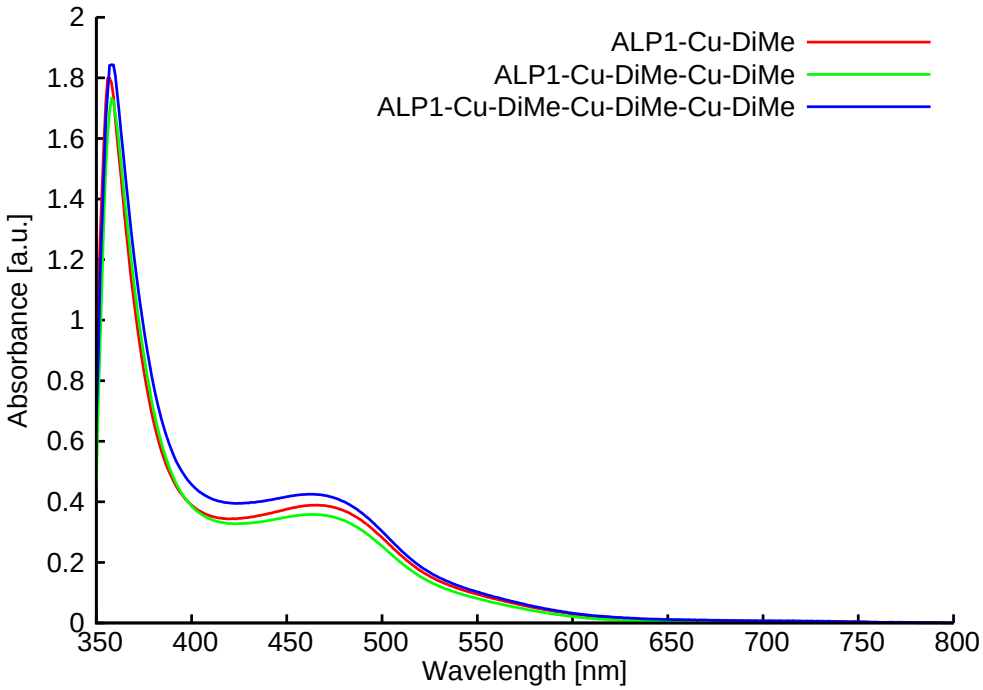

Figure 6.11: Solid state UV-Vis measurements of metalorganic chain building experiments.

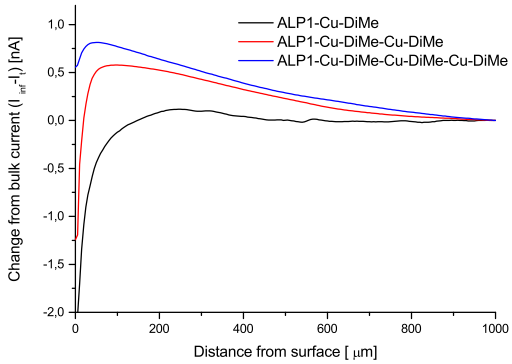

(a) SECM retraction curves in the dark.

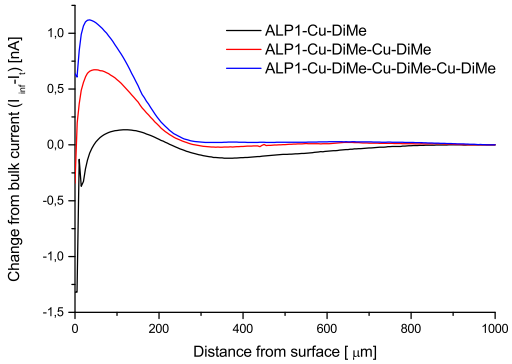

(b) SECM retraction curves under illumination (80 mW/cm^2).

Figure 6.12: SECM retraction curves of sensitized electrodes with 1,2 and 3 dipping cycles.

or just adhered in some other manner to the TiO_2 surface. The TiO_2 of an electrode that underwent three dipping cycles was scratched off and subjected to matrix-assisted laser desorption ionization (MALDI) spectrometry measurement (see Appendix 6.24 for the full measurement). This measurement revealed that there is a good chance the chain was at least built up to ALP1-Cu-DiMe-Cu-DiMe, since fragments of DiMe-Cu-DiMe have been identified. (See Figure 6.13). With the indication that chains had actually formed, leDSCs were assembled with electrodes of one, two and three dipping cycles. Their J-V curves and

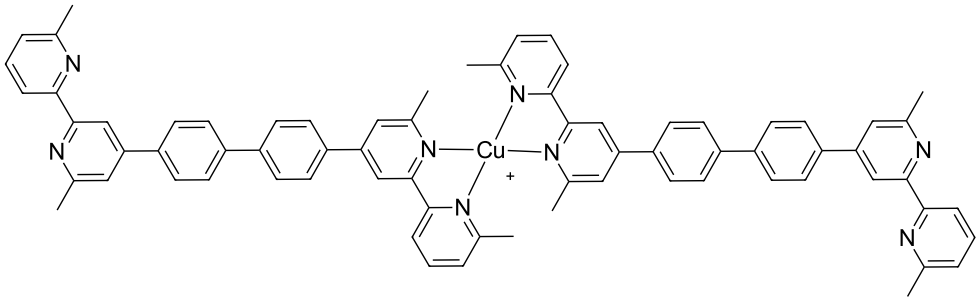

Figure 6.13: Highest identified mass of an ALP1-Cu-DiMe-Cu-DiMe-Cu-DiMe TiO_2 electrode measured with mass spectrometry MALDI-TOF.

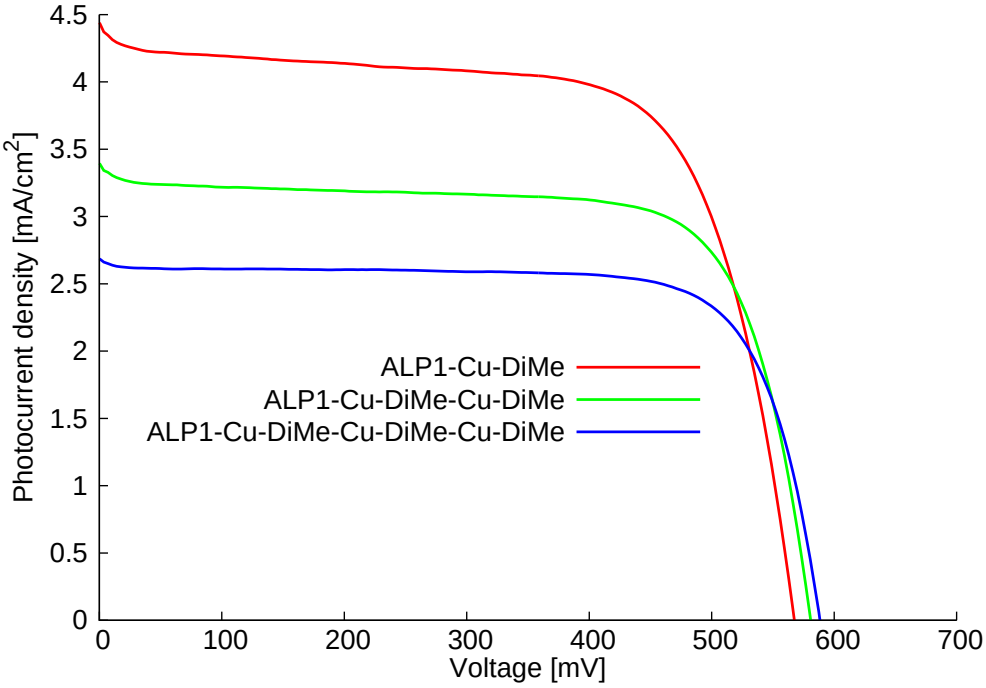

Figure 6.14: J-V curves of working electrodes with one (ALP1-Cu-DiMe), two (ALP1-Cu-DiMe-Cu-DiMe) and three (ALP1-Cu-DiMe-Cu-DiMe-Cu-DiMe) dipping cycles. Electrolyte 2 was used and all cells were masked.

Device Name	J_{sc} [mA/cm^2]	V_{OC} [mV]	FF [%]	η [%]
ALP1-Cu-DiMe	4.45	567	68.5	1.66
ALP1-Cu-DiMe-Cu-DiMe	3.40	580	72.5	1.42
ALP1-Cu-DiMe-Cu-DiMe-Cu-DiMe	2.69	588	75.4	1.19

Table 6.3: J-V parameters of working electrodes with one (ALP1-Cu-DiMe), two (ALP1-Cu-DiMe-Cu-DiMe) and three (ALP1-Cu-DiMe-Cu-DiMe-Cu-DiMe) dipping cycles. Electrolyte 2 was used and all cells were masked.

performance parameters are shown in Figure 6.14 and Table 6.3. The efficiency of these cells decreases consistently the more dipping cycles have been carried out. This can also be observed in current, which decreases with increasing number of dippings. The open circuit

voltage as well as the fill factor however increases consistently the more dippings have been conducted. A similar effect has been observed by Kroeze et al. [122] when aliphatic chainlengths on a ruthenium sensitizer have been varied. There as well, open circuit voltage has increased by chain length. However by increasing it over a certain point, current density decreased. These aliphatic chains have been reported to reduce recombination by forming a hydrophobic barrier and therefore inhibiting the triiodide ion to reach the TiO_2 surface. On the other hand, increasing the chainlength also reduced dye regeneration. [25, pp. 92] Since ALP1-Cu-DiMe was the most efficient dye, more iterations of it might not contribute to electron injection and effectively just being bulk, shielding the active dye from the electrolyte. That would retard recombination but also dye regeneration alike, increasing V_{OC} and decreasing J_{SC}. A better balance of these factors is desirable. Another reason for current density decrease in extended π-systems is aggregation of the chains which quenches the excited state of the dye molecules. By building longer chains the possibility of quenching is enhanced. This aggregation could possibly be reduced by adding cheno, a competeing co adsorbent, or by altering the structure and thereby introducing sterically hinered substituents. According to Kim at al. this reduces dye uptake but also often results in better efficiencies than just having exclusively rod shaped molecules in close proximity. [123]

6.4.1 Introducing a dinuclear mixed metal complex for light harvesting

The approach of multinuclear copper chains in DSCs has led to a decrease in current density. MALDI-TOF experiments and the linear current density decrease with chain length indicated that the chains have actually formed. The free coordination site also allows one to introduce a second metal complex, with the aim of enhancing light harvesting. Since ruthenium complexes are already widely known for their broad absorption, a ruthenium(II) complex with the bridging ligand MonoMe (RuMonoMe) was prepared. cis-Dichlorobis(bipyridine)ruthenium(II) was irradiated together with MonoMe in a Biotage microwave reactor at 150 °C for 1.5 h to give the desired Ru(II) complex (see Figure 6.15). [132]. Figure 6.16 shows the absorption spectrum of RuMonoMe compared to the ligands. RuMonoMe has the broadest and most intense absorption, which could be expected because of the additional MLCT at 455 m, and the shoulder at 425 nm. Furthermore there is a strong ligand centered charge transfer (LCCT) at 289 nm with a shoulder at 328 nm. Semi empirical PM3[1] calculations (see Figure 6.17) have revealed that the HOMO and LUMO orbitals of this complex are not aligned in a way that promotes electron injection in the

[1]Calculations have been performed using Spartan Wavefunction. These are PM3 level calculations, first geometry optimized with molecular mechanics. All are ground state calculations

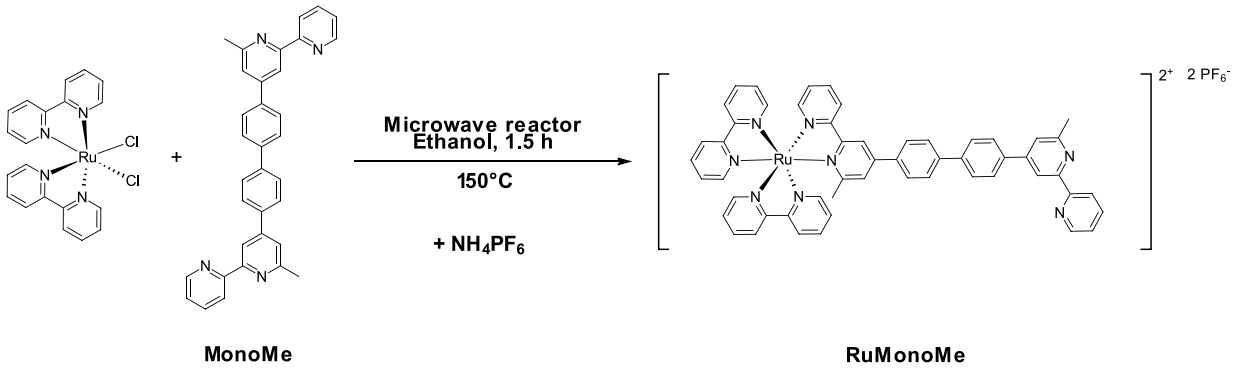

Figure 6.15: Reaction scheme of the synthesis of RuMonoMe

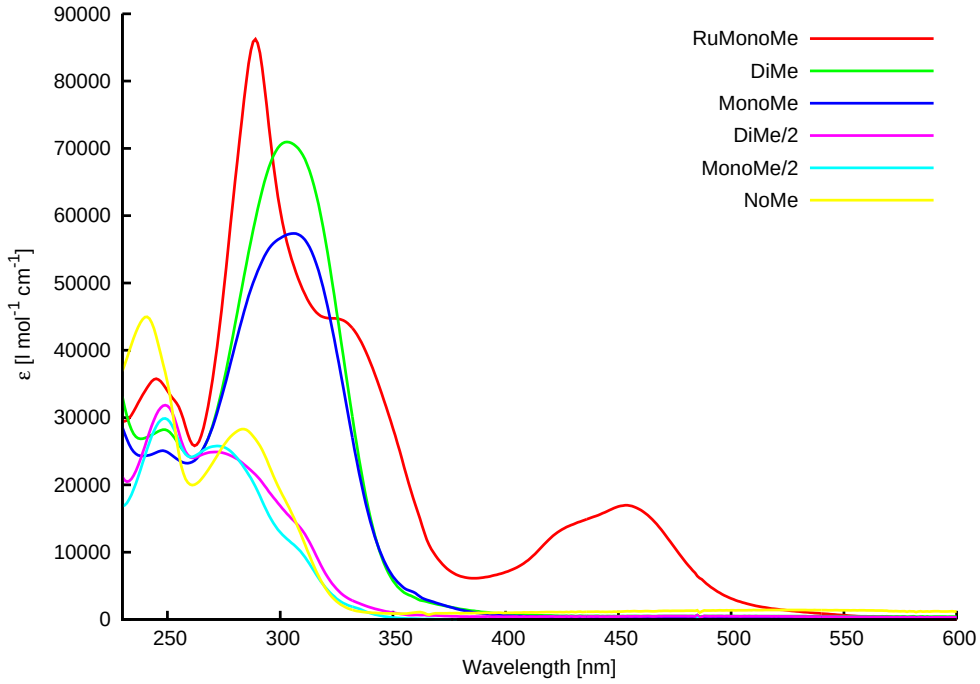

Figure 6.16: UV-Vis spectra of RuMonoMe compared to the synthesized back to back ligands and building blocks.

semiconductor. The LUMO of the dinuclear RuMonoMe-Cu-ALP1 complex, which would be optimal to be as close to the TiO_2 surface as possible for electron injection, is exclusively located at the ruthenium center. The contribution from the ruthenium complex (on the right in Figure 6.17) to electron injection was therefore believed to be minor at best. The HOMO on the other hand is located exclusively at anchoring ligand and partly on the 6,6' dimethylated capping ligand, which means the orbitals lye in the exact opposite directions to the preferred constellation. The RuMonoMe-Cu-ALP1 complex has been compared to the MonoMe-Cu-ALP1 complex as a sensitizer in leDSC performance (See Figures 6.18 and Table 6.4). As can be seen by additional dipping into the RuMonoMe complex, the current density could unexpectedly be increased by 0.87 mA/[cm^2]. EQE measurements revealed

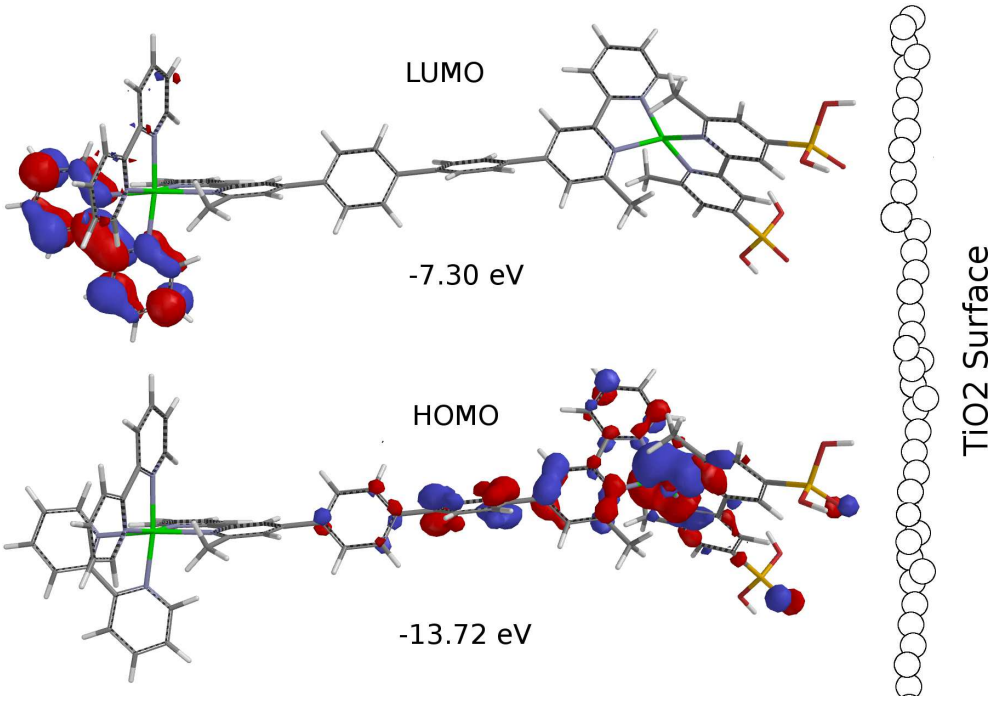

Figure 6.17: Calculations of the HOMO and LUMO orbitals of the heteronuclear complex

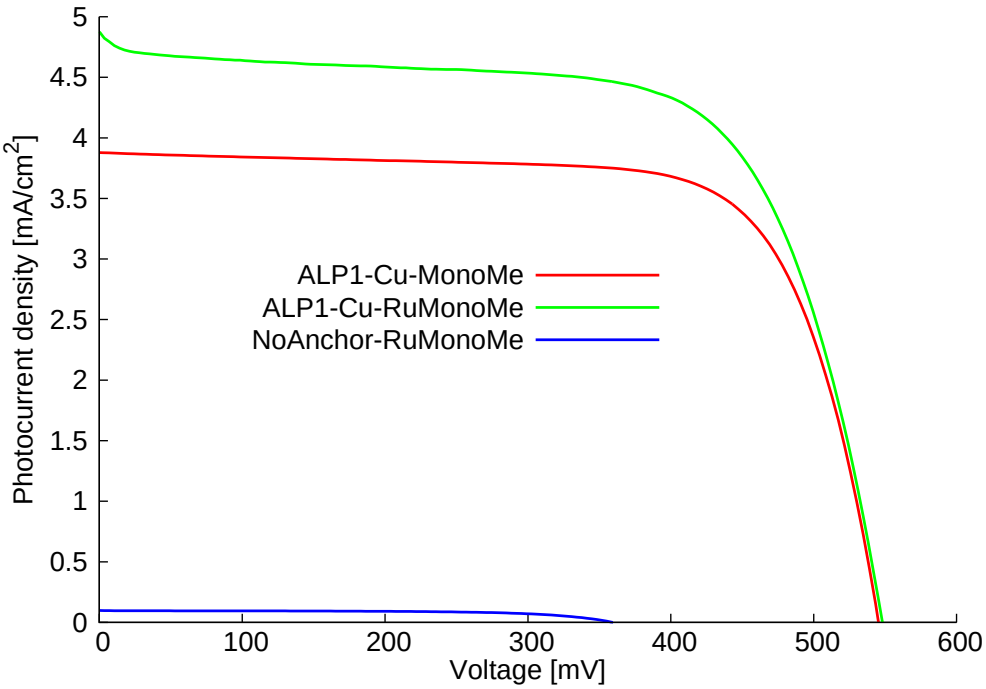

Figure 6.18: J-V curves of ALP1-Cu-RuMonoMe, ALP1-Cu-MonoMe and RuMonoMe without anchoring ligand. Electrolyte 2 was used and all cells have been masked.

that both complexes were most efficient at 470 nm, namely with 35% for RuMonoMe and 30% for the MonoMe capped complex (see Figure 6.19). The dinuclear complex seemed to be more efficient though with a better external quantum efficiency until 570 nm. Solid

Device Name	J_{sc} [mA/cm^2]	V_{OC} [mV]	FF [%]	η [%]
ALP1-Cu-MonoMe	3.88	545	72.2	1.53
ALP1-Cu-RuMonoMe	4.88	548	67.4	1.76
NoAchor-RuMonoMe	0.0980	359	63.80	0.0210

Table 6.4: J-V parameters of ALP1-Cu-RuMonoMe, ALP1-Cu-MonoMe and RuMonoMe without anchoring ligand. Electrolyte 2 was used and all cells have been masked.

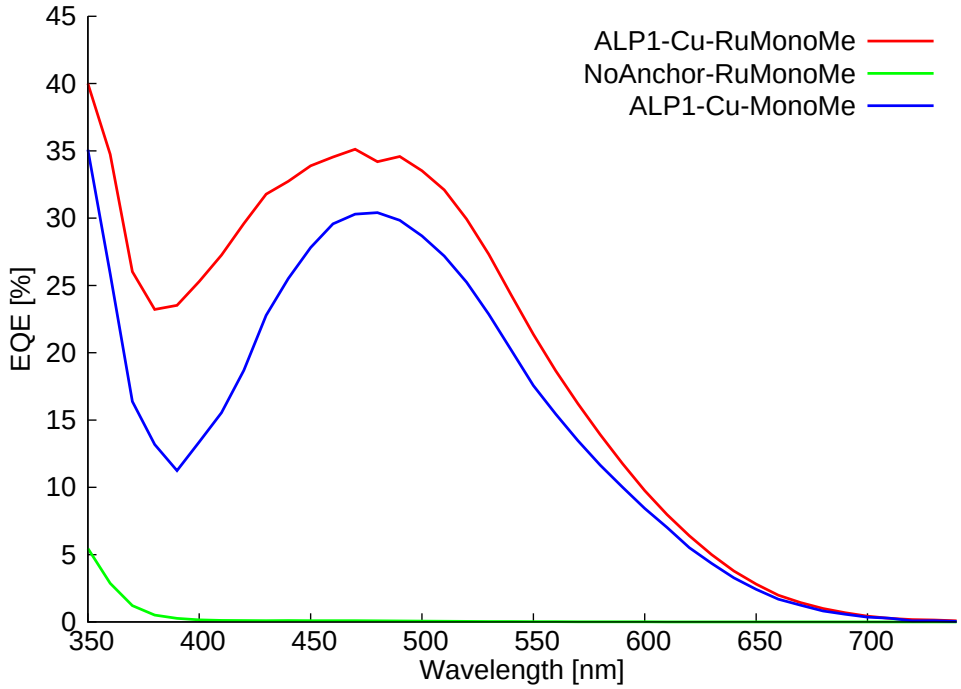

Figure 6.19: EQE measurements of RuMonoMe, MonoMe and RuMonoMe without anchoring ligand.

state UV-Vis spectra of electrodes dipped in the RuMonoMe additionally compared to the DiMe back to back ligand show a clear MLCT absorption blue-shift due to the capping ruthenium complex unit (see Figure 6.20). This leads to the assumption that RuMonoMe actually has an influence in photon collection and injection. By measuring just the RuMonoMe complex on the surface, the LCCT absorption of the anchoring ligand ALP1 is missing. Interesting would be an analogous experiment with a ruthenium complex of the better performing DiMe ligand, which unfortunately has not been isolated yet. The actual complex formation was checked by building a cell without anchoring ligand, since the free bipyridine coordination site might anchor to the TiO_2 by itself. However, this cell did not produce any significantly high current density, therefore electron injection is basically non-existent.

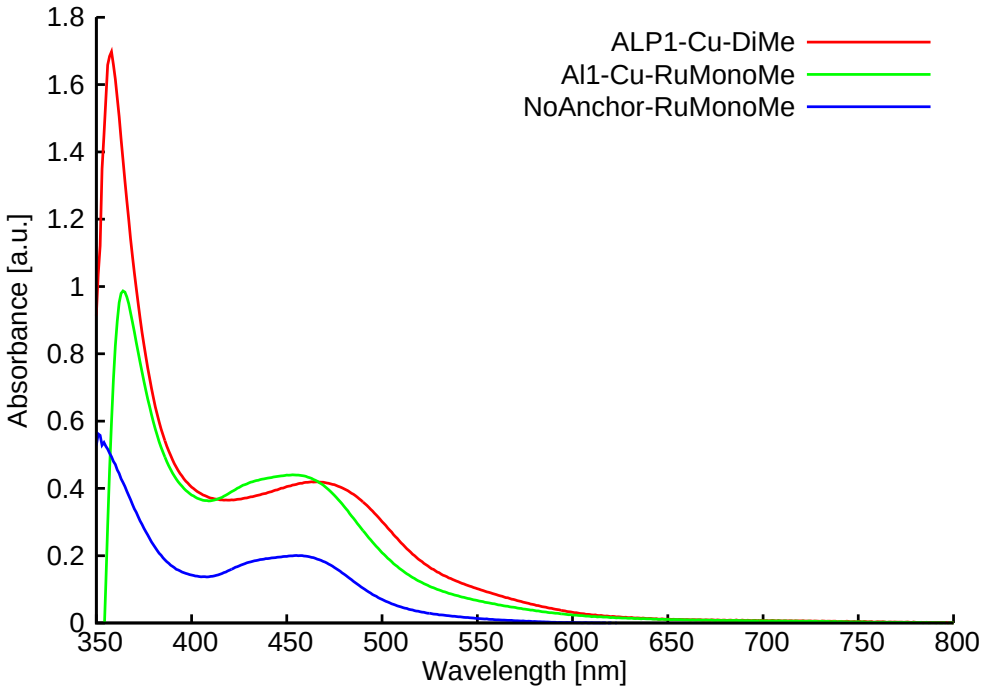

Figure 6.20: Solid state UV-Vis measurements of electrodes with ALP1-Cu-RuMonoMe, ALP1-Cu-DiME and RuMonoMe without anchoring ligand "NoAnchor" adsorbed to the TiO_2 surface

6.4.2 PEDOT cells

The MonoMe and DiMe ligands have been tested by incorporating them in two identical PEDOT ssDSCs each. The N719 Cell 2 of the experiment in Chapter 5/Section 5.4 has been plotted as well for comparison. Figure 6.21 and Table 6.5 show the results. Here as well, the DiMe ligand complex outperforms the MonoMe one. In PEDOT ssDSCs, V_{OC} is constantly

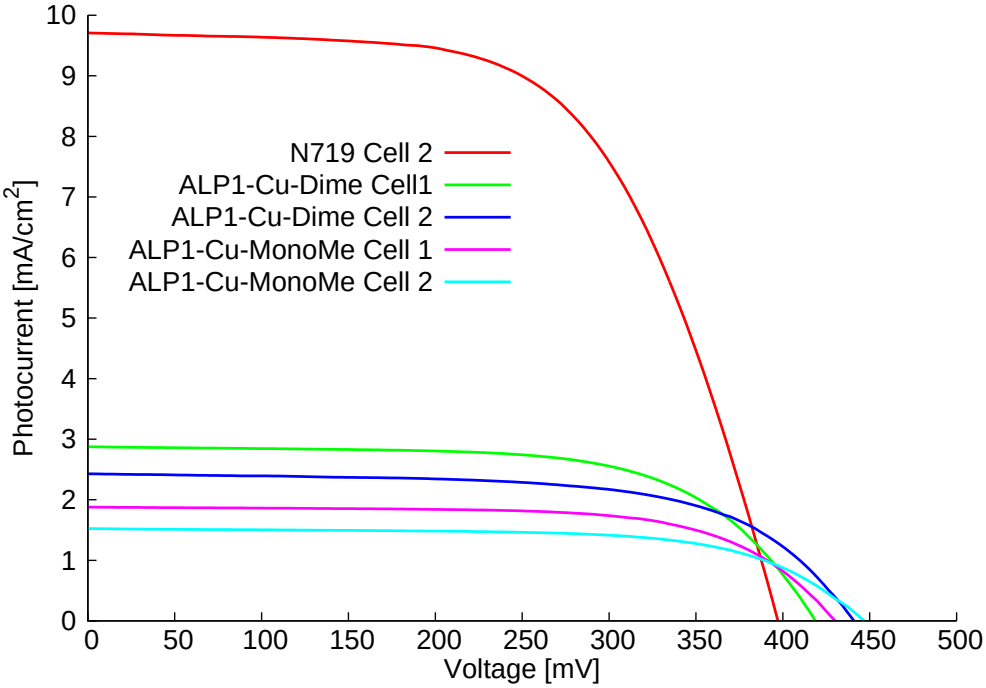

Figure 6.21: J-V measurements of PEDOT type ssDSCs on the day of assembly. All cells have been masked

Device Name	J_{sc} [mA/cm^2]	V_{OC} [mV]	FF [%]	η [%]
N719 Cell 2	9.72	397	60.4	2.33
ALP1-Cu-MonoMe Cell 1	1.53	447	65.5	0.448
ALP1-Cu-MonoMe Cell 2	1.88	430	66.5	0.538
ALP1-Cu-DiMe Cell 1	2.89	418	63.8	0.771
ALP1-Cu-DiMe Cell 2	2.44	440	62.7	0.673

Table 6.5: J-V parameters of PEDOT type ssDSCs on the day of assembly. All cells have been masked

higher in the back to back ligand capped complexes than in the N719 cell. This is the case for all six fabricated N719 cells in Chapter 5 Section 5.4 as well. In liquid electrolyte DSCs (see Section 6.3.2) on the other hand, the back to back ligands had a much lower V_{OC} than the N719 cells. This could be due to a favorable coordinating interaction of the PEDOT HTM with the vacant coordination site. In the EQE spectra of the PEDOT ssDSCs (Figure 6.22),

the ALP1-Cu-DiMe complex outperforms its monomethylated counterpart as it did in the leDSCs, although the values are smaller with 63% for N719, 19% for ALP1-Cu-DiMe and 12% for ALP1-Cu-MonoMe.

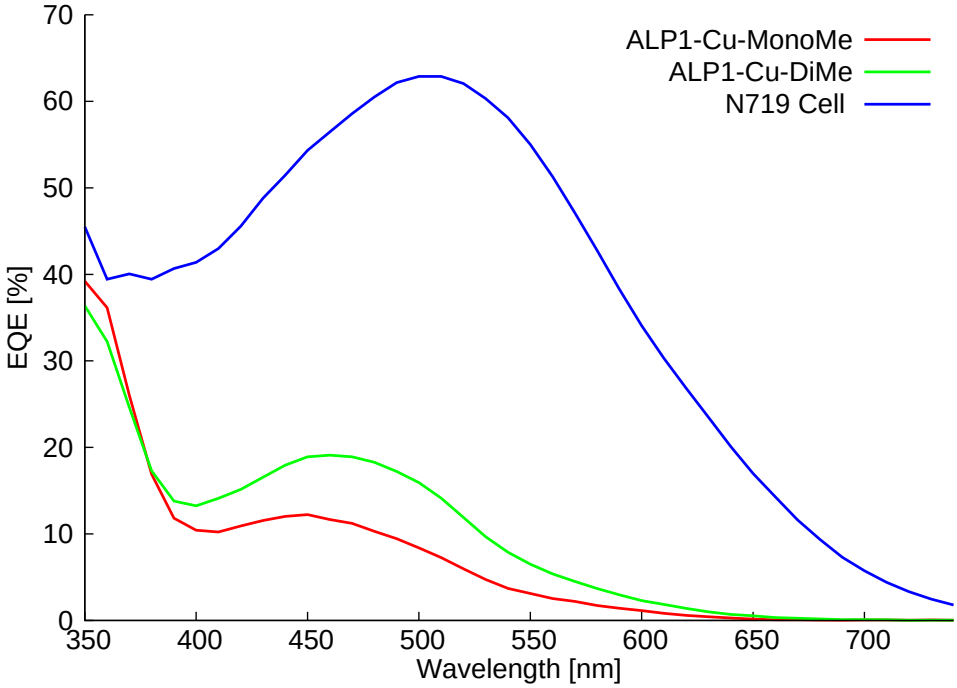

Figure 6.22: EQE measurements of the PEDOT type DSCs on day of assembly

6.5 Summary

In Summary, two new back to back ligands (MonoMe and DiMe) have been prepared and investigated for DSC performance as parts of metalorganic complexes (ALP1-Cu-MonoMe and ALP1-Cu-DiMe) in leDSCs and PEDOT ssDSCs. In ssDSCs, ALP1-Cu-MonoMe and ALP1-Cu-DiMe resulted in enhanced V_{OC} compared to the N719 cells. This behaviour was not observed for leDSCs, which could imply an interaction of the PEDOT HTM with the vacant bipyridine coordination site of the ligands as assumed in Chapter 4, to possibly result in better hole injection. That being the case would lower the energy level of the HTM valence band and enhance V_{OC} as a consequence. Furthermore, the possibility of building metalorganic chains on the TiO_2 surface and using them as a dye in leDSCs has been investigated. Although SECM experiments showed a higher tip current with increasing number of dipping cycles, the efficiency of the DSCs decreased the more cycles the electrode went through. A dinuclear mixed metal species (ALP1-Cu-RuMonoMe) has been built up on the TiO_2 surface and resulted in a current gain respective to it's mononuclear counterpart (ALP1-Cu-MonoMe). Additionally one previously reported [133] bipyridine back to back ligand (NoMe) has been tested in leDSCs as a copper(I) metalorganic complex (ALP1-Cu-NoMe).

6.6 Experimental Procedures

6.6.1 General

Chemicals: cis-Dichlorobis(bipyridine)ruthenium(II) was synthesized by Dr. Emma Dunphy. Part of the 1-(2-oxopropyl)pyridinium chloride used for reactions has been synthesized by Dr. Iain A. Wright. Other reagents and reactants were commercially available and were used without any further purification.

Solvents: Reactions were performed with commercial reagent grade quality solvents. If necessary, dry and oxygen free solvents have been used. For column chromatography, technical grade solvents were used. Photophysical measurements were carried out only with HPLC quality solvents.

Column chromatography, and spot thin layer chromatography: All column chromatography has been performed either with Merck silica gel 60 (0.063-0.200 mm), Fluka aluminium oxide 179944 or Merck aluminium oxide 90 standardized. Silica gel (PLC plates 20 x 20 cm, silica gel 60 F254 , 2 mm, Merck) and aluminium oxide (PLC plates 20 x 20cm, aluminium oxide 60 F254 , 1.5 mm, Merck) have been used for preparative layer chromatography. Spot thin layer chromatography was performed on silica gel plates (POLYGRAM SILG/UV254 and TLC silica gel 60 F254 , Merck) and alumium oxide plates (TLC aluminium oxide 60 F254 , neutral, Merck).

Microwave reactor: Microwave reactions were carried out in a Biotage Initiator 8 reactor with sealed tubes allowing pressures of up to 20 bar.

6.6.2 Analytical equipment

NMR: NMR spectra were recorded on Bruker AM250 (250 MHz), Bruker DPX400 (400 MHz) and Bruker DRX500 (500 MHz) spectrometers. For full assignments COSY, DEPT, HMBC, HMQC and NOESY experiments were recorded on the Bruker DRX500 by either C. E. Ertl or N. Hostettler. ^{1}H and ^{13}C NMR spectra were recorded at 25 °C. Chemical shifts are relative to the respective residual solvent peaks and solvent peak values from Mnova versions 6.1-9.1.

Mass spectrometry: FAB (NBA matrix) and electron impact (EI) mass spectra were

recorded by Dr. Heinz Nadig using Finnigan MAT 312 and VG 70-250 instruments, respectively. Electrospray ionisation (ESI) mass spectra were measured using a Finnigan MAT LCQ or a Bruker esquire ^{3000plus} instrument by Dr. Sven Brauchli.

Infrared spectroscopy: IR spectra were recorded on a Shimadzu FTIR-8400S spectrophotometer with neat samples using a golden gate attachment.

UV-Vis spectroscopy: Electronic absorption spectra were recorded on a 8453 Spectrophotometer or a Cary5000 UV-Vis-NIR instrument, both from Agilent.

Photoluminescence: Photoluminescence spectroscopy was performed on a Shimadzu RF-5301 PC spectrofluorophotometer. Values for the excitation and emission slits were kept as close as possible.

Microanalysis: The microanalyses were performed with Leco CHN-900 microanalyser by W.Kirsch or by Sylvie Mittelheisser on a Elementar Vario Micro Cube instrument.

X-ray diffraction: Crystal structure data was collected either on a Bruker-Nonius KappaAPEX CCD diffractometer or on a Stoe IPDS instrument by Dr. Jennifer Zampese or by Dr. Markus Neuburger. For the data reduction, solution and refinement, the programs COLLECT 18, DENZO/SCALEPACK 19, SIR92 20, Stoe IPDS software 21, SHELXL97 22 and CRYSTALS (version 12) were employed. Structures have been analyzed using CCDC Mercury (version 3.3).

Synthesis of 1-(2-oxopropyl)pyridinium chloride

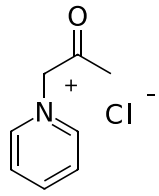

Pyridine (9.98 g, 10.2 ml, 125 mmol, 1.0 eq) was dissolved in dry diethyl ether (20.0 ml). Chloroacetone (11.6 g, 10.0 ml, 125 mmol, 1.0 eq) was added to the solution, which was stirred for 6 h at room temperature afterwards. The resulting white precipitate was filtered and dried on a high vacuum pump for 12 h. (10.4 g, 60.7 mmol, 49%). Analytical data is in agreement with the literature [134]

Synthesis of (E)-3-(4-bromophenyl)-1-(pyridin-2-yl)prop-2-en-1-one

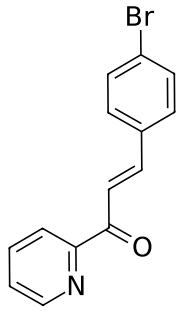

4-Bromobenzaldehyde (8.33 g, 45.0 mmol, 1.0 eq) and 6-methyl-2-acetylpyridine (5.45 g, 5.05 ml, 45.0 mmol, 1.0 eq) were dissolved in methanol (100 ml). Sodium hydroxide (2 $\%_{wt}$, 42.0 ml, aqueous) was added, whereupon the solution turned green. The reaction mixture was left to stir at room temperature for 4 h. The formed white precipitate was collected by filtration and washed carefully with water and methanol (3 x 20.0 ml each). The resulting light green solid was dried on the high vacuum for 12 h. (11.1 g, 38.6 mmol, 85%) [135] Analytical data is in agreement with the literature. [136]

Synthesis of 4-(4-bromophenyl)-6-methyl-2,2'-bipyridine (MonoMe/2)

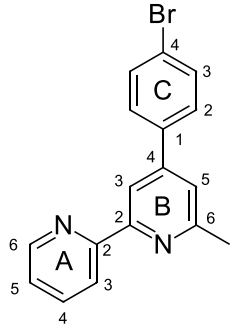

(E)-3-(4-bromophenyl)-1-(pyridin-2-yl)prop-2-en-1-one (2.00 g, 6.94 mmol, 1.0 eq) was dissolved in methanol (100 ml) and 1-(2-oxopropyl)pyridinium chloride (1.19 g, 6.94 mmol, 1.0 eq) was added. The reaction mixture was treated with ammonium acetate (16.0 g, 208 mmol, 30 eq) and refluxed for 24 h. It was left to cool down and put into the fridge over night. A precipitate had formed, was filtered and washed with water and methanol (3 x 15.0 ml each). After drying on the high vacuum, light yellow crystals were isolated. (1.44 g, 4.43 mmol, 65%). [135]

^{1}H NMR (500 MHz, $CDCl_3$) δ/ppm: 8.72 (ddd, J = 4.9, 1.8, 0.9 Hz, 1H, H^{A6}), 8.57 (d, J = 8.0 Hz, 1H, H^{A3}), 8.51 (s, 1H, H^{B3}), 7.90 (td, J = 7.8, 1.8 Hz, 1H, H^{A4}), 7.77–7.52 (m, 4H, $H^{C2/C3}$), 7.41 (d, J = 1.7 Hz, 1H, H^{B5})), 7.38 (ddd, J = 7.4, 5.0, 1.2 Hz, 1H, H^{A5}), 2.74 (s, 3H, H^{Me}). **^{13}C NMR** (126 MHz, $CDCl_3$) δ/ppm: 158.8 (C^{B6}), 155.36 ($C^{A2/B2}$), 149.2 (C^{B4}), 148.8 (C^{A6}), 137.9 (C^{A4}), 137.1 (C^{C1}), 132.5 ($C^{C2/C3}$), 129.0 ($C^{C2/C3}$), 124.3 (C^{A5}), 124.0 (C^{C4}), 122.2 (C^{A3}), 121.6 (C^{B5}), 116.9 (C^{B3}), 24.6 (C^{Me}). **IR** (solid, ν, cm^{-1}): 3051 (w) 2911 (w) 1601 (m) 1580 (m) 1567 (m) 1544 (m) 1485 (m) 1449 (m) 1408 (m) 1378 (m) 1260 (w) 1214 (w) 1137 (w) 1104 (w) 1072 (m) 1043 (w) 1007 (m) 994 (m) 906 (w) 894 (w) 870 (w) 822 (s) 791 (s) 743 (m) 731 (m) 714 (w) 696 (m) 655 (m) 635 (w) 621 (m) 580 (w) 562 (w) 540 (w) 478 (s). **MS** (MALDI m/z): 324.94 $[M+H]^+$ (calc:324.03) **UV-Vis**

(λ_{max} nm [ε/ $dm^{-3} \cdot mol^{-1} \cdot cm^{-1}$] CH_2Cl_2, c = $1.00 \cdot 10^{-5} \cdot mol \cdot l^{-1}$): 249 nm [29950], 274 [25815], 310 nm [sh, 9911] **Luminescence** ([nm], CH_2Cl_2, c = $1.00 \cdot 10^{-5}$ mol $\cdot$ l^{-1}, λ_{ex} = 249 nm): λ_{em} = 353 **Elem. Anal.** Calcd. for $C_{17}H_{13}BrN_2$: C 62.79, H 4.03, N 8.61; found: C 62.51, H 4.17, N 8.76.

Synthesis of 4,4'-bis(6-methyl-[2,2'-bipyridin]-4-yl)-1,1'-biphenyl (MonoMe)

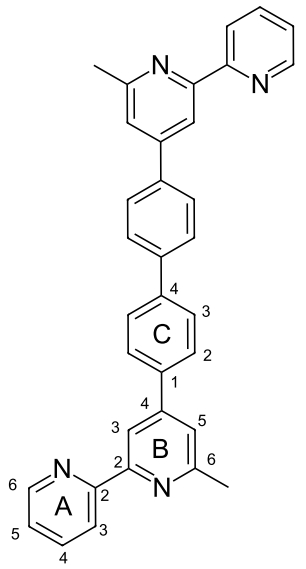

Triphenylphosphine (5.56 g, 21.0 mmol, 8.0 eq) and nickel(II)chloride hexahydrate (1.27 g, 5.36 mmol, 2.0 eq) were dissolved in dimethylformamide (28.0 ml) under a nitrogen atmosphere. Zinc powder (346 mg, 5.36 mmol, 2.0 eq) was added and the solution was left to stir for 1 h at 50 °C, whereupon it turned dark red. 4-(4-Bromophenyl)-6-methyl-2,2'-bipyridine (1.73 g, 5.36 mmol, 2.0 eq) was added and the mixture was left stirring at 50 °C for further 12 h after which the staring material had been consumed (reaction control with TLC on silica, cyclohexane : EtOAc, 9:3). The reaction mixture was poured onto a diluted aqueous ammonia solution (200 ml, 10%) and extracted with dichloromethane (3 x 50.0 ml). The organic phase was washed with water (3 x 50.0 ml), dried with magnesium sulfate and overlayed with ethanol (200 ml). The dichloromethane was removed under reduced pressure and the ethanol phase was put into the freezer (-20 °C) for 2 h. A white crystalline solid has been obtained by filtration. It was washed with cooled ethanol and dried on the high vacuum for 2h. (770 mg, 1.57 mmol, 59 %) [129]

^{1}H NMR (500 MHz, $CDCl_3$) δ/ppm: 8.72 (ddd, J = 4.8, 1.8, 0.9 Hz, 2H, H^{A6}), 8.53 (d, J= 1.6 Hz, 2H, H^{B3}), 8.50 (dt, J = 8.0, 1.1 Hz, 2H, H^{A3}), 7.90 – 7.86 (m, 4H, H^{C2}), 7.84 (dd, J = 7.8, 1.8 Hz, 2H, H^{A4}), 7.80 – 7.75 (m, 4H, H^{C3}), 7.47 (d, J= 1.6 Hz , 2H, H^{B5}), 7.34 (ddd, J = 7.5, 4.8, 1.2 Hz, 2H, H^{A5}), 2.74 (s, 6H, H^{Me}). **^{13}C NMR** (126 MHz, $CDCl_3$) δ/ppm: 158.6 (C^{B6}), 156.3 (C^{A2}), 156.13 (C^{B2}), 149.22, (C^{C4}), 149.20 (C^{A6}), 141.0 (C^{B4}), 137.8 (C^{C1}), 137.2 (C^{A4}), 127.8 (C^{C2}), 127.73 (C^{C3}), 124.1 (C^{A5}), 121.9 (C^{A3}), 121.4 (C^{B5}), 116.4 (C^{B3}), 25.0 (C^{Me}). **IR** (solid, ν, cm^{-1}): 3056 (w) 2959 (w) 2918 (w) 1911 (w) 1600 (m) 1580 (s) 1564 (s) 1545 (m) 1507 (m) 1472 (m) 1448 (m) 1425 (m) 1407 (m) 1389 (s) 1344 (m) 1260 (m) 1217 (m) 1111 (m) 1088 (m) 1074 (m) 1039 (m) 1004 (m) 988 (m) 964 (m) 907 (m) 888 (m) 848 (m) 821 (s) 791 (s) 740 (s) 732 (s) 681 (m) 667 (m) 647 (m) 628 (m) 620 (s) 582 (m) 564 (m) 548 (m) 525 (m) 498 (m) **MP**: 240 °C **UV-Vis**

(λ_{max} nm [ε/ $dm^{-3} \cdot mol^{-1} \cdot cm^{-1}$] CH_2Cl_2, c = $1.00 \cdot 10^{-5} \cdot mol \cdot l^{-1}$): 306 nm [57395] **Luminescence** ([nm], CH_2Cl_2, c = $1.00 \cdot 10^{-5}$ mol $\cdot$ l^{-1}, λ_{ex} = 306 nm): λ_{em} = 360, 377 **Elem. Anal.** Calcd. for $C_{34}H_{26}N_4$: C 83.24, H 5.34, N 11.42; found: C 83.49, H 5.43, N 11.54.

Synthesis of (E)-3-(4-bromophenyl)-1-(6-methylpyridin-2-yl)prop-2-en-1-one

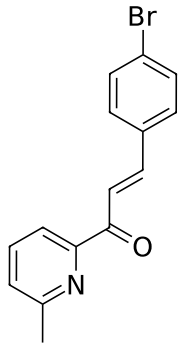

4-Bromobenzaldehyde (3.35 g, 18.1 mmol, 1.0 eq) and 6-methyl-2-acetylpyridine (2.47 g, 18.1 mmol, 1.0 eq) were dissolved in methanol (81.0 ml). Sodium hydroxide (17.0 ml, aqueous 2 %wt) was added whereupon the solution turned green. The reaction mixture was left to stir at room temperature for 4 h. The formed white precipitate was collected by filtration and washed carefully with water and methanol (3 x 20.0 ml each). The resulting light green solid was dried in a desiccator for 12 h. (4.70 g, 15.5 mmol, 85%) Analytics are in agreement with the literature. [135]

Synthesis of 4-(4-bromophenyl)-6,6'-dimethyl-2,2'-bipyridine (DiMe/2)

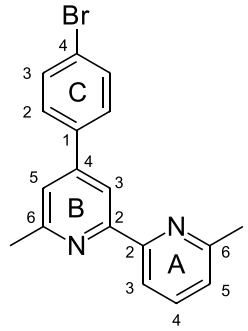

(E)-3-(p-Bromophenyl)-1-(6-methyl-2-pyridyl)-2-propen-1-one (2.00 g, 6.60 mmol, 1,0 eq) was dissolved in methanol (90.0 ml) and 1-(2-oxopropyl)pyridinium chloride (1.14 g, 6.60 mmol, 1.0 eq) was added. The reaction mixture was treated with ammonium acetate (15.3 g, 198 mmol, 30 eq) and refluxed for 24 h afterwards. It was left to cool down and put into the fridge overnight. A precipitate had formed which was filtered and washed with water and methanol (3 x 15.0 ml each). After drying in the desiccator over night, a light brown solid was isolated. (830 mg, 2.44 mmol, 37%). [135]

^{1}H NMR (500 MHz, $CDCl_3$) δ/ppm: 8.46 (s, 1H, H^{B3}), 8.28 (d, J = 7.8 Hz, 1H, H^{A3}), 7.74 (t, J = 7.7 Hz, 1H, H^{A4}), 7.68 - 7.56 (m, 4H, $H^{C2/C3}$), 7.36 (d, J = 1.6 Hz, 1H, H^{B5}), 7.20 (dd, J = 7.5, 0.9 Hz, 1H, H^{A5}), 2.71 (s, 3H, H^{MeB}), 2.68 (s, 3H, H^{MeA}) **^{13}C NMR** (126 MHz, $CDCl_3$) δ/ppm: 158.68 (C^{B2}), 158.11 (C^{A2}), 156,16 (C^{B6}), 155.13 (C^{A6}), 148.78 (C^{B4}), 137.68 (C^{A4}), 137.63 (C^{C1}), 132.22 (C^{C3}), 128.95 (C^{C2}), 123.79 (C^{A5}), 123.56 (C^{C4}), 121.10 (C^{B5}), 118.98 (C^{A3}), 116.68 (C^{B3}), 24.74 (C^{MeB}), 24.63 (C^{MeA}). **IR** : 2917 (w) 1607

(w) 1573 (m) 1545 (m) 1490 (m) 1458 (w) 1415 (m) 1381 (m) 1366 (m) 1258 (m) 1209 (w) 1157 (w) 1104 (w) 1075 (w) 1008 (m) 913 (w) 898 (w) 861 (w) 823 (s) 801 (s) 782 (m) 745 (m) 715 (m) 683 (s) 646 (m) 589 (s) 573 (s) 552 (s) 534 (s) 517 (s) 479 (m) **MS** (MALDI m/z): 339.12 $[M+H]^+$ (calc:338.04) **UV-Vis** (λ_{max} nm [ε/ $dm^{-3} \cdot mol^{-1} \cdot cm^{-1}$] CH_2Cl_2, c = $1.00 \cdot 10^{-5} \cdot mol \cdot l^{-1}$): 249 nm [31859], 272 nm [24878], 309 nm [sh, 13794] **Luminescence** ([nm], CH_2Cl_2, c = $1.00 \cdot 10^{-5}$ mol $\cdot l^{-1}$, λ_{ex} = 249 nm): λ_{em} = 356 **Elem. Anal.** Calcd. for $C_{18}H_{15}BrN_2$: C 63.73, H 4.46, N 8.26; found: C 63.59, H 4.64, N 8.61.

Synthesis of 4,4'-bis(6,6'-dimethyl-[2,2'-bipyridin]-4-yl)-1,1'-biphenyl (DiMe)

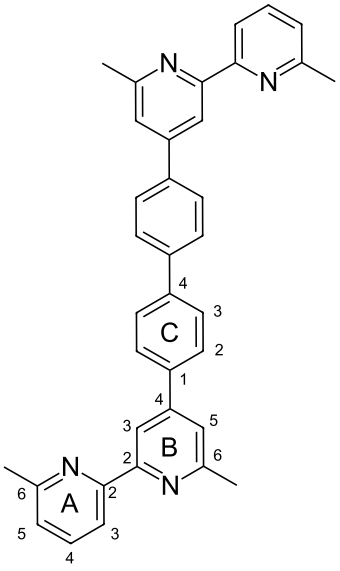

Triphenylphosphine (6.19 g, 23.6 mmol, 8.0 eq) and nickel(II)chloride hexahydrate (1.4 g, 5.90 mmol, 2.0 eq) were dissolved in dimethylformamide (30 ml) under a nitrogen atmosphere. Zinc powder (0.39 mg, 5.90 mmol, 2.0 eq) was added and the solution was left to stir for 1 h at 50 °C, whereupon it turned dark red. 4-(4-Bromophenyl)-6,6'-dimethyl-2,2'-bipyridine (2.00 g, 5.90 mmol, 2.0 eq) was added and the mixture was left stirring at 50 °C for further 12 h after which the staring material had been consumed (reaction control with TLC on silica, cyclohexane:EtOAc, 9:3). The reaction mixture was poured onto a diluted aqueous ammonia solution (200 ml, 10%) and extracted with dichloromethane (3 x 50.0 ml). The powder which had stayed in the organic phase was filtered off, recrystallized in toluene and washed with toluene and ethanol and to give colourless needles which were dried on the high vacuum for 2h. (430 mg, 0.829 mmol, 28 %) [129]

^{1}H NMR (500 MHz, MeCN) δ/ppm: 8.64 (s, 2H, H ^{B3}), 8.42 (s, 2H, H^{A3}), 7.95 - 7.90 (m, 4H, H^{C2}) 7.84 - 7.76 (m, 6H, H^{A4}+H^{C3}), 7.52 (s, 2H, H^{B5}), 7.25 (d, 2H, H^{A5}, 2.81 (s, 3H, $H^{B_{Me}}$), 2.73 (s, 3H, $H^{A_{Me}}$). **^{13}C NMR** (126 MHz, $CDCl_3$) δ/ppm: 158.17 (C^{B2}), 157.95 (C^{A2}), 156.40 $C^{A6/B6}$, 149.95 (C^{B4}), 141.27 (C^{C4}), 138.03 (C^{A4}), 137.44 (C^{C1}), 128.01 (C^{C2}), 127.87 (C^{C3}), 124.04 (C^{A5}), 121.48 (C^{B5}), 119.51 (C^{A3}), 117.35 (C^{B3}), 24.27 ($C^{A_{Me}}$), 24.09 ($C^{B_{Me}}$). **IR** (solid, ν, cm^{-1}): 3673 (w) 2989 (w) 2915 (w) 1604 (m) 1583 (s) 1539 (s) 1506 (m) 1459 (m) 1431 (m) 1414 (m) 1390 (m) 1259 (w) 1218 (w) 1158 (w) 1117 (w) 1074 (m) 1033 (m) 1005 (m) 896 (m) 874 (m) 859 (m) 850 (m) 848 (m) 829 (m) 820 (m) 805 (s) 779 (m) 750. (m) 661 (m) 625 (s) 593 (w) 571 (w) 554 (m) 536 (m) 527 (m) 515 (m) 500 (m). **MP:** 308 °C **UV-Vis** (λ_{max} nm [ε/ $dm^{-3} \cdot mol^{-1} \cdot cm^{-1}$] CH_2Cl_2, c = $1.00 \cdot 10^{-5} \cdot mol \cdot$

l^{-1}): 304 nm [71005] **Luminescence** ([nm], CH_2Cl_2, c = $1.00 \cdot 10^{-5}$ mol $\cdot$ l^{-1}, λ_{ex} = 303 nm): λ_{em} = 360, 377 **Elem. Anal.** Calcd. for $C_{36}H_{30}N_4$: C 83.37, H 5.83, N 10.80; found: C 83.53, H 5.92, N 10.81.

Synthesis of 4-nitro-2,2'-bipyridine N-oxide

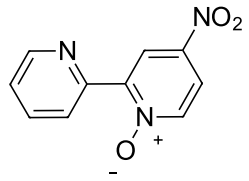

2,2'-Bipyridine N-oxide (5.00 g, 29.0 mmol, 1.0 eq.) was dissolved and sulphuric acid (95 %, 12.5 ml). A mixture of nitric acid (fuming, 100 %, 15.0 ml) in sulphuric acid (95 %, 10.0 ml) was added. To trap nitrous gases, a gas wash bottle charged with 1 M aqueous K_2CO_3 solution was attached. After refluxing for 6 h, the mixture was poured slowly into ice (200g). Once the ice had dissolved, the mixture was carefully rendered slightly basic with K_2CO_3. The formed precipitate was filtered off, suspended in 100 ml of water and stirred for 1 h. The suspension was filtered again. The remaining solid dissolved in dichloromethane and dried over magnesium sulphate. Removing the solvent under reduced pressure yielded a white solid. (3.14 g, 14.5 mmol, 48 %). [132] Analytics fit well with the literature. [132, pp. 161]

Synthesis of 4-bromo-2,2'-bipyridine N-oxide

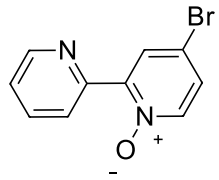

In a nitrogen atmosphere, 4-nitro-2,2'-bipyridine N-oxide (3.14 g, 14.4 mmol, 1.0 eq.) and acetyl bromide (9.42 ml, 127 mmol, 8.8 eq.) were dissolved in 44.0 ml glacial acetic acid and refluxed for 4 h at 120 °C. The mixture was poured into ice (32.0 g), neutralized afterwards with Na_2CO_3 and extracted with dichloromethane (3 x 50.0 ml). The organic layers were washed with cold water (15.0 ml) and dried with Na_2SO_4 and the solvent was removed under reduced pressure. The mixture of 4-bromo-2,2'-bipyridine N-oxide and 4-bromo-2,2'-bipyridine was subjected to column chromatography (Silica 60 neutral, ethyl acetate/cyclohexane/triethylamine 40:13:1) to give 4-bromo-2,2'-bipyridine (0.910 g, 3.87 mmol, 27 %, R_f= 0.9) and 4-bromo-2,2'-bipyridine N oxide (2.12 g, 8.44 mmol, 59 %, R_f= 0.2). Analytical data fits well with the literature. [137]

Synthesis of 4-bromo-2,2'-bipyridine

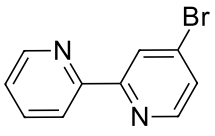

In a nitrogen atmosphere, 4-Bromo-2,2'-bipyridine N-oxide (2.12 g, 8.44 mmol, 1.0 eq.) was dissolved in 25.0 ml of dry chloroform and cooled to 0 °C with an ice bath. Phosphorus tribromide (7.30 g, 2.60 ml, 27.0 mmol, 3.2 eq.) was added slowly, whereupon a precipitate had formed. The mixture was refluxed for 4 h, poured into ice water (20.0-30.0 ml) and rendered basic with 6M sodium hydroxide solution. After extraction with $CHCl_3$, the organic phase was dried over magnesium sulphate. Evaporation of the solvent under reduced pressure yielded the product as a brown solid (1.85 g, 7.87 mmol, 93 %, R_f= 0.9) [137]

Analytical data fits well with the literature. [137]

Synthesis of 2,2'-4',4"-2",2"'-quaterpyridine (NoMe)

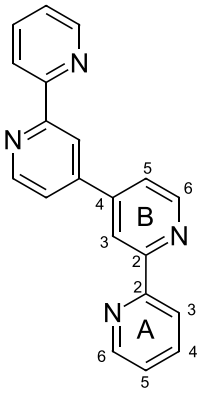

Triphenylphosphine (4.51 g, 17.2 mmol, 8.0 eq) and nickel(II) chloride hexahydrate (1.03 g, 4.3 mmol, 2.0 eq) were dissolved in dimethylformamide (25.0 ml) under a nitrogen atmosphere. Zinc powder (0.300 g, 4.3 mmol, 2.0 eq) was added and the solution was left to stir for 1 h at 50 °C. No color change was obtained after this time, so more zinc (this time the zinc was activated). To achieve activation, the zinc was suspended in water in a test tube and treated with a few droplets of HCl (37 %). After letting it bubble for a minute or two, the zinc was washed with water/ethanol/diethyl ether subsequentially by decanting.) was added, whereupon the mixture finally had turned dark red. It was left to stir for another hour. 4-Bromo-2,2'-bipyridine (1.02 g, 4.30 mmol, 2.0 eq.) was added and the mixture was left stirring at 50 °C for further 12 h after which the starting material had been consumed (reaction control with TLC on silica, ethyl acetate/cyclohexane/triethylamine, 40:13:1). The reaction mixture was poured into a diluted aqueous ammonia solution (150 ml, 32%) and extracted with dichloromethane (3 x 50.0 ml). The organic phase was washed with water and dried over magnesium sulphate. The solvent was removed under reduced pressure to yiel the crude product. A column (silica, methanol/dichloromethane, 1:99) followed by recrystallisation in ethanol yielded a white solid which was dried on the high vacuum pump for 1 h. (130 mg, 0.419 mmol, 19 %) [129]

^{1}H NMR (500 MHz, MeCN) δ/ppm: 8.82 (m, 4H, H $^{B3/B6}$), 8.73 (ddd, J = 4.8, 1.8, 0.9 Hz, 2H, H^{A6}), 8.50 (dt, J = 8.0, 1.1 Hz, m, 2H, H^{A3}), 7.88 (td, J = 7.7, 1.8 Hz, 2H, H^{A4}), 7.72 (dd, J = 5.1, 1.9 Hz, 2H, H^{B5}) 7.37 (ddd, J = 7.5, 4.8, 1.2 Hz, 2H, H^{A5}).[133] **^{13}C NMR** (126 MHz, $CDCl_3$) δ/ppm: 156.8 C^{A}2, 155.5 C^{B2}, 145.0 (C^{B6}), 149.0 (C^{A6}), 146.9 (C^{B4}), 137.31 (C^{A4}), 124.16 (C^{A5}), 121.7 (C^{B5}), 121.5 (C^{A3}), 119.1 (C^{B3}). **IR** (solid, ν, cm^{-1}): 3055 (w) 1593 (w) 1577 (s) 1563 (s) 1532 (s) 1451 (s) 1437 (s) 1368 (s) 1271 (w) 1245 (w) 1128 (w) 1089 (m) 1065 (m) 1040 (m) 987 (m) 893 (m) 829 (m) 788 (s) 743 (s) 665 (s) 619 (s) 575 (s) 454 (m) **MP:** 308 °C **MS** (MALDI m/z): 311.0 $[M+H]^+$ (calc:311.1) **UV-Vis** (λ_{max} nm [ε/ dm^{-3} · mol^{-1}· cm^{-1}] CH_2Cl_2, c = 1.00 · 10^{-5} · mol · l^{-1}): 241 nm [44886], 284 [28291] **Luminescence** ([nm], CH_2Cl_2, c = 1.00 · 10^{-5} mol · l^{-1}, λ_{ex} = 241 nm): λ_{em} = 349, 426 (sh) **Elem. Anal.** Calcd. for $C_{20}H_{14}N_4$: C 77.40, H 4.55, N 18.05; found: C 76.93, H 4.70, N 18.52.

Synthesis of bis(2,2-bipyridine-N,N')(4,4'-bis(6-methyl-[2,2'-bipyridin]-4-yl)-1,1'-biphenyl-N,N')ruthenium(II) hexafluorophosphate ($[Ru(bpy)_2(MonoMe)][PF_6]_2$)

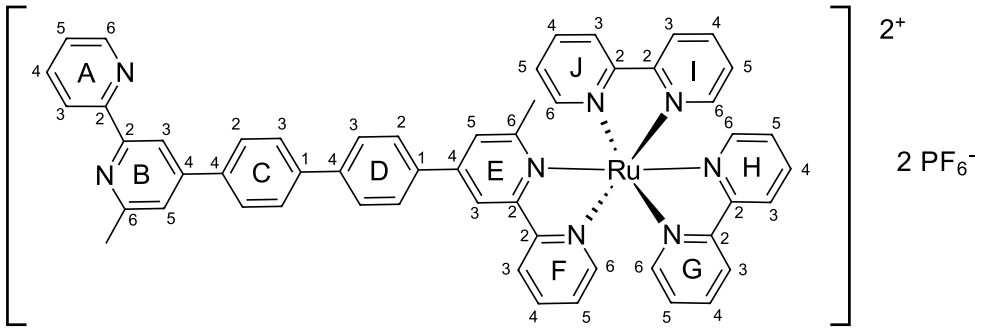

Cis-Dichlorobis(bipyridine)ruthenium(II) (200 mg, 0.413 mmol, 1.0 eq) and 6'-methyl-4-[p-(6'-methyl-1,4'-biphenyl-4-yl)phenyl]-2,2'-bipyridyl (MonoMe, 200 mg, 0.408 mmol, 1.0 eq) were suspended in ethanol (15.0 ml) and irradiated in a microwave reactor for 1.5 h at 120 °C. After adding an excess of ammonium hexafluorophosphate, the mixture was left to stir for 20 min, whereupon an orange precipitate had formed. It was filtered off and washed with water, ethanol and ether susequentially (20.0 ml each). The solid was dissolved in acetonitrile, dried over magnesium sulphate and the solvent was removed under reduced pressure. The crude product was subjected to column chromatography (Alox 90 neutral, acetonitrile/saturated aqueous potassium nitrate solution/water (A-SOL), 17:1:0.5) to isolate the two top spots (R_f=1). The solvent was removed under reduced pressure and the residue dissolved in water. An excess of ammonium hexafluorophosphate was added. The resulting precipitate was filtered off and washed carefully with water, ethanol and ether susequentially. A second column was done (Alox 60 basic, toluene/acetonitrile, 3:2, R_f=0.5) and the top spot was isolated. The solvent was removed under reduced pressure to yield an orange solid. (110 mg, 0.122 mmol, 29 %). [138, pp. 206]

^{1}H NMR (500 MHz, CD_2Cl_2) δ/ppm: 8.67 (ddd, J = 4.7, 1.9, 0.9 Hz, 1H, H^{A6}), 8.62 (d, J = 8.3 Hz, 1H, $H^{F3/G3/H3/I3/J3}$), 8.58 (d, J = 2.2 Hz, 1H, $H^{E3/B3}$), 8.54 (d, J = 1.6 Hz, 1H, $H^{E3/B3}$), 8.53 – 8.46 (m, 3H, H^{A3} + $2H^{F3/G3/H3/I3/J3}$), 8.46 – 8.38 (m, J = 10.5, 8.1, 1.0 Hz, 2H, $H^{F3/G3/H3/I3/J3}$), 8.16 – 8.05 (m, 4H, H^{F6} + $3H^{F4/G4/H4/I4/J4}$), 8.02 (td, J = 7.9, 1.5 Hz, 1H, $H^{F4/G4/H4/I4/J4}$), 8.00 – 7.93 (m, 3H, $H^{F4/G4/H4/I4/J4}$ + 2H $^{D2/C3}$), 7.91 – 7.83 (m, 5H, H^{A4} +$H^{C2/C3/D2/D3}$), 7.81 (d, J = 8.5 Hz, 2H, $H^{C2/D3}$), 7.73 (dd, J = 5.7, 1.3 Hz, 1H, $H^{F6/G6/H6/I6/J6}$), 7.68 – 7.62 (m, 2H, $H^{F6/G6/H6/I6/J6}$ + $H^{B5/E5}$), 7.57 – 7.51 (m, 2H, $H^{F5/G5/H5/I5/J5}$ + $H^{F6/G6/H6/I6/J6}$), 7.51 – 7.44 (m, 3H, $H^{B5/E5}$ + $H^{F5/G5/H5/I5/J5}$ + $H^{F6/G6/H6/I6/J6}$, 7.42 – 7.31 (m, 4H, H^{A5} + $3H^{F5/G5/H5/I5/J5}$), 2.69 (s, 3H, $H^{B_{Me}}$), 1.97 (s,

3H, $H^{E_{Me}}$). **^{13}C NMR** (126 MHz, CD_2Cl_2) δ/ppm: 165.5 ($C^{E6/B6}$), 159.1 ($C^{B6/E6}$), 158.7 + 157.9 + 157.5 + 157.4 + 157.3 + 157.0 + 156.4 + 156.3 (8C, $C^{A2,B2+E2-J2}$), 153.0 (C^{F6}), 151.7 + 151.5 + 151.4 (4C, $C^{G6/H6/I6/J6}$), 150.3 ($C^{B4/E4}$), 149.5 (C^{A6}), 149.16 ($C^{B4/E4}$), 143.0 ($C^{C1/D4}$), 140.7 ($C^{C1/D4}$), 139.0 ($C^{F4/G4/H4/I4/J4}$), 138.7 (2C, $C^{F4/G4/H4/I4/J4}$), 138.60 ($C^{C4/D1}$), 138.5 ($C^{F4/G4/H4/I4/J4}$), 138.3 ($C^{F4/G4/H4/I4/J4}$), 137.6 (C^{A4}), 134.8 $C^{C4/D1}$, 128.9 $C^{F5/G5/H5/I5/J5}$, 128.7 ($C^{F5/G5/H5/I5/J5}$), 128.5 (2C, $C^{C2/C3/D2/D3}$), 128.4 (C^{A5}), 128.3 + 128.2 + 128.16 (6C, $C^{C2/C3/D2/D3}$), 128.07 ($C^{F5/G5/H5/I5/J5}$), 1 $C^{F5/G5/H5/I5/J5}$ hidden underneath signals 128.53/128.36/128.19/128.16, 126.5 ($C^{B5/E5}$), 125.4 + 125.1 + 125.01 + 124.9 + 124.8 (5C, $C^{F3/G3/H3/I3/J3}$), 124.4 ($C^{F5/G5/H5/I5/J5}$), 121.7 (C^{A3}), 121.5 ($C^{B5/E5}$), 120.0 ($C^{B3/E3}$), 116.3 ($C^{B3/E3}$), 26.70 ($C^{B_{Me}/E_{Me}}$), 24.90 ($C^{B_{Me}/E_{Me}}$), **IR** (solid, ν, cm^{-1}): 3664 (w) 2919 (w) 1671 (w) 1603 (m) 1584 (m) 1566 (w) 1505 (w) 1462 (m) 1446 (m) 1392 (m) 1241 (m) 1162 (m) 1066 (m) 1003 (m) 827 (s) 761 (s) 730 (s) 682 (m) 620 (m) 555 (s). **MS** (ESI m/z): 452.10 $[M\text{-}2PF_6]^{2+}$ (calc: 452.13) **UV-Vis** (λ_{max} nm [ε/ $dm^{-3} \cdot mol^{-1} \cdot cm^{-1}$] MeCN, $c = 1.00 \cdot 10^{-5} \cdot mol \cdot l^{-1}$): 245 nm [35874], 289 nm 86085], 254 [sh, 31580], 331 [sh, 43802], 424 [sh, 13411], 453 nm [17045] **Luminescence** ([nm], MeCN, $c = 1.00 \cdot 10^{-5}$ $mol \cdot l^{-1}$, $\lambda_{ex} = 453$ nm): $\lambda_{em} = 375$, 615, 648 (sh) **Elem. Anal.** Calcd. for $C_{54}H_{42}N_8F_{12}P_2Ru_1$ + 1 H_2O: C 53.51, H 3.49, N 9.25; found: C 53.48, H 4.14, N 9.12.

Appendix 6.A SECM area scans of DSC electrodes

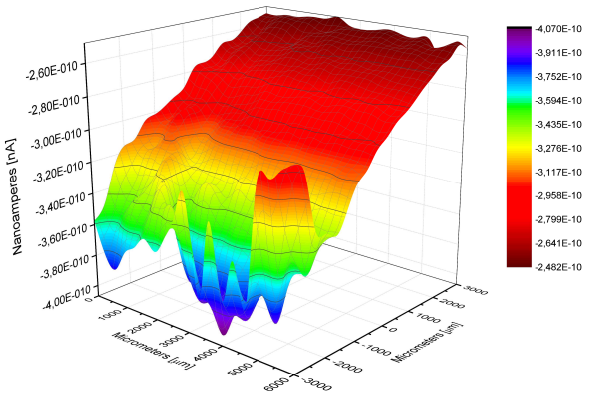

(a) Al-Cu-Bl measured in the dark.

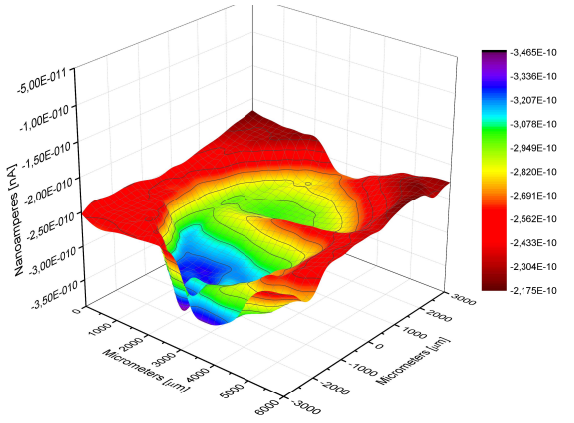

(b) Al-Cu-Bl measured under illumination.

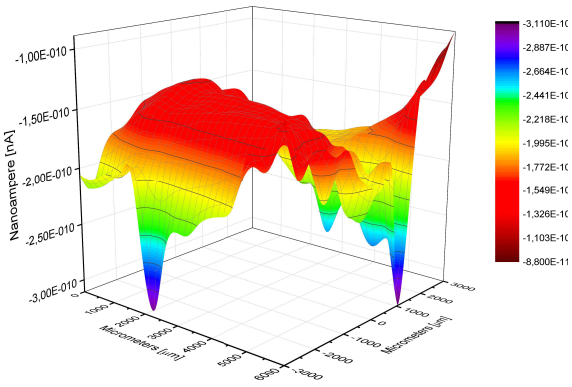

(c) Al-Cu-Bl-Cu-Bl measured in the dark.

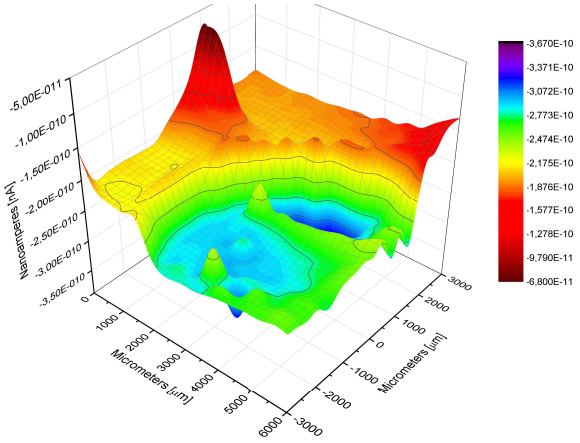

(d) Al-Cu-Bl-Cu-Bl measured under illumination.

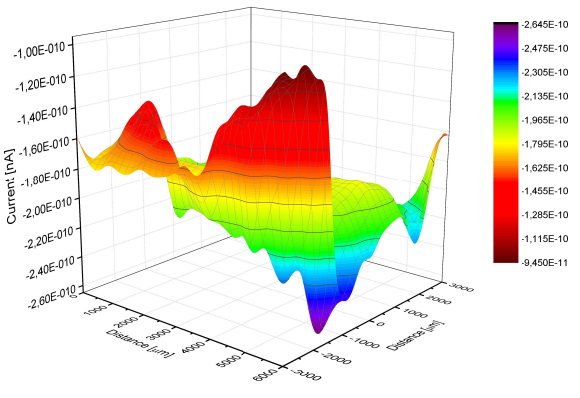

(e) Al-Cu-Bl-Cu-Bl-Cu-Bl measured in the dark.

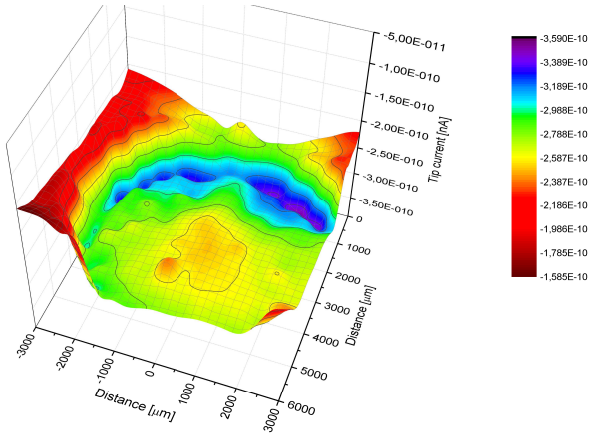

(f) Al-Cu-Bl-Cu-Bl-Cu-Bl measured under illumination.

Figure 6.23: SECM area scans of dyed TiO_2 electrodes measured in the dark ((a), (c), (e)) and under illumination ((b), (d), (f))

Appendix 6.B MALDI-TOF measurement of an ALP1-Cu-DiMe-Cu-DiME-Cu-DiMe TiO_2 electrode.

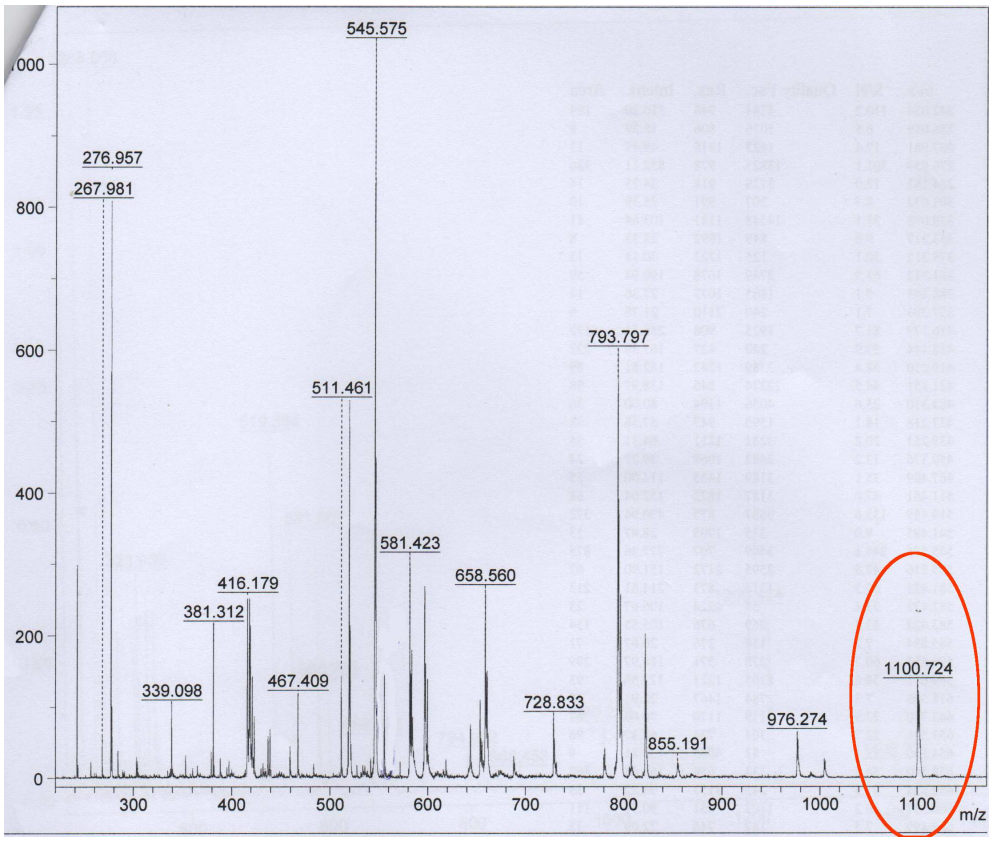

Figure 6.24: The encircled peak is the highest identified Mass of the metalorganic chain. It belongs to DiMe-Cu-DiMe: 1100.72 $[M+H]^+$ (calc:1099.42).

Appendix 6.C LeDSC measurements over time

Days after sealing [#] →		**0**	**11**	**14**	**21**
η [%] →	N719 Cell1	7.14	5.72	6.94	6.63
	N719 Cell2	7.17	5.34	6.56	6.36
	ALP1-Cu-DiMe Cell1	2.16	2.38	2.44	2.40
	ALP1-Cu-DiMe Cell2	2.18	2.26	2.37	2.37
	ALP1-Cu-MonoMe Cell1	1.69	1.90	1.82	1.94
	ALP1-Cu-MonoMe Cell2	1.56	1.94	1.96	1.93
	ALP1-Cu-NoMe Cell	1.06	1.43	1.45	1.42
ff [%] →	N719 Cell1	73.3	70.2	70.9	71.3
	N719 Cell2	72.9	70.6	70.7	71.7
	ALP1-Cu-DiMe Cell1	73.3	69.6	68.5	70.1
	ALP1-Cu-DiMe Cell2	74.0	70.9	69.7	71.3
	ALP1-Cu-MonoMe Cell1	73.7	72.0	72.7	73.1
	ALP1-Cu-MonoMe Cell2	72.1	67.6	66.3	67.7
	ALP1-Cu-NoMe Cell	72.3	70.2	68.7	70.5
$\mathbf{V}_{OC}$ **[mV]** →	N719 Cell1	630	643	664	652
	N719 Cell2	628	655	670	653
	ALP1-Cu-DiMe Cell1	566	599	602	587
	ALP1-Cu-DiMe Cell2	573	599	606	594
	ALP1-Cu-MonoMe Cell1	548	585	595	589
	ALP1-Cu-MonoMe Cell2	526	595	596	583
	ALP1-Cu-NoMe Cell	506	557	566	559
$\mathbf{J}_{SC}$ $[\mathbf{mA/cm^2}]$ →	N719 Cell1	15.5	12.7	14.7	14.3
	N719 Cell2	15.7	11.6	13.9	13.6
	ALP1-Cu-DiMe Cell1	5.20	5.72	5.92	5.83
	ALP1-Cu-DiMe Cell2	5.13	5.33	5.62	5.60
	ALP1-Cu-MonoMe Cell1	4.18	4.49	4.22	4.52
	ALP1-Cu-MonoMe Cell2	4.11	4.84	4.95	4.89
	ALP1-Cu-NoMe Cell	2.89	3.65	3.72	3.60

Table 6.6: Parameters over time for liquid electrolyte DSCs.

Appendix 6.D PEDOT ssDSC measurements over time

Days after sealing [#] →		**1**	**2**	**12**	**15**	**22**
η [%] →	N719 Cell	2.33	3.34	2.97	3.00	3.02
	ALP1-Cu-MonoMe Cell1	0.448	0.675	0.876	0.832	–
	ALP1-Cu-MonoMe Cell2	0.538	0.655	0.775	0.758	0.831
	ALP1-Cu-DiMe Cell1	0.771	0.937	0.918	0.898	0.925
	ALP1-Cu-DiMe Cell2	0.673	0.741	1.03	1.07	1.03
ff [%] →	N719 Cell	60.36	72.2	69.1	67.8	65.4
	ALP1-Cu-MonoMe Cell1	65.5	69.8	66.0	62.6	–
	ALP1-Cu-MonoMe Cell2	66.5	68.1	70.9	71.3	68.7
	ALP1-Cu-DiMe Cell1	63.8	69.3	72.2	73.7	72.4
	ALP1-Cu-DiMe Cell2	62.7	61.5	72.7	68.8	66.1
$\mathbf{V}_{OC}$ **[mV]** →	N719 Cell	397	492	485	494	464
	ALP1-Cu-MonoMe Cell1	447	515	551	561	–
	ALP1-Cu-MonoMe Cell2	430	508	513	520	491
	ALP1-Cu-DiMe Cell1	418	494	496	502	468
	ALP1-Cu-DiMe Cell2	440	474	521	535	524
$\mathbf{J}_{SC}$ $\mathbf{[mA/cm^2]}$ →	N719 Cell	9.72	9.40	8.88	8.96	9.96
	ALP1-Cu-MonoMe Cell1	1.53	1.88	2.41	2.37	–
	ALP1-Cu-MonoMe Cell2	1.88	1.90	2.13	2.05	2.46
	ALP1-Cu-DiMe Cell1	2.89	2.74	2.56	2.43	2.73
	ALP1-Cu-DiMe Cell2	2.44	2.54	2.72	2.91	2.96

Table 6.7: PEDOT ssDSC parameters over time. The cell MonoMe Cell1 fell apart on day 22, therefore no values were obtained.

Chapter 7

Conclusion

TiO_2 nanoparticles and pastes have been self fabricated and applied successfully in reproducible leDSCs. Furthermore, self made scattering layers have been applied to leDSCs, which enhanced the efficiency of our cells.

Working, but non-reproducible CuI ssDSCs have been fabricated. A previously non-reported dye has been assembled on the TiO_2 surface by incorporating the HTM directly into the light absorbing species (ALP1-Cu-HTM).

Successful assembly and reproducibility of ssDSCs featuring a solid state PEDOT HTM has been achieved with the standard dye N719. They have been stable in ambient atmosphere over 22 days and potentially more.

Additionally, two not previously reported back to back ligands (MonoMe and DiMe) have been investigated for performance in leDSCs and PEDOT ssDSCs.

Multinuclear copper species involving back to back ligands have been assembled on the TiO_2 surface. The performance in leDSCs decreased the longer the chain was presumably built. A dinuclear mixed metal species incorporating copper(I) and ruthenium(II) (ALP1-Cu-RuMonoMe) has been built up on the TiO_2 surface and resulted in a current gain respective to it's mononuclear counterpart (ALP1-Cu-MonoMe) in leDSCs. Furthermore, one previously reported (NoMe) bipyridine back to back ligand has been tested in leDSCs.

References

[1] YNHTI, Montagna, J. A., *The Industrial Revolution*, http://www.yale.edu/ynhti/curriculum/units/1981/2/81.02.06.x.html.

[2] D. Baxby, *Vaccine*, 1999, **17**, 301–307.

[3] Mitsubishi Heavy Industries Ltd., *History of Fossil Fuel Usage since the Industrial Revolution*, https://www.mhi-global.com/discover/earth/issue/history/history.html.

[4] Beyond Petroleum p.l.c. (BP p.l.c.), *BP Statistical Review of World Energy June 2014*, 2014.

[5] K. Andreeν, V. Kantarová and J. Bongaarts, *Demographic Components of Future Population Growth*, tech. rep., United Nations, Department of Economic and Social Affairs, Population Division, Technical Paper No. 2013/3.

[6] Swiss Federal Office of Energy SFOE, *Fossil fuels*, http://www.bfe.admin.ch/themen/00486/?lang=en.

[7] Australian Government, Bureau of Meteorology, *The Greenhouse Effect and Climate Change*, 2007, http://www.bom.gov.au/info/climate/change/gallery/4.shtml.

[8] Scripps institution of Oceanography UC San Diego, *The Keeling Curve*, https://scripps.ucsd.edu/programs/keelingcurve/.

[9] pveducation.org, *The Greenhouse Effect*, http://pveducation.org/pvcdrom/introduction/greenhouse-effect.

[10] Intergovernmental Panel on Climate Change (ipcc), *What is the Greenhouse Effect*, 2007, http://www.ipcc.ch/publications_and_data/ar4/wg1/en/faq-1-3.html.

[11] Swiss Federal Office of Energy (SFOE), *Fossil fuels*, http://www.eia.gov/oiaf/1605/ggccebro/chapter1.html.

[12] Intergovernmental Panel on Climate Change The WGI Contribution to the IPCC 5th Assessment Report, *Climate Change 2013: The Physical Science Basis*, 2013, http://www.ipcc.ch/report/ar5/wg1/.

[13] W. R. L. Anderegg, J. W. Prall, J. Harold and S. H. Schneider, *Proceedings of the National Academy of Sciences of the United States of America*, 2010, **107**, 12107–12109.

[14] Scitable, by nature education, *Solar Energy*, 2013, http://www.nature.com/scitable/spotlight/solar-energy-8731061.

[15] W. Palz, *Power for the World: The Emergence of Electricity from the Sun*, Pan Stanford Publishing Pte. Ltd., 2011.

[16] Fraunhofer Institute For Solar Energy Systems ISE, *Photovoltaics Report*, 2014, http://www.ise.fraunhofer.de/en/downloads-englisch/pdf-files-englisch/photovoltaics-report-slides.pdf.

[17] Am. Chem. Soc., *How a Solar Cell Works*, 2013, http://www.acs.org/content/acs/en/education/resources/highschool/chemmatters/past-issues/archive-2013-2014/how-a-solar-cell-works.html?cq_ck=1396892718960.

[18] A. Yella, H.-W. Lee, H. N. Tsao, C. Yi, A. K. Chandiran, M. K. Nazeeruddin, E. W.-G. Diau, C.-Y. Yeh, S. M. Zakeeruddin and M. Grätzel, *Science (New York, N.Y.)*, 2011, **334**, 629–634.

[19] A. Hagfeldt, G. Boschloo, L. Sun, L. Kloo and H. Pettersson, *Chem.Rev.*, 2010, **110**, 6595–6663.

[20] S. Ito, M. K. Nazeeruddin, P. Liska, P. Comte, R. Charvet, P. Péchy, M. Jirousek, A. Kay, S. M. Zakeeruddin and M. Grätzel, *Prog. Photovolt. Res. Appl.*, 2006, **14**, 589–601.

[21] B. O'Regan and M. Grätzel, *Nature*, 1991, **353**, 737–740.

[22] S. Mathew, A. Yella, P. Gao, R. Humphry-Baker, B. F. E. Curchod, N. Ashari-Astani, I. Tavernelli, U. Rothlisberger, M. K. Nazeeruddin and M. Grätzel, *Nat. Chem.*, 2014, **6**, 242–247.

[23] Dyesol Ltd., *Solid or liquid*, http://www.dyesol.com/media/wysiwyg/Documents/dsc-resource-library/Solid_or_Liquid_-_July_2013.pdf.

[24] M. Zayat, P. Garcia-Parejo and D. Levy, *Chem. Soc. Rev.*, 2007, **36**, 1270–1281.

[25] M. Bertoz, J. Bisquert, F. De Angelis, H. Desilvestro, F. Fabregat-Santiago, S. Fantacci, A. Hagfeldt, S. Ito, K.-J. Jiang, K. Kalyanasundaram, P. V. Kamat, L. Kavan, J.-E. Moser, M. K. Nazeeruddin, L. Peter, H. J. Snaith, G. Tulloch, S. Uchida, S. Yanagida, J.-h. Yum, M. Grätzel and S. Yanagida, *Dye Sensitized Solar Cells*, ed. K. Kalyanasundaram, EPFL Press, first edition, 2010.

[26] Solaronix SA, *Solaronix, Technology*, 2014, http://www.solaronix.com/solarcells/technology/.

[27] Y. Guo, G. Liu, Z. Ren, A. Piyadasa and P.-X. Gao, *CrystEngComm.*, 2013, **15**, 8345–8352.

[28] R. Lomoth and S. Ott, *Dalton Trans.*, 2009, 9952–9959.

[29] L. Kavan, M. Grätzel, S. E. Gilbert, C. Klemenz and H. J. Scheel, 1996, **650**, 6716–6723.

[30] Y. Lee and M. Kang, *Mater. Chem. Phys.*, 2010, **122**, 284–289.

[31] B. E. Van, B. E. V. Kuiken, N. Huse, H. Cho, M. L. Strader and S Michael, *J. Phys. Chem. Lett.*, 2012, **3**, 1695–1700.

[32] F. Gao, Y. Wang, D. Shi, J. Zhang, M. Wang, X. Jing, R. Humphry-Baker, P. Wang, S. M. Zakeeruddin and M. Grätzel, *J. Am. Chem. Soc.*, 2008, **130**, 10720–10728.

[33] Dyesol LTD., *N719 Industry Standard Dye*, 2014, `http://www.dyesol.com/products/dsc-materials/dyes/n719-industry-standard-dye.html`.

[34] Z.-S. Wang, H. Kawauchi, T. Kashima and H. Arakawa, *Coord. Chem. Rev.*, 2004, **248**, 1381–1389.

[35] P. Pechy, F. P. Rotzinger, M. K. Nazeeruddin, O. Kohle, S. M. Zakeeruddin, R. Humphry-Baker and M. Gratzel, *J. Chem. Soc., Chem. Commun.*, 1995, **1**, 65–66.

[36] *Sintering*, `http://www.princeton.edu/~achaney/tmve/wiki100k/docs/Sintering.html`.

[37] G. Mann, *Print: A Manual for Librarians and Students Describing in Detail the History, Methods, and Applications of Printing and Paper Making*, London, Grafton & Co, 1952.

[38] J. Krüger, Ph.D. Thesis, École Polytechnique Fédérale de Lausanne, 2003.

[39] Solaronix SA, *Platisol T, Platinum Catalyst Precursor Paint*, `http://www.solaronix.com/notes/Note_Platisol_T.pdf`.

[40] B. Qi and J. Wang, *J. Mater. Chem.*, 2012, **22**, 24315–24325.

[41] S. Zhang, M. Yanagida, X. Yang and L. Han, 2011, **4**, 60–62.

[42] H. J. Snaith, *Energy. Environ. Sci.*, 2012, **5**, 6513–6520.

[43] F. J. Malzner, S. Y. Brauchli, E. Schönhofer, E. C. Constable and C. E. Housecroft, *Polyhedron*, 2014, **82**, 116–121.

[44] C. Schneider, W. Rasband and K. Eliceiri, *Nature Methods*, 2012, **9**, 671–675.

[45] A. Mcevoy, T. Markvart and L. Castañer, *Solar Cells: Materials Manufacture and Operation*, Elsevier Ltd., second edition, 2013.

[46] *Advanced Quantum Efficiency Analysis*, `http://www.kepu.dicp.ac.cn/photo/07sl02/+Thin-Film%20Crystalline%20Silicon%20Solar%20Cells%20Physics%20and%20Technology/3.pdf`.

[47] B. Bozic-Weber, E. C. Constable, S. O. Fürer, C. E. Housecroft, L. J. Troxler and J. A. Zampese, *Chem. Commun.*, 2013, **49**, 7222–7224.

[48] M. D. Products, *Automatic Surface Area Analyzer Mascorb® Series HM model-1200series, Principle*, 2011, http://mountech.co.jp/en/product/mountech/macsorb_process.html.

[49] Horiba Scientific, *BET Theory*, http://www.horiba.com/scientific/products/particle-characterization/technology/surface-area/.

[50] Particle Analytical, *Brunauer, Emmet and Teller (BET) Theory*, 2014, http://particle.dk/methods-analytical-laboratory/surface-area-bet/surface-area-bet-theory/.

[51] S. Brunauer, P. H. Emmett and E. Teller, *J. Am. Chem. Soc.*, 1936, **60**, 309–319.

[52] Zentrum für Mikroskopie der Universität Basel, *Wissenswertes ums- und über das Raster-Elektronenmikroskop*, https://zmb.unibas.ch/remtemlm/wissenswertes-ueber-das-raster-elektronenmikroskop/.

[53] JEOL Ltd., *Scanning Electron Eicroscope A To Z, Basic Knowledge For Using The SEM*, https://zmb.unibas.ch/fileadmin/zmb/redaktion/home/PDF/SEM_A_To_Z_light.pdf.

[54] E. Meyer, *Prog. Surf. Sci.*, 1992, **41**, 3–49.

[55] R Rajasekaran, *AFM Principles and Application in Biosciences*, 2008, www.advancedbiotech.in/32AFM.pdf.

[56] C. J. Martin, B. Bozic-Weber, E. C. Constable, T. Glatzel, C. E. Housecroft and I. A. Wright, *Electrochim. Acta*, 2014, **119**, 86–91.

[57] R. Nave, *Fermi Level*, http://hyperphysics.phy-astr.gsu.edu/hbase/solids/fermi.html#c1.

[58] *Quasi Fermi Energies*, http://www.tf.uni-kiel.de/matwis/amat/semi_en/kap_2/backbone/r2_3_2.html.

[59] H. J. Snaith, *Adv. Funct. Mater*, 2010, **20**, 13–19.

[60] S. Ito, T. N. Murakami, P. Comte, P. Liska, C. Grätzel, M. K. Nazeeruddin and M. Grätzel, *Thin Solid Films*, 2008, **516**, 4613–4619.

[61] V. K. Vendra, T. Nguyen, T. Druffel, D. A. Amos, J. Jasinski and K. S. Mahendra, *J. Mater. Chem. A*, 2014, **2**, 3543–3550.

[62] A. Zaban, S. T. Aruna, S. Tirosh, B. A. Gregg and Y. Mastai, *J. Phys. Chem. B*, 2000, **104**, 4130–4133.

[63] S. Siidergren, A. Hagfeldt and S.-E. Lindquist, *J. Phys. Chem.*, 1994, **98**, 5552–5556.

[64] F. Cao, G. Oskam, G. J. Meyer and P. C. Searson, *J. Phys. Chem.*, 1996, **100**, 17021–17027.

[65] M.-K. Son, H. Seo, S.-K. Kim, N.-Y. Hong, B.-M. Kim, S. Park, K. Prabakar and H.-J. Kim, *Int. J. Photoenergy*, 2012, **2012**, 1–8.

[66] T. Watson, C. Charbonneau, D. Bryant and D. Worsley, *Int. J. Photoenergy*, 2012, **2012**, 1–8.

[67] G. Boschloo and A. Hagfeldt, *Acc. Chem. Res.*, 2009, **42**, 1819–1826.

[68] I. Montanari, J. Nelson and J. R. Durrant, *J. Phys. Chem. B*, 2002, **106**, 12203–12210.

[69] B.-T. Xiong, B.-X. Zhou, Z.-Y. Zhu, T. Gao, L.-H. Li, J. Cai and W.-M. Cai, *Chin. J. Chem.*, 2008, **26**, 70–76.

[70] T. Stergiopoulos, E. Rozi, C.-S. Karagianni and P. Falaras, *Nanoscale Res. Lett.*, 2011, **6**, article number 307.

[71] P. Würfel, *Physics of Solar Cells: From Basic Principles to Advanced Concepts*, Wiley VCH, 2009.

[72] I. G. Yu, Y. J. Kim, H. J. Kim, C. Lee and W. I. Lee, *J. Mater. Chem.*, 2011, **21**, 532–538.

[73] Y. Wang, E. Chen, H. Lai, B. Lu, Z. Hu, X. Qin, W. Shi and G. Du, *Ceram. Int.*, 2013, **39**, 5407–5413.

[74] K. Tennakone, G. R. R. A. Kumara, A. R. Kumarasinghe, K. G. U. Wijayantha and P. M. Sirimanne, *Semicond. Sci. Technol.*, 1995, **10**, 1689–1693.

[75] U. Bach, D. Lupo, P. Comte, J. E. Moser, F. Weissörtel, J. Salbeck, H. Spreitzer and M. Grätzel, *Nature*, 1998, **395**, 583–585.

[76] D. K. Roh, W. S. Chi, H. Jeon, S. J. Kim and J. H. Kim, *Adv. Funct. Mater*, 2014, **24**, 379–386.

[77] A. Fujishima, Q.-B. Meng, K. Takahashi, X.-T. Zhang, I. Sutanto, T. Rao and O. Sato, *Langmuir*, 2003, **19**, 3572–3574.

[78] B. Peng, G. Jungmann, C. Jäger, D. Haarer, H.-W. Schmidt and M. Thelakkat, *Coord. Chem. Rev.*, 2004, **248**, 1479–1489.

[79] U. Bach, Ph.D. Thesis, École Polytechnique Fédérale de Lausanne, 2000.

[80] S. Dhiraj, G. D. Sharma and M. S. Roy, *Res. J. Chem. Sci.*, 2012, **2**, 61–71.

[81] M. Buchalska, J. Kuncewicz, E. Świtek, P. Labuz, T. Baran, G. Stochel and W. Macyk, *Coord. Chem. Rev.*, 2013, **257**, 767–775.

[82] T. Daeneke, T.-H. Kwon, A. B. Holmes, N. W. Duffy, U. Bach and L. Spiccia, *Nat. Chem.*, 2011, **3**, 211–215.

[83] G. Li, M. Liang, H. Wang, Z. Sun, L. Wang, Z. Wang and S. Xue, *Chem. Mater.*, 2013, **25**, 1713–1722.

[84] P. P. Boix, K. Nonomura, N. Mathews and S. G. Mhaisalkar, *Mater. Today*, 2014, **17**, 16–23.

[85] P. Gao, M. Grätzel and M. K. Nazeeruddin, *Energy. Environ. Sci.*, 2014, **1**, 2448–2463.

[86] R. Lessmann and I. A. Hümmelgen, *Mat. Res.*, 2004, **7**, 467–471.

[87] G. Kumara, M Okuya, K Murakami, S Kaneko, V. Jayaweera and K Tennakone, *J. Photochem. Photobiol. A*, 2004, **164**, 183–185.

[88] L. Kavan and M Grätzel, *Electrochim. Acta*, 1995, **40**, 643–652.

[89] S.-J. Moon, Ph.D. Thesis, École Polytechnique Fédérale de Lausanne, 2011.

[90] A. C. Arango, L. R. Johnson, V. N. Bliznyuk, Z. Schlesinger, S. A. Carter and H.-H. Hörhold, *Adv. Mater.*, 2000, **12**, 1689–1692.

[91] A. Konno and E. Premalal, *J. Photopolym. Sci. Technol.*, 2010, **23**, 279–282.

[92] S. Ito, P. Chen, P. Comte, M. K. Nazeeruddin, P. Liska and M. Grätzel, *Prog. Photovolt: Res. Appl.*, 2007, **15**, 603–612.

[93] J. A. Christians, R. C. M. Fung and P. V. Kamat, *J. Am. Chem. Soc.*, 2014, **136**, 758–64.

[94] M. Gu, P. Gao, X.-L. Liu, S.-M. Huang, B. Liu, C. Ni, R.-K. Xu and J.-M. Ning, *Materials Research Bulletin*, 2010, **45**, 636–639.

[95] W. H. Nguyen, C. D. Bailie, E. L. Unger and M. D. McGehee, *J. Am. Chem. Soc.*, 2014, **136**, 10996–11001.

[96] H. Snaith and L. Schmidt-Mende, *Adv. Mater.*, 2007, **19**, 3187–3200.

[97] J. Dewalque, P. Colson, G. K. V. Thalluri, F. Mathis, G. Chêne, R. Cloots and C. Henrist, *Org. Electro.*, 2014, **15**, 9–15.

[98] G. R. A. Kumara, S. Kaneko, M. Okuya and K. Tennakone, *Langmuir*, 2002, **18**, 10493–10495.

[99] A. Fujishima and X.-T. Zhang, *Proc. Jpn. Acad., Ser. B*, 2005, **81**, 33–42.

[100] V. Perera and K. Tennakone, *Sol. Energ. Mat. Sol. Cells*, 2003, **79**, 249–255.

[101] M. N. Amalina, A. A. E. Najwa, M. H. Abdullah, M. Z. Musa and M. Rusop, *IOP Conf. Ser.: Mater. Sci. Eng.*, 2013, **46**, article number 012012.

[102] J. Chen, J. Xia, K. Fan and T. Peng, *Electrochim. Acta*, 2011, **56**, 5554–5560.

[103] J. B. Ayers and W. H. Waggoner, *J. Inorg. Nucl. Chem.*, 1971, **33**, 721–733.

[104] T. Taguchi, X.-t. Zhang, I. Sutanto, K.-i. Tokuhiro, T. N. Rao, H. Watanabe, T. Nakamori, M. Uragami and A. Fujishima, *Chem. Commun.*, 2003, 2480–2481.

[105] B. Li, L. Wang, B. Kang, P. Wang and Y. Qiu, *Sol. Energ. Mat. Sol. Cells*, 2006, **90**, 549–573.

[106] P. M. Sirimanne and H. Tributsch, *J. Solid State Chem.*, 2004, **177**, 1789–1795.

[107] A. Kay and M. Grätzel, *Chem. Mater.*, 2002, **14**, 2930–2935.

[108] Q.-B. Meng, K. Takahashi, X.-T. Zhang, I. Sutanto, T. N. Rao, O. Sato and A Fujishima, *Langmuir*, 2003, **19**, 3572–3574.

[109] M. K. Nazeeruddin, A. Kay, E. Müller, I. Rodicio, P. Liska, N. Vlachopoulos and M. Grätzel, *J. Am. Chem. Soc.*, 1993, **115**, 6382–6390.

[110] Z. Zhang, Ph.D. Thesis, École Polytechnique Fédérale de Lausanne, 2008.

[111] B. Bozic-Weber, S. Y. Brauchli, E. C. Constable, S. O. Fürer, C. E. Housecroft, F. J. Malzner, I. A. Wright and J. A. Zampese, *Dalton Trans.*, 2013, **42**, 12293–12308.

[112] G. R. R. A. Kumara, A Konno and G. K. R. Senadeera, *Sol. Energ. Mat. Sol. C.*, 2001, **69**, 195–199.

[113] P. Qin, S. Tanaka, S. Ito, N. Tetreault, K. Manabe, H. Nishino, M. K. Nazeeruddin and M. Grätzel, *Nat. Commun.*, 2014, **5**, 1–6.

[114] J. K. Koh, J. Kim, B. Kim, J. H. Kim and E. Kim, *Adv. Mater.*, 2011, **23**, 1641–1646.

[115] P. M. Sirimanne, T. Jeranko, P. Bogdanoff and S. Fiechter, *Semicond. Sci. Technol.*, 2003, **18**, 708–712.

[116] N. Fukuri, N. Masaki, T. Kitamura, Y. Wada and S. Yanagida, *Journal of Physical Chemistry B*, 2006, **110**, 25251–25258.

[117] H. Meng, D. F. Perepichka and F. Wudl, *Angew. Chem. Int. Ed.*, 2003, **42**, 658–661.

[118] H. J. Snaith and M. Grätzel, *Appl. Phys. Lett.*, 2006, **89**, 262114 (3 pages).

[119] D. Bi, G. Boschloo and A. Hagfeldt, *Nano: Brief Reports and Reviews*, 2014, **09**, article number 1440001.

[120] A. Furube, R. Katoh, K. Hara, T. Sato, S. Murata, H. Arakawa and M. Tachiya, *Journal of Physical Chemistry B*, 2005, **109**, 16406–16414.

[121] J. Kim, J. K. Koh, B. Kim, S. H. Ahn, H. Ahn, D. Y. Ryu, J. H. Kim and E. Kim, *Adv. Funct. Mater*, 2011, **21**, 4633–4639.

[122] J. E. Kroeze, N. Hirata, S. Koops, K Nazeeruddin, L. Schmidt-Mende, M. Grätzel and J. R. Durrant, *J. Am. Chem. Soc.*, 2006, **128**, 16376–16383.

[123] B.-G. Kim, K. Chung and J. Kim, *Chem. Eur. J.*, 2013, **19**, 5220–5230.

[124] N. Alonso-Vante and J.-P. Sauvage, *Dalton Trans.*, 1994, **11**, 1649–1654.

[125] C.-W. Lee, H.-P. Lu, C.-M. Lan, Y.-L. Huang, Y.-R. Liang, W.-N. Yen, Y.-C. Liu, Y.-S. Lin, E. W.-G. Diau and C.-Y. Yeh, *Chem. Eur. J.*, 2009, **15**, 1403–1412.

[126] J. M. Cole, K. S. Low, H. Ozoe, P. Stathi, C. Kitamura, H. Kurata, P. Rudolf and T. Kawase, *Phys. Chem. Chem. Phys.*, 2014, DOI: `10.1039/c4cp02645d`.

[127] M. K. Nazeeruddin, P. Liska, J. Moser, N. Vlachopoulos and M. Gratzel, *Helv. Chim. Acta*, 1990, **73**, 1788–1803.

[128] S. Ardo and G. J. Meyer, *Chem. Soc. Rev.*, 2009, **38**, 115–164.

[129] M. Tiecco, L. Testaferri, M. Tingoli, D. Chianelli and M. Montanucci, *Synthesis*, 1984, **9**, 736–738.

[130] C. Janiak, *J. Chem. Soc., Dalton Trans.*, 2000, **21**, 3885–3896.

[131] G. Honey and P. Steel, *Acta Crystallogr. Sect. C-Cryst. Struct. Commun.*, 1991, **47**, 2247–2249.

[132] Ana Hernandez Redondo, Ph.D. Thesis, University of Basel, 2009.

[133] P. J. Steel, A. J. Downard, G. E. Honey and L. F. Phillips, *Inorg. Chem.*, 1991, **30**, 2259–2260.

[134] P. Rao, M. Amini, H. Li, A. G. Habeeb and E. E. Knaus, *Bioorg. Med. Chem. Lett.*, 2003, **13**, 2205–2209.

[135] J.-H. Li and M. Higuchi, *J Inorg Organomet Polym*, 2010, **20**, 10–18.

[136] C. Fan, X. Wang, P. Ding, J. Wang, Z. Liang and X. Tao, *Dyes Pigm.*, 2012, **95**, 757–767.

[137] K. Kodama, A. Kobayashi and T. Hirose, *Tetrahedron Lett.*, 2013, **54**, 5514–5517.

[138] P. Kopecky, Ph.D. Thesis, University of Basel, 2012.